Applications and high performance computing-based method developments for plasmon-adsorbate interactions

by

Olivia Hull

B.S., Wichita State University, 2017

AN ABSTRACT OF A DISSERTATION

submitted in partial fulfillment of the requirements for the degree

DOCTOR OF PHILOSOPHY

Department of Chemistry
College of Arts and Sciences

KANSAS STATE UNIVERSITY
Manhattan, Kansas

2023

Abstract

Plasmonic nanoparticles have been shown to facilitate bond breakage under mild conditions on molecules that are traditionally difficult to activate. However, the exact mechanism through which plasmonic nanoparticles drive reactions on nearby molecules is unclear. Modeling plasmonic photocatalysis is computationally demanding, typically requiring methods beyond the workhorse ground-state density functional theory (DFT). Our efforts focus on modeling this process, developing new methods to model this process, and enabling these methods to run faster and scale better in high performance computing environments. Herein, we first present investigations of plasmon-adsorbate interactions via time-dependent DFT and the non-adiabatic Ehrenfest dynamics method, finding that the dissociation process we investigate is symmetry- and electric field-dependent. Next, we apply a method we developed in the massively parallel BerkeleyGW code, called "subspace summation," to the problem of H_2 on gold to study the effects that individual bands produce on the collective modes of the system. Following this application, we describe our development efforts for the subspace summation method. Finally, we describe our efforts to alleviate parallel file I/O bottlenecks within the BerkeleyGW code, which enables significantly faster time-to-solution for systems requiring large amounts of compute resources.

Applications and high performance computing-based method developments for plasmon-adsorbate interactions

by

Olivia Hull

B.S., Wichita State University, 2017

A DISSERTATION

submitted in partial fulfillment of the requirements for the degree

DOCTOR OF PHILOSOPHY

Department of Chemistry
College of Arts and Sciences

KANSAS STATE UNIVERSITY
Manhattan, Kansas

2023

Approved by:

Major Professor
Christine M. Aikens

Copyright

Abstract

Plasmonic nanoparticles have been shown to facilitate bond breakage under mild conditions on molecules that are traditionally difficult to activate. However, the exact mechanism through which plasmonic nanoparticles drive reactions on nearby molecules is unclear. Modeling plasmonic photocatalysis is computationally demanding, typically requiring methods beyond the workhorse ground-state density functional theory (DFT). Our efforts focus on modeling this process, developing new methods to model this process, and enabling these methods to run faster and scale better in high performance computing environments. Herein, we first present investigations of plasmon-adsorbate interactions via time-dependent DFT and the non-adiabatic Ehrenfest dynamics method, finding that the dissociation process we investigate is symmetry- and electric field-dependent. Next, we apply a method we developed in the massively parallel BerkeleyGW code, called "subspace summation," to the problem of H_2 on gold to study the effects that individual bands produce on the collective modes of the system. Following this application, we describe our development efforts for the subspace summation method. Finally, we describe our efforts to alleviate parallel file I/O bottlenecks within the BerkeleyGW code, which enables significantly faster time-to-solution for systems requiring large amounts of compute resources.

Table of Contents

List of Figures

List of Tables

Acknowledgements

First and foremost, I would like to thank my advisor, Christine Aikens, for being an incredible mentor, for providing me the opportunity to work on the projects contained herein, for her guidance and support in pursuing these projects, and for our many riveting discussions on quantum and computational chemistry. Thank you for continually challenging me to be a better researcher, and for being a kind and patient presence throughout the more tumultuous times of the past few years.

I would like to thank the fellow Aikens group members with whom I have had the pleasure of working alongside over the years, most especially Shana Havenridge, Zhen Liu, Gowri Udayangani Kuda-Singappulige, Fahri Alkan, Yuchen Wang, and Pratima Pandeya, as well as Bin Liu and the Liu group members for our many fruitful joint group meetings.

I'd like to thank Derek Vigil-Fowler, whose mentorship and collaboration has had a profound impact on the course of my professional life and research interests, and whose conversations on high performance computing, on physics, and on life, I treasure greatly. I'd specifically like to thank Derek for his collaboration on Chapters 5-7. I am grateful to Mauro del Ben for his help on Chapter 7, and am thankful to Jacob Clary and Ravishankar Sundararaman for the advice and post-processing scripts they provided me regarding the RPA and DFT calculations of Chapter 5. I am extremely grateful for the funding and opportunities that the Department of Energy Computational Science Graduate Fellowship provided me. Without this fellowship, I would not have met Derek, Mauro, Jacob, and Shankar in the first place.

I would like to thank committee members Professor Brett Esry, Professor Paul Smith, Professor Peter Sues, and Professor Anna Zolkiewska for their time and constructive feedback.

Finally, I would like to thank my family for their never-ending support and encouragement throughout my whole life, and especially during the last few years of my Ph.D.

Chapter 1 - General Introduction

1.1 Introduction

The plasmon resonance of noble metal nanoparticles gives rise to a variety of unique and useful features, and as such, sees widespread application in a number of fields, like sensing and detection,[1] medicine,[2,3] photovoltaics,[4] and catalysis.[5–11] This highly tunable plasmon resonance can be thought of as a collective "sloshing" of free surface electrons at the so-called plasmon resonance frequency.[12] A desired frequency can be achieved by altering the size, the shape, or the dielectric environment of the NP. Thus, plasmonic NPs can be readily adapted to a variety of purposes. We are particularly interested in plasmonic NPs for the purpose of plasmon-mediated photocatalysis, and much of our efforts focus on probing nanoparticle-adsorbate interactions with theoretical methods, developing new approaches to probe this process, and enabling these approaches to run faster and scale better in high performance computing environments.

In plasmon-mediated photocatalysis, noble metal NPs have been shown to break bonds and facilitate molecular activations that have been traditionally challenging to accomplish. Such activations include H_2 splitting,[6] CO_2 reduction,[7] water splitting,[9] O_2 activation,[11] and more.[8,10] These processes typically occur under benign conditions such as room temperature and pressure. However, these processes often suffer from low yield (<2%).[13] A mechanistic understanding of these processes has not yet been well-developed, which hinders the ability to systematically improve the efficiency. Given the aforementioned tunability of plasmonic nanoparticles, there is significant interest in identifying which factors play a role in the efficiency of plasmonic photocatalysis.[14]

While experimental investigations can offer some insight into the mechanisms driving plasmon-mediated photocatalysis, they cannot yet explore the process in full, atomistic detail,

and may suffer from environmental control challenges, like the effects of coupling between nanoparticles, solvent effects, and others.[15–19] Meanwhile, theoretical investigations have the potential to offer deep insight into the catalysis process; however, such theoretical investigations present many of their own challenges, especially regarding the trade-offs they must make in accuracy, computational efficiency, and information availability.

The challenges involved in the theoretical modeling of plasmon-mediated photocatalysis range from technical issues like the accuracy vs. computational cost of a given method and its various approximations, which information is relevant to extract from a given method, and even the method-type itself. Theoretical studies can be broadly divided into two camps: those that use potential energy surfaces (PES) to understand the system and its dynamics, and those that use a given "real-time" approach. In real-time approaches, typically the density matrix of the system is propagated in time upon laser excitation, often with little regard to the existence of the distinct underlying potential energy surfaces (i.e. an Ehrenfest dynamics-type approach).[20–24] In the PES approach, conclusions are drawn from the topography of excited state surfaces.[6,14,25,26] Sometimes, surface-based dynamics calculations are performed on these surfaces (i.e. a surface hopping-type approach).[27] Thus, the two approaches differ vastly in philosophy and results, though, luckily, not always conclusions. In this work, we take a real-time approach.

There are two common mechanism types for plasmon-mediated photocatalysis. One mechanism is the "indirect excitation" approach. In this mechanism, the excited plasmon mode decays into hot electron/hot hole pairs. These hot carriers can then transfer to the unoccupied orbitals of the adsorbate, activating the molecule for further transformation.[6,28–32] The other mechanism is the "direct excitation" approach, also known as chemical interface damping.[33–38] In this approach, the plasmon mode "decays" by directly exciting into an unoccupied orbital of the

adsorbate.[35] In this case, it is presumed that the adsorbate orbitals hybridize into the NP orbitals involved in the plasmon excitation, hence excitation of the plasmon leads to "direct" excitation of the molecule as well. In this work, we place special emphasis on the chemical interface damping mechanism, taking an orbital-based approach to understand the electron and electron-nuclear dynamics of atomic Ag nanowires with adsorbed small molecules in Chapters 3 and 4. Chapter 5 focuses on the chemical interface damping effects of H_2 on the collective excitations of Au(111).

Nanoparticles are challenging to model theoretically. We primarily employ density functional theory and related excited-state methods. We are interested in excited-state properties, with our overarching goal being to investigate the coupling of a plasmonic excitation to an adsorbate and the ways that this coupling impacts the behavior of the system upon excitation. Such modeling presents complications. First, obtaining excited-state properties is inherently costly, whether those properties are obtained in a perturbative regime, like with linear response time-dependent density functional theory[39] (LR-TDDFT) or within the random phase approximation (RPA),[40,41] or in a propagative regime, like with real-time time-dependent density functional theory (RT-TDDFT)[42,43] or Ehrenfest dynamics.[20] We make use of all these methods, and these kinds of calculations are considerably more expensive than standard ground-state calculations, quickly approaching computational intractability with increasing system size. Second, beyond the inherent cost of excited-state methods, because we are investigating the coupling of an adsorbate to a metal system, we must employ higher levels of theory than if we were to study the metal system alone, such as through use of long-range corrected density functionals in place of the workhorse generalized gradient approximation functionals in order to better approximate charge-transfer phenomena between the two subsystems.[44–47] Thus, we must

make careful decisions in our choice of modeling systems to balance computational tractability and accuracy.

We can choose to employ model systems that retain key properties of a "full" system, and this sort of approximation is central to our work in Chapters 2 and 3. This enables us to take a molecular orbital-based approach, where the basis functions are atom-centered. On the other end of the spectrum from atom-centered techniques, where the boundary condition is that the wavefunction decays to zero at infinite distance from the system, is that of periodic boundary techniques. In this case, the system is represented as a unit cell, and periodic boundary conditions are imposed such that the wavefunctions are infinitely spatially repeating. For nanoparticles, this means modeling the nanoparticle as an infinite surface. Such techniques are called "planewave" techniques, because the basis set used in these calculations is a set of planewaves.

One must make a choice between taking a molecular orbital-based approach or taking the spatially infinite planewave-based approach. This decision carries implications in what type of system can be modeled efficiently, or at all. The planewave basis is generally used in calculations in which one or more infinitely repeating spatial dimensions are present, and is applicable to nanoparticles that are sufficiently large that the particular region of interest on the surface is isolated from any outside effects beyond the surface itself. However, an unignorable drawback exists due to the fact that, in reality, nanoscale confinement effects give rise to important nanoparticle properties, and these confinement effects are lost in a periodic system. On the other hand, molecular orbital bases are the standard approach in chemistry. A major drawback of this quantum chemistry approach is that, because these calculations become increasingly computationally intractable with increasing system size, nanoparticles beyond the "nanocluster" size are generally intractable for high-fidelity molecular orbital approaches,

especially in the context of nanoparticle-adsorbate interactions because of the added complications in correctly capturing these interactions. Extending to more atoms requires increasingly severe approximation in the electronic description of the nanoparticle, and an electron-nuclear picture slips away entirely even quicker. Thus, in this regard, nanoparticles are sized such that they are inherently difficult to model, as they sit in the middle between these two descriptions, often too large to be modeled with the most accurate levels of theory in atom-centered methods, and too small for all of their properties to be captured in full detail in periodic boundary-type methods.

In this work, we make use of both techniques to study plasmon-adsorbate interactions, and we are careful in striking a balance between chemical accuracy and computational viability for both methods. Chapters 2 and 3 employ atom-centered quantum mechanical techniques to study the activation and dissociation of small molecules from atomic silver nanowires. Because of the computational demand of the methods used, these systems are very small, with the wires ranging in size from 6 to 10 atoms. These atomic wires share fundamental physics and key properties with larger nanoparticles. In these cases, we extrapolate "upward" to realistically sized nanoparticles. In Chapter 2, we take care to evaluate a variety of density functionals, identifying that long-range corrected functionals are necessary for this work. We evaluate the effects of the wire length on properties like the absorption spectrum, obtained through linear response time-dependent density functional theory. We employ real-time time-dependent density functional theory and Ehrenfest dynamics to understand how the nanowire may facilitate adsorbate activation of N_2 in a particular orientation with an applied laser pulse.

In Chapter 3, we expand the scope of examined systems by evaluating the non-adiabatic Ehrenfest dynamics for Ag_8N_2 and Ag_8H_2 in multiple adsorbate orientations, with multiple

different applied laser pulses, and at a variety of electric field strengths. We use Hirshfeld charges to examine how charge transfers between the Ag_8 and adsorbate subsystems with time. We use Fourier transforms to obtain approximate vibrational frequencies for the small particles. We accompany these electron-nuclear dynamics calculations with electron-only calculations, in which the nuclei are unable to move. We obtain time-dependent orbital populations by projecting the time-dependent electron density onto the set of ground-state orbitals, which allows us to examine which orbitals are populated or de-populated within the first 5 fs of the simulation. We achieve both activation and dissociation, depending on the system under study and the parameters applied.

Chapter 5 employs planewave techniques, examining the effects of H_2 on the (111) surface of gold in simulated electron energy loss spectroscopy (EELS). Extended surfaces share many similarities with nanoparticles, especially larger-sized nanoparticles with more band-like structures than their quantized nanocluster counterparts. In this case, we extrapolate "downward," from an infinite surface to a nanoparticle. We utilize the "subspace summation" method (developed in Chapter 6) within the RPA to study how inclusion or exclusion of H_2-hybridized bands affects the simulated EELS of the systems under study.

In Chapter 6, we discuss two methods we develop within the BerkeleyGW code in order to carry out the H_2-on-Au application work in Chapter 5. In order to perform the calculations outlined in Chapter 4, we must first develop a partial occupation RPA method within BerkeleyGW. BerkeleyGW, until this point, has been an RPA+GW code designed primarily for semiconductors. That the semiconductor band gap is well-defined enables the BerkeleyGW code to make some simplifications to the RPA and GW implementations relative to the full governing equations, and these approximations are incorporated into the core parallelism of the code. Thus,

developing a partial occupation method compatible with the existing parallelism of the code is a major focus of the work. The primary motivation behind the partial occupation implementation is to facilitate the use of BerkeleyGW in the computational study of metals. Electronic structure calculations of metals benefit from the application of partial occupations because metals have a complex electronic structure at the Fermi level, and no well-defined band gap. That a band may cross the Fermi energy, suddenly changing its occupation from fully occupied to fully unoccupied, produces numerical issues. The implementation of partial occupations in BerkeleyGW enables us to extend the code to metals in addition to semiconductors, which allows us to study the H_2-Au(111) systems of Chapter 5.

The second development needed in order to study the problem presented in Chapter 5 is that of a "subspace summation" in the RPA polarizability implementation of BerkeleyGW. Here, we seek to include only bands of interest in the computation of the RPA polarizability, which is a sum over all possible (occupied, unoccupied) pairings. Such a method allows us to understand how the RPA EELS spectrum of a system is affected by the inclusion (or exclusion) of particular bands, giving us a method to probe how the H_2 in the system affects the collective modes of the gold. This method also involves careful interaction with the BerkeleyGW parallelism. Combined, these two methods allow us to probe the EELS spectrum of H_2-on-Au while treating the system more computationally feasibly than previously possible in BerkeleyGW, i.e. with partial occupations.

The overarching motivation for this dissertation is that we meet in the middle between the atom-centered atomic wire approach and the planewave surface approach, generating valuable understanding of nanoparticle processes from both types of approximate models. In both atom-centered and planewave techniques, until we have access to more powerful computers and better

scaling of methods, the issues in choosing a model, in choosing a method, and in choosing what information to extract from the model and method, will exist. Thus, the seventh chapter of this dissertation focuses on work done in pure high performance computing, alleviating critical bottlenecks of the BerkeleyGW code. BerkeleyGW is the massively parallel solid state physics package utilized in Chapter 5 and across the globe as a highly scalable and performant RPA+GW code. This work improves the parallel file I/O of the BerkeleyGW code by an order of magnitude on high performance machines, reducing I/O overhead during computation run-time, which allows us to run larger calculations faster, conserving compute hours on the leadership-class machines that these types of calculations often require.

While high performance computing (HPC) developments do not fall under the purview of traditional physical chemistry research, they are nonetheless a critical component of computational chemistry. The HPC developments herein enable computation of larger and more varied chemical systems, in the case of the wavefunction I/O developments and in the case of the partial occupations developments, respectively. Thus, through our HPC parallel algorithm developments, we extend the range of materials for which these computational methods can be applied.

Taken together, the works presented herein advance our understanding of plasmonic particle-adsorbate interactions by modeling activation and dissociation dynamics directly in Chapters 3 and 4, by probing the structure-EELS relationship directly with the subspace summation method in Chapter 5, by developing the methods that enable us to carry out these calculations in Chapter 6, and by removing critical bottlenecks in the code that affect our ability to carry out these calculations quickly and effectively in Chapter 7.

1.2 References

(1) Le Ru, E. C.; Etchegoin, P. G. Single-Molecule Surface-Enhanced Raman Spectroscopy. *Annu. Rev. Phys. Chem.* **2012**, *63* (1), 65–87. https://doi.org/10.1146/annurev-physchem-032511-143757.

(2) Huang, X.; Jain, P. K.; El-Sayed, I. H.; El-Sayed, M. A. Plasmonic Photothermal Therapy (PPTT) Using Gold Nanoparticles. *Lasers Med. Sci.* **2007**, *23* (3), 217. https://doi.org/10.1007/s10103-007-0470-x.

(3) Huang, X.; El-Sayed, I. H.; Qian, W.; El-Sayed, M. A. Cancer Cell Imaging and Photothermal Therapy in the Near-Infrared Region by Using Gold Nanorods. *J. Am. Chem. Soc.* **2006**, *128* (6), 2115–2120. https://doi.org/10.1021/ja057254a.

(4) Jang, Y. H.; Jang, Y. J.; Kim, S.; Quan, L. N.; Chung, K.; Kim, D. H. Plasmonic Solar Cells: From Rational Design to Mechanism Overview. *Chem. Rev.* **2016**, *116* (24), 14982–15034. https://doi.org/10.1021/acs.chemrev.6b00302.

(5) Christopher, P.; Linic, S. Engineering Selectivity in Heterogeneous Catalysis: Ag Nanowires as Selective Ethylene Epoxidation Catalysts. *J. Am. Chem. Soc.* **2008**, *130* (34), 11264–11265. https://doi.org/10.1021/ja803818k.

(6) Mukherjee, S.; Libisch, F.; Large, N.; Neumann, O.; Brown, L. V.; Cheng, J.; Lassiter, J. B.; Carter, E. A.; Nordlander, P.; Halas, N. J. Hot Electrons Do the Impossible: Plasmon-Induced Dissociation of H2 on Au. *Nano Lett.* **2013**, *13* (1), 240–247. https://doi.org/10.1021/nl303940z.

(7) Yu, S.; Wilson, A. J.; Heo, J.; Jain, P. K. Plasmonic Control of Multi-Electron Transfer and C–C Coupling in Visible-Light-Driven CO2 Reduction on Au Nanoparticles. *Nano Lett.* **2018**, *18* (4), 2189–2194. https://doi.org/10.1021/acs.nanolett.7b05410.

(8) Wang, F.; Li, C.; Chen, H.; Jiang, R.; Sun, L.-D.; Li, Q.; Wang, J.; Yu, J. C.; Yan, C.-H. Plasmonic Harvesting of Light Energy for Suzuki Coupling Reactions. *J. Am. Chem. Soc.* **2013**, *135* (15), 5588–5601. https://doi.org/10.1021/ja310501y.

(9) Lee, J.; Mubeen, S.; Ji, X.; Stucky, G. D.; Moskovits, M. Plasmonic Photoanodes for Solar Water Splitting with Visible Light. *Nano Lett.* **2012**, *12* (9), 5014–5019. https://doi.org/10.1021/nl302796f.

(10) Marimuthu, A.; Zhang, J.; Linic, S. Tuning Selectivity in Propylene Epoxidation by Plasmon Mediated Photo-Switching of Cu Oxidation State. *Science* **2013**, *339* (6127), 1590–1593. https://doi.org/10.1126/science.1231631.

(11) Christopher, P.; Xin, H.; Linic, S. Visible-Light-Enhanced Catalytic Oxidation Reactions on Plasmonic Silver Nanostructures. *Nat. Chem.* **2011**, *3* (6), 467–472. https://doi.org/10.1038/nchem.1032.

(12) Willets, K. A.; Van Duyne, R. P. Localized Surface Plasmon Resonance Spectroscopy and Sensing. *Annu. Rev. Phys. Chem.* **2007**, *58* (1), 267–297. https://doi.org/10.1146/annurev.physchem.58.032806.104607.

(13) Kumar, P. V.; Rossi, T. P.; Kuisma, M.; Erhart, P.; Norris, D. J. Direct Hot-Carrier Transfer in Plasmonic Catalysis. *Faraday Discuss.* **2019**, *214* (0), 189–197. https://doi.org/10.1039/C8FD00154E.

(14) Libisch, F.; Cheng, J.; Carter, E. A. Electron-Transfer-Induced Dissociation of H2 on Gold Nanoparticles: Excited-State Potential Energy Surfaces via Embedded Correlated Wavefunction Theory. *Z. Für Phys. Chem.* **2013**, *227* (9–11), 1455–1466. https://doi.org/10.1524/zpch.2013.0406.

(15) Elias, R. C.; Linic, S. Elucidating the Roles of Local and Nonlocal Rate Enhancement Mechanisms in Plasmonic Catalysis. *J. Am. Chem. Soc.* **2022**, *144* (43), 19990–19998. https://doi.org/10.1021/jacs.2c08561.

(16) Zhang, J.; Zhang, L.; Zhang, Q.; Luo, Y. Unveiling a Counterintuitive Intermode Interplay in a Prototype Plasmonic Nanosystem. *J. Phys. Chem. Lett.* **2022**, *13* (44), 10388–10394. https://doi.org/10.1021/acs.jpclett.2c02934.

(17) Kelly, K. L.; Coronado, E.; Zhao, L. L.; Schatz, G. C. The Optical Properties of Metal Nanoparticles: The Influence of Size, Shape, and Dielectric Environment. *J. Phys. Chem. B* **2003**, *107* (3), 668–677. https://doi.org/10.1021/jp026731y.

(18) Long, L.; Ju, W.; Yang, H.-Y.; Li, Z. Dimensional Design for Surface-Enhanced Raman Spectroscopy. *ACS Mater. Au* **2022**, *2* (5), 552–575. https://doi.org/10.1021/acsmaterialsau.2c00005.

(19) Stiles, P. L.; Dieringer, J. A.; Shah, N. C.; Van Duyne, R. P. Surface-Enhanced Raman Spectroscopy. *Annu. Rev. Anal. Chem.* **2008**, *1* (1), 601–626. https://doi.org/10.1146/annurev.anchem.1.031207.112814.

(20) Li, X.; Tully, J. C.; Schlegel, H. B.; Frisch, M. J. Ab Initio Ehrenfest Dynamics. *J. Chem. Phys.* **2005**, *123* (8), 084106. https://doi.org/10.1063/1.2008258.

(21) Hull, O. A.; Lingerfelt, D. B.; Li, X.; Aikens, C. M. Electronic Structure and Nonadiabatic Dynamics of Atomic Silver Nanowire–N2 Systems. *J. Phys. Chem. C* **2020**, *124* (38), 20834–20845. https://doi.org/10.1021/acs.jpcc.0c02979.

(22) Guan, M.; Chen, D.; Hu, S.; Zhao, H.; You, P.; Meng, S. Theoretical Insights into Ultrafast Dynamics in Quantum Materials. *Ultrafast Sci.* **2022**, *2022*, 1–16. https://doi.org/10.34133/2022/9767251.

(23) Yan, L.; Ding, Z.; Song, P.; Wang, F.; Meng, S. Plasmon-Induced Dynamics of H2 Splitting on a Silver Atomic Chain. *Appl. Phys. Lett.* **2015**, *107* (8), 083102. https://doi.org/10.1063/1.4929611.

(24) Zhang, Y.; Yan, L.; Guan, M.; Chen, D.; Xu, Z.; Guo, H.; Hu, S.; Zhang, S.; Liu, X.; Guo, Z.; Li, S.; Meng, S. Indirect to Direct Charge Transfer Transition in Plasmon-Enabled CO2 Photoreduction. *Adv. Sci.* **2022**, *9* (2), 2102978. https://doi.org/10.1002/advs.202102978.

(25) Wu, Q.; Zhou, L.; Schatz, G. C.; Zhang, Y.; Guo, H. Mechanistic Insights into Photocatalyzed H2 Dissociation on Au Clusters. *J. Am. Chem. Soc.* **2020**, *142* (30), 13090–13101. https://doi.org/10.1021/jacs.0c04491.

(26) Zhang, Y.; Nelson, T.; Tretiak, S.; Guo, H.; Schatz, G. C. Plasmonic Hot-Carrier-Mediated Tunable Photochemical Reactions. *ACS Nano* **2018**. https://doi.org/10.1021/acsnano.8b03830.

(27) Subotnik, J. E.; Jain, A.; Landry, B.; Petit, A.; Ouyang, W.; Bellonzi, N. Understanding the Surface Hopping View of Electronic Transitions and Decoherence. *Annu. Rev. Phys. Chem.* **2016**, *67* (1), 387–417. https://doi.org/10.1146/annurev-physchem-040215-112245.

(28) Brongersma, M. L.; Halas, N. J.; Nordlander, P. Plasmon-Induced Hot Carrier Science and Technology. *Nat. Nanotechnol.* **2015**, *10* (1), 25–34. https://doi.org/10.1038/nnano.2014.311.

(29) Christopher, P.; Moskovits, M. Hot Charge Carrier Transmission from Plasmonic Nanostructures. *Annu. Rev. Phys. Chem.* **2017**, *68* (1), 379–398. https://doi.org/10.1146/annurev-physchem-052516-044948.

(30) Govorov, A. O.; Zhang, H.; Gun'ko, Y. K. Theory of Photoinjection of Hot Plasmonic Carriers from Metal Nanostructures into Semiconductors and Surface Molecules. *J. Phys. Chem. C* **2013**, *117* (32), 16616–16631. https://doi.org/10.1021/jp405430m.

(31) Manjavacas, A.; Liu, J. G.; Kulkarni, V.; Nordlander, P. Plasmon-Induced Hot Carriers in Metallic Nanoparticles. *ACS Nano* **2014**, *8* (8), 7630–7638. https://doi.org/10.1021/nn502445f.

(32) Liu, J. G.; Zhang, H.; Link, S.; Nordlander, P. Relaxation of Plasmon-Induced Hot Carriers. *ACS Photonics* **2017**. https://doi.org/10.1021/acsphotonics.7b00881.

(33) Wu, K.; Chen, J.; McBride, J. R.; Lian, T. Efficient Hot-Electron Transfer by a Plasmon-Induced Interfacial Charge-Transfer Transition. *Science* **2015**, *349* (6248), 632–635. https://doi.org/10.1126/science.aac5443.

(34) Boerigter, C.; Campana, R.; Morabito, M.; Linic, S. Evidence and Implications of Direct Charge Excitation as the Dominant Mechanism in Plasmon-Mediated Photocatalysis. *Nat. Commun.* **2016**, *7* (1), 10545. https://doi.org/10.1038/ncomms10545.

(35) Boerigter, C.; Aslam, U.; Linic, S. Mechanism of Charge Transfer from Plasmonic Nanostructures to Chemically Attached Materials. *ACS Nano* **2016**, *10* (6), 6108–6115. https://doi.org/10.1021/acsnano.6b01846.

(36) Bosbach, J.; Hendrich, C.; Stietz, F.; Vartanyan, T.; Träger, F. Ultrafast Dephasing of Surface Plasmon Excitation in Silver Nanoparticles: Influence of Particle Size, Shape, and Chemical Surrounding. *Phys. Rev. Lett.* **2002**, *89* (25), 257404. https://doi.org/10.1103/PhysRevLett.89.257404.

(37) Lee, S. Y.; Tsalu, P. V.; Kim, G. W.; Seo, M. J.; Hong, J. W.; Ha, J. W. Tuning Chemical Interface Damping: Interfacial Electronic Effects of Adsorbate Molecules and Sharp Tips of Single Gold Bipyramids. *Nano Lett.* **2019**, *19* (4), 2568–2574. https://doi.org/10.1021/acs.nanolett.9b00338.

(38) Foerster, B.; Joplin, A.; Kaefer, K.; Celiksoy, S.; Link, S.; Sönnichsen, C. Chemical Interface Damping Depends on Electrons Reaching the Surface. *ACS Nano* **2017**, *11* (3), 2886–2893. https://doi.org/10.1021/acsnano.6b08010.

(39) Casida, M. E. Time-Dependent Density Functional Response Theory for Molecules. In *Recent Advances in Computational Chemistry*; WORLD SCIENTIFIC, 1995; Vol. 1, pp 155–192. https://doi.org/10.1142/9789812830586_0005.

(40) Adler, S. L. Quantum Theory of the Dielectric Constant in Real Solids. *Phys. Rev.* **1962**, *126* (2), 413–420. https://doi.org/10.1103/PhysRev.126.413.

(41) Wiser, N. Dielectric Constant with Local Field Effects Included. *Phys. Rev.* **1963**, *129* (1), 62–69. https://doi.org/10.1103/PhysRev.129.62.

(42) Goings, J. J.; Lestrange, P. J.; Li, X. Real-Time Time-Dependent Electronic Structure Theory. *Wiley Interdiscip. Rev. Comput. Mol. Sci.* **2018**, *8* (1), e1341. https://doi.org/10.1002/wcms.1341.

(43) Li, X.; Govind, N.; Isborn, C.; DePrince, A. E.; Lopata, K. Real-Time Time-Dependent Electronic Structure Theory. *Chem. Rev.* **2020**, *120* (18), 9951–9993. https://doi.org/10.1021/acs.chemrev.0c00223.

(44) Rabilloud, F. UV-Visible Absorption Spectra of Metallic Clusters from TDDFT Calculations. *Eur. Phys. J. D* **2013**, *67* (1), 18. https://doi.org/10.1140/epjd/e2012-30448-x.

(45) Rabilloud, F. Description of Plasmon-like Band in Silver Clusters: The Importance of the Long-Range Hartree-Fock Exchange in Time-Dependent Density-Functional Theory Simulations. *J. Chem. Phys.* **2014**, *141* (14), 144302. https://doi.org/10.1063/1.4897260.

(46) Rabilloud, F. Assessment of the Performance of Long-Range-Corrected Density Functionals for Calculating the Absorption Spectra of Silver Clusters. *J. Phys. Chem. A* **2013**, *117* (20), 4267–4278. https://doi.org/10.1021/jp3124154.

(47) Moore, J. E.; Morton, S. M.; Jensen, L. Importance of Correctly Describing Charge-Transfer Excitations for Understanding the Chemical Effect in SERS. *J. Phys. Chem. Lett.* **2012**, *3* (17), 2470–2475. https://doi.org/10.1021/jz300492p.

Chapter 2 - Technical Introduction

2.1 Introduction

Throughout this dissertation, we utilize a variety of computational techniques. These techniques primarily involve density functional theory (DFT),[1] both planewave and atom-centered. Atom-centered techniques include ground-state DFT, linear response time-dependent DFT (LR-TDDFT),[2,3] electron-only real-time time-dependent DFT (RT-TDDFT),[4–6] and full electron-nuclear time dependent dynamics via joining RT-TDDFT with Ehrenfest dynamics (RT-TDDFT/ED).[7–9] Planewave techniques are used as inputs into the BerkeleyGW random phase approximation (RPA) implementation.[10–12] All of these techniques offer particular advantages and disadvantages. We review these techniques, discuss their strengths and weaknesses, and resolve how each fits into the work found in this dissertation.

In addition to the theoretical techniques outlined above, we dedicate a subsection of this chapter to pure high performance computing developments, which allow us to expand the scope of systems to which these techniques apply by enabling us to carry out these calculations more efficiently. HPC development is a critical component of computational chemistry research, without which we are greatly restricted in the size and kind of calculations we can execute. We discuss the relevant HPC techniques, methods, and libraries, which includes MPI parallelism and common MPI patterns, and the HDF5 file I/O library.

2.2 Ground-state Density Functional Theory

Density functional theory is the most popular and successful electronic structure method today, with over 47,000 citations on the seminal work of Kohn and Sham ("KS-DFT") that

enabled its widespread use by developing a practical implementation of the theory.[13] While DFT has many forms and flavors, the central idea of KS-DFT is that a many-body system of interacting electrons can be treated as a system of non-interacting electrons in an effective potential. Determining the form of the effective potential is a research effort that is still on-going. Despite this, DFT has seen widespread adoption in solid-state physics, materials science, and chemistry on account of its favorable balance between accuracy and computational feasibility. In this section, we first provide an overview of the DFT method, then detail the specific DFT methods we utilize in this work.

2.2.1 Introduction to DFT

Modern density functional theory is based on the two Hohenberg-Kohn (HK) theorems.[1,14] The first theorem is an existence theorem, stating that the electron density of a system uniquely determines its Hamiltonian. If the Hamiltonian is solved and the wavefunctions obtained, then any observable can be computed. Thus, the electron density determines all properties of the system. The second theorem establishes a variational principle for DFT: the functional of the electron density that produces the ground-state energy of the system is minimized if and only if the input density is the true ground-state density. The second theorem produces the variational equation:

$$\delta\big(E - \mu\rho(\boldsymbol{r})\big) = 0 \qquad \text{(Eq. 2.1)}$$

where we search for the electron density $\rho(\boldsymbol{r})$ that minimizes the energy E, subject to the constraint that $\int \rho(\boldsymbol{r})\, d\boldsymbol{r} = N$, the total number of electrons in the system, with μ the Lagrange multiplier. Eventually, one obtains the Euler-Lagrange equation that is the DFT equivalent to the time-independent Schrödinger equation:[15]

$$v(\boldsymbol{r}) + \frac{\delta F_{HK}}{\delta \rho(\boldsymbol{r})} = \mu \qquad \text{(Eq. 2.2)}$$

with $v(\boldsymbol{r})$ the external potential and $F_{HK}[\rho] = T[\rho] + V_{ee}[\rho]$, where $T[\rho]$ is the electronic kinetic energy functional and $V_{ee}[\rho]$ is the electron-electron interaction functional.

While the Hohenberg-Kohn theorems tell us that the electron density uniquely determines all properties of a system, and that we can variationally solve for the ground-state density, they do not provide any details of a practical implementation. Both the form of $T[\rho]$ and $V_{ee}[\rho]$ are unknown. It was not until the development of Kohn-Sham (KS) DFT that DFT became widely applicable. In the Hohenberg-Kohn theorems, there is no clear way to treat the kinetic energy nor V_{ee}. KS-DFT remedies the first issue while casting the DFT equation into a form that closely resembles the Hartree-Fock equation. First, Kohn and Sham introduce a reference system Hamiltonian of non-interacting electrons that yields the same electron density as the exact electron density:

$$H_{ref} = -\sum_{i}^{N} \frac{1}{2}\nabla_i^2 + \sum_{i}^{N} v_{eff,i}(\boldsymbol{r}) = \sum_{i}^{N} h_{ref,i} \qquad \text{(Eq. 2.3)}$$

so that $h_{ref,i} = -\frac{1}{2}\nabla_i^2 + v_{eff,i}(\boldsymbol{r})$. H_{ref} excludes direct electron-electron interactions, and we instead make an approximate attempt at capturing these in v_{eff}. Introducing molecular orbitals $\{\psi_i\}$, the reference electron density can be written:

$$\rho = \sum_{i}^{N} |\psi_i|^2 \qquad \text{(Eq. 2.4)}$$

with N, the number of electrons, running over the N lowest eigenstates of H_{ref}. Now, given the reference system, the HK functional F_{HK} can be written as $F_{HK}[\rho] = T[\rho] + E_{xc}[\rho] + J[\rho]$, where T is the kinetic energy functional of the reference system:

$$\mathrm{T}[\rho] = \sum_{i}^{N} \left\langle \psi_i \middle| -\frac{1}{2}\nabla_i^2 \middle| \psi_i \right\rangle \qquad \text{(Eq. 2.5)}$$

and $J[\rho]$ the Coulombic interaction energy:

$$J[\rho] = \frac{1}{2}\int\int \frac{\rho(\boldsymbol{r})\rho(\boldsymbol{r}')}{|\boldsymbol{r}-\boldsymbol{r}'|} d\boldsymbol{r} d\boldsymbol{r}' \qquad \text{(Eq. 2.6)}$$

and the "garbage collection" term $E_{xc}[\rho]$ is the infamous exchange-correlation energy functional, which, in theory, contains the difference between the exact kinetic energy and the reference kinetic energy, the nonclassical part of V_{ee} (not accounted for in $J[\rho]$), and the self-interaction of the system. That is, the exchange-correlation term contains all of the leftovers of the interacting system that are unaccounted for in T and J. In this way, the Kohn-Sham equations are technically exact. In practice, we do not know the exact form of V_{xc}, and the dark art of approximating this functional is an active area of research. After revisiting the Euler-Lagrange equation (eq. 2.2), applying this reference-system formalism, and minimizing with respect to the reference system orbitals subject to the condition of orthonormality, we eventually arrive at the Kohn-Sham equations:[13]

$$-\frac{1}{2}\nabla^2\psi_i(\boldsymbol{r}) + \left[V_{ext}(\boldsymbol{r}) + \int \frac{\rho(\boldsymbol{r}')}{|\boldsymbol{r}-\boldsymbol{r}'|} d\boldsymbol{r}' + V_{xc}\right]\psi_i(\boldsymbol{r}) = \epsilon_i\psi_i(\boldsymbol{r}) \qquad \text{(Eq. 2.7)}$$

We can write $V_{eff} = V_{ext}(\boldsymbol{r}) + \int \frac{\rho(\boldsymbol{r}')}{|\boldsymbol{r}-\boldsymbol{r}'|} d\boldsymbol{r}' + V_{xc}$ so that (eq. 2.7) becomes:

$$\left[-\frac{1}{2}\nabla^2 + V_{eff}\right]\psi_i(\boldsymbol{r}) = \epsilon_i\psi_i(\boldsymbol{r}) \qquad \text{(Eq. 2.8)}$$

where equation 2.8 is a system of one-electron equations which, when solved, represents the many-electron system in terms of single-particle orbitals. In other words, we are solving for the single-particle orbitals of a fictitious non-interacting system, where all the many body interactions of the true interacting system are re-cast as an effective potential that the non-

interacting electrons experience. Because V_{eff} depends on the electron density, and therefore the set of single-particle orbitals, the KS-DFT equations are a pseudo-eigenvalue problem that are solved iteratively to self-consistency, where we must first guess V_{eff}, and at each iteration, update the density, then update V_{eff}. The eigenfunctions $\{\psi_i\}$ and their eigenvalues $\{\epsilon_i\}$ are often interpreted as molecular orbitals and their corresponding eigenenergies, respectively. While $\{\psi_i\}$ and $\{\epsilon_i\}$ are technically purely mathematical constructs, interpreting them as physically meaningful has yielded surprising success, and such interpretation is common.[16–20]

The eigenfunctions $\{\psi_i\}$ are generally represented as a linear combination of basis functions:

$$\psi_a = \sum_{i=1}^{N} c_{ai}\phi_i \qquad \text{(Eq. 2.9)}$$

This treatment allows us to write equation 2.8 as a matrix equation to determine the expansion coefficients $\{c_{ia}\}$:

$$\sum_{j}^{N}\langle\phi_i|H_{ref}|\phi_j\rangle c_{aj} = \epsilon_a \sum_{j}^{N}\langle\phi_i|\phi_j\rangle c_{aj} \qquad \text{(Eq. 2.10)}$$

$$= \sum_{j}^{N} H_{ref} c_{aj} = \epsilon_a \sum_{j}^{N} S_{ij} c_{aj}$$

The choice of basis set (and accompanying boundary conditions) is an important one. These fall under two broad categories: planewave and atom-centered bases. We discuss these choices in more detail in sections 2.2.2 and 2.2.3.

The second critical choice is that of the exchange-correlation functional. Because of the fact that the exchange-correlation functional is unknown, the fact that there is no known prescription with which to systematically improve the exchange-correlation functional, and the

fact that the accuracy of DFT hinges on what form the exchange-correlation functional takes, there has been extensive research into developing density functionals, which continues to this day.[21–23] John Perdew detailed a hierarchy of chemical accuracy for DFT, dubbed the "Jacob's Ladder of DFT".[24] The lowest rung on the latter is the local density approximation (LDA), or LDA functional. As the name suggests, this exchange-correlation functional depends only on the local density. The next rung is the generalized gradient approximation (GGA), which depends on the local density and the gradient of the local density. One rung up from GGA is meta-GGAs, which depend on the gradient of the density or the Laplacian of the density, sometimes called the kinetic energy density, or both. At the next rung, we encounter "hybrid" and "long-range corrected" functionals, which depend on the occupied orbitals in addition to the density. This dependence arises because these functionals incorporate the Hartree-Fock exchange operator, which requires explicit consideration of the single-particle orbitals. DFT is known to fail for long-range interactions like charge transfer, and these types of exchange-correlation functionals help to remedy this issue.[25] The final rung on the ladder, and the closest to "chemical accuracy heaven" is that of generalized random phase approximations (RPA), which we discuss in a later section. These "functionals" depend on both occupied and unoccupied orbitals of the system, and are considerably more accurate than true DFT functionals for many properties of chemical systems, though are also much more computationally expensive.

2.2.2 Atom-centered DFT

Atom-centered DFT is sometimes called the linear combination of atomic orbitals (LCAO) approach or local basis (LB) approach. LCAO is a familiar concept in chemistry, since LCAO applies broadly to molecular orbital (MO) theory. In MO theory, we think of molecular

orbitals as linear combinations of the atomic orbitals of the atoms that comprise the molecule of interest. MO theory is a powerful tool for gaining qualitative insight into a system, finding success in organic and inorganic chemistry even without solving any sort of Schrödinger-like equation. On the other hand, DFT can be thought of as one particular means with which to produce molecular orbitals, and one where we *do* solve a Schrödinger-like equation. Thus, while the eigenfunctions and eigenvalues of equation 2.8 are indeed strictly mathematical constructs, we can relate them to the familiar MO theory orbitals, and these relations often produce meaningful insight into the system under interest. In the case of atom-centered DFT, we must choose how to represent these atomic orbitals, whose linear combination will give rise to the molecular orbitals of the system.

One choice of atomic orbital is that of Slater-type orbitals (STO), where a STO centered on atom a takes the form:[26]

$$\chi_{nlm}^{STO}(\zeta, r - R_a) = NY_l^m(\theta_a, \phi_a) r^{n-1} e^{-\zeta|r-R_a|} \qquad \text{(Eq. 2.11)}$$

where *n*, *l*, and *m* are the principle, angular, and magnetic quantum numbers respectively, *r* is the position of the electron, R_a is the position of atom *a*, *N* is the normalization constant, $Y_l^m(\theta_a, \phi_a)$ is a spherical harmonic defined by *m* and *l*, and ζ is the Slater orbital exponent, a positive number which controls the diffuseness of the function. A large ζ yields small, dense orbitals that decay to zero more rapidly as $|r - R_a|$ increases, and a small ζ yields a large diffuse function that decays more slowly. In atom-centered DFT, the boundary condition is that the function must eventually decay to 0.

A second choice of orbital is that of Gaussian-type orbitals (GTO), which look much the same as STOs:

$$\chi_{nlm}^{GTO}(\alpha, r - R_a) = NY_l^m(\theta_a, \phi_a) r^{2n-2-1} e^{-\alpha|r-R_a|^2} \qquad \text{(Eq. 2.12)}$$

The key difference is that the GTOs have zero slope at $r = R_a$, and the STOs have a cusp at $r = R_a$. Slater-type orbitals better describe the qualitative features of molecular orbitals, like in the fact that they display the correct cusp behavior and decay behavior, and so fewer are needed in a basis set expansion compared to GTOs. GTOs have no cusp, and they decay too rapidly at large $|r - R_a|$.[27] GTOs are far more convenient to evaluate though, because the product of two Gaussian functions is another Gaussian function. Thus, one compromise is use of the STO-NG basis sets, where:[28]

$$\chi^{STO} = \sum_{i=1}^{N} c_i \chi^{GTO}(\alpha_i) \qquad \text{(Eq. 2.13)}$$

so that each STO basis function is itself a linear combination of some number N GTOs, which is more convenient to evaluate than a pure STO. Beyond the STO-NG sets, creation of a basis sets comprised of basis functions represented as a linear combination of these Gaussian "primitive functions" has proven useful. Another common class of basis functions are split-valence basis sets, in which the valence orbitals are represented by multiple basis functions (each of which can be represented as some fixed linear combination of GTOs). If a basis set represents the valence orbitals using two GTOs, the set is called a "double zeta" basis set. If there are three GTOs, the set is a "triple zeta" basis, and so on. In our nanowire work, we utilize the lanl2dz basis set, named because it is a double zeta ("dz") basis set developed at Los Alamos National Laboratory (LANL).[29,30] The lanl2dz is a type of "effective core potential" basis set. Because core atomic orbitals are minimally affected by molecular formation, effective core potential bases replace the explicit treatment of the core electrons with an effective potential that represents the effect of these core electrons on the valence electrons.[28,31] The approximation of replacing core electrons with an effective potential is common in both atom-centered and planewave DFT.

2.2.3 Planewave DFT

The planewave formulation of DFT looks quite different than the atom-centered approach, and indeed, the types of systems that the planewave formulation excels at modeling are quite different than the systems that atom-centered DFT excels at modeling. In particular, planewave DFT uses planewaves as the basis and imposes periodic boundary conditions so that the system of interest in confined to an infinitely repeating unit cell. Thus, planewave DFT is especially well-suited to modeling structures which repeat in one or more spatial dimensions, like bulk materials (infinitely repeating in all three spatial dimensions), surfaces (infinitely repeating in two spatial dimensions), or wires (infinitely repeating in one spatial dimension). Planewave DFT can be used to model systems that have no repeating dimension by making the unit cell sufficiently large that the "neighboring cells" do not interact with each other, but in general, atom-centered DFT is better suited for this task. Planewave DFT represents the system of interest in terms of a unit cell, with lattice points that are invariant under translation:[32,33]

$$\boldsymbol{R} = n_1\boldsymbol{a_1} + n_2\boldsymbol{a_2} + n_3\boldsymbol{a_3} \qquad \text{(Eq. 2.14)}$$

where n_1, n_2, and n_3 are integers and the lattice vectors $\boldsymbol{a_1}$, $\boldsymbol{a_2}$, and $\boldsymbol{a_3}$ span the unit cell with volume Ω. It is generally more convenient to work in reciprocal space, where we can define reciprocal lattice vectors $\boldsymbol{b_1}$, $\boldsymbol{b_2}$, and $\boldsymbol{b_3}$ which span the reciprocal lattice. The reciprocal lattice vectors are found by:

$$\boldsymbol{b_1} = 2\pi\frac{\boldsymbol{a_2}\times\boldsymbol{a_3}}{\det(\boldsymbol{a_1}\boldsymbol{a_2}\boldsymbol{a_3})} \qquad \text{(Eq. 2.15)}$$

with the other two vectors found by permuting the indices, and with $\Omega = \det(\boldsymbol{a_1}\boldsymbol{a_2}\boldsymbol{a_3})$. A unit cell in the reciprocal lattice is called a Brillouin zone, and the primitive unit cell is called the first Brillouin zone.

Bloch's theorem states that the solutions of the Schrödinger equation for a periodic potential take the form:

$$\psi_{\boldsymbol{k}}(\boldsymbol{r}) = e^{\boldsymbol{ikr}} u_{\boldsymbol{k}}(\boldsymbol{r}) \qquad \text{(Eq. 2.16)}$$

with $u_{\boldsymbol{k}}(\boldsymbol{r} + \boldsymbol{R}) = u_{\boldsymbol{k}}(\mathbf{r})$, where R is a translation vector of the lattice. In other words, $u_{\boldsymbol{k}}(\mathbf{r})$ is a periodic function with a period corresponding to the crystal lattice. $e^{\boldsymbol{ikr}}$ is a planewave, signifying that $\psi_{\boldsymbol{k}}(\boldsymbol{r})$ changes only up to a phase factor under translation, and **k** is the crystal moment, a quantum number that arises due to this translational symmetry. A consequence of Bloch's theorem is that our DFT problem need only be solved within the first Brillouin zone. In a planewave basis, the periodic function takes the form:

$$u_{n\boldsymbol{k}}(\boldsymbol{r}) = \frac{1}{\Omega} \sum_{|\boldsymbol{G}| \leq G_{max}} c_{\boldsymbol{G};nk} e^{i\boldsymbol{G}\cdot r} \qquad \text{(Eq. 2.17)}$$

where we introduce n to order the wavefunctions, and we expand $u_{\boldsymbol{nk}}(\boldsymbol{r})$ in terms of planewaves with wave-vector lengths $|\mathbf{G}|$. The g-vectors are reciprocal lattice vectors, i.e.,

$$\boldsymbol{G} = n_1 \boldsymbol{a_1} + n_2 \boldsymbol{a_2} + n_3 \boldsymbol{a_3} \qquad \text{(Eq. 2.18)}$$

The number of g-vectors corresponds to all the planewaves with wavevector lengths $|\boldsymbol{G}| \leq G_{max}$. Generally, rather than specifying a G_{max} in a planewave calculation, a kinetic energy cutoff is specified, where $E_{kin,cutoff} = \frac{G_{max}^2}{2}$. It is called the kinetic energy cut-off because planewaves are a solution to the free electron Schrödinger equation ($T = -1/2\nabla^2$, $V = 0$), which yield a total energy $G^2/2$ for a given planewave (and because $V = 0$, the total energy is equal to the kinetic energy). Thus, the cut-off energy determines the size of the basis set.

Now,

$$\psi_{n\boldsymbol{k}}(\boldsymbol{r}) = \frac{1}{\Omega} \sum_{|\boldsymbol{G}| \leq G_{max}} c_{\boldsymbol{G};nk} e^{i\boldsymbol{G}\cdot r} e^{\boldsymbol{ikr}} = \frac{1}{\Omega} \sum_{|\boldsymbol{G}| \leq G_{max}} c_{\boldsymbol{G};nk} e^{i(k+\boldsymbol{G})\cdot r} \qquad \text{(Eq. 2.19)}$$

While *n* is an integer, **k** is continuous. In theory, Bloch's theorem requires us to calculate wavefunctions for all $u_{\boldsymbol{k}}(\boldsymbol{r} + \boldsymbol{R}) = u_{\boldsymbol{k}}(\boldsymbol{r})$ in the first Brillouin zone. Thus, in theory, we must integrate over the Brillouin zone, and, for example, the electron density would be calculated as:

$$\rho(\boldsymbol{r}) = \frac{\Omega}{(2\pi)^3} \int_{1st\ BZ} \left(\sum_{n=1}^{N_{electrons}} |\psi_{n\boldsymbol{k}}(\boldsymbol{r})|^2 \right) d\boldsymbol{k} = \frac{\Omega}{(2\pi)^3} \int_{1st\ BZ} \left(\sum_{n=1}^{N_{electrons}} |u_{n\boldsymbol{k}}(\boldsymbol{r})|^2 \right) d\boldsymbol{k} \quad \text{(Eq. 2.20)}$$

In practice, $u_{\boldsymbol{k}}(\boldsymbol{r})$ often depends only weakly on **k**, which is why we can get away with sampling only a small number of **k** in the Brillouin zone through schemes like the Monkhorst-pack sampling procedure; so, for example, the electron density would become:[34]

$$\rho(\boldsymbol{r}) = \frac{\Omega}{(2\pi)^3} \sum_{\boldsymbol{k}} \sum_{n=1}^{N_{electrons}} |\psi_{n\boldsymbol{k}}(\boldsymbol{r})|^2 \quad \text{(Eq. 2.21)}$$

at some finite number of **k**. In practice, the number of k-points included in a calculation is a convergence parameter.

The KS Hamiltonian is nearly independent for each k-point; i.e., in a periodic system,

$$H = \sum_{\boldsymbol{k}} H_k \text{ with } H_{\boldsymbol{k}} \psi_{n\boldsymbol{k}}(\boldsymbol{r}) = \epsilon_{n\boldsymbol{k}} \psi_{n\boldsymbol{k}}(\boldsymbol{r}) \quad \text{(Eq. 2.22)}$$

The "near independence" comes from the fact that the electron density is summed across k-points, and V_{eff} depends on the electron density. To make the idea of k-points a bit clearer, we stated earlier that a system with no periodic behavior (e.g., a molecule) can be modeled with planewave DFT as long as the unit cell is large enough that "neighboring cells" do not interact with each other, i.e. the solutions $\{\psi_{n\boldsymbol{k}}\}$ decay to zero at the edges of the box. In this case, we have only one k-point, the Γ point, with (k_x, k_y, k_z) = (0, 0, 0). With only this k-point, $H_{\boldsymbol{k}=\boldsymbol{0}} \psi_{n\boldsymbol{k}=\boldsymbol{0}}(\boldsymbol{r}) = \epsilon_{n\boldsymbol{k}=\boldsymbol{0}} \psi_{n\boldsymbol{k}=\boldsymbol{0}}(\boldsymbol{r})$ so that $H\psi_n(\boldsymbol{r}) = \epsilon_n \psi_n(\boldsymbol{r})$

In other words, we recover the molecular orbital result. In the periodic case, instead of molecular orbitals, we have bands, where for a given quantum number *n*, the band varies at each k-point, with a band energy $\epsilon_{n\boldsymbol{k}}$. The set of bands $\{\psi_n\}$ at a given k-point are like a set of molecular orbitals for that k-point. Plotting the band energies at various k-points allows us to create band structure plots. Band structure plots are the k-point dependent version of molecular orbital energy plots. If we integrate across the energy, this yields a total density of states plot, i.e., DOS(*E*)*dE* = number of levels between *E* and *E*+*dE*.[35]

Casting planewave DFT and atom-centered DFT as only a matter of basis set choice is perhaps a bit misleading. It may be more accurate to state that the planewave basis is the suitable basis for calculations with periodic symmetry, and atom-centered basis sets are most suitable for calculations with no periodic symmetry, as this difference in symmetry is at the core of the difference between the two methods.

2.3 Excited State Techniques

Ground-state DFT has had a profound impact on the field of computational chemistry, though the ground-state formalism of section 2.2 necessarily leaves excited state information inaccessible. To access excited state information, we can operate in either a perturbative regime, as is done for LR-TDDFT and RPA, or a propagative regime, as is done in real-time TDDFT. The foundation of both is the Runge-Gross theorem, which states that there is a one-to-one mapping of the time-dependent potential and the density of the system.[36] TDDFT is directly related to the time-dependent Schrödinger equation (TDSE), similar to how time-independent DFT is directly related to the time-independent Schrödinger equation. The TDSE for a many-body system of N particles is given by:

$$i\frac{\partial}{\partial t}\Psi(r_1, r_2, .., r_N, t) = H(r_1, r_2, .., r_N, t)\Psi(r_1, r_2, .., r_N, t) \quad \text{(Eq. 2.23)}$$

with

$$H(t) = T + V_{ee}(t) + V_{ext}(t) \quad \text{(Eq. 2.24)}$$

and

$$T = \sum_{j=1}^{N} -\frac{1}{2}\nabla^2, \quad V_{ee}(t) = \frac{1}{2}\sum_{i\neq j}^{N}\frac{1}{|\boldsymbol{r}_i - \boldsymbol{r}_j|} \quad \text{(Eq. 2.25)}$$

with V_{ext} the external potential. Like in the ground-state case, we want to solve in terms of the (now time-dependent) density instead of the many-body wavefunction, with:

$$\rho(r, t) = \int dr_2 \ldots dr_N |\Psi(r, r_2, \ldots, r_N, t)|^2 \quad \text{(Eq. 2.26)}$$

The Runge-Gross theorem provides the justification for re-casting the time-dependent Schrödinger equation in terms of the time-dependent electron density, in much the same way the Hohenberg-Kohn theorems provide the analogous basis in the ground-state case. The first HK theorem states that there is a one-to-one correspondence between the static external potential and the static ground-state density:

$$v(r) \Leftrightarrow \rho(r) \quad \text{(Eq. 2.27)}$$

Similarly, the Runge-Gross theorem states that there is a one-to-one correspondence between the time-dependent external potential and the time-dependent density. There are a few additional complications to the Runge-Gross theorem relative to the first HK theorem, though. The electron density is in a one-to-one correspondence with a class of external potentials, $v(r, t) + \alpha(t)$, rather than a single external potential, where $\alpha(t)$ is purely time-dependent.[37] This yields a time-dependent phase-factor in the wavefunction (note that this term vanishes in computing observables). Additionally, the time-dependent external potential has a one-to-one

correspondence with the time-dependent density and also a given initial state, Ψ_0. Thus, the Runge-Gross theorem yields:

$$v(r,t) \; + \; \alpha(t) \overset{\Psi_0}{\Leftrightarrow} \rho(r,t) \qquad \text{(Eq. 2.28)}$$

The original formulation of the Runge-Gross theorem stipulated that $v(r, t)$ must be analytic at t_0, but has since been extended to other forms of potentials (though a general proof for an arbitrary $v(r, t)$ does not exist). With the Runge-Gross theorem in hand, we can construct time-dependent Kohn-Sham (TDKS) equations, similar to how we constructed time-independent Kohn-Sham equations in the ground-state case. That is, we can construct a fictitious system of non-interacting particles in a time-dependent effective potential that yields the same time-dependent density $\rho(r,t)$ as the full interacting system. The TDKS equation takes the form:

$$i\frac{\partial}{\partial t}\psi_i(\boldsymbol{r},t) = \left[-\frac{1}{2}\nabla^2 + v_{eff}[\rho](r,t)\right]\psi_i(\boldsymbol{r},t) \qquad \text{(Eq. 2.29)}$$

with

$$v_{eff}[\rho](r,t) = v_{ext}(r,t) + \; v_c[\rho](r,t) + \; v_{xc}[\rho](r,t) \qquad \text{(Eq. 2.30)}$$

Here, $v_c[\rho](r,t)$ represents the time-dependent Coulomb potential, given as $v_c[\rho](r,t) = \int \frac{\rho(\boldsymbol{r}',\boldsymbol{t})}{|\boldsymbol{r}-\boldsymbol{r}'|}\, d\boldsymbol{r}'$. The term $v_{xc}[\rho](r,t)$ represents the exchange-correlation potential. Finally, the time-dependent electron density is given as:

$$\rho(r,t) = \sum_{i}^{occ} |\psi_i(r,t)|^2 \qquad \text{(Eq. 2.31)}$$

with ψ_i the single-particle Kohn-Sham wavefunctions. Similar to the time-independent case, while the formalism is formally exact, the exact form of v_{xc} is unknown. Time-dependent exchange-correlation functionals are trickier than the time-independent case, because in theory the time-dependent exchange correlation kernel is a function of the entire history of the electron

density, rather than just the density at some time *t*. This "memory dependence" is clearly no issue in the time-independent case. In the time dependent case, in practice the memory dependence of the functional is often too computationally costly, and is not considered. What we have presented so far is applicable to both perturbative and propagative time-dependent methods. Now, we focus on the perturbative case.

2.3.1 Linear Response Time-Dependent Density Functional Theory

The central idea of linear-response TDDFT is that if we apply a small perturbation to our system, we can treat the potential as a static potential plus some small time-dependent perturbation.[37] In other words, if $v(r,t) = v(r) + \delta v(r,t)$ with $\delta v(r,t) \ll v(r)$, then we can treat TDDFT as ground-state DFT plus the linear response to the time-dependent perturbation $v(r,t)$, with $\delta v(r,t) \Leftrightarrow \delta\rho(r,t)$. In such a case, the first order response can be written as:

$$\delta\rho(r_1,t_1) = \int\int dr_2 dt_2 \chi(r_1,t_1,r_2,t_2)\delta v(r_2,t_2) \qquad \text{(Eq. 2.32)}$$

where χ is the polarizability of the system. We can also cast LR-TDDFT in terms of a Kohn-Sham problem, i.e. we can have:

$$\delta v_{eff}(r,t) = \delta v_{ext}(r,t) + \delta v_H(r,t) + \delta v_{xc}(r,t) \qquad \text{(Eq. 2.33)}$$

where the Hartree term contains the instantaneous static Coulomb interaction:

$$\delta v_H(r_1,t_1) = \iint dr_2 dt_2 \frac{1}{|r_2 - r_1|}\,\delta(t_1,t_2)\,\delta\rho(r_2,t_2) \qquad \text{(Eq. 2.34)}$$

and the exchange-correlation term is given as:

$$\delta v_{xc}(r_1,t_1) = \iint dr_2 dt_2 f_{xc}[\rho](r_1,t_1,r_2,t_2)\delta\rho(r_2,t_2) \qquad \text{(Eq. 2.35)}$$

with $f_{xc}[\rho](r_1,t_1,r_2,t_2) = \frac{\delta v_{xc}[\rho](r_1,t_1)}{\delta\rho(r_2,t_2)}$. Now, with the KS effective potential, which we will now label v^{KS} instead of v_{eff}, we have a corresponding KS polarizability, χ^{KS}:

$$\delta\rho(r_1,t_1) = \int\int dr_2 dt_2 \chi^{KS}(r_1,t_1,r_2,t_2)\delta v^{KS}(r_2,t_2) \quad \text{(Eq. 2.36)}$$

Following the works of Adler and Wiser, we can write χ^{KS} as:[10,11]

$$\chi^{KS}(r_1,r_2,\omega) = \sum_i\sum_j (f_i^{KS} - f_j^{KS}) \frac{\psi_j^{KS}(r_1)\psi_i^{KS*}(r_1)\psi_i^{KS}(r_2)\psi_j^{KS*}(r_2)}{\omega - \left(\epsilon_j^{KS} - \epsilon_i^{KS}\right) + i\eta} \quad \text{(Eq. 2.37)}$$

where ϵ_i^{KS} are the KS orbital energies, ψ_i^{KS} are the corresponding KS wavefunctions, and f_i^{KS} is the occupation. The η is an infinitesimal value, a mathematical construct to ensure well-defined Fourier transforms, since we can transform between a time and frequency domain. Note that time and frequency are connected by a Fourier transform, so we have transformed to frequency-space in equation 2.37. Finally, we can express the polarizability of the full, interacting system in terms of the KS polarizability, the coulomb kernel, and the exchange correlation kernel:

$$\chi = \chi^{KS} + \chi^{KS}(v_c + f_{xc})\chi \quad \text{(Eq. 2.38)}$$

This is a central result of linear response theory. We will see that, once we know this polarizability, computing an absorption spectrum or an electron energy loss spectrum are each only a few steps away.

2.3.2 Casida's Equation

The Casida equation is a special and highly convenient form of LR-TDDFT. In quantum chemistry, the phrasing "the Casida equation" is sometimes used interchangeably with "LR-TDDFT," but the Casida equation is a particular form of LR-TDDFT, and so is less general than LR-TDDFT on the whole. To obtain the excitation energies of the system, one must obtain the

poles of χ. After identification of the fact that the search for the poles of χ can be re-cast into an eigenvalue problem and after significant algebraic rearrangement and substitution of equation 2.38 into the density response, we can obtain a matrix equation known as Casida's equation:[2,38,39]

$$\Omega\vec{F}_I = \Delta_I^2\vec{F}_I \qquad \text{(Eq. 2.39)}$$

where Δ_I is the excitation energy, with Ω given by (ignoring spin):

$$\Omega_{ia,kb} = \delta_{ik}\delta_{ab}\Delta_{ia}^2 + 2\sqrt{\Delta_{ia}}K_{ia,kb}\sqrt{\Delta_{kb}} \qquad \text{(Eq. 2.40)}$$

where the orbital energy difference is $\Delta_{ia} = \epsilon_a - \epsilon_i$, with ϵ_j the KS orbital energies, with *i,k* denoting occupied orbitals and *a, b* unoccupied orbitals. Finally, $K_{ia,kb}$ is given by

$$K_{ia,kb} = K_{ia,kb}^H + K_{ia,kb}^{xc} \qquad \text{(Eq. 2.41)}$$

with

$$K_{ia,kb}^H = \iint dr_1 dr_2 \varphi_i^*(r_1)\,\varphi_a(r_1)\frac{1}{|r_1 - r_2|}\varphi_b^*(r_2)\varphi_k(r_2) \qquad \text{(Eq. 2.42)}$$

$$K_{ia,kb}^{xc} = \iint dr_1 dr_2 \varphi_i^*(r_1)\,\varphi_a(r_1) f^{xc}\varphi_b^*(r_2)\varphi_k(r_2) \qquad \text{(Eq. 2.43)}$$

Finally, the eigenvector $\vec{F}_I$ in equation 2.39 can be used to construct an approximate excited state wavefunction as a linear combination of single-particle excitations:

$$|\Psi_I\rangle = \sum_{ia}\sqrt{\frac{2\Delta_{ia}}{\Delta_I}}F_{ia,I}\,\hat{c}^\dagger\hat{c}|\Psi_0\rangle \qquad \text{(Eq. 2.44)}$$

with $\hat{c}^\dagger$ and $\hat{c}$ the creation and annihilation operators and $|\Psi_0\rangle$ the wavefunction (Slater determinant) of the occupied KS orbitals. Once equation 2.39 is solved, an oscillator strength for each excitation can also be obtained. For singlet excitations, this is given by:

$$f_I = \frac{2}{3}\Delta_I\left|\sum_{ia}\sqrt{\frac{2\Delta_{ia}}{\Delta_I}}F_{ia,I}\,\langle\varphi_i|\vec{r}|\varphi_a\rangle\right|^2 \qquad \text{(Eq. 2.45)}$$

Casida's equation is extremely useful for computing an absorption spectrum. Once the excitation energies and their oscillator strengths are known, one can convolve this stick spectrum with a Lorentzian to obtain an absorption spectrum. That each excitation obtained via Casida's equation can be understood as a linear combination of single-particle excitations (equation 2.44) allows us much deeper insight into these excitations relative to obtaining excitation energies and oscillator strengths alone. We make heavy use of this type of analysis in Chapters 3 and 4.

2.3.3 The Random Phase Approximation (RPA)

The random phase approximation (RPA) can be considered a form or LR-TDDFT, and we view it this way in our work in Chapter 5. RPA originated in condensed matter physics, and was developed by Bohm and Pines in the 1950s to describe jellium, a system of electrons experiencing a uniform background positive charge.[40] Despite this seemingly narrow origin, RPA can be applied to any system of interacting particles, and is now an important concept in many areas of physics and chemistry. This broad applicability can make RPA conceptually confusing, as there are many ways to think about it, many ways to derive it, and many areas in which RPA sees use. In quantum chemistry, we often discuss RPA in the context of exchange-correlation functionals in density functional theory, with RPA's claim to fame being that it sits at the top of Perdew's famous "Jacob's Ladder of Chemical Accuracy," which outlines a hierarchy of density functionals, with the class on each higher rung more accurate than the last.[24] We also often discuss RPA in the context of LR-TDDFT, since RPA can be accurately described as the most simple version of LR-TDDFT. How can something be "like a density functional" and also be a version of LR-TDDFT?

The central quantity that unites RPA as both being "like a density functional" and a form of LR-TDDFT is its treatment of polarizability. Specifically, in equation 2.38, when f_{xc} is neglected, we call this "direct RPA."[41] When f_{xc} is non-zero, there are many forms it can take, and we call this set of methods generalized RPA. RPA can be treated "like a density functional" on account of the adiabatic connection fluctuation-dissipation theorem, which provides an exact expression for electron correlation in terms of the interacting density response function.[42,43] In other words, we can compute a correlation energy from the random phase approximation via this theorem. Then, we can combine this correlation energy with the exact exchange energy (i.e., the exact exchange in Hartree-Fock). Thus, we obtain an $E_{xc} = E_{c,RPA,} + E_{exact\ exchange}$, and to obtain the RPA total energy, we would first obtain a DFT total energy, so that $E_{RPA} = E_{DFT} - E_{xc,DFT} + (E_{c,RPA} + E_{exact\ exchange})$. So, RPA in this context is not so much a density functional as it is a means to obtain an exchange-correlation energy, which we would normally obtain using a density functional in DFT. RPA is further connected to DFT in that, in quantum chemistry, we use a mean-field starting point to compute both $E_{c,RPA}$ and $E_{exact\ exchange}$, i.e., we feed into the requisite $E_{c,RPA}$ and $E_{exact\ exchange}$ equation mean-field eigenfunctions and eigenenergies. I include this discussion for the sake of completeness in discussing RPA in the context of quantum chemistry and to provide the context for which RPA sits at the top of the "Jacob's ladder of chemical accuracy," discussed in section 2.2. However, in this work, we leverage RPA in the LR-TDDFT context to obtain electron energy loss (EEL) spectra, rather than leverage RPA in the exchange-correlation context to obtain more accurate ground-state properties.

In particular, we are interested in the EEL spectra of surfaces. In this case, we work in reciprocal space, employing the planewave-DFT formalism outlined in section 2.2.3 to obtain the

KS energies and wavefunctions. In reciprocal space with a planewave basis, the frequency-dependent KS polarizability is given as:[44]

$$\chi^{KS}_{\boldsymbol{G},\boldsymbol{G}'}(\boldsymbol{q},\omega) = \frac{2}{\Omega}\sum_{nn'\boldsymbol{k}} (f_{n\boldsymbol{k}} - f_{n'\boldsymbol{k}+\boldsymbol{q}}) \frac{n_{n\boldsymbol{k},n'\boldsymbol{k}+\boldsymbol{q}}(\boldsymbol{G}) n^{*}_{n\boldsymbol{k},n'\boldsymbol{k}+\boldsymbol{q}}(\boldsymbol{G}')}{\omega + \epsilon_{n\boldsymbol{k}} - \epsilon_{n'\boldsymbol{k}+\boldsymbol{q}} + i\eta} \qquad \text{(Eq. 2.46)}$$

with

$$n_{n\boldsymbol{k},n'\boldsymbol{k}+\boldsymbol{q}}(\boldsymbol{G}) \equiv \left\langle n\boldsymbol{k}\middle| e^{-i(\boldsymbol{q}+\boldsymbol{G})\boldsymbol{r}} \middle| n'\boldsymbol{k}+\boldsymbol{q}\right\rangle \qquad \text{(Eq. 2.47)}$$

where Ω is the volume of the cell, $f_{n\boldsymbol{k}}$ the occupation number of KS band *n* at k-point $\boldsymbol{k}$, $\epsilon_{n\boldsymbol{k}}$ the KS eigenenergy of band *n* at k-point $\boldsymbol{k}$, and **q** the specific point in reciprocal space at which we compute the polarizability, since in general the polarizability of the system depends on the momentum of the perturbation. The factor of 2 is present to account for spin (assuming a spin-degenerate system) Once we obtain the RPA polarizability, we can obtain a microscopic dielectric function via the relation:

$$\varepsilon^{-1} = 1 + v_c\chi \qquad \text{(Eq. 2.48)}$$

or, explicitly in reciprocal space with a planewave basis:

$$\varepsilon^{-1}_{\boldsymbol{G}\boldsymbol{G}'}(\boldsymbol{q},\omega) = \delta_{\boldsymbol{G}\boldsymbol{G}'} + \frac{4\pi}{|\boldsymbol{q}+\boldsymbol{G}|^2}\chi_{\boldsymbol{G}\boldsymbol{G}'}(\boldsymbol{q},\omega) \qquad \text{(Eq. 2.49)}$$

from which we can obtain a macroscopic dielectric function:[44,45]

$$\varepsilon_M = \frac{1}{\varepsilon^{-1}_{00}(\boldsymbol{q},\omega)} \qquad \text{(Eq. 2.50)}$$

where ε^{-1}_{00} corresponds to the microscopic dielectric function at **G**=0, **G**′=0. In other words, the macroscopic dielectric is the inverse of the **G**=0, **G**′=0 element of ε^{-1} at each frequency ω. The macroscopic dielectric is related to many experimental properties. The EEL spectrum (or "loss function") is given as -Im($\varepsilon^{-1}_M(\boldsymbol{q},\omega)$), and the optical absorption spectrum is given as Im($\varepsilon_M(q \to 0,\omega)$). The dielectric constant is given as $\lim_{\boldsymbol{q}\to 0} \varepsilon_M(\boldsymbol{q},\omega = 0)$.[37]

2.3.4 Real-time TDDFT

The linear-response formalism, by definition, operates in a perturbative regime, since the fundamental assumption is a small, time-dependent perturbation yields a small, time-dependent density response. However, if we wish to study the time-dependent properties of a system under non-linear regimes, then the LR-TDDFT method no longer applies. In our work, we excite atomic nanowires with strong electric fields. Such a process cannot be modeled with LR-TDDFT. Thus, we turn to real-time TDDFT (RT-TDDFT) instead.

In RT-TDDFT, the key idea is to re-cast the time-dependent KS equation (eq. 2.29) in terms of the density matrix of the system, then propagate the density matrix in real-time via numerical integration according to this equation. Note that in equation 2.29, a time-dependent external potential (e.g. an electric field) can be introduced, and, if present, is included in the V_{ext} term. The TDDFT equation for the density matrix takes the form:[5]

$$i\frac{d\boldsymbol{P}(t)}{dt} = [\boldsymbol{H}(t), \boldsymbol{P}(t)] \qquad \text{(Eq. 2.51)}$$

and is called the quantum Liouville equation of motion. $\boldsymbol{P}(t)$ is the time-dependent density matrix, with matrix elements given by:

$$P_{\mu\nu}(t) = \sum_i c_{\mu i}^*(t) c_{\nu i}(t) \qquad \text{(Eq. 2.52)}$$

where $c_{\nu i}(t)$ are the time-dependent expansion coefficients of molecular orbital i:

$$\varphi_i = \sum_\mu c_\mu(t)\, \phi_\mu \qquad \text{(Eq. 2.53)}$$

with ϕ_μ the μ'th basis function. In equation 2.51, $\boldsymbol{H}(t)$ is the matrix form of the time-dependent KS operator, equation 2.24, with matrix elements given by:

$$H_{\mu\nu}(t) = \langle \phi_\mu | H(t) | \phi_\nu \rangle \qquad \text{(Eq. 2.54)}$$

There are many methods to numerically integrate equation 2.51. Our work utilizes the modified midpoint unitary transformation method, which is well-described in ref [4]. We make use of the dipole approximation in our work, which assumes that the time-dependent electric field only couples to the molecule via its dipole moment. With the time-dependent perturbation given as $H'(t)$, this yields:[4]

$$H'(t) = \boldsymbol{E}(t) \cdot \boldsymbol{\mu} \qquad \text{(Eq. 2.55)}$$

Like LR-TDDFT, RT-TDDFT can be used to obtain a simulated absorption spectrum, for example by applying a delta-impulse function and then collecting the imaginary component of the Fourier transform of the time-dependent transition dipole moment scaled by the field intensity. If strong electric fields are applied, then we can access non-linear dynamics that are out of reach of LR-TDDFT. In addition to the transition dipole moment, we can obtain time-dependent orbital populations, which involves projecting the electron density onto the ground-state orbitals of the system. Such an analysis provides insight into which orbitals are involved in a transition, though we note that this is an approximation, since time-dependent orbitals themselves do not exist.

2.3.5 Ehrenfest Dynamics

While time-dependent density functional theory can provide a wealth of insight into excited-state electron dynamics, it is adiabatic in nature. That is, a central approximation in the electronic methods discussed so far is that we consider the nuclei of a system to be so slowly moving relative to the electronic motion that we can approximate the nuclei as static.[7] In other words, we assume that electrons adjust instantaneously to nuclear motion. Such an assumption allows us to make an enormous simplification to the Schrödinger equation, since we can treat the

electronic and nuclear subsystems separately.[46] This is called the Born-Oppenheimer approximation. However, if we want to model electron-nuclear processes, like the activation and dissociation of small molecules in the presence of silver nanowires in Chapters 3 and 4, we cannot make use of methods that employ the Born-Oppenheimer approximation. Instead, we utilize the non-adiabatic Ehrenfest dynamics method.[9] Ehrenfest dynamics is a "mixed quantum-classical" method, which propagates the classical nuclei on a superposition of electronic states.[9] Ehrenfest dynamics produces two coupled equations of motion, one for the quantum mechanical treatment of the electron dynamics, and one for the classical treatment of the nuclei. In this approximation, nuclei experience an average force from the electronic states.[8] The two equations are solved simultaneously, which allows us to study, for example, how the adsorbates in Chapters 3 and 4 activate in the presence of the wire, as we can examine how the adsorbate bond lengths change over time upon application of an applied electric field.

2.3 High Performance Computing

2.3.1 Introduction

All of the calculations reported in Chapters 3 – 5 require the use of high performance computing in some form. High performance computing is the practice of orchestrating compute resources to act in tandem to solve a large computational problem. When we make mention of "an HPC," we refer to the supercomputers or compute clusters that we utilize to perform HPC computations. A typical HPC contains many "compute nodes," which act as discrete compute units with their own computer processing units (CPUs), memory, and, increasingly commonly, one or more graphics processing units (GPUs). These nodes are then physically connected via ethernet, infiniband, or similar, which allows for high-speed communication between nodes. In

high performance computing, we may utilize one node (or part of one node) to run a poorly-scaling calculation for many weeks, or, in the more exciting case, utilize hundreds or thousands of nodes to solve a highly scalable calculation in a matter of minutes or hours. Here, scaling refers to how efficiently a problem runs on many compute resources vs. a few compute resources. A code that scales perfectly will, if given twice the amount of compute resources (e.g. CPUs), finish in half the time.

There are multiple levels of parallelism within an HPC. There is parallelism in which compute units do not share memory, which is typically implemented through a protocol called MPI, or "message passing interface" (though we note that shared-memory implementations of MPI do exist). There is also shared-memory parallelism, in which independent compute units can access the same regions of memory. Shared-memory parallelism may be implemented via directive-based paradigms such as OpenMP, or more directly through the use of p-threads or similar. GPUs represent yet another level of parallelism. In this work, we focus on MPI parallelism. Nodes do not share memory with each other, so massive parallelism is typically achieved through the efficient use of MPI; i.e., calculations in which hundreds or thousands of nodes are recruited necessarily require MPI parallelism. Then, a given pool of resources collected under one MPI task may further divide up the work assigned to the task via thread or GPU parallelism, or both.

2.3.2 MPI Parallelism

MPI is a standard for distributed-memory programming, with common implementations of MPI including Intel MPI, OpenMPI, and MPICH. These different implementations may work differently under the hood, i.e., implement different algorithms for the same message-passing

functions. The outcome of a given MPI call will necessarily be the same whether the code was compiled with Intel MPI, OpenMPI, or MPICH (or others) as long as the implementation adheres to the MPI standard, though performance may differ between implementations.[47]

Central to MPI is the concept of an MPI task. An MPI task can be an entire compute node, or down to a single CPU. When executing MPI-enabled code, the user may specify the number of MPI tasks. Each MPI task executes a copy of the code, and each task is given its own MPI rank (or label), and tasks communicate via the set of functions dictated by the MPI standard. MPI tasks are often called "processes." Some may use the term "CPU" or "core" to refer to an MPI task, but while cores can be MPI tasks, MPI tasks need not be cores. In this work, we use the terminology "MPI task," or sometimes just "task."

There are many types of MPI communication calls that a task can execute. These calls can be divided into two main categories: whether a call is "blocking" or "non-blocking," and whether a call is "collective" or "point-to-point". Blocking or non-blocking refers to whether or not the MPI call returns before (non-blocking) or after (blocking) the operation initiated by the call completes.[48] If a call is collective, all MPI tasks in the communication group must execute the call. If a call is point-to-point, then it is carried out between a pair of MPI tasks. In this work, we make heavy use of collective calls. In particular, we utilize the MPI collective calls MPI_BCAST and MPI_REDUCE and the point-to-point calls MPI_SENDV and MPI_RECV.

MPI_BCAST is a broadcasting function that sends information from one MPI task, the "root", to all other MPI tasks in a specified communication group. This communication type is visualized in Figure 2.1. It is collective because all tasks in the group must participate in the call. Broadcasting is a common and extremely useful communication pattern. Broadcasting is useful in cases where one MPI task has information that all other MPI tasks need. For example, if all

MPI tasks need the data contained in a particular file, one task may read the file, then broadcast this information to the other tasks. Of course, there are a variety of other ways for this file-reading task to send out the information to the other tasks in need, and some methods may be more efficient than others. Broadcasting performance depends on the number of tasks being broadcasted to, and the amount of information being sent.

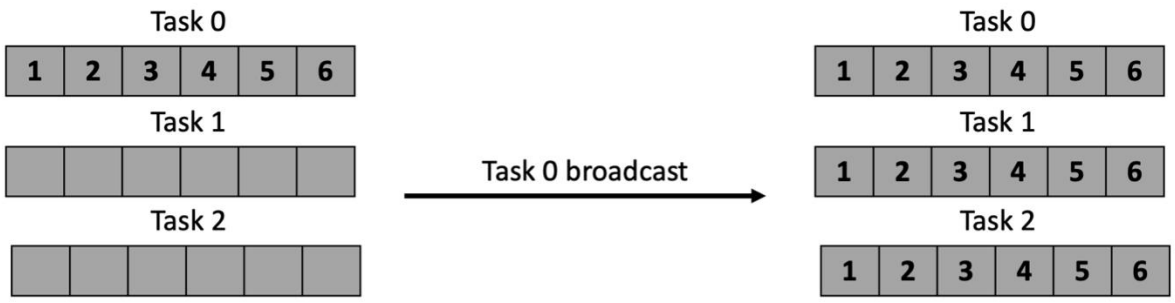

Figure 2.1 Visualization of an MPI_BCAST call. Task 0 owns an array filled with integers from one to six. Upon broadcasting, Task 1 and Task 2 receive all data contained in this array.

MPI_REDUCE can be thought of, in some ways, as the opposite of a broadcast call. Instead of one MPI task sending out information to all other MPI tasks, all other MPI tasks are sending information to one receiving "root" task. MPI_REDUCE performs a mathematical operation on the data it is sending. For example, if each MPI task is performing some local sum, then the global sum can be obtained by the root task by invoking an MPI_REDUCE call with a sum-operation specified (Figure 2.2). In our work, we use MPI_REDUCE calls to send data in an array, when each task may only have data that belongs to a portion of the array. In this case, the other array entries are initialized to 0, so that when the sum reduction is performed, the result is that each MPI task's array is condensed into a single buffer on the root task (Figure 2.3).

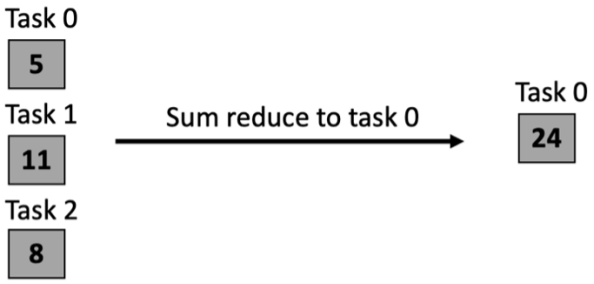

Figure 2.2 Visualization of a simple MPI_REDUCE sum reduction, where the receiving task, task 0, obtains a sum of the data held by each task upon completion of the reduce call.

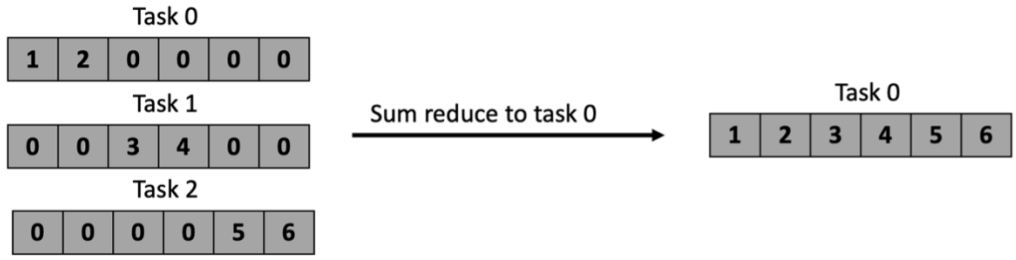

Figure 2.3 Visualization of a more complex MPI_REDUCE sum reduction, where the root task, task 0, obtains the data owned by each MPI task. Because each MPI task's array only has information in a region of the array that does not overlap with the other MPI tasks, ultimately the root task obtains a global array containing all of the information from all of the tasks. This is a useful method to send all data of a global array to a root task when each task owns (and knows) only a portion of the array.

While collective calls require all tasks in a communication group to participate, point-to-point calls involve only two processes. Point-to-point communication involves "send" and "receive" MPI calls (which have both blocking and non-blocking variants), where one MPI task simply invokes a send call, specifying which data is to be sent to which other MPI task, and this other MPI task invokes a receive call to obtain this data. Point-to-point communication gives rise to "cyclic distribution" communication patterns, where data is passed around from task-to-task in a ring-like fashion.

2.3.3 HDF5

HDF5 is a filetype with an associated library of routines that enable creation, reading, and writing of HDF5 files.[49] HDF5 stands for "hierarchical data format," and allows the user to store data in the file in a way that is conceptually similar to how one might store data in files on a computer within some directory structure, where datasets within an HDF5 file are accessed via a specified path much like how one might access a file in a directory via the command line interface. Beyond its intuitive organization scheme, the HDF5 filetype offers many advantages, like the fact that the filetype is highly portable and the associated HDF5 library facilitates creation of highly flexible and powerful read/write routines within an HDF5-enabled code. The partial I/O capabilities of HDF5 are utilized heavily in this work.

In HDF5 terminology, a dataset contains both dataset elements and metadata that describes the elements. The metadata can contain a variety of information, but will commonly at least contain the datatype of the data (integer, float, etc., and more exotically, datatypes like arrays, enums, strings, user-defined types, and more), and the dataspace, which describes the rank and dimensions of the array of data.[50] Dataspaces are important in HDF5 partial I/O, as we can use them to select arbitrary subsections of the data to transfer from disk to a memory buffer. These arbitrary selections are called hyperslabs. When a hyperslab is specified, the HDF5 library performs I/O operations on only this selection, rather than all of the elements of a dataset. This is an extremely powerful feature, especially when working with very large datasets. In selecting a hyperslab, we specify the starting location, the stride, the count, and the block size. We can then take unions of these hyperslabs to create any sort of hyperslab shape. Using these hyperslab selections, HDF5 can then transfer the corresponding data into a memory buffer.[51] A visualization of hyperslab selection is shown in Figure 2.4.

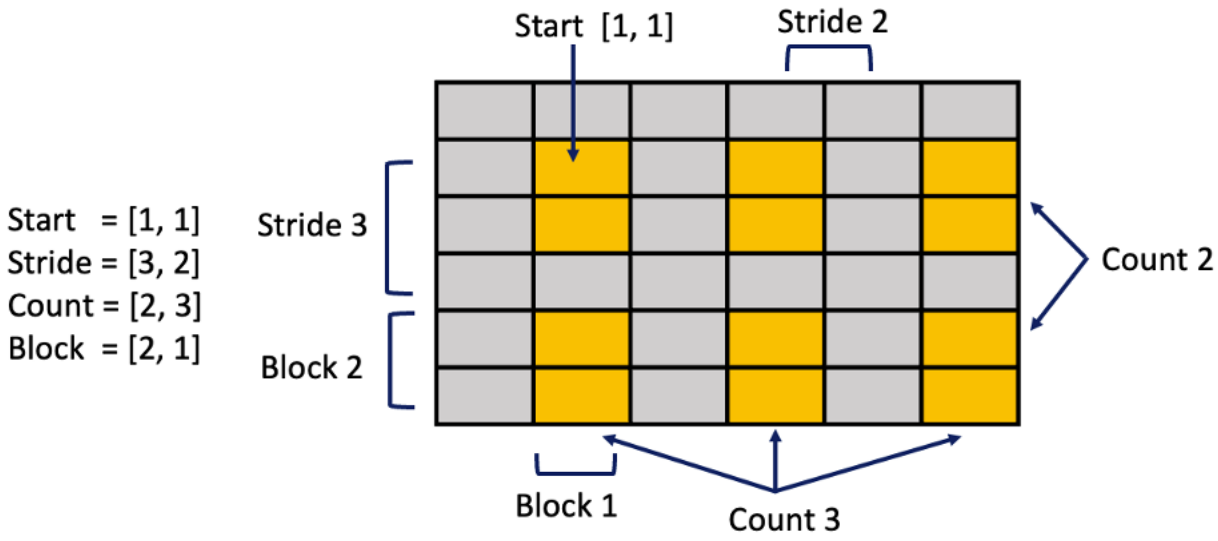

Figure 2.4 Hyperslab selection from a dataspace shown as orange elements, with parameters shown on the left of the figure. First element denotes the row dimension, with the second element denoting the column dimension. The start provides the starting location of the hyperslab within the dataspace. The stride denotes the number of elements between the start of each block. The count denotes the number of blocks in each dimension. Block denotes the size of the individual blocks. Figure adapted from Ref. [50].

One of the most powerful features of HDF5 I/O for high performance computing applications is that it can be used for parallel I/O, which allows multiple MPI tasks access to a single file.[52] Parallel HDF5 utilizes MPI-IO under the hood to achieve high performance parallel reads and writes. Because parallel HDF5 acts on top of MPI-IO, we can continue to work exclusively with HDF5 calls, and simply define hyperslab regions in an MPI task-specific way. An example of this is shown in Figure 2.5, where MPI tasks select a hyperslab row based on the rank of the task.

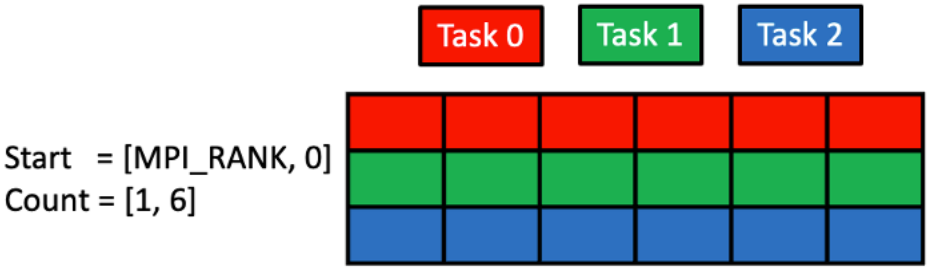

Figure 2.5 A parallel HDF5 example. The starting row element is given by the rank of the MPI task. Each task starts at column element 0. The count of each MPI-specific hyperslab is one row, six columns. Upon successful reading, MPI task 0 will have only the data contained in the first row, task 1 will have only the data contained in the second row, and so on.

2.4 Conclusion

I have discussed in this chapter the background and details of the methods used in the coming chapters. In Chapters 3 and 4, we utilize atom-centered ground-state DFT, Casida's equation and LR-TDDFT, real-time TDDFT, and Ehrenfest dynamics to study the behavior of a small molecule attached to an atomic Ag nanowire. In Chapter 5, we utilize planewave DFT and RPA EEL spectra to study the interaction of H_2 with a gold surface. In Chapters 6, we develop MPI-parallel methods based on RPA to study the problem in Chapter 5. In Chapter 7, we utilize MPI and HDF5 in high performance computing developments to improve the efficiency of the code that we use in Chapters 5 and 6.

2.5 References

(1) Hohenberg, P.; Kohn, W. Inhomogeneous Electron Gas. *Phys. Rev.* **1964**, *136* (3B), B864–B871. https://doi.org/10.1103/PhysRev.136.B864.

(2) Casida, M. E. Time-Dependent Density Functional Response Theory for Molecules. In *Recent Advances in Computational Chemistry*; WORLD SCIENTIFIC, 1995; Vol. 1, pp 155–192. https://doi.org/10.1142/9789812830586_0005.

(3) Casida, M. E.; Huix-Rotllant, M. Progress in Time-Dependent Density-Functional Theory. *Annu. Rev. Phys. Chem.* **2012**, *63* (1), 287–323. https://doi.org/10.1146/annurev-physchem-032511-143803.

(4) Goings, J. J.; Lestrange, P. J.; Li, X. Real-Time Time-Dependent Electronic Structure Theory. *Wiley Interdiscip. Rev. Comput. Mol. Sci.* **2018**, *8* (1), e1341. https://doi.org/10.1002/wcms.1341.

(5) Provorse, M. R.; Isborn, C. M. Electron Dynamics with Real-Time Time-Dependent Density Functional Theory. *Int. J. Quantum Chem. 116* (10), 739–749. https://doi.org/10.1002/qua.25096.

(6) Li, X.; Govind, N.; Isborn, C.; DePrince, A. E.; Lopata, K. Real-Time Time-Dependent Electronic Structure Theory. *Chem. Rev.* **2020**, *120* (18), 9951–9993. https://doi.org/10.1021/acs.chemrev.0c00223.

(7) Tully, J. C. Perspective: Nonadiabatic Dynamics Theory. *J. Chem. Phys.* **2012**, *137* (22), 22A301. https://doi.org/10.1063/1.4757762.

(8) Crespo-Otero, R.; Barbatti, M. Recent Advances and Perspectives on Nonadiabatic Mixed Quantum–Classical Dynamics. *Chem. Rev.* **2018**. https://doi.org/10.1021/acs.chemrev.7b00577.

(9) Ding, F.; Goings, J. J.; Liu, H.; Lingerfelt, D. B.; Li, X. Ab Initio Two-Component Ehrenfest Dynamics. *J. Chem. Phys.* **2015**, *143* (11), 114105. https://doi.org/10.1063/1.4930985.

(10) Adler, S. L. Quantum Theory of the Dielectric Constant in Real Solids. *Phys. Rev.* **1962**, *126* (2), 413–420. https://doi.org/10.1103/PhysRev.126.413.

(11) Wiser, N. Dielectric Constant with Local Field Effects Included. *Phys. Rev.* **1963**, *129* (1), 62–69. https://doi.org/10.1103/PhysRev.129.62.

(12) Deslippe, J.; Samsonidze, G.; Strubbe, D. A.; Jain, M.; Cohen, M. L.; Louie, S. G. BerkeleyGW: A Massively Parallel Computer Package for the Calculation of the Quasiparticle and Optical Properties of Materials and Nanostructures. *Comput. Phys. Commun.* **2012**, *183* (6), 1269–1289. https://doi.org/10.1016/j.cpc.2011.12.006.

(13) Kohn, W.; Sham, L. J. Self-Consistent Equations Including Exchange and Correlation Effects. *Phys. Rev.* **1965**, *140* (4A), A1133–A1138. https://doi.org/10.1103/PhysRev.140.A1133.

(14) The Hohenberg-Kohn Theorems. In *A Chemist's Guide to Density Functional Theory*; John Wiley & Sons, Ltd, 2001; pp 33–40. https://doi.org/10.1002/3527600043.ch4.

(15) *Conceptual Density Functional Theory | Chemical Reviews*. https://pubs.acs.org/doi/full/10.1021/cr990029p (accessed 2022-12-20).

(16) Stowasser, R.; Hoffmann, R. What Do the Kohn−Sham Orbitals and Eigenvalues Mean? *J. Am. Chem. Soc.* **1999**, *121* (14), 3414–3420. https://doi.org/10.1021/ja9826892.

(17) Baerends, E. J.; Gritsenko, O. V. A Quantum Chemical View of Density Functional Theory. *J. Phys. Chem. A* **1997**, *101* (30), 5383–5403. https://doi.org/10.1021/jp9703768.

(18) van Meer, R.; Gritsenko, O. V.; Baerends, E. J. Physical Meaning of Virtual Kohn–Sham Orbitals and Orbital Energies: An Ideal Basis for the Description of Molecular Excitations. *J. Chem. Theory Comput.* **2014**, *10* (10), 4432–4441. https://doi.org/10.1021/ct500727c.

(19) Chong, D. P.; Gritsenko, O. V.; Baerends, E. J. Interpretation of the Kohn–Sham Orbital Energies as Approximate Vertical Ionization Potentials. *J. Chem. Phys.* **2002**, *116* (5), 1760–1772. https://doi.org/10.1063/1.1430255.

(20) Gritsenko, O. V.; Braïda, B.; Baerends, E. J. Physical Interpretation and Evaluation of the Kohn–Sham and Dyson Components of the ε–I Relations between the Kohn–Sham Orbital Energies and the Ionization Potentials. *J. Chem. Phys.* **2003**, *119* (4), 1937–1950. https://doi.org/10.1063/1.1582839.

(21) Toulouse, J. Review of Approximations for the Exchange-Correlation Energy in Density-Functional Theory. arXiv September 9, 2022. http://arxiv.org/abs/2103.02645 (accessed 2022-12-20).

(22) Peverati, R.; Truhlar, D. G. Quest for a Universal Density Functional: The Accuracy of Density Functionals across a Broad Spectrum of Databases in Chemistry and Physics. *Philos. Trans. R. Soc. Math. Phys. Eng. Sci.* **2014**, *372* (2011), 20120476. https://doi.org/10.1098/rsta.2012.0476.

(23) Mardirossian, N.; Head-Gordon, M. Thirty Years of Density Functional Theory in Computational Chemistry: An Overview and Extensive Assessment of 200 Density Functionals. *Mol. Phys.* **2017**, *115* (19), 2315–2372. https://doi.org/10.1080/00268976.2017.1333644.

(24) Perdew, J. P.; Schmidt, K. Jacob's Ladder of Density Functional Approximations for the Exchange-Correlation Energy. *AIP Conf. Proc.* **2001**, *577* (1), 1–20. https://doi.org/10.1063/1.1390175.

(25) Chai, J.-D.; Head-Gordon, M. Systematic Optimization of Long-Range Corrected Hybrid Density Functionals. *J. Chem. Phys.* **2008**, *128* (8), 084106. https://doi.org/10.1063/1.2834918.

(26) Attila Szabo; Neil S. Ostlund. *Modern Quantum Chemistry: Introduction to Advanced Electronic Structure Theory*. https://store.doverpublications.com/0486691861.html (accessed 2022-12-20).

(27) Magalhães, A. L. Gaussian-Type Orbitals versus Slater-Type Orbitals: A Comparison. *J. Chem. Educ.* **2014**, *91* (12), 2124–2127. https://doi.org/10.1021/ed500437a.

(28) Ira N. Levine. *Quantum Chemistry*, 7th ed.; Pearson, 2016.

(29) Wadt, W. R.; Hay, P. J. Ab Initio Effective Core Potentials for Molecular Calculations. Potentials for Main Group Elements Na to Bi. *J. Chem. Phys.* **1985**, *82* (1), 284–298. https://doi.org/10.1063/1.448800.

(30) Hay, P. J.; Wadt, W. R. Ab Initio Effective Core Potentials for Molecular Calculations. Potentials for the Transition Metal Atoms Sc to Hg. *J. Chem. Phys.* **1985**, *82* (1), 270–283. https://doi.org/10.1063/1.448799.

(31) Xu, X.; Truhlar, D. G. Accuracy of Effective Core Potentials and Basis Sets for Density Functional Calculations, Including Relativistic Effects, As Illustrated by Calculations on Arsenic Compounds. *J. Chem. Theory Comput.* **2011**, *7* (9), 2766–2779. https://doi.org/10.1021/ct200234r.

(32) Kratzer, P.; Neugebauer, J. The Basics of Electronic Structure Theory for Periodic Systems. *Front. Chem.* **2019**, *7*.

(33) Hutchinson, M.; Fleurat-Lessard, P.; Anciaux-Sedrakian, A.; Stosic, D.; Bédorf, J.; Tariq, S. Plane-Wave Density Functional Theory. In *Electronic Structure Calculations on Graphics Processing Units*; John Wiley & Sons, Ltd, 2016; pp 135–172. https://doi.org/10.1002/9781118670712.ch7.

(34) Monkhorst, H. J.; Pack, J. D. Special Points for Brillouin-Zone Integrations. *Phys. Rev. B* **1976**, *13* (12), 5188–5192. https://doi.org/10.1103/PhysRevB.13.5188.

(35) Roald Hoffman. *Solids and Surfaces: A Chemist's View of Bonding in Extended Structures | Wiley*. Wiley.com. https://www.wiley.com/en-us/Solids+and+Surfaces%3A+A+Chemist%27s+View+of+Bonding+in+Extended+Structures-p-9780471187103 (accessed 2022-12-20).

(36) Runge, E.; Gross, E. K. U. Density-Functional Theory for Time-Dependent Systems. *Phys. Rev. Lett.* **1984**, *52* (12), 997–1000. https://doi.org/10.1103/PhysRevLett.52.997.

(37) Valerio Olevano. TDDFT, Excitations and Spectroscopy. In *Structures on Different Time Scales: Volume 1*; De Gruyter, 2018; p 101. https://doi.org/10.1515/9783110433920.

(38) Robert Rüger. Approximations in Density Functional Based Excited State Calculations, Vrije Universiteit Amsterdam, 2018.

(39) Domínguez, A.; Aradi, B.; Frauenheim, T.; Lutsker, V.; Niehaus, T. A. Extensions of the Time-Dependent Density Functional Based Tight-Binding Approach. *J. Chem. Theory Comput.* **2013**, *9* (11), 4901–4914. https://doi.org/10.1021/ct400123t.

(40) Bohm, D.; Pines, D. A Collective Description of Electron Interactions. I. Magnetic Interactions. *Phys. Rev.* **1951**, *82* (5), 625–634. https://doi.org/10.1103/PhysRev.82.625.

(41) Glasbrenner, M.; Graf, D.; Ochsenfeld, C. Benchmarking the Accuracy of the Direct Random Phase Approximation and σ-Functionals for NMR Shieldings. *J. Chem. Theory Comput.* **2022**, *18* (1), 192–205. https://doi.org/10.1021/acs.jctc.1c00866.

(42) Ren, X.; Rinke, P.; Joas, C.; Scheffler, M. Random-Phase Approximation and Its Applications in Computational Chemistry and Materials Science. *J. Mater. Sci.* **2012**, *47* (21), 7447–7471. https://doi.org/10.1007/s10853-012-6570-4.

(43) Olsen, T.; Patrick, C. E.; Bates, J. E.; Ruzsinszky, A.; Thygesen, K. S. Beyond the RPA and GW Methods with Adiabatic Xc-Kernels for Accurate Ground State and Quasiparticle Energies. *Npj Comput. Mater.* **2019**, *5* (1), 1–23. https://doi.org/10.1038/s41524-019-0242-8.

(44) Yan, J.; Mortensen, Jens. J.; Jacobsen, K. W.; Thygesen, K. S. Linear Density Response Function in the Projector Augmented Wave Method: Applications to Solids, Surfaces, and Interfaces. *Phys. Rev. B* **2011**, *83* (24), 245122. https://doi.org/10.1103/PhysRevB.83.245122.

(45) Yan, J.; Thygesen, K. S.; Jacobsen, K. W. Nonlocal Screening of Plasmons in Graphene by Semiconducting and Metallic Substrates: First-Principles Calculations. *Phys. Rev. Lett.* **2011**, *106* (14), 146803. https://doi.org/10.1103/PhysRevLett.106.146803.

(46) Nelson, T. R.; White, A. J.; Bjorgaard, J. A.; Sifain, A. E.; Zhang, Y.; Nebgen, B.; Fernandez-Alberti, S.; Mozyrsky, D.; Roitberg, A. E.; Tretiak, S. Non-Adiabatic Excited-State Molecular Dynamics: Theory and Applications for Modeling Photophysics in Extended Molecular Materials. *Chem. Rev.* **2020**, *120* (4), 2215–2287. https://doi.org/10.1021/acs.chemrev.9b00447.

(47) *MPI-2: Extensions to the Message-Passing Interface*. https://www.mcs.anl.gov/research/projects/mpi/mpi-standard/mpi-report-2.0/mpi2-report.htm (accessed 2022-12-31).

(48) Marc Snir; Steve Otto; Steven Huss-Lederman; David Walker; Jack Dongarra. *MPI: The Complete Reference*. https://netlib.org/utk/papers/mpi-book/mpi-book.html (accessed 2022-12-20).

(49) Folk, M.; Heber, G.; Koziol, Q.; Pourmal, E.; Robinson, D. An Overview of the HDF5 Technology Suite and Its Applications. In *Proceedings of the EDBT/ICDT 2011 Workshop on Array Databases*; AD '11; Association for Computing Machinery: New York, NY, USA, 2011; pp 36–47. https://doi.org/10.1145/1966895.1966900.

(50) Quincey Koziol. Introduction to HDF5, 2014. https://bluewaters.ncsa.illinois.edu/liferay-content/document-library/Documentation%20Documents/Workshops/Advanced%20User%20Workshop%20Oct%202014/HDF5-Intro-v2.pdf.

(51) The HDF Group. *Chapter 7: HDF5 Dataspaces and Partial I/O*. http://davis.lbl.gov/Manuals/HDF5-1.8.7/UG/12_Dataspaces.html (accessed 2022-12-20).

(52) Byna, S.; Breitenfeld, S.; Dong, B.; Koziol, Q.; Pourmal, E.; Robinson, D.; Soumagne, J.; Tang, H.; Vishwanath, V.; Warren, R. ExaHDF5: Delivering Efficient Parallel I/O on Exascale Computing Systems. *J. Comput. Sci. Technol.* **2020**, *35* (1), 145–160. https://doi.org/10.1007/s11390-020-9822-9.

Chapter 3 - Electronic Structure and Nonadiabatic Dynamics of Atomic Silver Nanowire-N_2 Systems

Olivia A. Hull, David B. Lingerfelt, Xiaosong Li, and Christine M. Aikens

Reprinted with permission from J. Phys. Chem. C. **2020**, 124, 38, 20834 – 20845.

3.1 Abstract

Plasmonic nanoparticles can facilitate bond breaking and drive reactions of nearby molecules. Some of these processes involve bond activations which are traditionally challenging to accomplish. However, there is uncertainty in our understanding of the mechanisms through which plasmonic nanoparticles activate bonds, and exactly how the plasmon resonance facilitates the bond breakage. Herein, we evaluate Ag_nN_2 (n = 4, 6, 8) model systems via real-time time-dependent density functional theory (RT-TDDFT), linear response time-dependent density functional theory (LR-TDDFT), and Ehrenfest dynamics with a long-range corrected functional in order to better understand the charge-transfer process between the Ag system and the adsorbed small molecule. We find that charge-transfer states exist between Ag_n Σ-orbitals and antibonding orbitals of N_2. Ehrenfest dynamics calculations reveal symmetry- and electric-field-dependent activation of N_2 when coupled to the wire. This study serves as a step towards understanding the time-dependent electron and electron-nuclear dynamics that arise due to the interactions between plasmonic nanowires and small molecules.

3.2 Introduction

Plasmonic nanoparticles (NPs) find application in a variety of fields, including catalysis,[1–7] medicine,[8,9] photovoltaics,[10] chemical detection and sensing,[11] and more. Much of the utility of plasmonic NPs arises from their optical properties, which differ from their bulk-metal counterparts due to quantum confinement effects that occur on the nanometer length scale. As these effects depend strongly on the size and shape of the particle, the optical properties of plasmonic NPs are highly tunable. However, certain aspects of the optical properties of NPs can be difficult to study experimentally, often owing to the presence of a solid support, electromagnetic coupling between neighboring particles, or other complicating factors. Hence, computational chemistry methods serve as powerful tools for the systematic investigation of the optical and electronic properties of plasmonic NPs. An understanding of these properties is fundamental to the rational design of such particles for applications.

The localized surface plasmon resonance often falls within the visible light range for noble metal NPs. The plasmon resonance peak is typically strongly absorbing, and excitation gives rise to intense local electromagnetic fields at the nanoscale.[3] Qualitatively, a localized surface plasmon resonance can be thought of as a collective "sloshing" of free surface electrons upon irradiation of the NP with light of a certain frequency. This motion can cause high-energy orbitals of a nearby molecule to become populated, and thereby facilitate reactions of the molecule that cannot be promoted in its electronic ground-state via thermal processes. Hence, plasmonic noble metal nanomaterials are being increasingly regarded as a new class of photocatalysts which facilitate reactions under more facile conditions than traditional synthetic routes.

Plasmonic NPs can selectively break bonds and drive reactions on nearby molecules under benign conditions. Some of these processes involve bond activations which are traditionally challenging to accomplish. In 2008, Christopher and Linic reported that Ag nanowires can serve as selective ethylene epoxidation catalysts.[1] Since then, plasmon-enhanced photocatalytic processes including H_2 splitting,[2] CO_2 reduction,[3] O_2 activation,[7] NH_3 oxidation,[4] propylene epoxidation,[6] water splitting,[5] and more have been reported. To provide a specific illustration of the "benign conditions," using colloidal gold NPs as catalysts, Jain and coworkers accomplished the plasmon-mediated reduction of CO_2 to methane and ethane under visible light excitation with turnover numbers of 6.8 and 5.6 NP^{-1} in 10 hours respectively.[3] However, while feats such as visible-light-activated CO_2 reduction offer exciting prospects, efficiency and selectivity in these processes is not guaranteed. While some plasmon-mediated processes are high yield and/or highly selective, others may suffer from low yield and/or poor selectivity, and protocols to fine-tune efficiency or selectivity are currently largely empirical in nature. The mechanisms through which plasmonic NPs activate bonds, and exactly how the localized surface plasmon facilitates the bond breakage, are not fully understood, and this lack of mechanistic understanding hinders the ability of researchers to systematically improve the process.

Chemical interface damping describes the change in hot carrier distribution caused by the adsorption of the molecular species onto the NP, and is thought to play a role in plasmon-mediated photocatalysis.[12] The adsorbed species can form hybridized metal-adsorbate bonding and antibonding orbitals. If the hybridized bonding orbitals are of significant metal character, and the hybridized antibonding orbitals are of significant adsorbate character, then a direct excitation from bonding to antibonding orbital can result in the "hot carrier" activation of the adsorbate.[12] Several studies have shown that the presence of chemical interface damping plays

an important role in plasmon-mediated photocatalysis.[13–16] However, other processes are also thought to be important in plasmon-mediated photocatalysis. For example, a study by Ma, et al. showed that single particle excitation states nearly resonant with the plasmonic state should be present for the plasmon mode to decay into hot carriers, which then drive chemistry on the nearby adsorbate.[17] Which factors are critical or required for catalysis to occur, including the interplay between chemical interface damping and plasmonic decay into hot carriers, is unclear at the present time. Developing an understanding of the electronic structure of NP-adsorbate systems, their electron dynamics, the role of the plasmon resonance in the catalytic activity, and how these factors may direct plasmon-mediated photocatalysis is the motivation of the work herein.

In our work, we utilize model nanoclusters to study the NP-adsorbate systems. Nanoclusters are nanoparticles comprised of only 10s of atoms. Nanoclusters are an appealing system choice for understanding plasmon-mediated photocatalysis through the lens of quantum chemistry and molecular orbital theory as the states in these systems are quantized in contrast to the band-like picture of larger nanoparticles. While the plasmon resonance of large-sized NPs can often be satisfactorily described through classical electrodynamics such as Mie Theory,[18] this classical picture of oscillating charge density breaks down for clusters of sufficiently small size (< 10 nm).[19] In these small clusters, the occupied and valence bands become quantized such that the plasmon resonance is instead described by a constructive addition of single-particle transitions. This phenomenon is sometimes referred to as a "quantum plasmon" or a "quantum plasmon-like excitation".[20,21] There is evidence to suggest that very small nanoclusters (< 2.5 nm) have plasmon modes that decay into hot carriers dominated by sp-to-sp transitions, while the plasmons of larger sized nanoparticles decay into carriers arising from d-to-sp transitions.[22]

Further, whether clusters that display a quantum plasmon will have photocatalytic behavior that behaves analogously to systems that are adequately described by classical methods (e.g. in nanoparticles with > 10 nm diameter) remains an open question.

The collective excitation of a quantum plasmon can be described in terms of configuration interaction (CI), where each Slater determinant describes a single excitation, and the weights on the Slater determinants are approximately equal and of the same sign (constructive).[20,23] The CI-like description of the quantum plasmon is convenient for several reasons. First, the linear response time-dependent density functional theory (LR-TDDFT),[24] one of the most common and readily accessible methods for computing an absorption spectrum within the DFT approximation, describes excitations as weighted combinations of single-particle transitions. Thus, the CI-like description of the quantum plasmon is inherently built into LR-TDDFT since the single-particle excitations and corresponding weights that comprise a collective peak are determined as part of the calculation.[20,25,26] Second, this CI-like description of the plasmon as a collective excitation of single particle states provides a means to interpret the symmetry-adapted molecular orbital picture ubiquitous in computational chemistry for these collective excitations. Finally, the CI-like description offers a route to understand plasmon resonances through a quantum mechanical, rather than classical, approach, which is critical for the study of small, plasmonic nanoclusters.

We focus on the Ag_n wire system (n = 4, 6, 8) with an adsorbed N_2, i.e. an N_2 molecule placed on the end of a linear chain of silver atoms. Even numbers of Ag atoms are used so that the wire system is closed-shell. This system is particularly suitable for theoretical study due to its minimal size and consequent computational tractability, high symmetry, and the fact that the Ag_n wire has been investigated theoretically in the literature, which provides a foundation for

interpreting the results of the Ag_nN_2 system.[20,25,26] A previous work by Meng and coworkers performed simulations under similar conditions as the present work in order to study H_2 splitting on an Ag_n atomic wire with n = 4, 6, 9, 12.[27] N_2 is investigated as the adsorbed molecule because it is a closed shell system whose lowest unoccupied molecular orbitals are of π^* symmetry, which are the proper symmetry to interact with the delocalized Π orbitals of the wire system. Hence, we can analyze possible routes of wire-molecule coupling via orbital hybridization with electronic-structure level insights, where it is thought that the molecular orbitals of the adsorbed species hybridize directly into the nanoparticle plasmon mode.[13] Furthermore, the N_2 molecule is extremely stable and difficult to dissociate due to its strong triple bond, so plasmon-enhanced activation of this bond would be a valuable catalytic achievement.

In all, we seek to understand the nature of the coupling between N_2 and the Ag_n nanowire through the CI-description of the quantum plasmon. First, we determine the appropriate level of theory to use in our calculations on the Ag_nN_2 system. We compare the results of various functionals of the generalized gradient approximation (GGA) and long-range corrected (LC) classes for several properties, and benchmark against the HF,[28] MP2,[29] and CCSD[30] wavefunction methods. After determining the appropriate functional, we identify modes of interest via LR-TDDFT, then analyze the electron/nuclear dynamics associated with excitation of these modes via real-time time-dependent density functional theory/Ehrenfest dynamics calculations (RT-TDDFT/ED).

3.3 Methods

To investigate the coupling of N_2 on a Ag_n nanowire, we examine how the transverse and longitudinal plasmon modes of the wire change upon N_2 adsorption. Various geometries of N_2

around the wire were sampled in Gaussian 16[31] with the LanL2DZ basis set[32–34] both through geometry optimization calculations and single-point energy calculations at fixed geometries. In the geometry optimization calculations, N_2 and Ag_n are initially optimized separately. The optimized coordinates are then combined to obtain Ag_nN_2. The Ag_nN_2 structure is optimized with Ag atoms frozen, allowing N_2 to orient about the wire without breaking the linear symmetry of the wire. It is important to note that while the Ag_n atomic wires are useful as a model, their geometries are not global or deep local minima on the potential energy surface, and they do not readily exist in nature except under specialized conditions.[35] However, despite these drawbacks, the wire systems are theoretically illuminating, and conclusions drawn from these systems can be generalized to explain analogous phenomena in larger, more experimentally viable systems.

We compare predicted geometry, binding energy, dipole moment, degree of N_2-Ag_n orbital mixing, and calculated absorption spectrum with the GGA functionals PBE,[36] BP86,[37,38] M06L,[39] VSXC,[40] HCTH,[41] B97D,[42] and BLYP[37,43] against the hybrid and/or LC functionals LC-ωPBE,[44] LC-ωHPBE,[44] M06,[45] CAM-B3LYP,[46] wb97,[47] wb97x,[47] and wb97xd.[48] We note that CAM-B3LYP, unlike the other LC functionals, does not exhibit 100% Hartree-Fock exchange at long-range, but rather 65% HF and 35% B88 exchange at long-range.[46] These functionals were chosen as they are commonly used GGA (or LC) functionals that are implemented in the Gaussian 16 package. The BP86, LC-ωPBE, and CAM-B3LYP functionals have been shown to have success with AgNP systems in particular.[49–52] We compare these results against the HF, MP2, and CCSD wavefunction methods.

For the linear response time-dependent density functional theory (LR-TDDFT) calculations, we use the standard implementation in the Gaussian 16 package. We utilize the real-time time-dependent density functional theory (RT-TDDFT) code in a Gaussian 16

development version.[53] RT-TDDFT propagates the system's density matrix in time, giving access to the full (potentially nonlinear) electronic response to arbitrary time-dependent electric field perturbations. RT-TDDFT provides real-time dipole moments, orbital populations, and off-diagonal density matrix elements at each time step. Other dynamical information, like the absorption spectrum, can be derived from these quantities. LR-TDDFT provides complementary information on electron dynamics by finding the poles of the system's linear response function to a small perturbation, which yields the excitation energies and corresponding transition densities in term of linear combinations of transitions between occupied and virtual orbitals.[54]

For convenience we rely primarily on LR-TDDFT to compute electron-only excited-state quantities like the absorption spectrum. The LR method also directly provides information about which single excitations contribute to an absorption spectrum peak. This information is accessible through RT-TDDFT, but it is less readily available.[55] Thus, we perform LR-TDDFT calculations to examine how the N_2 alters the absorption spectrum and plasmon modes of the linear silver chains. In the absorption spectra presented within, the LR-TDDFT-calculated stick spectrum is convolved with a Lorentzian broadening function with a full-width at half-maximum of 0.2 eV.

The RT-TDDFT code can be coupled with the mean-field Ehrenfest dynamics (ED) method to include nuclear motion in the calculation. In the RT-TDDFT and RT-TDDFT/ED calculations, the Ag_8N_2 system was separately perturbed with a continuous wave electric field corresponding to the transverse and longitudinal plasmon excitation energies of the structure. The field is turned on at 0 fs and off at 20 fs. Over the course of the 20 fs, the field is ramped up (first 1 fs) and then down (final 1 fs) in strength with a trapezoidal envelope. Field strengths between 0.001 to 0.05 a.u. were used. We utilize the RT-TDDFT/ED code to explore activation

and dissociation processes of N_2 due to the presence of the wire. We measure the N-N bond distance by taking the average length across the calculation after the electric field has been turned off, i.e. excluding the first 20 fs. We perform RT-TDDFT calculations as supplements to the RT-TDDFT/ED results as RT-TDDFT allows access to time-dependent orbital population information. In our RT-TDDFT/ED calculations we use an electronic step size of 0.00025 fs and a nuclear step size of 0.1 fs for a minimum of 100 fs with default initial velocities on all atoms. We run the RT-TDDFT/ED calculations both with the Ag atoms frozen and unfrozen. In our RT-TDDFT calculations, we use an electronic time step of 0.0006 fs for a minimum of 100 fs.

3.4 Results and Discussion

We use DFT methods to develop an understanding of the nature of the coupling between N_2 and Ag_n. Coupling may produce several charge transfer states in the region of interest, which is the energy range between and including the longitudinal and transverse quantum plasmon peaks. Depending on the type of charge-transfer state, different functional classes handle charge transfer states with varying accuracy. Given the importance of avoiding spurious excitations in this region, we first discuss appropriate functional choices.

Several properties of the Ag_n and Ag_nN_2 systems depend on the choice of DFT functional type. In particular, we find that the predicted stable geometry, states involved in the transverse and longitudinal plasmon modes, and degree of N_2-Ag_n orbital mixing depend on the choice of DFT functional class to a significant degree. Due to the demanding nature of ab-initio electronic structure calculations on noble metal nanocluster systems, GGA DFT functionals are often employed and have been shown to perform well for Ag cluster systems.[52,56-59] However, GGA functionals are local by definition, as they depend only on the electron density and the gradient

of the electron density at any given point. Hence, GGA functionals can miscalculate properties that depend on non-local effects. An example is in the calculation of charge-transfer states, which GGA functionals are known to handle poorly under certain common circumstances.[60] Long-range corrected (LC) functionals switch to Hartree-Fock (HF) exchange after a certain distance, and so incorporate non-local effects while still maintaining other benefits of DFT over HF (e.g. improved accuracy).[52] However, LC functionals come at a higher computational price. The significantly reduced computational cost makes GGA functionals an appealing alternative to their expensive, long-range corrected cousins. Thus, we evaluate whether the GGA functional class provides sufficient accuracy for the Ag_nN_2 system.

There are many degrees of freedom available for N_2 to orient around the wire, and the most energetically favorable positions were found to vary by DFT functional type. The preferred positions are the "bent" and "linear" orientations shown in Figure 3.1, in which N_2 binds to the end of the silver nanowire. Other starting geometries were sampled but were not found to be stable. After geometry optimization, GGA functionals favor a bent geometry with an Ag-Ag-N angle ranging from 156.73 to 171.60 degrees, while wavefunction methods and LC functionals prefer the linear orientation. "Side-on"-type arrangements, with the N_2 perpendicular to the wire, are energetically unfavorable relative to the end-on arrangements. Single point energy calculations of each functional at the two optimized geometries confirm that the LC functionals consistently yield a lower energy at the linear orientation, while the GGA methods find a lower energy for the bent orientation. The wavefunction methods (HF, MP2, CCSD) preferred the

linear orientation. These results suggest that the linear orientation is favored over the bent orientation.

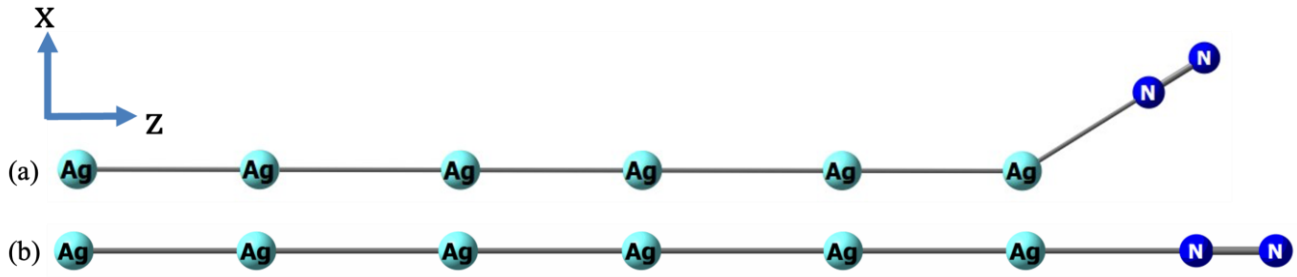

Figure 3.1 Representative "bent" (a) and "linear" (b) geometries of the Ag_6N_2 systems.

The Ag_6N_2 binding energies for the linear geometry are shown in Table 3.1. The binding energies are calculated by separately optimizing the nanowire, N_2 molecule and Ag_6N_2 cluster and applying the equation: $E(Ag_6) + E(N_2) - E(Ag_6N_2)$. CCSD yields a binding energy of 6.60 kcal/mol. The DFT methods with binding energies closest to the CCSD-calculated binding energies are wb97xd, M06, and M06L, with absolute differences in binding energy $|E_{CCSD} - E_{DFT}|$ of 0.11, 0.12, and 0.17 kcal/mol respectively. It is important to note that while CCSD is often a reasonable benchmark, these calculations employ the LanL2DZ basis set, which is a relatively small double-zeta basis set. At some point, an insufficiently sized basis set can limit the accuracy of an otherwise high-level method like CCSD. However, using a larger basis set renders the CCSD calculations intractable for these systems. Thus, while the CCSD values reported here do provide benchmark guidance, they should not be considered "gold standard" quality benchmarks.

We report the total dipole moment computed by each method in Table 3.1. The CCSD calculated dipole moment is 3.975 D. A recent study by Hait and Head-Gordon evaluated the quality of the dipole moment (μ) of a system as a stand-in for electron density; that is, an accurate dipole moment suggests an accurate overall electron density distribution.[61] The DFT

methods with dipole moments closest to CCSD are wb97, wb97x, and CAM-B3LYP, with absolute differences $|\mu_{CCSD} - \mu_{DFT}|$ of 0.003, 0.039 and 0.068 D respectively. The large magnitude of the dipole moment can be attributed to the geometry of the system. While N_2 and Ag_n are each separately non-polar systems, combining the two yields a separation of charge, which results in a dipole moment. The magnitude of the dipole moment is amplified by the length of the system, as the separation of the charge occurs over a distance of approximately 17 Å for the Ag_6N_2 system. Hence, the dipole moment is larger than one might initially expect upon combination of the two non-polar systems. While the dipole moment values are in particularly good agreement with CCSD for some functionals, there is no obvious or systematic difference in the dipole calculated via GGA-type functionals versus LC-type functionals for linear arrangements of the Ag_6N_2 system (Table 3.1). Thus, the dipole moment calculations do not yield clear results that a GGA-type or LC-type functional is preferred.

Table 3.1 Calculated binding energies and dipole moments of the linear Ag_6N_2 wire system. The difference in binding energy from CCSD was calculated as $E_{binding, CCSD} - E_{binding, method}$ and the difference in total dipole from CCSD was calculated as $\mu_{CCSD} - \mu_{method}$.

	Binding energy (kcal/mol)	Difference in binding energy from CCSD (kcal/mol)	Total dipole (D)	Difference in total dipole from CCSD (D)
HF	-34.38	40.98	3.129	0.846
MP2	6.62	0.02	3.911	0.064
CCSD	6.60	-	3.975	-
LC-ωPBE	7.26	0.66	3.601	0.374
LC-ωHPBE	7.26	0.65	3.597	0.378
CAM-B3LYP	7.76	1.15	4.043	-0.068
ωb97	9.33	2.72	3.973	0.003
ωb97x	8.52	1.91	3.937	0.039
ωb97xd	6.71	0.11	3.807	0.168
M06	6.49	0.12	3.890	0.086
M06L	6.44	0.17	3.718	0.257
B97D[a]	-	-	-	-
HCTH[a]	-	-	-	-
BLYP	5.97	0.64	3.789	0.186
PBE	7.18	0.57	3.762	0.213
B3LYP	5.68	0.93	3.799	0.176
BP86	6.09	0.52	3.821	0.154

(a) B97D and HCTH failed to converge in the linear orientation.

Another quantity of interest, both in evaluating the viability of functionals and as a means to understand charge transfer and electron transfer between the wire and the adsorbate, is the degree to which atomic orbitals originating from the two nitrogen atoms hybridize with atomic orbitals originating from the Ag atoms to produce the molecular orbitals of the system. To analyze the degree of mixing, we employ c-squared population analysis, where the contribution of basis function *a* in spin orbital *i* is defined as $\Theta_{i,a} = \frac{c_{a,i}^2}{\sum_b c_{b,i}^2}$ where $c_{c,j}$ corresponds to the coefficient on basis function *c* in the linear expansion corresponding to spin orbital *j*.[62] This analysis offers insight into the degree to which the N_2 orbitals hybridize with the Ag orbitals. As orbitals are not unique, i.e. a new set of orbitals with the same total energy can be obtained through some unitary transformation on the orbital coefficient matrix, we must take care in ascribing physical meaning to the orbitals. However, since we employ an atom-centered basis set, the Kohn-Sham (KS, for DFT) or Fock canonical (for HF or other single-reference wavefunction methods) orbitals are analogous to the molecular orbitals of the linear combination of atomic orbitals (LCAO) approach, especially as these canonical orbitals are symmetry-adapted. Hence, canonical orbitals in particular are useful for analyzing the symmetries of the total system, which is helpful in the CI-like plasmon mode analysis discussed in the introduction. We return to this analysis when we compare the LR-TDDFT results of the Ag_n wire to the Ag_nN_2 system. In this section, we examine similarities and differences between the c-squared population analyses for different functionals.

The percentage of all atomic orbitals originating from both nitrogen atoms in a given molecular orbital is reported in Table 3.2 for the representative LC functional LC-ωPBE and the representative GGA functional BP86. In general, the GGA orbitals do not hybridize as extensively as the LC orbitals. This is qualitatively evident from the MO pictures in Figure 3.2

and is validated by the c-squared population analysis in Table 3.2. While comparisons between GGA and LC orbitals can be readily made, comparison between DFT and wavefunction methods is not straightforward. HF-based virtual orbitals tend to be diffuse and higher energy in comparison to KS orbitals.[63] For Ag_nN_2 this diffusivity results in N_2 basis function contributions to a given orbital which are much less than the DFT counterparts.

Table 3.2 Percent of N_2 atomic orbitals in the molecular orbital. π_{N2}^* is denoted as such because it resembles the N_2 π^* orbital. The other orbitals are labeled following the convention of the standalone Ag_n wire systems. N1 refers to the nitrogen atom bonded to the wire, while N2 refers to the terminal nitrogen atom.

	LC-ωPBE (%)		BP86 (%)	
	N1	N2	N1	N2
Π_3	3.51	1.64	2.15	0.55
Π_2	10.27	7.23	3.08	1.06
Π_1	9.62	8.41	1.78	0.73
π_{N_2}*	38.14	45.28	46.72	50.49
Σ_3	0.59	0.12	1.61	0.20
Σ_2	0.59	0.10	0.89	0.12
Σ_1	0.19	0.03	0.32	0.09

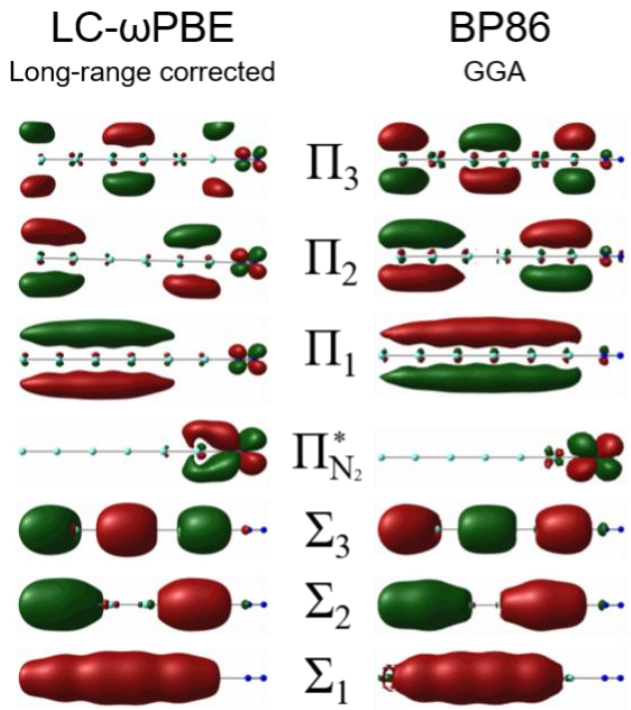

Figure 3.2 Orbitals involved in the transverse plasmon mode for LC-ωPBE (long-range corrected) and BP86 (GGA) for linear Ag_6N_2, with an isovalue of 0.02. π_{N2}^* is denoted as such because it resembles the N_2 π^* orbital. The other orbitals are labeled following the convention of the standalone Ag_n wire systems.

Finally, we turn our attention towards the key comparison, for our purposes, in choosing the proper functional type: the absorption spectrum. The absorption spectrum is important for two reasons. First, our analysis relies on identifying the quantum plasmon excitations and other states that may result in a charge transfer from the Ag_n to N_2. Second, in TDDFT it is well known that GGA functionals can perform poorly in computing charge transfer states.[50–52] The energies of charge transfer states under GGA can be underestimated by multiple eV. Further, GGA functionals are prone to producing spurious, low-oscillator strength charge transfer states in a LR-TDDFT calculation. These spurious states borrow oscillator intensity from non-spurious states, decreasing the intensity of the non-spurious states.[52] These effects are thought to be due to the incorrect asymptotic form of the GGA exchange-correlation functional, which decays

exponentially rather than as $1/r$.[47] On the other hand, LC functionals use DFT exchange at short range, but switch to 100% Hartree-Fock exchange asymptotically. Thus, LC functionals exhibit the correct asymptotic behavior and often more accurately predict the energies of charge-transfer states.[52] Further, LC functionals may reduce the number of spurious, low-energy charge-transfer states. However, there are situations in which GGA functionals can accurately describe charge-transfer states, like when the spatial overlap of the donor and acceptor states is significant.[60] Thus, the results of the LR-TDDFT simulated absorption spectrum plays a vital role in determining whether or not a GGA functional is appropriate for the Ag_nN_2 system.

The results of an LR-TDDFT calculation on the representative GGA functional BP86 and representative LC functional LC-ωPBE for Ag_6 and Ag_6N_2 in the linear orientation using the LC-ωPBE-obtained linear geometry are shown in Figure 3.3. The Ag_6 absorption spectra are in reasonable agreement. In particular, the longitudinal and transverse plasmon modes are in line with expectations based on the CI-like plasmon analysis and their energies agree.[20,26] The GGA functional overestimates oscillator strength of the d-band transitions in the 3-4 eV range relative to LC-ωPBE, but the spectra are in otherwise good agreement. On the other hand, the Ag_6N_2 absorption spectra differ greatly. In the GGA BP86 spectrum, the longitudinal mode has lost significant oscillator strength to the peaks surrounding it. Furthermore, the degeneracy of the x- and y-polarized transitions comprising the transverse peak has been broken in the BP86 calculation, and the oscillator strengths of the two transitions differ. Given the symmetry of the system, such a deviation is likely an artifact. Finally, the BP86 stick spectrum of Ag_6N_2 shows a multitude of low intensity states that are not present in the LC-ωPBE stick spectrum. Taking into consideration the known issue of GGA functionals producing spurious states and/or severely underestimating the energies of charge-transfer states in conjunction with the likelihood of the

Ag_6N_2 system producing charge transfer states, it seems that the BP86 functional does not offer as robust of a simulated absorption spectrum as the LC-ωPBE functional. These spectral results are not specific just to BP86 and LC-ωPBE; they are general across the GGA and LC functionals examined in this work.

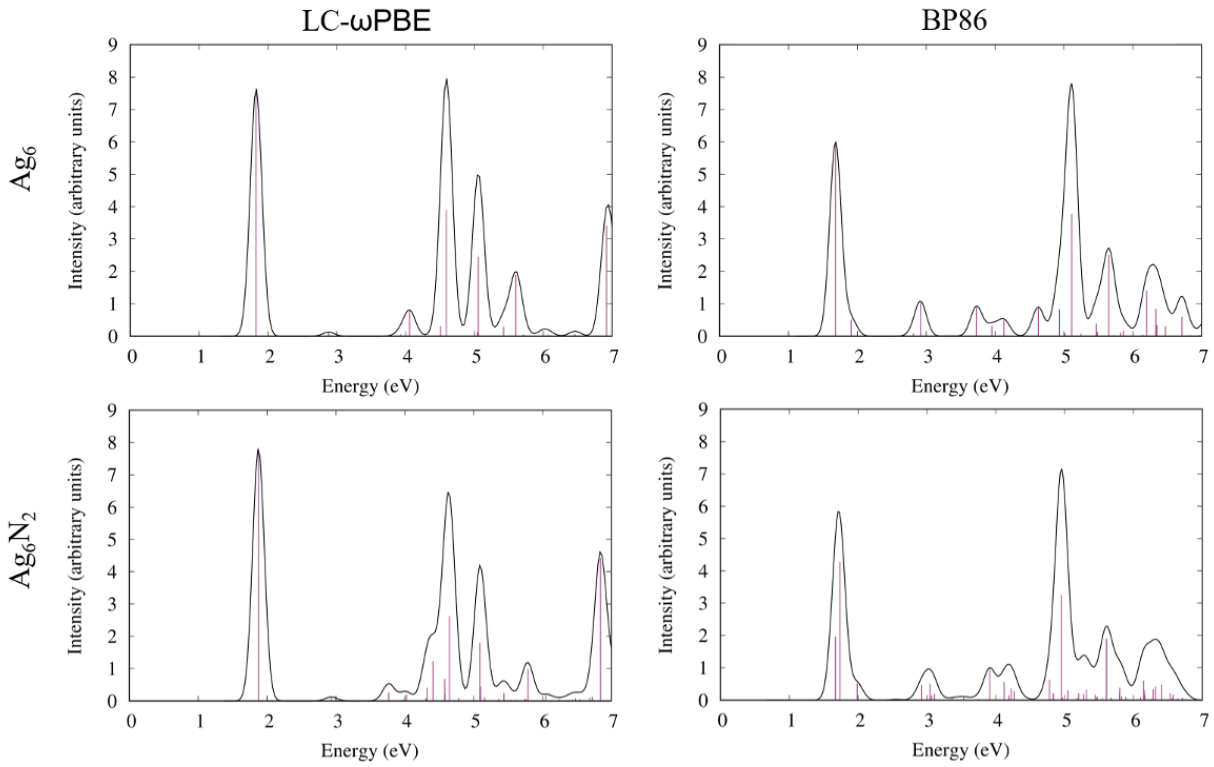

Figure 3.3 Linear response excitation spectra for Ag_6 (top row) and Ag_6N_2 (bottom row) for the representative long-range corrected functional LC-ωPBE (left column) and the representative GGA functional BP86 (right column).

For some of the properties considered, there is not a significant difference between the GGA and LC functional results, or the differences do not make clear which class yields a more accurate result. This is the case for dipole moments, binding energies, and degrees of orbital mixing. However, because the GGA functional class consistently predicts a ground-state geometry different than the geometry predicted by the LC and wavefunction methods, this

suggests that the GGA functional type may not be appropriate for the Ag_nN_2 system. Furthermore, peaks suggestive of the known GGA charge-transfer artifacts appear in the GGA LR-TDDFT absorption spectrum, which indicates that we likely cannot rely on the GGA class to accurately capture the absorption spectrum of this system. Thus, we employ an LC functional for this work.

In order to determine the proper LC functional, we follow the literature recommendation in conjunction with our own benchmarking results. Benchmarking GGA/LC DFT functional studies on silver clusters by Franck Rabilloud find that the LC-ωPBE functional performs well in computing charge transfer states and the plasmon-like bands.[51,52] Jensen and coworkers found that, of the GGA and LC-functionals they examined, the LC-ωPBE functional reproduces experimental absorption spectra and their theoretical benchmark, equation-of-motion coupled-cluster singles and doubles (EOM-CCSD), for silver clusters.[64] Jensen and coworkers also showed that LC-ωPBE is an appropriate functional to study the nonresonant chemical mechanism of surface-enhanced Raman spectroscopy on silver clusters. This study, similar to the present, involved examining the effects of adsorbed molecules on the electronic structure of silver clusters.[65] In the following analysis, the LC-ωPBE/LanL2DZ level of theory is employed unless specified otherwise.

3.5 Electronic Structure and Optical Properties

Real-time time-dependent density functional theory (RT-TDDFT) and linear response time-dependent density functional theory (LR-TDDFT) investigations on model Ag_n nanowire systems have described the transverse and longitudinal plasmon modes in the absorption spectrum in terms of collective excitations of single-particle states.[20,23,25,26] Due to the cylindrical symmetry of the systems, the delocalized molecular orbitals can be labeled as Σ, Π, and so on. The transverse plasmon mode is characterized by a collective excitation of occupied Σ-type orbitals into unoccupied Π-type orbitals. That is, the excitation is comprised of $\Sigma_n \rightarrow \Pi_n$ transitions, where the number of states involved increases with wire length. Meanwhile, the longitudinal mode is classified as being comprised of Σ-to-Σ transitions and occurs at a lower energy than the transverse mode. These excitations and the orbitals involved are shown in Figure 3.4. We use this interpretation as the basis for understanding the Ag_nN_2 systems.

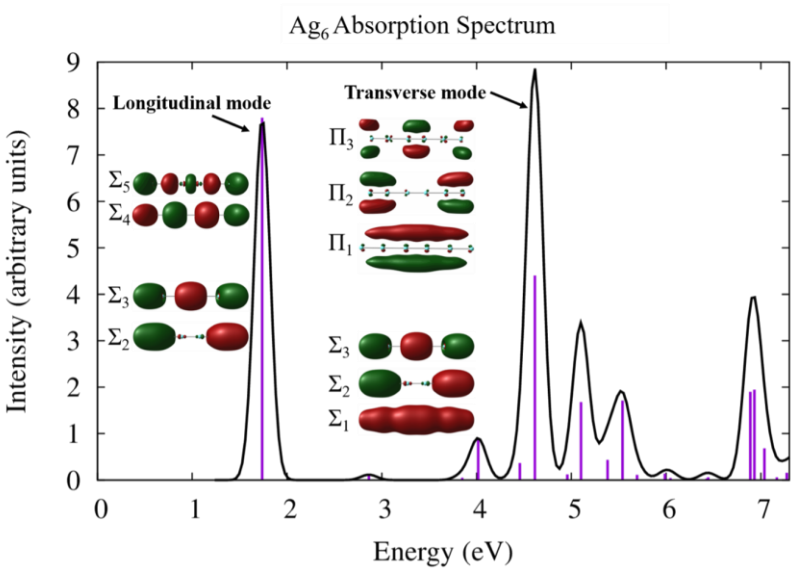

Figure 3.4 The longitudinal and transverse quantum plasmon modes of the linear Ag_6 wire at the LC-ωPBE/LanL2DZ level of theory. The longitudinal mode is comprised of Σ_2 to Σ_5 and Σ_3 to Σ_4 single particle transitions. The transverse mode is comprised of Σ_n to Π_n transitions (n = 1, 2, 3). Orbitals are shown with an isovalue of 0.02.

In LR-TDDFT calculations of each of the three linear Ag_nN_2 systems, the antibonding π^* orbital of N_2 mixes with the Π molecular orbitals of the wire system to yield hybridized orbitals with nonnegligible N_2 π^* antibonding character. (We note that while the particle-in-a-cylinder-type symmetry that enables the symmetry-based orbital designators Σ_n, Π_n, etc. of the wire system is broken in Ag_nN_2 due to the addition of N_2, we keep these designators for the Ag_nN_2 systems in order to highlight similarities between the Ag_nN_2 orbitals and the analogous Ag_n orbitals.) Additionally, one unoccupied orbital in each of the Ag_nN_2 systems arises primarily from the N_2 π^* antibonding orbital. The Σ-type Ag_n orbitals do not mix with the N_2 σ orbitals to the same extent, though some hybridization is present (about three times less than with orbitals of π symmetry). In the LR-TDDFT calculated absorption spectrum, the longitudinal and transverse plasmon modes largely maintain the same energies as compared to Ag_n (Figure 3.4). The transverse plasmon mode in both Ag_n and Ag_nN_2 is a collective excitation comprised of Σ-to-Π transitions. However, in the Ag_nN_2 case, additional single particle transitions contribute to the collective transverse peak in the absorption spectrum. Chiefly, in the LR-TDDFT calculation, the orbital corresponding to the N_2 π^* contributes to the transverse peak. This result implies that the N_2 π^* antibonding orbital accepts electron density from the Ag_n Σ orbitals upon excitation at the transverse plasmon resonance energy. In addition to the coupling of the N_2 π^* antibonding orbital into the Ag_n plasmon excitation, the Ag_n Π orbitals gain N_2 π^* antibonding characteristics, which suggests that electron density around the N_2 antibonding orbital increases through direct excitation into the Π system via, for example, the transverse plasmon mode, or through other transitions that involve the Ag_n Π orbitals.

New peaks arise in the absorption spectrum of Ag_nN_2 that are not present in the absorption spectra of Ag_n and N_2 separately, signifying that coupled states are created upon N_2 adsorption. For example, in each of the Ag_nN_2 systems, a peak arises from the collective excitation of the Ag_n Σ bonds into the N_2 π^* antibonding orbital around 3.76-3.85 eV. In Ag_4N_2, only the Σ_2 (HOMO) excites into the N_2 π^* orbital. In Ag_6N_2, the Σ_3 (HOMO), Σ_2 (HOMO-1) and Σ_1 (HOMO-2) orbitals collectively excite into the N_2 π^*. In Ag_8N_2, the Σ_4 (HOMO), Σ_3 (HOMO-1), and Σ_2 (HOMO-2) orbitals contribute. The existence of this peak suggests that direct excitation from the silver chain into the N_2 π^* antibonding-type orbital is possible.

The length of the Ag_n chain does not significantly alter the form of the Ag_nN_2 absorption spectrum, though the number of orbitals participating in a given excitation generally increases. As the chain length grows, the number of occupied Ag_n Σ orbitals and unoccupied Ag_n Π orbitals increase, yielding more states with which the N_2 π^* antibonding orbital can interact. The number of states involved in the collective plasmon modes increases, though the general form of $\Sigma \rightarrow \Sigma$ or $\Sigma \rightarrow \Pi$ persists for longitudinal or transverse modes, respectively. The chain length in both Ag_n and Ag_nN_2 affects the energy and oscillator strength of the longitudinal plasmon mode. The transverse "width" remains fixed (with a width of one Ag atom) as the number of Ag atoms in the chain increases, results in a transverse mode essentially invariant to the chain length.

We find that charge transfer states arise due to coupling between Ag_n Σ-orbitals and the antibonding orbitals of N_2. These states persist upon variation of the Ag_n chain length for Ag_nN_2. However, the extent of the coupling depends on the type of orbital. The empty N_2 π^* orbitals couple effectively with the Ag_n Π-orbitals. While both the presence of charge-transfer states involving excitation into an N_2 antibonding orbital and the hybridization of N_2 antibonding orbitals into the Ag_n transverse plasmon mode offer potential routes of N_2 dissociation, the

existence of these states is not sufficient to guarantee dissociation, as shown in the next section in which we investigate the electron-nuclear dynamics of the Ag_nN_2 system.

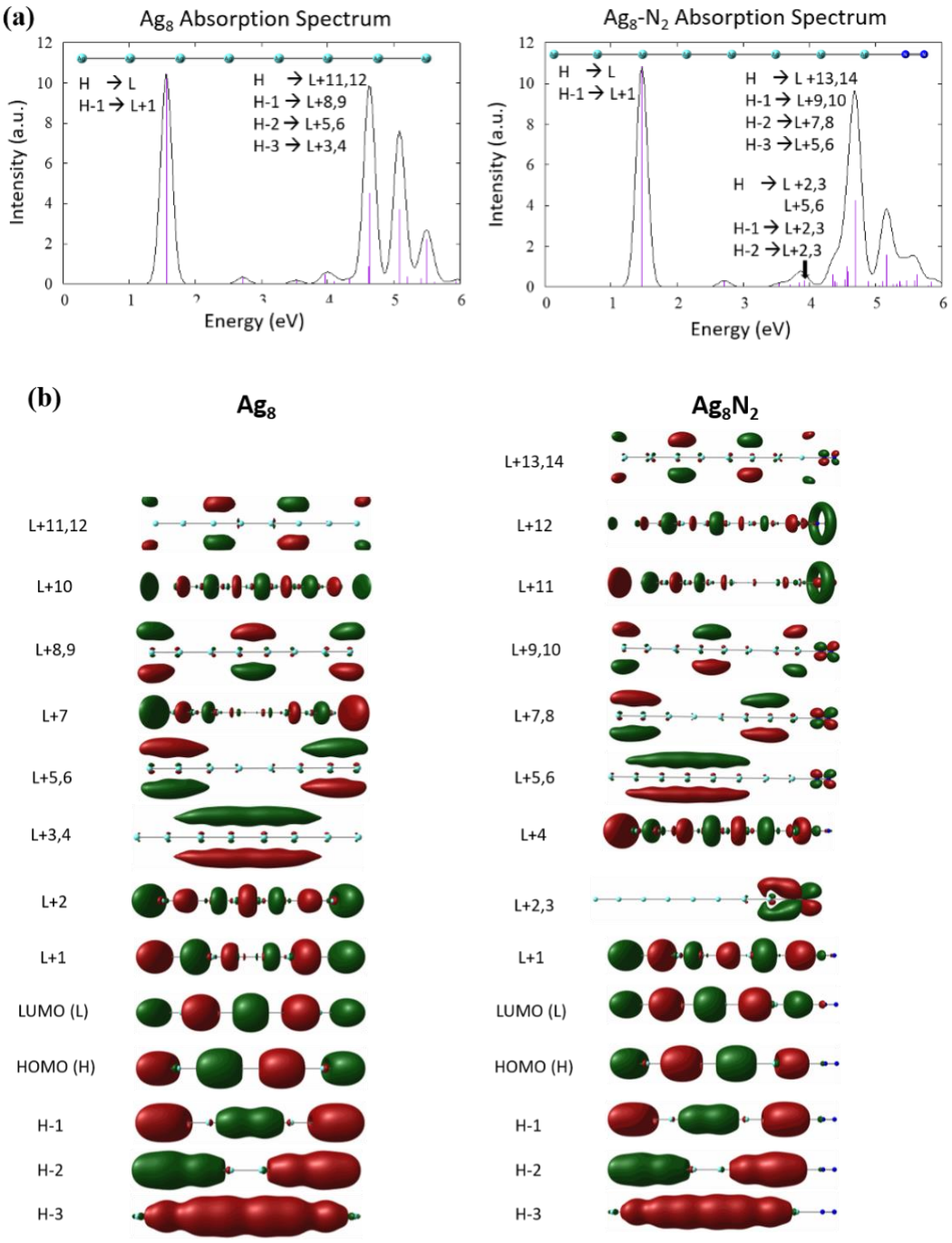

Figure 3.5 (a) Comparison of Ag_8 and Ag_8N_2 linear response excitation spectra. (b) Comparison of Ag_8 and Ag_8N_2 orbitals involved in the linear response excitation spectra. Orbitals are shown with an isovalue of 0.02.

3.6 Electron/Nuclear Dynamics

We investigate the role of the Ag_8 plasmon mode in activating a N_2 molecule oriented linearly with the wire using coupled real-time time-dependent density functional theory/Ehrenfest dynamics (RT-TDDFT/ED) calculations. We perform these calculations with the Ag_8 chain both frozen and unfrozen. In our calculations, we monitor the length of the N-N bond to determine the degree of activation. In our LC-ωPBE/LanL2DZ calculations, the optimized N_2 bond length in the linear orientation of Ag_8N_2 is 1.119 Å and the calculated bond length in isolated N_2 is 1.123 Å. A continuous-wave electric field is applied at the transverse and longitudinal plasmon mode energies with electric field strengths of 0.001, 0.01, 0.02, 0.03, 0.04, and 0.05 a.u. These field strengths are strong relative to the field strengths commonly used in RT-TDDFT to obtain, for example, an absorption spectrum. As the oscillator strength of the quantum plasmon mode increases with chain length, it will be the subject of a future investigation to determine more precisely the role of the electric field in the adsorbate activation, and how the strength of the field necessary to achieve activation or dissociation of an adsorbate varies with the length of the wire. Previous works by Meng and coworkers have utilized electric fields of similar strengths (0.05 a.u. and 0.045 a.u.) to examine other plasmon-driven catalytic processes on Ag_n (n = 4, 6, 9, 12) wires and an Au_{20} pyramidal structure.[27,66]

In order to mitigate loss of the plasmon resonance due to Ag atom movement, we first carry out calculations in which the Ag atoms are frozen. With a continuous wave electric field resonant with the transverse plasmon mode (4.70 eV), we observe activation of the N-N bond. The degree of activation is dependent on the electric field strength. The 0.05 a.u. field yields an average N-N bond distance of 1.17 Å. The 0.04, 0.03, 0.02, 0.01, and 0.001 a.u. fields yield average N-N bond lengths of 1.16, 1.16, 1.14, 1.14, and 1.13 Å respectively. We expect the

transverse mode to activate the N-N bond given our hypothesis that population of orbitals with N_2 antibonding character leads to activation. In this case, N_2 π^* hybridization into the Ag_8 Π orbitals offers a route for plasmon-mediated excitation into a state with significant N_2 π^* character.

Electron-only dynamics using RT-TDDFT calculations with a continuous wave electric field corresponding to the transverse plasmon mode energy polarized along the x-axis of the wire reveal expected changes in populations of orbitals based on LR-TDDFT results: the Π_1, Π_2, and N_2 π^*-type orbitals all show significant increases in population within the first 5 fs for the 0.03 a.u. and 0.01 a.u. fields. The 0.05 a.u. field results in less population of these orbitals but more population of higher-energy Π orbitals. We note that comparison between the RT-TDDFT orbital population analysis and the Ehrenfest dynamics calculations can only be reasonably carried out for the first few fs of the calculations, because in the ED calculations the N_2 begins to migrate away from the wire soon after the simulation begins.

We also perform RT-TDDFT/ED calculations in which the frequency of the continuous wave electric field corresponds to the longitudinal plasmon mode energy (1.47 eV) and the electric field is polarized along the z-axis of the wire. In this case, we observe either full dissociation of the N_2 or non-dissociative N_2 activation depending on the strength of the applied electric field. With the 0.05 a.u. field, the N_2 bond length grows linearly starting at 40 fs, exceeding 7 Å by 90 fs (Figure 3.6). With the 0.04 a.u. field, the N_2 bond grows to 1.4 Å by 30 fs, plateauing until 90 fs before reaching 1.7 Å by 100 fs. In the 0.03, 0.02, 0.01, and 0.001 a.u.

field strength simulations, the N_2 bond distance averages 1.31, 1.21, 1.16, and 1.13 Å respectively.

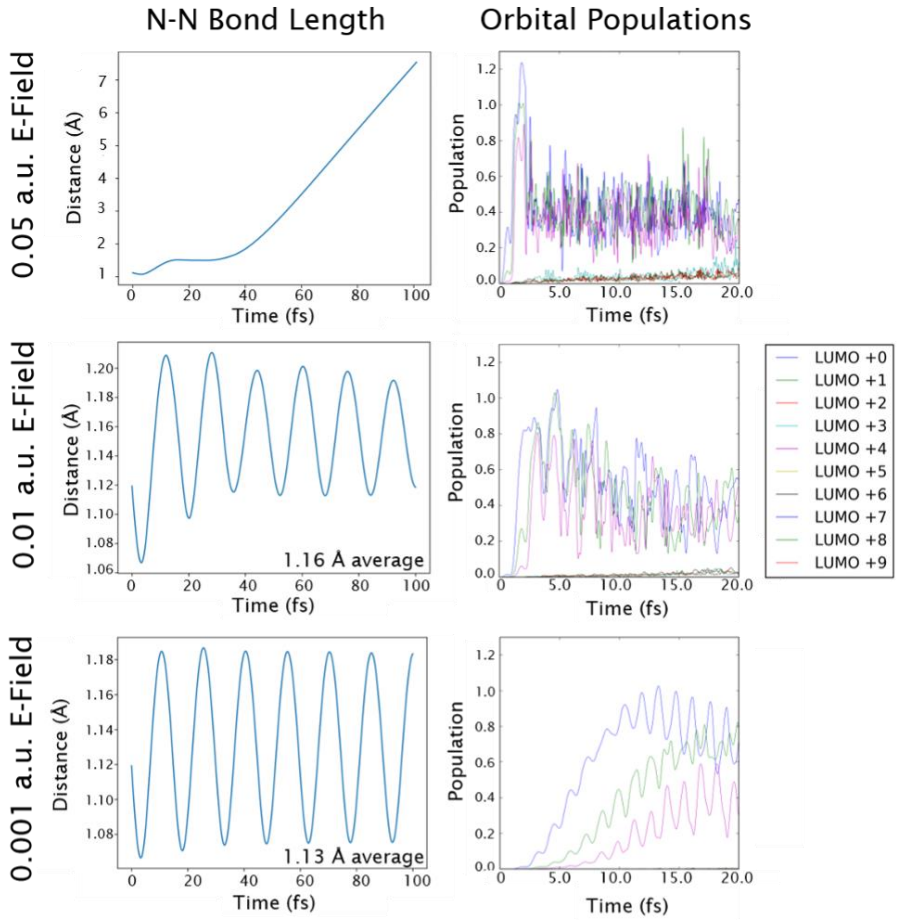

Figure 3.6 N-N bond length and orbital populations of systems excited at the longitudinal plasmon resonance with 0.001, 0.01, and 0.05 a.u. electric field strengths. Designations of LUMO + n correspond to the Ag_8N_2 orbitals in Figure 3.5b.

RT-TDDFT calculations show that within the first two fs, the Σ_5 (LUMO), Σ_6 (LUMO+1), and Σ_7 (LUMO+4) orbitals become populated with 1.2, 1.0, and 0.9 electrons respectively for the 0.05 a.u. electric field in resonance with the longitudinal plasmon mode energy. RT-TDDFT calculations with the 0.03 and 0.01 a.u. fields at the longitudinal plasmon mode energy show similar degrees of populations of these orbitals, though their population grows less quickly. These orbitals each contain a node between the two nitrogen atoms (Figure

3.7). Thus, N_2 bond activation may be due to population of orbitals containing N_2 σ*-like character. The percent contribution of N_2 atomic orbitals to these MOs are lower than the N_2 contributions to the Π-type orbitals at 1.05%, 2.52%, and 2.09% for LUMO (Σ_5), LUMO+1 (Σ_6), and LUMO+4 (Σ_7) respectively. Population of these orbitals is field-dependent, where stronger fields populate the LUMO, LUMO+1, and LUMO+4 more quickly than the weaker fields. While this result is surprising, Meng and coworkers observed similar behavior in an atomic silver chain-H_2 system in a strong electric field. Specifically, they demonstrated the dissociation of H_2 on Ag_n chains (n = 4, 6, 8, 10, 12) through Ehrenfest dynamics simulations.[27] In particular, they showed an increase in electron density around the region corresponding to the H_2 antibonding orbital and a subsequent H_2 bond activation/dissociation after application of an electric Gaussian wavepacket with energy centered on the longitudinal plasmon mode of the wire at 0.05 a.u. electric field strength. In our case, a similar phenomenon may be occurring with the N_2 σ^* antibonding orbital.

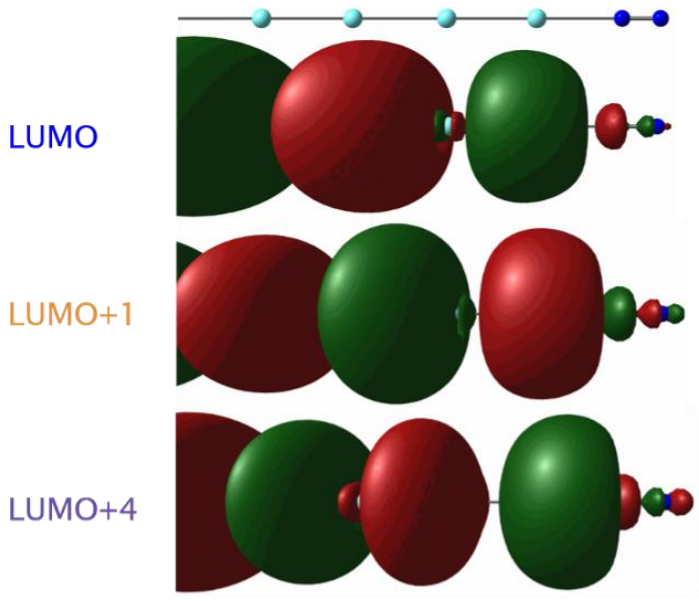

Figure 3.7 A "zoomed-in" view of the LUMO (Σ_5), LUMO+1 (Σ_6), and LUMO+4 (Σ_7) orbitals of Ag_8N_2 with an isovalue of 0.01. This view shows the node between the two nitrogen atoms in the three orbitals. The wire with no overlay is shown for reference.

In all cases, for an equivalent field strength, the RT-TDDFT/ED calculation corresponding to excitation of the transverse plasmon mode yields a shorter average N_2 bond length than excitation of the longitudinal mode. It is a surprising result that, for instance, in the 0.03 a.u. field case, the N_2 π^*-type orbital is populated with over 0.9 electrons within the first 2.5 fs yet the average N_2 bond length in the corresponding RT-TDDFT/ED calculation is 1.16 Å, which represents a relatively modest degree of activation compared to the computed 1.12 Å nitrogen-nitrogen bond length of the ground-state Ag_8N_2 structure. In comparison, the analogous longitudinal excitation with a field strength of 0.03 a.u. yields an average N_2 bond length of 1.31 Å. Furthermore, we find that the degree of N_2 activation upon excitation of the charge transfer state at 3.85 eV, in which Σ-type orbitals from the wire system excite into an N_2 π^*-type orbital, is much less than the resulting activation from the longitudinal plasmon mode, but competitive with the transverse plasmon mode. Exciting with an electric field strength of 0.03 a.u. results in an activation to an average bond length of 1.15 Å. This may arise because both the transverse plasmon mode and the charge transfer mode have much weaker oscillator strengths than the longitudinal plasmon mode as shown in the LR-TDDFT spectrum (Figure 3.5a).

In the RT-TDDFT/ED calculations in which the Ag atoms are free to move, the wire begins to bend and distort within 20-30 fs (Figure 3.8). This distortion disrupts the collective plasmon excitations due to symmetry-breaking. Investigating plasmon decay of the Ag_n wires through low-lying vibrational modes will be the focus of a future investigation. Despite distortion of the wire structure, these systems achieve similar degrees of N_2 activation as calculations with frozen Ag atoms. That these calculations achieve similar long-time N_2 average bond distances despite losing the collective plasmon mode as the calculation proceeds suggests that activation of N_2 by

the Ag_8 plasmon mode occurs quickly. In both the frozen and unfrozen calculations, the N_2 migrates away from the wire as the calculation proceeds. In calculations with no Ag_8 present, no N_2 activation occurs, i.e. calculations on isolated N_2 with continuous wave electric fields corresponding to the longitudinal and transverse plasmon resonances of the composite system do not result in any elongation of the average N_2 bond length. Thus, the presence of the atomic Ag_n wire is required for activation of the N_2 adsorbate.

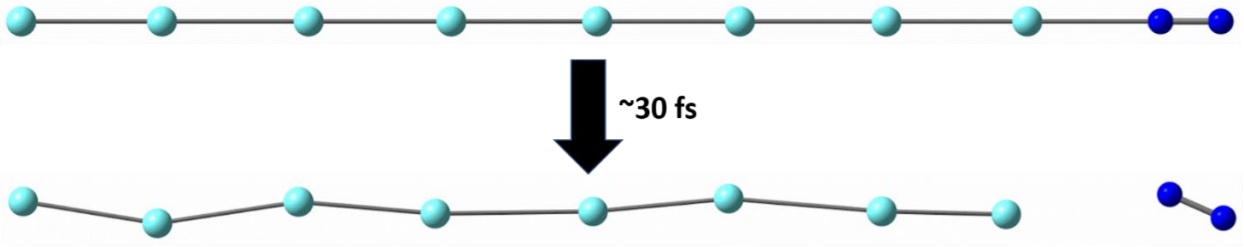

Figure 3.8 A typical RT-TDDFT/ED calculation on the Ag_8N_2 wire at t=0 fs and t=30 fs with unfrozen silver atoms.

3.7 Conclusion

We have performed a DFT investigation on plasmon-enhanced bond activation in Ag_nN_2 atomic wire systems. Long-range corrected DFT functionals are appropriate for studying cluster-N_2 interactions; GGA functionals likely do not provide sufficient accuracy in capturing the geometry and the charge-transfer states between the two subsystems. Charge transfer states arising between the Ag_n and N_2 subsystems were analyzed. We found that N_2 atomic orbitals hybridize into the Ag_n orbitals responsible for the longitudinal and transverse plasmon modes. These hybridized modes offer routes in which N_2 antibonding-like orbitals can be excited, leading to activation of the N_2 bond.

To test the extent to which the N_2 bond activates upon excitation at the longitudinal and transverse plasmon mode energies, we carried out real-time time-dependent DFT/Ehrenfest dynamics studies on the Ag_8N_2 system. These calculations demonstrated N_2 bond activation upon application of a continuous wave electric field for the first 20 fs of the calculation. The degree of activation was both field strength- and frequency-dependent. The longitudinal mode excitation resulted in a greater degree of activation than the transverse mode excitation or the charge transfer mode excitation. This result is surprising given that the N_2 π^* hybridization into the Ag_8 Π orbitals is more extensive than the N_2 σ-type hybridization. The degree of N_2 activation is largely independent of whether or not the Ag atoms are frozen in the calculation, suggesting that activation occurs quickly. Examining how the photocatalytic behavior evolves with nanoparticle size will be the subject of future investigations. In all, we have found that it is possible to activate N_2 terminally attached to a silver atomic chain upon application of a strong electric field at the plasmon mode energies of the system.

3.8 Acknowledgments

This material is based on work supported by the Department of Energy under grant DE-SC0012273. O.H. is supported by the Department of Energy Computational Science Graduate Fellowship under grant number DE-SC0019323. The computing for this project was performed on the Beocat Research Cluster at Kansas State University, which is funded in part by NSF grants CHE-1726332, CNS-1006860, EPS-1006860, and EPS-0919443. The development of the first-principles electronic dynamics is supported by the U.S. Department of Energy (DE-SC0006863 to X.L.). The development of the linear-response TDDFT method for computational spectroscopy was supported by the National Science Foundation (CHE-1856210 to X.L.).

3.9 References

(1) Christopher, P.; Linic, S. Engineering Selectivity in Heterogeneous Catalysis: Ag Nanowires as Selective Ethylene Epoxidation Catalysts. *J. Am. Chem. Soc.* **2008**, *130*, 11264–11265.

(2) Mukherjee, S.; Libisch, F.; Large, N.; Neumann, O.; Brown, L. V.; Cheng, J.; Lassiter, J. B.; Carter, E. A.; Nordlander, P.; Halas, N. J. Hot Electrons Do the Impossible: Plasmon-Induced Dissociation of H_2 on Au. *Nano Lett.* **2013**, *13*, 240–247.

(3) Yu, S.; Wilson, A. J.; Heo, J.; Jain, P. K. Plasmonic Control of Multi-Electron Transfer and C–C Coupling in Visible-Light-Driven CO_2 Reduction on Au Nanoparticles. *Nano Lett.* **2018**, *18*, 2189–2194.

(4) Wang, F.; Li, C.; Chen, H.; Jiang, R.; Sun, L.-D.; Li, Q.; Wang, J.; Yu, J. C.; Yan, C.-H. Plasmonic Harvesting of Light Energy for Suzuki Coupling Reactions. *J. Am. Chem. Soc.* **2013**, *135*, 5588–5601.

(5) Lee, J.; Mubeen, S.; Ji, X.; Stucky, G. D.; Moskovits, M. Plasmonic Photoanodes for Solar Water Splitting with Visible Light. *Nano Lett.* **2012**, *12*, 5014–5019.

(6) Marimuthu, A.; Zhang, J.; Linic, S. Tuning Selectivity in Propylene Epoxidation by Plasmon Mediated Photo-Switching of Cu Oxidation State. *Science* **2013**, *339*, 1590–1593.

(7) Christopher, P.; Xin, H.; Linic, S. Visible-Light-Enhanced Catalytic Oxidation Reactions on Plasmonic Silver Nanostructures. *Nat. Chem.* **2011**, *3*, 467–472.

(8) Huang, X.; Jain, P. K.; El-Sayed, I. H.; El-Sayed, M. A. Plasmonic Photothermal Therapy (PPTT) Using Gold Nanoparticles. *Lasers Med. Sci.* **2007**, *23*, 217.

(9) Huang, X.; El-Sayed, I. H.; Qian, W.; El-Sayed, M. A. Cancer Cell Imaging and Photothermal Therapy in the Near-Infrared Region by Using Gold Nanorods. *J. Am. Chem. Soc.* **2006**, *128*, 2115–2120.

(10) Jang, Y. H.; Jang, Y. J.; Kim, S.; Quan, L. N.; Chung, K.; Kim, D. H. Plasmonic Solar Cells: From Rational Design to Mechanism Overview. *Chem. Rev.* **2016**, *116*, 14982–15034.

(11) Le Ru, E. C.; Etchegoin, P. G. Single-Molecule Surface-Enhanced Raman Spectroscopy. *Annu. Rev. Phys. Chem.* **2012**, *63*, 65–87.

(12) Christopher, P.; Moskovits, M. Hot Charge Carrier Transmission from Plasmonic Nanostructures. *Annu. Rev. Phys. Chem.* **2017**, *68*, 379–398.

(13) Boerigter, C.; Aslam, U.; Linic, S. Mechanism of Charge Transfer from Plasmonic Nanostructures to Chemically Attached Materials. *ACS Nano* **2016**, *10*, 6108–6115.

(14) Boerigter, C.; Campana, R.; Morabito, M.; Linic, S. Evidence and Implications of Direct Charge Excitation as the Dominant Mechanism in Plasmon-Mediated Photocatalysis. *Nat. Commun.* **2016**, *7*, 10545.

(15) Wu, K.; Chen, J.; McBride, J. R.; Lian, T. Efficient Hot-Electron Transfer by a Plasmon-Induced Interfacial Charge-Transfer Transition. *Science* **2015**, *349*, 632–635.

(16) Bosbach, J.; Hendrich, C.; Stietz, F.; Vartanyan, T.; Träger, F. Ultrafast Dephasing of Surface Plasmon Excitation in Silver Nanoparticles: Influence of Particle Size, Shape, and Chemical Surrounding. *Phys. Rev. Lett.* **2002**, *89*, 257404.

(17) Ma, J.; Wang, Z.; Wang, L.-W. Interplay between Plasmon and Single-Particle Excitations in a Metal Nanocluster. *Nat. Commun.* **2015**, *6*, 1–11.

(18) Mie, G. Beiträge Zur Optik Trüber Medien, Speziell Kolloidaler Metallösungen. *Ann. Phys.* **1908**, *330*, 377–445.

(19) Sinha-Roy, R.; García-González, P.; Weissker, H.-C.; Rabilloud, F.; Fernández-Domínguez, A. I. Classical and Ab Initio Plasmonics Meet at Sub-Nanometric Noble Metal Rods. *ACS Photonics* **2017**, *4*, 1484–1493.

(20) Guidez, E. B.; Aikens, C. M. Quantum Mechanical Origin of the Plasmon: From Molecular Systems to Nanoparticles. *Nanoscale* **2014**, *6*, 11512–11527.

(21) Tame, M. S.; McEnery, K. R.; Özdemir, Ş. K.; Lee, J.; Maier, S. A.; Kim, M. S. Quantum Plasmonics. *Nat. Phys.* **2013**, *9*, 329–340.

(22) Román Castellanos, L.; Kahk, J. M.; Hess, O.; Lischner, J. Generation of Plasmonic Hot Carriers from D-Bands in Metallic Nanoparticles. *J. Chem. Phys.* **2020**, *152*, 104111.

(23) Guidez, E. B.; Aikens, C. M. Plasmon Resonance Analysis with Configuration Interaction. *Phys. Chem. Chem. Phys.* **2014**, *16*, 15501–15509.

(24) Casida, M. E. Time-Dependent Density Functional Response Theory for Molecules. In *Recent Advances in Computational Chemistry*; WORLD SCIENTIFIC, 1995; Vol. 1, pp 155–192.

(25) Donati, G.; Lingerfelt, D. B.; Aikens, C. M.; Li, X. Molecular Vibration Induced Plasmon Decay. *J. Phys. Chem. C* **2017**, *121*, 15368–15374.

(26) Ding, F.; Guidez, E. B.; Aikens, C. M.; Li, X. Quantum Coherent Plasmon in Silver Nanowires: A Real-Time TDDFT Study. *J. Chem. Phys.* **2014**, *140*, 244705.

(27) Yan, L.; Ding, Z.; Song, P.; Wang, F.; Meng, S. Plasmon-Induced Dynamics of H_2 Splitting on a Silver Atomic Chain. *Appl. Phys. Lett.* **2015**, *107*, 083102.

(28) Hartree, D. R.; Hartree, W. Self-Consistent Field, with Exchange, for Beryllium. *Proc. R. Soc. Lond. Ser. - Math. Phys. Sci.* **1935**, *150*, 9–33.

(29) Møller, Chr.; Plesset, M. S. Note on an Approximation Treatment for Many-Electron Systems. *Phys. Rev.* **1934**, *46*, 618–622.

(30) Purvis, G. D.; Bartlett, R. J. A Full Coupled-cluster Singles and Doubles Model: The Inclusion of Disconnected Triples. *J. Chem. Phys.* **1982**, *76*, 1910–1918.

(31) Frisch, M. J.; Trucks, G. W.; Schlegel, H. B.; Scuseria, G. E.; Robb, M. A.; Cheeseman, J. R.; Scalmani, G.; Barone, V.; Petersson, G. A.; Nakatsuji, H.; Li, X.; Caricato, M.; Marenich, A. V.; Bloino, J.; Janesko, B. G.; Gomperts, R.; Mennucci, B.; Hratchian, H. P.; Ortiz, J. V.; Izmaylov, A. F.; Sonnenberg, J. L.; Williams; Ding, F.; Lipparini, F.; Egidi, F.; Goings, J.; Peng, B.; Petrone, A.; Henderson, T.; Ranasinghe, D.; Zakrzewski, V. G.; Gao, J.; Rega, N.; Zheng, G.; Liang, W.; Hada, M.; Ehara, M.; Toyota, K.; Fukuda, R.; Hasegawa, J.; Ishida, M.; Nakajima, T.; Honda, Y.; Kitao, O.; Nakai, H.; Vreven, T.; Throssell, K.; Montgomery Jr., J. A.; Peralta, J. E.; Ogliaro, F.; Bearpark, M. J.; Heyd, J. J.; Brothers, E. N.; Kudin, K. N.; Staroverov, V. N.; Keith, T. A.; Kobayashi, R.; Normand, J.; Raghavachari, K.; Rendell, A. P.; Burant, J. C.; Iyengar, S. S.; Tomasi, J.; Cossi, M.; Millam, J. M.; Klene, M.; Adamo, C.; Cammi, R.; Ochterski, J. W.; Martin, R. L.; Morokuma, K.; Farkas, O.; Foresman, J. B.; Fox, D. J. *Gaussian 16 Rev. C.01*; Wallingford, CT, 2016.

(32) Hay, P. J.; Wadt, W. R. Ab Initio Effective Core Potentials for Molecular Calculations. Potentials for the Transition Metal Atoms Sc to Hg. *J. Chem. Phys.* **1985**, *82*, 270–283.

(33) Hay, P. J.; Wadt, W. R. Ab Initio Effective Core Potentials for Molecular Calculations. Potentials for K to Au Including the Outermost Core Orbitals. *J. Chem. Phys.* **1985**, *82*,

(34) Wadt, W. R.; Hay, P. J. Ab Initio Effective Core Potentials for Molecular Calculations. Potentials for Main Group Elements Na to Bi. *J. Chem. Phys.* **1985**, *82*, 284–298.

(35) Nazin, G. V.; Qiu, X. H.; Ho, W. Atomic Engineering of Photon Emission with a Scanning Tunneling Microscope. *Phys. Rev. Lett.* **2003**, *90*, 216110.

(36) Perdew, J. P.; Burke, K.; Ernzerhof, M. Generalized Gradient Approximation Made Simple. *Phys. Rev. Lett.* **1996**, *77*, 3865–3868.

(37) Becke, A. D. Density-Functional Exchange-Energy Approximation with Correct Asymptotic Behavior. *Phys. Rev. A* **1988**, *38*, 3098–3100.

(38) Perdew, J. P. Density-Functional Approximation for the Correlation Energy of the Inhomogeneous Electron Gas. *Phys. Rev. B* **1986**, *33*, 8822–8824.

(39) Zhao, Y.; Truhlar, D. G. A New Local Density Functional for Main-Group Thermochemistry, Transition Metal Bonding, Thermochemical Kinetics, and Noncovalent Interactions. *J. Chem. Phys.* **2006**, *125*, 194101.

(40) Van Voorhis, T.; Scuseria, G. E. A Novel Form for the Exchange-Correlation Energy Functional. *J. Chem. Phys.* **1998**, *109*, 400–410.

(41) Boese, A. D.; Handy, N. C. New Exchange-Correlation Density Functionals: The Role of the Kinetic-Energy Density. *J. Chem. Phys.* **2002**, *116*, 9559–9569.

(42) Grimme, S. Semiempirical GGA-type Density Functional Constructed with a Long-Range Dispersion Correction. *J. Comput. Chem.* **2006**, *27*, 1787–1799.

(43) Lee, C.; Yang, W.; Parr, R. G. Development of the Colle-Salvetti Correlation-Energy Formula into a Functional of the Electron Density. *Phys. Rev. B* **1988**, *37*, 785–789.

(44) Rohrdanz, M. A.; Martins, K. M.; Herbert, J. M. A Long-Range-Corrected Density Functional That Performs Well for Both Ground-State Properties and Time-Dependent Density Functional Theory Excitation Energies, Including Charge-Transfer Excited States. *J. Chem. Phys.* **2009**, *130*, 054112.

(45) Zhao, Y.; Truhlar, D. G. The M06 Suite of Density Functionals for Main Group Thermochemistry, Thermochemical Kinetics, Noncovalent Interactions, Excited States, and Transition Elements: Two New Functionals and Systematic Testing of Four M06-Class Functionals and 12 Other Functionals. *Theor. Chem. Acc.* **2008**, *120*, 215–241.

(46) Yanai, T.; Tew, D. P.; Handy, N. C. A New Hybrid Exchange–Correlation Functional Using the Coulomb-Attenuating Method (CAM-B3LYP). *Chem. Phys. Lett.* **2004**, *393*, 51–57.

(47) Chai, J.-D.; Head-Gordon, M. Systematic Optimization of Long-Range Corrected Hybrid Density Functionals. *J. Chem. Phys.* **2008**, *128*, 084106.

(48) Chai, J.-D.; Head-Gordon, M. Long-Range Corrected Hybrid Density Functionals with Damped Atom–Atom Dispersion Corrections. *Phys. Chem. Chem. Phys.* **2008**, *10*, 6615–6620.

(49) Anak, B.; Bencharif, M.; Rabilloud, F. Time-Dependent Density Functional Study of UV-Visible Absorption Spectra of Small Noble Metal Clusters (Cu_n, Ag_n, Au_n, n = 2–9, 20). *RSC Adv.* **2014**, *4*, 13001–13011.

(50) Rabilloud, F. UV-Visible Absorption Spectra of Metallic Clusters from TDDFT Calculations. *Eur. Phys. J. D* **2013**, *67*, 18.

(51) Rabilloud, F. Description of Plasmon-like Band in Silver Clusters: The Importance of the Long-Range Hartree-Fock Exchange in Time-Dependent Density-Functional Theory Simulations. *J. Chem. Phys.* **2014**, *141*, 144302.

(52) Rabilloud, F. Assessment of the Performance of Long-Range-Corrected Density Functionals for Calculating the Absorption Spectra of Silver Clusters. *J. Phys. Chem. A* **2013**, *117*, 4267–4278.

(53) Li, X.; Tully, J. C.; Schlegel, H. B.; Frisch, M. J. Ab Initio Ehrenfest Dynamics. *J. Chem. Phys.* **2005**, *123*, 084106.

(54) Fischer, S. A.; Cramer, C. J.; Govind, N. Excited State Absorption from Real-Time Time-Dependent Density Functional Theory. *J. Chem. Theory Comput.* **2015**, *11*, 4294–4303.

(55) Rossi, T. P.; Kuisma, M.; Puska, M. J.; Nieminen, R. M.; Erhart, P. Kohn–Sham Decomposition in Real-Time Time-Dependent Density-Functional Theory: An Efficient Tool for Analyzing Plasmonic Excitations. *J. Chem. Theory Comput.* **2017**, *13*, 4779–4790.

(56) Birke, R. L.; Znamenskiy, V.; Lombardi, J. R. A Charge-Transfer Surface Enhanced Raman Scattering Model from Time-Dependent Density Functional Theory Calculations on a Ag_{10}-Pyridine Complex. *J. Chem. Phys.* **2010**, *132*, 214707.

(57) Johnson, H. E.; Aikens, C. M. Electronic Structure and TDDFT Optical Absorption Spectra of Silver Nanorods. *J. Phys. Chem. A* **2009**, *113*, 4445–4450.

(58) Harb, M.; Rabilloud, F.; Simon, D. Structure and Optical Properties of Core-Shell Bimetallic Ag_nNi_n Clusters: Comparison with Pure Silver and Nickel Clusters. *J. Chem. Phys.* **2009**, *131*, 174302.

(59) Alkan, F.; Aikens, C. M. TD-DFT and TD-DFTB Investigation of the Optical Properties and Electronic Structure of Silver Nanorods and Nanorod Dimers. *J. Phys. Chem. C Nanomater. Interfaces* **2018**, *122*, 23639–23650.

(60) Peach, M. J. G.; Benfield, P.; Helgaker, T.; Tozer, D. J. Excitation Energies in Density Functional Theory: An Evaluation and a Diagnostic Test. *J. Chem. Phys.* **2008**, *128*, 044118.

(61) Hait, D.; Head-Gordon, M. How Accurate Is Density Functional Theory at Predicting Dipole Moments? An Assessment Using a New Database of 200 Benchmark Values. *J. Chem. Theory Comput.* **2018**, *14*, 1969–1981.

(62) Lu, T.; Chen, F. Multiwfn: A Multifunctional Wavefunction Analyzer. *J. Comput. Chem.* **2012**, *33*, 580–592.

(63) Cramer, Christopher J. *Essentials of Computational Chemistry: Theories and Models*, 1st ed.; Wiley: Chichester, England, 2002.

(64) Silverstein, D. W.; Jensen, L. Assessment of the Accuracy of Long-Range Corrected Functionals for Describing the Electronic and Optical Properties of Silver Clusters. *J. Chem. Phys.* **2010**, *132*, 194302.

(65) Moore, J. E.; Morton, S. M.; Jensen, L. Importance of Correctly Describing Charge-Transfer Excitations for Understanding the Chemical Effect in SERS. *J. Phys. Chem. Lett.* **2012**, *3*, 2470–2475.

(66) Yan, L.; Xu, J.; Wang, F.; Meng, S. Plasmon-Induced Ultrafast Hydrogen Production in Liquid Water. *J. Phys. Chem. Lett.* **2018**, *9*, 63–69.

Chapter 4 - Theoretical Investigations on the Plasmon-Mediated Dissociation of Small Molecules in the Presence of Silver Atomic Wires

Olivia A. Hull and Christine M. Aikens

Reproduced with permission from Journal of Physical Chemistry, submitted for publication.

4.1 Abstract

Plasmonic nanoparticles can promote bond activation in adsorbed molecules under relatively benign conditions via excitation of the nanoparticle's plasmon resonance. As the plasmon resonance often falls within the visible light region, plasmonic nanomaterials are a promising class of catalyst. However, the exact mechanisms through which plasmonic nanoparticles activate the bonds of nearby molecules are still unclear. Herein, we evaluate Ag_8-X_2 (X = N, H) model systems via real-time time-dependent density functional theory (RT-TDDFT), linear response time-dependent density functional theory (LR-TDDFT), and Ehrenfest dynamics in order to better understand the bond activation processes of N_2 and H_2 facilitated by the presence of the atomic silver wire under excitation at the plasmon resonance energies. We find that dissociation is possible for both small molecules at high electric field strength. Activation of each adsorbate is symmetry- and electric field-dependent, and H_2 activates at lower electric field strengths than N_2. This work serves as a step towards understanding the complex time-dependent electron and electron-nuclear dynamics between plasmonic nanowires and adsorbed small molecules.

4.2 Introduction

Plasmonic nanoparticles (NPs) have generated significant research interest owing to their highly tunable optical properties.[1–3] These properties, and their tunability, are a direct consequence of the symmetries of the particles and the confinement effects that arise due to the nanometer length scale of these systems. Plasmonic nanoparticles find application in catalysis,[1,4–12] photovoltaics,[13–15] sensing and detection,[16–19] medicine,[20–22] and more. Photocatalysis is an area of particular interest, as plasmonic nanoparticles have been shown to activate adsorbates like O_2,[12] H_2,[7] CO_2,[8] H_2O,[10] and others.[9,11,23] Many of these adsorbates are not easily activated through traditional means, yet experiment shows that plasmonic photocatalysis can occur under relatively benign conditions, such as room temperature and pressure and low light intensity.

Plasmonic NPs achieve this photocatalytic activity through excitation of the plasmon resonance. The plasmon resonance can be thought of as the collective oscillation of free surface electrons, which occurs at a particular plasmon resonance frequency. The plasmon resonance frequency is readily tunable based on the size and shape of the particle, among other factors. While the plasmon resonance plays an important role in plasmonic photocatalysis, the exact means of activation are not fully understood. There has been intense research effort in defining and distinguish the mechanisms through which the plasmonic particles achieve activation, but uncertainty remains.[24–27] To further obfuscate the issue, in small nanoclusters where quantum effects dominate, there are numerous ways to identify or define the plasmon resonance.[28–31] In this paper, we employ the "quantum plasmon" framework, which identifies plasmonic peaks in small clusters as coherent excitations of multiple single-particle transitions with near-equal transition coefficients as computed by linear response time-dependent density functional theory.[31,32]

Given the tunability of the plasmon resonance and the fact that the plasmon resonance plays an important role in plasmon-mediated photocatalysis, there is significant research interest in understanding exactly how the plasmon resonance affects the catalysis process, and how to harness the tunability of the resonance for this purpose.[2] As the process depends on the electronic structure and the electron-nuclear dynamics of the system, computational methods are well-suited to systematically investigate a plasmonic system of interest.

Theoretical investigations can offer detailed insight into the catalysis process. These methods can access important quantities like the electronic structure of the equilibrium system, the electron dynamics of the system upon excitation, and depending on the methods employed, coupled electron-nuclear dynamics to model activation and dissociation firsthand. However, modeling plasmonic photocatalysis is computationally demanding by nature, and becomes increasingly demanding as the size of the system or fidelity of the model is increased. The challenges involved in the theoretical modeling of plasmon-mediated photocatalysis range from technical issues like the accuracy vs. computational cost of a given method and its various approximations, to which information is relevant to extract from a given method, and even to the method-type itself.

Theoretical studies can be broadly divided into two camps: those that use potential energy surfaces (PES) to understand the system and its dynamics, and those that use a given "real-time" approach. In real-time approaches, typically the density matrix of the system is propagated in time upon perturbation by laser of a particular frequency and envelope, often without accessibility to distinct underlying potential energy surfaces (i.e. an Ehrenfest dynamics-type approach). In the PES approach, the topography of excited state surfaces is investigated. Sometimes, dynamics

calculations are performed on these surfaces (e.g. surface hopping-type approaches) to provide transition probabilities between surfaces.[33]

In real-time approaches, there are several common approximations. Chief among them is in the choice of system model. Some studies have employed a jellium model for the nanoparticle portion of the system, such as in the work by Schatz and coworkers. This study found dissociation of the H_2 adsorbate on the jellium system at high field strengths.[34] Others, like our previous work[35] and that of Yan, et al.,[36] rely on small clusters that share key properties with more realistically sized nanoclusters in order to retain computational tractability. Others may examine realistically sized nanocluster-adsorbate systems with local density or generalized gradient-based functionals.[37] In these cases, similar to the jellium case, dissociation is achieved upon excitation at the quantum plasmon mode at a high electric field strength. Others still compute transition probabilities within the framework of electron-only dynamics rather than with explicit surfaces, which provides valuable information on electron-hole pairs and their probabilities of formation.[38,39] In all of these cases, density functional theory (DFT) is employed, which is less detailed than correlated wavefunction methods. Correlated wavefunction methods, while less common due to their computational cost, have been utilized in the unit cell-based embedding method PES-approach by Carter and coworkers, where the authors treat a portion of the system with a correlated wavefunction method and the remainder of the system with DFT in order to obtain excited state potential energy surfaces of the surface-adsorbate system.[40] However, in general, DFT is the workhorse method in the field.

Herein, we employ a model system of an atomic Ag_8 wire that retains key properties of larger wires. In particular, the system is too small to support a traditional plasmon mode, and instead exhibits longitudinal and transverse "quantum plasmon" modes. While the plasmon mode

of large nanoparticles can be described through the classical Mie theory,[3] this picture breaks down for small clusters, where the states involved are sufficiently discretized. However, the picture of "sloshing electron density" remains. In this case, the plasmon excitation can be described as a constructive addition of multiple single-particle transitions (or excited determinants). The multideterminantal excitations in silver and gold nanoparticles are collective in nature and grow to match the plasmon peaks as the particle size increases. As the particle size decreases, fewer determinants contribute to the plasmon. For the atomic scale nanowires, the transverse peak is still collective. However, the longitudinal peak becomes a single-particle transition at this size. Nonetheless, one can think of this as the limiting case as N → 1, where N is the number of determinants that comprises the plasmon-like excitation. The longitudinal peak in atomic scale wires still arises from delocalized sp → sp transitions with similar physics to the collective plasmons of larger nanorods. Thus, although this peak has 'single-particle' character, it is analogous in many ways to the 'plasmonic' transitions of larger systems. We refer the reader to more extensive discussions on this topic by Guidez and Aikens,[31,32] and Gieseking.[41,42] Studying a quantum plasmon excitation has several advantages, mainly in that it allows us to develop an understanding of plasmon-mediated photocatalysis through the lens of quantum chemistry rather than through a classical electrodynamics approach. That the quantum plasmon descriptor is especially appropriate for small, computationally tractable clusters, is appealing as well.

In this work, we build on a previous report in which we evaluated the electronic structure and dynamics of a system of N_2 on Ag_n (n = 6, 8, 10) wires.[35] We expand this initial report to study both N_2 and H_2 as the adsorbate molecule, to study the adsorbate in multiple orientations, and to study both the longitudinal and transverse quantum plasmon excitations of the Ag_8 wire.

We find that in each adsorbate case the longitudinal plasmon mode leads to greater activation and/or dissociation for a given adsorbate configuration.

4.3 Methods

In all calculations, we employ the LC-ωPBE functional[43] and lanl2dz basis set,[44–46] as this functional/basis set combination has been found to perform well in our own benchmarking on the Ag_6N_2 system, and the LC-ωPBE functional is known to perform well for silver clusters.[47–50] The Ag_8N_2 and Ag_8H_2 structures were optimized in Gaussian 16[51] by first separately finding the geometry minima of the wire and small molecule, then combining the optimized structures to obtain Ag_8X_2 (X = N, H). The Ag_8X_2 structure is then optimized with the Ag atoms frozen, allowing the small molecule to orient about the wire while maintaining the linear symmetry of the wire. We apply this procedure to four cases: Ag_8N_2 and Ag_8H_2 each in the parallel orientation (figure 4.1a) and the perpendicular orientation (figure 4.1b). For the Ag_8H_2 case, the parallel Ag-H distance is 2.53 Å, as is the distance to the center of the H_2 in the perpendicular case. In both Ag_8H_2 cases, the H_2 interatomic distance is found to be 0.75 Å.

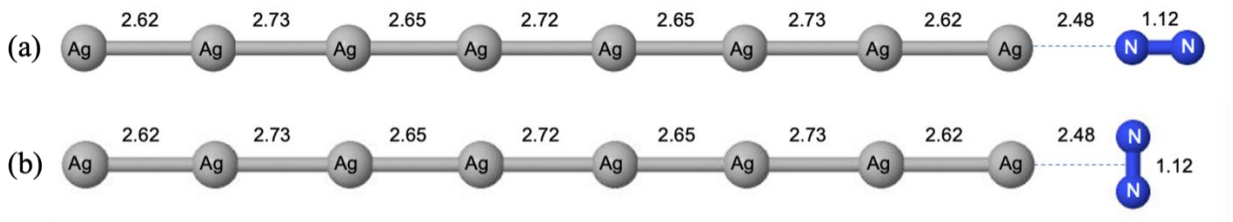

Figure 4.1 Ag_8N_2 structures. (a) "parallel" N_2 geometry, (b) "perpendicular" N_2 geometry. In the parallel case, we define N1 (H1) as the adsorbate atom closest to the wire, and N2 (H2) the terminal adsorbate atom. In the perpendicular case, N1 (H1) is defined as the atom above the longitudinal axis, and N2 (H2) the atom below.

We employ linear response time-dependent density functional theory (LR-TDDFT) to compute simulated absorption spectra using the standard implementation of the Gaussian 16 package. LR-TDDFT describes a given excitation in terms of linear combinations of single-particle transitions. Thus, in the molecular orbital picture, it provides information on which occupied-to-virtual orbital transitions comprise an excitation. In LR-TDDFT, a stick spectrum is obtained directly from the excitation energies and oscillator strengths of the excitations. In the absorption spectra presented herein, we convolve the stick spectrum with a Lorentzian broadening function with a full width at half-maximum (FWHM) of 0.2 eV.

We employ linear response time-dependent density functional theory (LR-TDDFT) to compute simulated absorption spectra using the standard implementation of the Gaussian 16 package. LR-TDDFT describes a given excitation in terms of linear combinations of single-particle transitions. Thus, in the molecular orbital picture, it provides information on which occupied-to-virtual orbital transitions comprise an excitation. In LR-TDDFT, a stick spectrum is obtained directly from the excitation energies and oscillator strengths of the excitations. In the absorption spectra presented herein, we convolve the stick spectrum with a Lorentzian broadening function with a full width at half-maximum (FWHM) of 0.2 eV. Absorption spectra intensities are shown in arbitrary units.

Electron-only real-time time-dependent density functional theory (RT-TDDFT) provides dynamical information on a system by obtaining its electronic response to an electric field perturbation. Unlike LR-TDDFT, RT-TDDFT is not limited to the perturbative regime, and the electronic response can be non-linear. RT-TDDFT provides access to the time-dependent dipole moment and other time-dependent quantities like time-dependent orbital populations (by projecting electron densities onto the ground-state orbitals).[52] We use a development version of

Gaussian 16 for our RT-TDDFT calculations.[53] We apply a continuous-wave electric field at electric field strengths of 0.001, 0.01, 0.03, and 0.05 atomic units (a.u.) at a given excitation energy of interest, which are the transverse and longitudinal plasmon excitations of the system. The electric field has a trapezoidal envelope, which is ramped to maximum intensity from 0-1 fs, then sustained at this intensity for 18 fs, before ramping down in the final 1 fs, for a total of 20 fs of "on" electric field. The equation for this field is shown in equations 4.1 and 4.2, where *t* is measured in fs:

$$E(t) = A(t)\sin(\omega t) \quad \text{(Eq. 4.1)}$$

$$A(t) = \begin{cases} E_0 t, & 0 < t < 1 \\ E_0, & 1 \leq t \leq 19 \\ -E_0(t-20), & 19 < t < 20 \end{cases} \quad \text{(Eq. 4.2)}$$

where E_0 represents the maximum electric field strength and ω is the frequency that corresponds to the excitation energy of interest.

We use an electronic step size of 0.0006 fs for the Ag_8N_2 cases. Each simulation is run for a minimum of 70 fs. In these electron-only calculations, we report only the first 20 fs of the 70 fs, since these calculations are used to compare against the results of the coupled Ehrenfest dynamics calculations, and as the adsorbate moves further away from the wire in the Ehrenfest dynamics calculations, comparison with RT-TDDFT results becomes increasingly tenuous.

Electron-only RT-TDDFT can be coupled with the mean-field Ehrenfest dynamics (ED) method to incorporate nuclear motion into a simulation, which we denote here as RT-TDDFT/ED. RT-TDDFT/ED allows for nuclear motion as described under the Ehrenfest scheme, where the nuclei are propagated based on the average forces from the electronic degrees of freedom at a given time step. Under this scheme, we can observe activation and dissociation of the N_2 or H_2 bond under a given excitation. As in the RT-TDDFT case, we use a development version of Gaussian 16 for our RT-TDDFT/ED calculations. Again, we apply the 20 fs

trapezoidal-envelope continuous wave electric field. We use an electronic step size of 0.00025 fs and a nuclear step size of 0.1 fs for a minimum of 70 fs with default initial velocities on the adsorbate atoms. The Ag atoms are frozen. Field strengths of 0.05, 0.04, 0.03, 0.02, 0.01, and 0.001 a.u. are used. These electric field strengths are far outside the perturbative regime. As noted in works employing similar methodologies by Schatz and coworkers[34] and Meng and coworkers,[37] due to the high computational cost of dynamical quantum mechanics methods like Ehrenfest dynamics, dissociation or activation dynamics must be observed within the relatively short time window of the simulation in order to maintain computational feasibility, which necessitates a strong electric field strength. Second, the duration of the applied electric field (20 fs in this work) is short compared to experimental irradiation times (~ 1 s), which leads to less energy transfer. Ongoing work in our group has explored the electric field relationship to the length of the silver atomic wires, finding that as the size of the particle increases, the applied electric field strength can decrease. We excite the system at the energies corresponding to the transverse and longitudinal plasmon excitations.

4.4 Results and Discussion

4.4.1 Parallel Ag_8N_2 at 0.03 a.u. Electric Field Strength

In order to detail the computation and analysis process, we first walk through our approach with an example calculation, which is the response of the Ag_8N_2 system to a 0.03 a.u. continuous-wave electric field. In this case, our Ehrenfest dynamics results show activation of the N_2 bond, but not dissociation. First, to determine the appropriate energy at which to excite the system, both for the 0.03 a.u. electric field and for any other electric field for a given wire-

small molecule orientation, we perform an LR-TDDFT calculation to identify interesting excitations of the system and their corresponding energies. The LR-TDDFT results (figure 4. 2a) tell us the excitation energies and which single-particle transitions comprise each stick excitation. In this section we focus on the peak at 1.47 eV, which is comprised of two single-particle transitions, a HOMO → LUMO and HOMO – 1 → LUMO + 1. The orbitals are shown in (b).

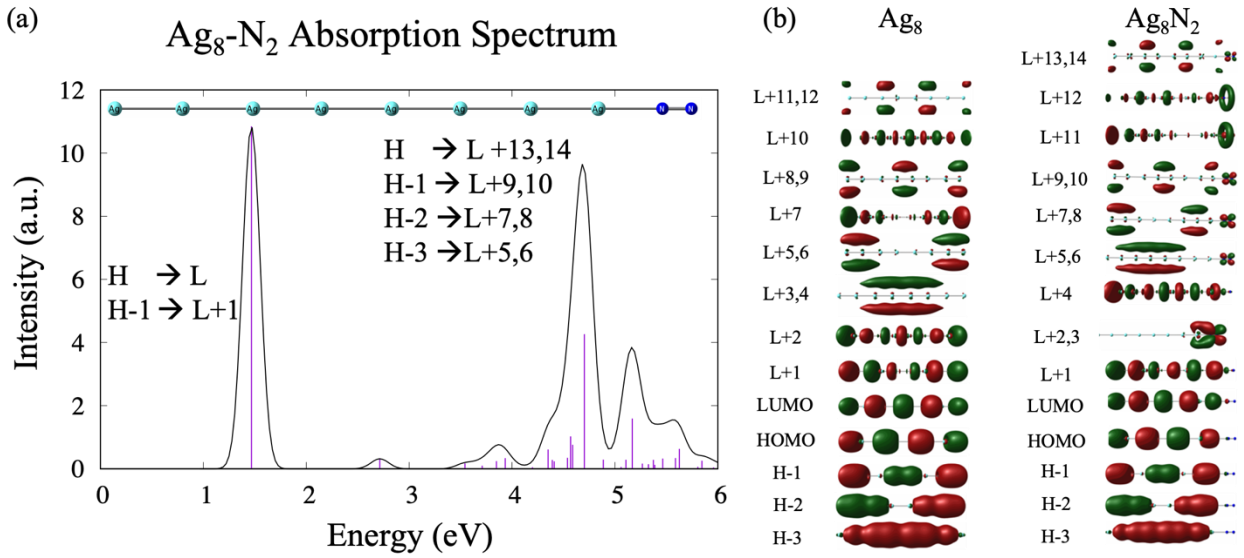

Figure 4.2 (a) LR-TDDFT absorption spectrum of parallel-oriented Ag_8N_2. The quantum plasmon peaks are labeled, and the corresponding single-particle transitions are shown, where "H" denotes HOMO and "L" denotes LUMO. In the LR-TDDFT spectrum, a.u. denotes "arbitrary units" (b) The orbitals in the range of relevant single-particle transitions for the longitudinal and transverse plasmon modes shown in (a). Figure adapted from reference 35.[35]

After identifying the peak of interest, we can perform an Ehrenfest dynamics calculation in which we excite this state of interest. We excite the system by driving the continuous wave electric field at the energy of the longitudinal plasmon-like mode identified via LR-TDDFT for 20 fs, then let the system propagate field-free for another 50 fs. From the Ehrenfest dynamics calculation, we can extract the nuclear coordinates at each time step, and from this information

generate plots of bond distances over time and, if the bond distance over time oscillates due to nuclear vibrations rather than dissociates, compute a Fourier transform of the bond distance data to yield the frequency of the vibration.

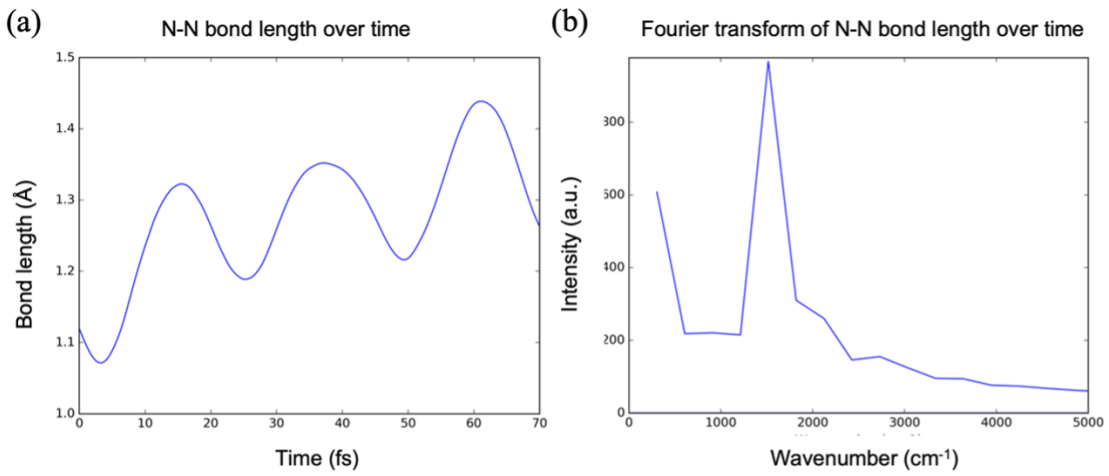

Figure 4.3 (a) N-N bond length across 70 fs RT-TDDFT/ED calculations in which a 0.03 a.u. electric field is applied, exciting at the longitudinal plasmon resonance energy. Plots for all possible electric field and N_2 orientations are shown in Figure A.1. (b) Fourier transform of the data shown in (a), which provides information about the vibrational frequency of the N-N bond across the simulation. The intensity is shown in arbitrary units.

The 0.03 a.u. electric field causes the N_2 molecule to vibrate around an average bond distance of 1.31 Å at a frequency of 1500 cm^{-1}, and we see that the average bond length continues to grow across the simulation, even after the electric field is turned off. The N_2 vibrational mode of Ag_8N_2 identified by Hessian normal mode analysis is 2408 cm^{-1} (the isolated N_2 bond frequency computed by Hessian normal mode analysis is 2382 cm^{-1}) and the optimized bond distance of N_2 in the equilibrium Ag_8N_2 system is 1.12 Å, which shows that excitation at the longitudinal plasmon resonance of the wire increases the average bond length of N_2 and decreases its vibrational frequency, indicating activation of the bond. When the isolated N_2 molecule is subject to identical conditions (i.e. the same applied electric field) and identical

analysis, we find an N-N average bond distance of 1.19 Å vibrating at a frequency of 2050 cm^{-1}. Thus, the presence of the wire is an important ingredient in the activation of the N_2.

Another quantity of interest obtained from a real-time calculation is the time-dependent dipole moment. As the time-dependent dipole moment is calculated as a charge times a distance, it provides insight into the amount of electron density displacement across the system as a function of time. The static dipole moment of the system is quite large, at 4.82 D (parallel) and 3.00 D (perpendicular). This can be explained by the fact that, while Ag_8 and N_2 are both separately relatively nonpolar systems, combining the two results in a separation of charge. With the dipole arising from charge across a distance, and the length of the system being considerable at 22.3 Å (parallel) and 22.0 Å (perpendicular), the static dipole moment is larger than one might expect upon combination of two non-polar systems.

Over the time period of the simulations, the N_2 molecule moves away from the wire and, in dissociative cases, the N atoms move away from each other. Because of this, the time-dependent dipole moment of an RT-TDDFT/ED calculation is difficult to interpret. Instead, we examine the time-dependent dipole moment results of the corresponding electron-only RT-TDDFT calculation, where all nuclei are frozen in place. For electron-only quantities, we present only the first 20 fs of the 70 fs simulation and note that the most interesting dynamics occur within the first 5 fs.

In the first five femtoseconds of the electron-only dynamics, we see a surge in the z-directional (longitudinal) dipole moment, signifying a large amount of electron density displacement from one end of the wire to the other. When the system is excited at a perturbative electric field strength, the dipole tends to follow the electric field (Figure A.2) At non-

perturbative field strengths, such as at 0.03 a.u., self-interaction of the dipole moment causes interference, disrupting its ability to track with the electric field (Figure 4.4).

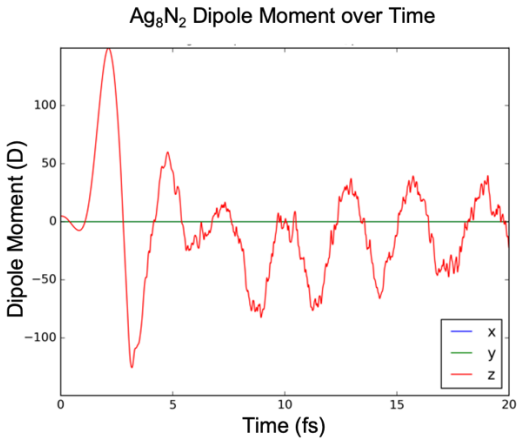

Figure 4.4 Time-dependent dipole for the first 20 fs of the electron-only RT-TDDFT calculation in which the longitudinal plasmon mode is excited with a 0.03 a.u. electric field. Note that the x- and y- directional dipoles overlay each other, as dipole moment experiences no change in either of these directions.

In addition to the time-dependent dipole moment, time-dependent orbital populations can be obtained as part of an RT-TDDFT calculation. Here, the electron density is projected onto the ground-state orbitals of the system at each time step. Since this analysis relies on the electronic structure at equilibrium geometry, time dependent orbital populations are only available in an electron-only dynamics calculation. In the first 20 fs of the electron-only simulation, the populations of the LUMO, LUMO+1, LUMO+4, and LUMO+11 rapidly increase on initial application of the electric field, with the LUMO spiking to a population of 0.97 at t = 1.96 fs. The LUMO+1, LUMO+4, and LUMO+11 have the same symmetry as the LUMO (i.e. Σ - symmetry, or cylindrical symmetry about the longitudinal axis). In the LR-TDDFT absorption spectrum, the longitudinal plasmon peak is comprised of the HOMO → LUMO and HOMO – 1 → LUMO + 1 transitions. Here, we see the involvement of additional transitions between

orbitals with matching Σ-symmetry due to the non-perturbative nature of the applied electric field. In conjunction with the population of the LUMO, LUMO+1, LUMO+4, and LUMO+11 orbitals rapidly increasing, the population in HOMO, HOMO-1, HOMO-2, and HOMO-3 rapidly decreases.

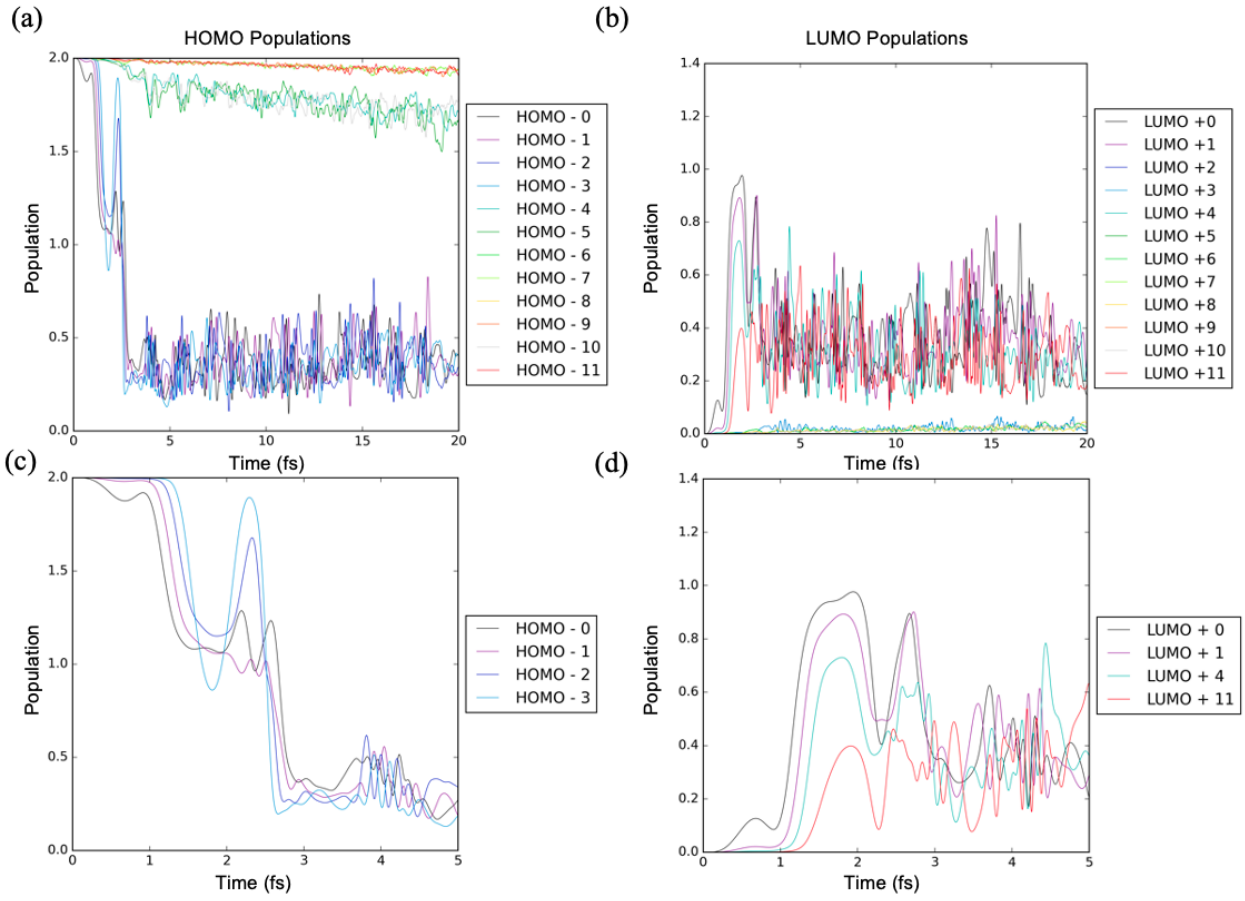

Figure 4.5 Time-dependent orbital populations for the 0.03 a.u. electric field, longitudinally excited parallel Ag_8N_2 system electron-only RT-TDDFT calculation. (a) Depicts population of initially occupied molecular orbitals, while (b) depicts the population of initially unoccupied orbitals. HOMO and LUMO populations for all simulations are shown in Figures A.3-A.6. (c) and (d) show the first 5 fs of orbital populations of the most affected occupied and unoccupied molecular orbitals respectively.

Finally, we carry out Hirshfeld population analysis at each time step on both the RT-TDDFT/ED calculation and the electron-only calculation. In this section, we present the ED

results for the 0.03 a.u. electric field, parallel N_2 orientation, and longitudinal excitation system, though the full Hirshfeld population results for all Ag_8N_2 systems can be found in figures A.7-A.8, and the electron-only results can be found in figures A.9-A.10. We briefly discuss some of the differences between the RT-TDDFT and RT-TDDFT/ED results in section 4.4.2. Atomic populations are not experimental observables, and because of this, there are multiple schemes to partition partial charges amongst atoms. We choose Hirshfeld population analysis in order to avoid the basis set dependence of Mulliken-type methods.[54] Since the Hirshfeld method is density-based and relies on atomic reference densities, it is a better candidate for the RT-TDDFT/ED cases, where the electron density is propagated in time and atoms may migrate away from each other. Figure 4.6a partitions the Hirshfeld charges into N and Ag; the green line is the sum of the charge on both N atoms, while the blue line is the sum of all charge on each of the eight Ag atoms. The negative charge transfer to the adsorbate peaks at a charge of q = -0.935 at t = 15.3 fs. Figure 4.6b further partitions the adsorbate subsystem into atoms N1 and N2, where N1 is the nitrogen atom closest to the wire at the start of the simulation. The terminal N2 initially picks up more negative charge than N1. This charge transfer profile provides support for the idea that transient negative ions play an important role in plasmon-mediated molecular activations.[55] For this system (parallel adsorbate, longitudinal plasmon excitation, 0.03 a.u. field strength), a transient negative ion forms within the first 5 fs of the simulation, then dissipates around 42 fs into the simulation. This charge then oscillates between the two N atoms and the Ag wire. The maximum charge difference between the two nitrogen atoms, defined as $|q_{N1}-q_{N2}|$, is found to be 0.66, occurring 11.7 fs into the simulation.

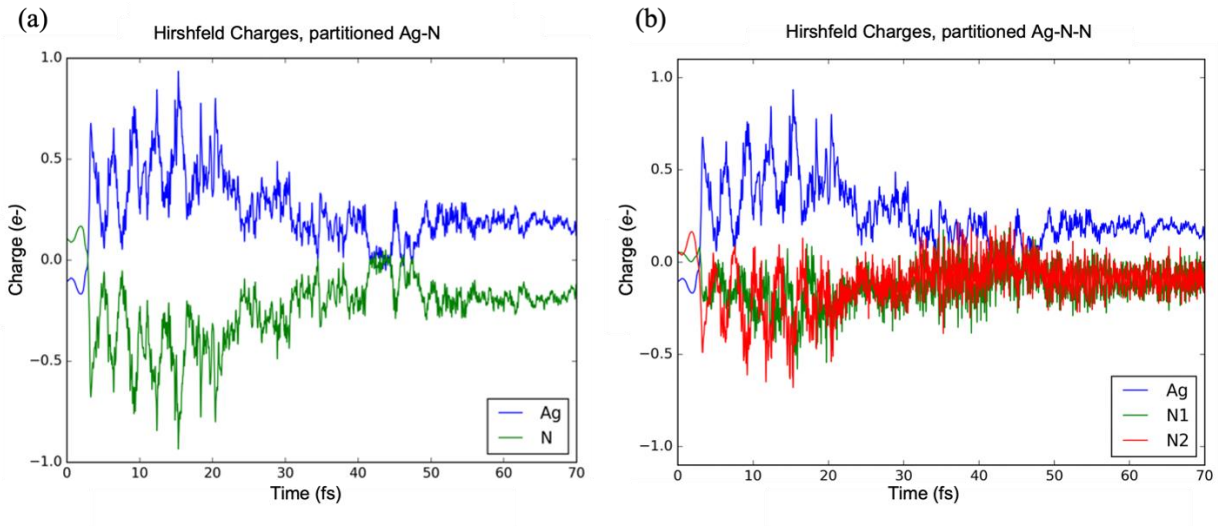

Figure 4.6 Time-dependent Hirshfeld charges. In (a), the charges are divided into Ag and N subsystems, where the Ag subsystem is the sum of all charges on each of the eight Ag atoms, and the N subsystem is the sum of the charges on the two N atoms. In (b), the Ag subsystem remains the same, but the charges on the two N atoms are plotted separately. N1 denotes the N atom closest to the wire at the start of the simulation, and N2 denotes the terminal N atom.

The Hirshfeld charge data, bond length data, and frequency analysis obtained from the RT-TDDFT/ED simulation, alongside electron-only dynamics to obtain orbital populations and dipole moment, provide insight into the charge transfer process that enables activation of the adsorbate. RT-TDDFT/ED data shows an overall increasing bond length with simulation time and a dominant N_2 vibrational frequency of about 1500 cm^{-1}. The average N_2 bond length in the 0.03 a.u. electric field is 1.31 Å, or 117% of the equilibrium length. The maximum bond length achieved is 1.44 Å, or 128% the equilibrium bond length, demonstrating activation of N_2. Meanwhile, the electron-only dipole moment shows a surge upon initial application of the field, signifying a large displacement of the electron density across the length of the wire. Simultaneously, the population of Σ-symmetry unoccupied orbitals rapidly grows as the population of the HOMO to HOMO-3 depletes in the first 5 fs. Finally, Hirshfeld charge analysis

of the electron-nuclear dynamics calculation shows charge transfer occurs from the wire subsystem to the adsorbate, peaking at a charge of -0.935 *e*- at 15.3 fs.

4.4.2 Ag_8N_2 Electron- and Electron-Nuclear Dynamics

While the above discussion presents a detailed analysis for a representative adsorbate orientation, excitation energy, and electric field strength, in this section, we focus primarily on comparing the time-dependent N-N bond distance and maximum charge on the N_2 in a series of RT-TDDFT/ED calculations. The systems examined are the possible combinations of the "parallel" (with longitudinal and transverse plasmon peaks at 1.47 eV and 4.68 eV, respectively) and "perpendicular" geometries (with longitudinal and transverse plasmon peaks at 1.46 eV and 4.64 eV, respectively) (Figure 2.a), continuous-wave excitation at the longitudinal and transverse plasmon mode energies, and electric field strengths of 0.05, 0.04, 0.03, 0.02, 0.01, and 0.001 a.u. for a total of 24 different Ag_8N_2 RT-TDDFT/ED simulations (Figure A.1). From the N-N bond distance over time, we compute the N-N vibrational frequency via Fourier transform. We note that, due to the length of the calculations and consequently the relatively small number of oscillation cycles, the Fourier transform data is broad and contains a high amount of uncertainty. Despite this, general trends in the vibrational frequencies can be observed.

From Table 4.1 we observe that excitation of the longitudinal plasmon resonance leads to the most activation at a given field strength. Activation is most favorable in the "parallel" orientation, where dissociation is observed for the 0.05 a.u. field case. In the "perpendicular" orientation, the N_2 also becomes activated, but to a generally lesser degree (or the same degree, in the 0.01 and 0.001 a.u. field cases). Some activation is observed for excitation of the transverse plasmon as well (4.68 eV), but not to the extent of the longitudinal plasmon case (1.47

eV), which may be due to the increased oscillator strength of the longitudinal plasmon relative to the transverse. Importantly, without the wire present, no activation of N_2 is observed, despite the significant strength of the applied electric field.

Table 4.1 Average N-N interatomic distance across 70 fs of RT-TDDFT/ED simulation. The truncated systems shown in the "adsorbate orientation and electric field polarization" cells represent the four possible orientation/electric field combinations. Respectively, these are parallel-oriented adsorbate excited at the longitudinal plasmon mode, perpendicular-oriented adsorbate excited at the longitudinal plasmon mode, parallel-oriented adsorbate excited at the transverse plasmon mode, and perpendicular-oriented adsorbate excited at the transverse plasmon mode. Corresponding bond length plots are found in Figure A.1.

	field strength (a.u.)	0.05	0.04	0.03	0.02	0.01	0.001
Adsorbate orientation and electric field polarization	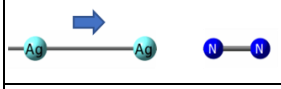	3.83 Å	1.41 Å	1.30 Å	1.21 Å	1.16 Å	1.13 Å
	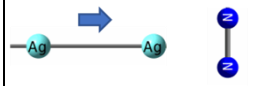	1.33 Å	1.27 Å	1.23 Å	1.18 Å	1.16 Å	1.13 Å
	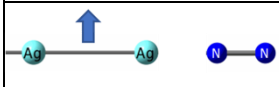	1.17 Å	1.16 Å	1.16 Å	1.14 Å	1.14 Å	1.13 Å
	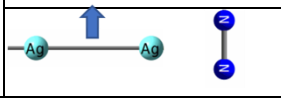	1.18 Å	1.18 Å	1.17 Å	1.15 Å	1.14 Å	1.13 Å

The table of N-N average vibrational frequencies (Table 4.2) provides insight into the degree of activation for the cases that do not fully dissociate. In the N_2 case, this is for all but one simulation. For comparison, the isolated N_2 stretching mode computed via Hessian normal mode calculation is 2383 cm^{-1}, whereas the N_2 stretching mode of Ag_8N_2 is 2408 cm^{-1}. In general, the vibrational frequency decreases as the electric field increases, which is consistent with the notion that as a bond becomes more activated, it becomes weaker and its vibrational frequency decreases. The lowest N_2 vibrational frequencies are achieved for high field strengths that are longitudinally polarized, with N_2 in the parallel orientation becoming particularly activated. Further, for the cases in which the N_2 does not dissociate, the downward trend in the N_2

vibrational frequency generally tracks with the upward trend in bond length as the field strength increases. Note that excitation of the transverse plasmon mode does not strongly affect the N_2 vibrational frequency when N_2 is in either of the parallel or perpendicular orientations.

Table 4.2 N_2 vibrational frequency (cm^{-1}) across 70 fs RT-TDDFT/ED simulations for the systems described in Table 4.1.

	field strength (a.u.)	0.05	0.04	0.03	0.02	0.01	0.001
Adsorbate orientation and electric field polarization	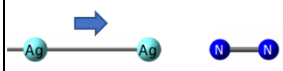	-	1200	1500	1700	2100	2300
	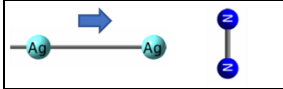	1100	1700	1500	2100	2200	2300
	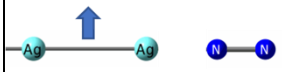	2100	2000	2000	2100	2300	2200
	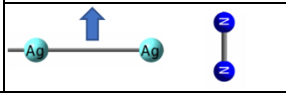	1900	2000	1900	2000	2200	2200

Table 4.3 compiles the maximum Hirshfeld charge obtained on the N_2 molecule across each simulation. Full Hirshfeld charge data plots are shown in Figure A.7. Data for the timestep at which the maximum charge occurs is available in Table A.1. In general, calculations with stronger field strengths yield a more negative maximum charge, and this peak charge tends to occur earlier in the simulation. For a given electric field strength, the longitudinally polarized field with parallel-oriented N_2 sees the most charge transfer from the wire to the N_2, with the amount of charge transferred increasing as the field strength increases. The transverse-polarized electric field cases see little charge transfer in comparison to the longitudinally-polarized cases at a given field strength. The longitudinal field with perpendicular N_2 case sees considerably more charge transfer than the transverse field cases, but less than when the N_2 is oriented parallel to the wire. These results are consistent with the degree of activation (Table 4.1) and the change in N_2 vibrational frequency (Table 4.2). Cases in which more charge is transferred correlate with

higher average N-N bond lengths and lower vibrational frequencies. In the transverse field case, little bond activation is seen, along with little charge transfer.

Table 4.3 Maximum Hirshfeld charge (e^-) obtained on N_2 subsystem across 70 fs of RT-TDDFT/ED simulation. The time at which the maximum charge is obtained is found in Table A.1.

	field strength (a.u.)	0.05	0.04	0.03	0.02	0.01	0.001
Adsorbate orientation and electric field polarization	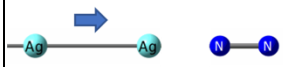	-1.06	-0.94	-0.94	-0.77	-0.44	-0.21
	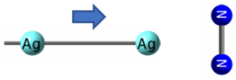	-0.82	-0.73	-0.86	-0.65	-0.47	-0.21
	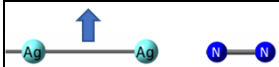	-0.42	-0.39	-0.32	-0.26	-0.25	-0.10
	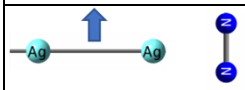	-0.29	-0.37	-0.28	-0.25	-0.16	-0.09

In addition to the maximum Hirshfeld charge, we compute the maximum charge difference between N1 and N2 in each simulation, summarized in Table 4.4. Data on when the maximum charge difference occurs is available in Table A.2, and the full Ag-N-N-partitioned Hirshfeld charge data is found in Figure A.8. The trend in data for maximum $|q_{N1} - q_{N2}|$ generally follows the same trend as the maximum Hirshfeld charge, where the parallel-oriented N_2 at longitudinal plasmon excitation obtains the maximum charge separation for a given field strength, with perpendicularly-oriented N_2 at longitudinal plasmon mode obtaining smaller but still significant charge separations. Each transverse excitation case sees little charge separation, irrespective of field strength or N_2 orientation. It is possible that the greater degree of charge separation across parallel-oriented N_2 in the longitudinal case encourages the greater degree of activation relative to the perpendicular case. We hypothesize that the polarization of the bond may help facilitate the bond breakage.

Table 4.4 Maximum Hirshfeld charge difference obtained as $|q_{N1} - q_{N2}|$ across 70 fs of RT-TDDFT/ED simulation. The time at which the maximum charge difference is obtained is found in Table A.2.

	field strength (a.u.)	0.05	0.04	0.03	0.02	0.01	0.001
Adsorbate orientation and electric field polarization	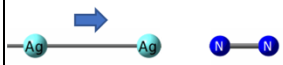	1.10	0.84	0.66	0.41	0.25	0.08
	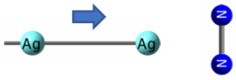	0.45	0.55	0.39	0.22	0.19	0.06
	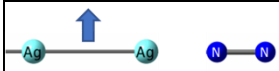	0.29	0.20	0.22	0.18	0.11	0.03
	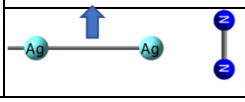	0.24	0.22	0.18	0.13	0.09	0.03

The results obtained from the RT-TDDFT/ED simulations suggest that the orientation of the molecule along the wire is important for activation, that the degree of activation scales with the strength of the electric field, and that excitation of the transverse plasmon mode activates the system significantly less than the longitudinal plasmon mode, regardless of adsorbate orientation or field strength.

We can examine equivalent electron-only RT-TDDFT calculations for each RT-TDDFT/ED case. Again, projecting the electron density at a given timestep onto the ground-state orbitals can provide qualitative insight into the electron dynamics of the system through orbital population analysis, alongside electron-only time-dependent dipole and charge data. The electron-only dynamics data is reported in figures A.2-A.6 and figures A.9-A.10.

As in the RT-TDDFT/ED case that includes both electron and nuclear dynamics, we find that that the incident electric field matters more than the orientation of the N_2. Population

analysis (figures A.3-A.6) reveals that the orbitals involved in a given simulation are those that are expected based on symmetry considerations, i.e. $\Sigma \rightarrow \Sigma$ transitions for the field polarized to the longitudinal plasmon, and $\Sigma \rightarrow \Pi$ transitions for the transverse case. With the stronger electric fields, more orbitals are involved than those found in the LR-TDDFT absorption calculation. For example, in the LR-TDDFT longitudinal plasmon excitation with N_2 in the parallel orientation, we find that the orbitals involved are the HOMO-1, HOMO, LUMO, and LUMO+1. In the longitudinal excitation electron-only dynamics, we find for field strengths of 0.01 a.u. or stronger that other unoccupied orbitals of Σ-symmetry, the LUMO+4 and LUMO+11, become occupied in addition to the LUMO and LUMO+1, and that the HOMO-2 and HOMO-3, in addition to the HOMO-1 and HOMO, lose occupation. Given that LR-TDDFT is a perturbative method, and field strengths of 0.01 a.u. or greater are not in the perturbative regime, observing additional symmetry-allowed single-orbital transitions within a given excitation is reasonable. However, it is unclear how or whether these additional single-particle excitations play an important role in the adsorbate activation process, as the population data is not available in the case of the full RT-TDDFT/ED simulations.

Electron-only time-dependent dipole moment and Hirshfeld charge data is also available from the electron-only calculations (figures A.9-A.10). These quantities generally resemble their electron-nuclear counterparts at the start of the simulation, which is when the electron-only and electron-nuclear systems most closely resemble each other. Comparison of the electron-only Hirshfeld charge data with the electron-nuclear data in the first 20 fs reveals that nuclear motion plays a role in the charge transfer process (figures A.9-A.10). Whereas electron-only charge oscillations tend to rebound to neutral or near-neutral charge, the simulations with mixed

electron/nuclear dynamics tend to maintain a charge separation, i.e. demonstrate less "charge rebounding." Thus, nuclear motion may aid in maintaining the initial charge separation.

4.4.3 Parallel Ag_8H_2 at 0.03 a.u. Electric Field Strength

While the N_2 results show dissociation and/or activation as a function of electric field strength, the N_2 molecule itself has a relatively complicated electronic structure, and the interplay between the electronic structure and dynamics outcomes is complex. In an effort to simplify the molecular electronic structure aspect of the model, we investigate Ag_8H_2 systems. In the H_2 case, any dissociative route likely results in population of the H_2 σ* orbital (or orbitals with H_2 σ* character). Similar to Ag_8N_2, we first provide the LR-TDDFT results, the RT-TDDFT/ED and electron-only RT-TDDFT calculations, and their analyses, for the parallel-oriented H_2 excited at the longitudinal plasmon resonance with an electric field strength of 0.03 a.u. We first compute the LR-TDDFT absorption spectrum (Figure 4.7) and examine the single-particle transitions involved in the longitudinal and transverse plasmon peaks.

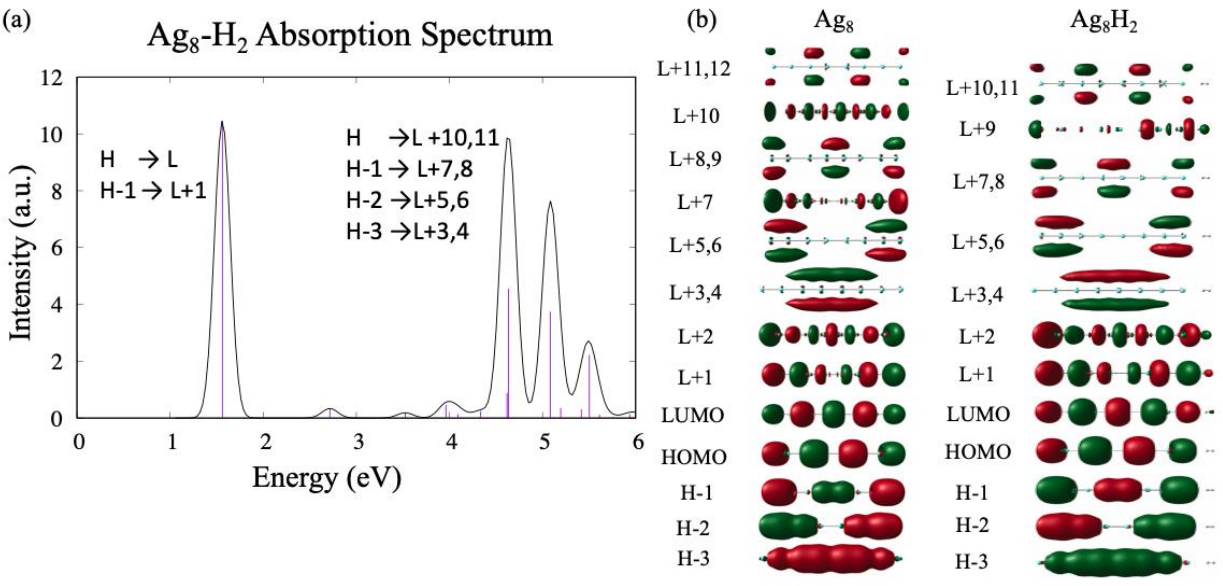

Figure 4.7 (a) LR-TDDFT absorption spectrum, with a.u. denoting arbitrary units. (b) The corresponding molecular orbitals of parallel-oriented Ag_8H_2.

Between Ag_8N_2 and Ag_8H_2, the symmetry of the transitions involved do not change for either the longitudinal or transverse modes, with the longitudinal mode comprised of $\Sigma_4 \rightarrow \Sigma_5$ and $\Sigma_3 \rightarrow \Sigma_6$ transitions (HOMO → LUMO and HOMO – 1 → LUMO + 1), and the transverse mode comprised of the $\Sigma_n \rightarrow \Pi_n$ transitions, where n = 1, 2, 3, 4. The energies of the two quantum plasmon peaks in Ag_8H_2 (Figure 4.7) are slightly shifted from the Ag_8N_2 case (Figure 4.2), with the longitudinal mode occurring at 1.44 eV and the transverse mode at 4.66 eV for the parallel oriented H_2 system (1.46 eV and 4.64 eV for the perpendicularly oriented H_2 case, respectively). Unlike the Ag_8N_2 case, the unoccupied Π orbitals contain no contribution from H_2-based atomic orbitals. That is, no hybridization of an H_2 π^* orbital is found in the Π orbitals of the system, as expected. Meanwhile, the unoccupied Σ orbitals do retain H_2 σ^* character.

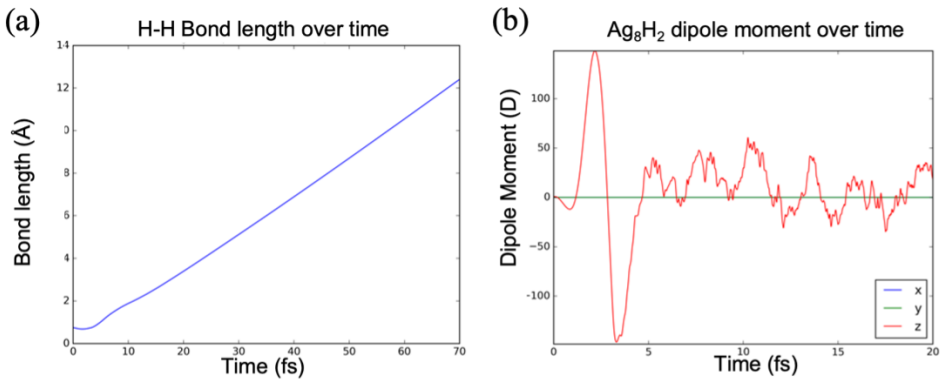

Figure 4.8 (a) H-H bond distance over 70 fs in the RT-TDDFT/ED simulation for parallel-oriented Ag_8H_2 excited at the longitudinal plasmon frequency with 0.03 a.u. electric field strength. Bond distances for all Ag_8H_2 cases are shown in Figure A.11. (b) Time-dependent dipole corresponding to the equivalent electron-only RT-TDDFT calculation.

For the sake of comparison with the Ag_8N_2 case presented, we focus on the parallel-oriented adsorbate configuration. However, unlike Ag_8N_2, the orientation for Ag_8H_2 with H_2

perpendicular to the wire is lower in energy by -0.037 eV. On plotting the H-H bond distance over time, we see rapid dissociation occur soon after the onset of the electric field, with the two H atoms over 12 Å apart by 70 fs (Figure 4.8a). This is unlike the analogous Ag_8N_2 result, where the N_2 achieves a maximum of 0.32 Å bond elongation compared to the N_2 equilibrium bond, but ultimately does not dissociate within the simulation time frame (Figure 4.3). The accompanying Fourier transform for this Ag_8H_2 calculation is not shown, as the H_2 bond length does not demonstrate any oscillatory behavior throughout the course of the simulation. The time-dependent dipole moment (Figure 4.8b) appears similar to the analogous N_2 case (Figure 4.4) within the first 20 fs, especially in that a large electron density displacement is evident in the first few fs of the calculation. The time-dependent electron-only dipole moment is shown for all Ag_8H_2 cases in Figure A.12.

Similar to the N_2 case, we partition the RT-TDDFT/ED Hirshfeld charges into Ag and H (Figure 4.9a) and Ag, H1, H2 (Figure 4.9b), where H1 is the H atom closest to the wire at the start of the simulation. The charge profile of the Ag_8N_2 system (Figure 4.6) appears significantly different than Ag_8H_2. In the Ag_8H_2 case, a large surge in charge separation occurs around 3 fs. The Ag_8 subsystem gains 1.2 *e*- positive charge as the H_2 subsystem gains 1.2 *e*- negative charge, where the peak charge of -1.22 (units of *e*- used for all charges) is obtained at 3.4 fs. Thus, charge transfer occurs very soon after the start of the simulation, and at 5 fs, the H_2 bond length is 1.01 Å, or 135% of the equilibrium bond length. The equivalent Ag_8N_2 system does not obtain its maximum adsorbate charge until 15.3 fs, where it reaches -0.94 on the N_2. The Ag_8N_2 system achieves its maximum bond length of 1.44 Å at 61.6 fs, at which point the charge on N_2 is -0.25. In the first 10 fs of the calculations, the charge difference between H1 and H2 is much less than that of N1 and N2. However, in cases in which the H_2 activates but does not dissociate, the

charge oscillations between H1 and H2 follow similar trends to that of the non-dissociated N1 and N2 (figures A.13-A.14). Despite very different methodology, we find that our H_2 charge transfer results are consistent with those found in Ref. 34, in that each finds the number of electrons increasing on the H_2 in the first 15 fs.

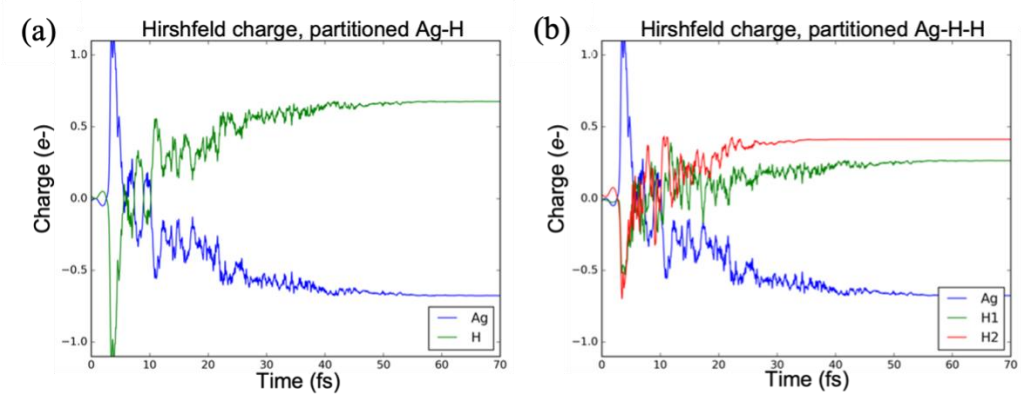

Figure 4.9 Hirshfeld charge over 70 fs of RT-TDDFT/ED simulation. (a) shows partitioning of charge into Ag and H subsystems. (b) plots the charge for each H atom separately.

The orbital populations can be extracted from the electron-only dynamics. We stress again that, soon after the start of the simulation, the electron-only dynamics will not mirror RT-TDDFT/ED results, especially in the case of a quickly dissociating adsorbate. Thus, we present only the first 20 fs of orbital populations, noting that, in this particular case, even by 20 fs, the H_2 in the Ehrenfest dynamics calculation has achieved an inter-hydrogen distance of 3.49 Å, over quadruple the equilibrium bond length. Similar to the Ag_8N_2 case, we see rapid initial population of the unoccupied Σ-geometry orbitals, and simultaneous depletion of the corresponding Σ occupied orbitals (Figure 4.10). Like Ag_8N_2 (Figure 4.5), we see more Σ-type orbitals involved than is suggested by the LR-TDDFT calculation, which is due to the non-perturbative strength of the electric field.

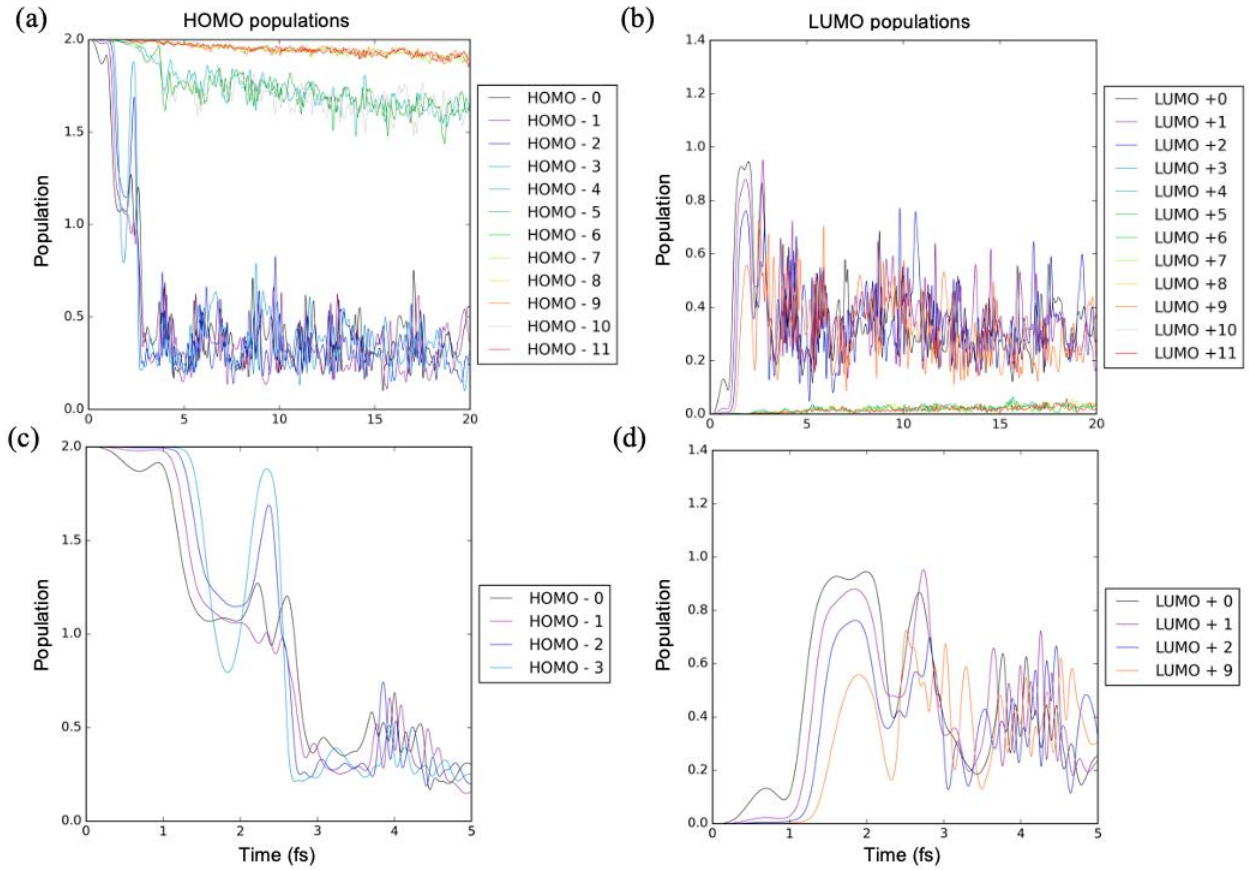

Figure 4.10 Time-dependent orbital populations for the corresponding 0.03 a.u. electric field, longitudinally excited Ag_8H_2 system electron-only RT-TDDFT calculation. (a) depicts population of initially occupied molecular orbitals, while (b) depicts the population of initially unoccupied orbitals. The HOMO and LUMO keys correspond to the orbitals in Figure 4.7b. Plots for all simulations are located in figures A.15-A.18. (c) and (d) show the first 5 fs of orbital populations of the most affected occupied and unoccupied molecular orbitals respectively.

In general, the markers of activation are present in both the Ag_8N_2 and Ag_8H_2 cases. The electron-only orbital populations appear especially similar, even in the time at which population occurs and the degree of population. The sudden occupation of the Σ-type unoccupied orbitals, the large shift in dipole moment, and the charge transfer from the wire to the adsorbate are present in both the Ag_8N_2 and Ag_8H_2 cases. It is possible that H_2 dissociation occurs with the

0.03 a.u. applied field whereas N_2 dissociation does not because H_2 is more weakly bound with a single σ bond, as opposed to the triple bond of N_2.

4.4.4 Ag_8H_2 Electron- and Electron-Nuclear Dynamics

Similar to the Ag_8N_2 case, we now focus on the average bond length and frequency data of the Ag_8H_2 RT-TDDFT/ED simulations, alongside the H_2 charge and $|q_{H1} - q_{H2}|$ charge difference data. Table 4.5 contains the average bond length of H_2 across the RT-TDDFT/ED simulations. In the H_2 case, the longitudinal plasmon excitation of the wire with parallel-oriented H_2 results in dissociation at the 0.03, 0.04, and 0.05 a.u. field strengths. The longitudinal plasmon excitation of the wire with perpendicularly oriented H_2 results in dissociation for the 0.05 a.u. electric field case. This contrasts with the analogous N_2 calculations, where only the parallel-longitudinal 0.05 a.u. case achieves full dissociation within 70 fs (Table 4.1). The trend of the longitudinal plasmon resonance activating significantly more than the transverse resonance holds for H_2 as well as N_2, as does the orientation trend that the parallel adsorbate typically activates more than the perpendicular adsorbate.

Table 4.5 Average H-H interatomic distance across 70 fs of RT-TDDFT/ED simulation. Corresponding plots are found in Figure A.11.

	field strength (a.u.)	0.05	0.04	0.03	0.02	0.01	0.001
Adsorbate orientation and electric field polarization	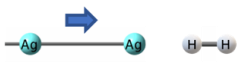	11.50 Å	7.89 Å	7.83 Å	0.81 Å	0.79 Å	0.76 Å
	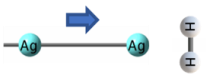	4.00 Å	0.88 Å	0.83 Å	0.77 Å	0.90 Å	0.75 Å
	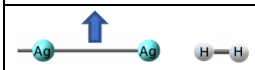	0.84 Å	0.83 Å	0.79 Å	0.78 Å	0.76 Å	0.76 Å
	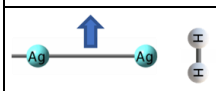	0.85 Å	0.90 Å	0.77 Å	0.76 Å	0.75 Å	0.75 Å

H_2 vibrational activation (Table 4.6) sees similar trends to the N_2 vibrational activation (Table 4.2) in that, as the electric field increases, the H_2 vibrational frequency tends to decrease. In both the N_2 and H_2 case, with our data, it is impossible to ascertain whether or not the decreases in vibrational frequency are due to excitement onto higher vibrational states (e.g. in the anharmonic well of the ground electronic state, which leads to lower vibrational frequencies as the vibrational energy level increases), or due to excitement onto higher electronic states, which tend to have shallower wells and will result in the same outcome. RT-TDDFT/ED calculations do not allow for analysis of either of these quantities. Thus, we can observe the decreasing frequency with increasing electric field and correlate this to the increase in adsorbate activation, but cannot assert whether this activation is vibrational or electronic in nature.

Table 4.6 H_2 vibrational frequency (cm^{-1}) across 70 fs RT-TDDFT/ED simulation.

	field strength (a.u.)	0.05	0.04	0.03	0.0	0.01	0.001
Adsorbate orientation and electric field polarization	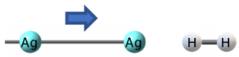	-	-	-	3600	3600	4100
	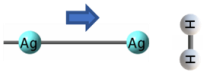	-	2900	4000	4100	3400	4000
	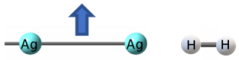	3300	3300	3700	4000	4400	4000
	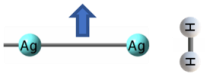	3400	3100	3900	4100	4000	4100

The maximum charge obtained on the H_2 subsystem (Table 4.7) does not correlate as strongly to H_2 activation as the maximum charge on N_2 tracks with N_2 activation (Table 4.3). The maximum charge difference between the two H atoms also correlates less strongly with activation than the N_2 case. For each quantity, there is a general trend that for a given field

strength, the parallel-longitudinal simulations gain the most charge and obtain the largest charge difference (Table 4.8), followed by perpendicular-longitudinal, then parallel-transverse, and finally perpendicular-transverse. This is consistent with the N_2 results. However, the trend in correlation between electric field strength and maximum adsorbate charge and maximum adsorbate charge difference is less clear in the H_2 case. While the Hirshfeld charge analysis reveals charge transfer occurring in both the N_2 and H_2 cases, H_2 tends to pick up a smaller maximum charge and maximum charge difference, while still activating more readily. This may be due in part to N_2's increased ability to house additional negative charge relative to H_2, given its more complex electronic structure and availability of lower-lying unoccupied orbitals. N_2 may have more channels of activation and dissociation due to these lower lying orbitals, as well as its increased orbital hybridization into the wire relative to H_2. A comparison of electron-only and electron-nuclear Hirshfeld charges for the first 20 fs of simulation can be found in figures A.19-A.20. The difference in degree of "charge rebounding" as discussed for the Ag_8N_2 case in section 4.4.2 appears much less significant in the Ag_8H_2 case. The significant activation of H_2 within 20 fs in the RT-TDDFT/ED results (Figure A.11) more severely limits comparison between the Hirshfeld charges of electron-nuclear and electron-only calculations.

Table 4.7 Maximum negative Hirshfeld charge obtained on the H_2 subsystem across 70 fs of RT-TDDFT/ED simulation. The time at which the maximum charge occurs is listed in Table A.3.

	field strength (a.u.)	0.05	0.04	0.03	0.02	0.01	0.001
Adsorbate orientation and electric field polarization	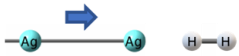	-0.86	-0.67	-1.22	-0.99	-0.61	-0.07
	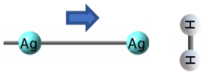	-0.55	-0.50	-0.65	-0.60	-0.52	-0.08
	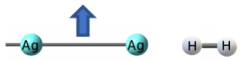	-0.32	-0.30	-0.17	-0.16	-0.05	0.00
	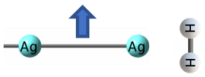	-0.24	-0.47	-0.19	-0.15	-0.05	0.00

Table 4.8 Maximum Hirshfeld charge difference obtained as $|q_{H1} - q_{H2}|$ across 70 fs of RT-TDDFT/ED simulation. The time at which the maximum charge difference occurs is listed in Table A.4.

	field strength (a.u.)	0.05	0.04	0.03	0.02	0.01	0.001
Adsorbate orientation and electric field polarization	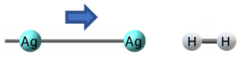	0.48	0.82	0.56	0.28	0.09	0.04
	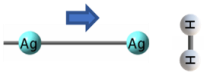	0.40	0.33	0.32	0.15	0.19	0.04
	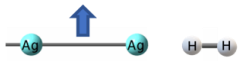	0.30	0.19	0.14	0.11	0.07	-
	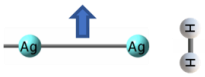	0.20	0.24	0.10	0.10	0.06	-

Examining the average bond length for the parallel-longitudinal case side-by-side (Table 4.9), the H_2 case activates slightly more as a percent of the equilibrium bond length for a given field strength, and more cases result in full dissociation. These results, together, suggest that cleavage of the Σ bond is important in both cases, as the parallel orientation with excitation at the longitudinal resonance promotes symmetry-allowed access to the adsorbate Σ bonds, and the transverse mode, despite allowing easier access to excitation to the H_2 and N_2 σ* orbitals in their

perpendicular orientations, is a weaker excitation than the longitudinal mode. Moreover, the transverse peak is comprised of degenerate x- and y- directional excitations, while the RT-TDDFT/ED calculations excite only one of the two directions, effectively halving the oscillator strength, which may explain why the transverse excitation only minimally activates the adsorbate. We have shown the percent-hybridization of the adsorbate atomic orbitals into the frontier molecular orbitals in tables A.5 and A.6.

Table 4.9 Comparison of average adsorbate bond length in Å across 70 fs of RT-TDDFT/ED simulation between Ag_8H_2 and Ag_8N_2. Parentheses denote the length as a percentage of the equilibrium bond length, shown in the rightmost column.

Field Strength (a.u.)	0.05	0.04	0.03	0.02	0.01	0.001	0.00
Ag_8H_2	11.50 (n/a)	7.89 (n/a)	7.83 (n/a)	0.81 (109%)	0.79 (107%)	0.76 (103%)	0.74
Ag_8N_2	2.47 (n/a)	1.41 (126%)	1.30 (116%)	1.21 (108%)	1.16 (103%)	1.13 (101%)	1.12

4.5 Conclusion

We have examined an array of real-time dynamics calculations of Ag atomic wire-adsorbate systems, analyzing both Ehrenfest dynamics and electron-only dynamics of these systems. We examine adsorbate orientations perpendicular and parallel to the wire, and we examine excitations at the longitudinal and transverse plasmon energies. The adsorbates examined are H_2 and N_2, where we find that H_2 generally activates or dissociates more readily than N_2 for the same electric field, adsorbate orientation, and excitation energy. For all cases, excitation at the longitudinal mode activates the adsorbate considerably more than the transverse mode. The degree of activation of adsorbate depends on the strength of the electric field, where electric field strengths of 0.05, 0.04, 0.03, 0.02, 0.01, and 0.001 a.u. are examined. Through

Hirshfeld population analysis, we observe charge transfer from the wire to the adsorbate. In the N_2 case, the degree of charge transfer tracks generally with the strength of the electric field. The same trend does not hold for the H_2 case, which may be due to the more limited electronic structure of H_2, which has fewer channels in which to gain additional negative charge. In each case, we can observe the formation of an adsorbate transient negative ion. We postulate that adsorbate Σ bond cleavage is critical in both cases. In the H_2 case, this is the only dissociation channel. In the N_2 case, the dependence on the parallel orientation and the longitudinal excitation suggests that Σ bond cleavage plays a pivotal role. In the parallel case, we observe significant charge differences between the nitrogen atom closest to the atomic wire and the nitrogen atom further from the wire, which may aid in dissociation.

4.6 Acknowledgments

We gratefully acknowledge David Lingerfelt and Xiaosong Li for the RT-TDDFT and RT-TDDFT/ED code. This material is based on work supported by the Department of Energy under grant DE-SC0012273. O.H. is supported by the Department of Energy Computational Science Graduate Fellowship under grant number DE-SC0019323. The computing for this project was performed on the Beocat Research Cluster at Kansas State University, which is funded in part by NSF grants CHE-1726332, CNS-1006860, EPS-1006860, and EPS-0919443.

4.7 References

(1)) Robatjazi, H.; Yuan, L.; Yuan, Y.; Halas, N. J. Heterogeneous Plasmonic Photocatalysis: Light-Driven Chemical Reactions Introduce a New Approach to Industrially-Relevant Chemistry. In *Emerging Trends in Chemical Applications of Lasers*; ACS Symposium Series; American Chemical Society, 2021; Vol. 1398, pp 363–387.

(2) Zhang, Z.; Zhang, C.; Zheng, H.; Xu, H. Plasmon-Driven Catalysis on Molecules and Nanomaterials. *Acc. Chem. Res.* **2019**, *52*, 2506–2515.

(3) Kelly, K. L.; Coronado, E.; Zhao, L. L.; Schatz, G. C. The Optical Properties of Metal Nanoparticles: The Influence of Size, Shape, and Dielectric Environment. *J. Phys. Chem. B* **2003**, *107*, 668–677.

(4) Gellé, A.; Jin, T.; de la Garza, L.; Price, G. D.; Besteiro, L. V.; Moores, A. Applications of Plasmon-Enhanced Nanocatalysis to Organic Transformations. *Chem. Rev.* **2020**, *120*, 986–1041.

(5) Christopher, P.; Linic, S. Engineering Selectivity in Heterogeneous Catalysis: Ag Nanowires as Selective Ethylene Epoxidation Catalysts. *J. Am. Chem. Soc.* **2008**, *130*, 11264–11265.

(6) Zhang, Y.; He, S.; Guo, W.; Hu, Y.; Huang, J.; Mulcahy, J. R.; Wei, W. D. Surface-Plasmon-Driven Hot Electron Photochemistry. *Chem. Rev.* **2018**, *118*, 2927–2954.

(7) Mukherjee, S.; Libisch, F.; Large, N.; Neumann, O.; Brown, L. V.; Cheng, J.; Lassiter, J. B.; Carter, E. A.; Nordlander, P.; Halas, N. J. Hot Electrons Do the Impossible: Plasmon-Induced Dissociation of H_2 on Au. *Nano Lett.* **2013**, *13*, 240–247.

(8) Yu, S.; Wilson, A. J.; Heo, J.; Jain, P. K. Plasmonic Control of Multi-Electron Transfer and C–C Coupling in Visible-Light-Driven CO2 Reduction on Au Nanoparticles. *Nano Lett.* **2018**, *18*, 2189–2194.

(9) Wang, F.; Li, C.; Chen, H.; Jiang, R.; Sun, L.-D.; Li, Q.; Wang, J.; Yu, J. C.; Yan, C.-H. Plasmonic Harvesting of Light Energy for Suzuki Coupling Reactions. *J. Am. Chem. Soc.* **2013**, *135*, 5588–5601.

(10) Lee, J.; Mubeen, S.; Ji, X.; Stucky, G. D.; Moskovits, M. Plasmonic Photoanodes for Solar Water Splitting with Visible Light. *Nano Lett.* **2012**, *12*, 5014–5019.

(11) Marimuthu, A.; Zhang, J.; Linic, S. Tuning Selectivity in Propylene Epoxidation by Plasmon Mediated Photo-Switching of Cu Oxidation State. *Science* **2013**, *339*, 1590–1593.

(12) Christopher, P.; Xin, H.; Linic, S. Visible-Light-Enhanced Catalytic Oxidation Reactions on Plasmonic Silver Nanostructures. *Nat. Chem.* **2011**, *3*, 467–472.

(13) Carretero-Palacios, S.; Jiménez-Solano, A.; Míguez, H. Plasmonic Nanoparticles as Light-Harvesting Enhancers in Perovskite Solar Cells: A User's Guide. *ACS Energy Lett.* **2016**, *1*, 323–331.

(14) Jang, Y. H.; Jang, Y. J.; Kim, S.; Quan, L. N.; Chung, K.; Kim, D. H. Plasmonic Solar Cells: From Rational Design to Mechanism Overview. *Chem. Rev.* **2016**, *116*, 14982–15034.

(15) Wang, Q.; Domen, K. Particulate Photocatalysts for Light-Driven Water Splitting: Mechanisms, Challenges, and Design Strategies. *Chem. Rev.* **2020**, *120*, 919–985.

(16) Le Ru, E. C.; Etchegoin, P. G. Single-Molecule Surface-Enhanced Raman Spectroscopy. *Annu. Rev. Phys. Chem.* **2012**, *63*, 65–87.

(17) Saha, K.; Agasti, S. S.; Kim, C.; Li, X.; Rotello, V. M. Gold Nanoparticles in Chemical and Biological Sensing. *Chem. Rev.* **2012**, *112*, 2739–2779.

(18) Mayer, K. M.; Hafner, J. H. Localized Surface Plasmon Resonance Sensors. *Chem. Rev.* **2011**, *111*, 3828–3857.

(19) Aragay, G.; Pons, J.; Merkoçi, A. Recent Trends in Macro-, Micro-, and Nanomaterial-Based Tools and Strategies for Heavy-Metal Detection. *Chem. Rev.* **2011**, *111*, 3433–3458.

(20) Yadid, M.; Feiner, R.; Dvir, T. Gold Nanoparticle-Integrated Scaffolds for Tissue Engineering and Regenerative Medicine. *Nano Lett.* **2019**, *19*, 2198–2206.

(21) Huang, X.; Jain, P. K.; El-Sayed, I. H.; El-Sayed, M. A. Plasmonic Photothermal Therapy (PPTT) Using Gold Nanoparticles. *Lasers Med. Sci.* **2007**, *23*, 217.

(22) Huang, X.; El-Sayed, I. H.; Qian, W.; El-Sayed, M. A. Cancer Cell Imaging and Photothermal Therapy in the Near-Infrared Region by Using Gold Nanorods. *J. Am. Chem. Soc.* **2006**, *128*, 2115–2120.

(23) Liang, C.; Lu, Z.-A.; Wu, J.; Chen, M.-X.; Zhang, Y.; Zhang, B.; Gao, G.-L.; Li, S.; Xu, P. Recent Advances in Plasmon-Promoted Organic Transformations Using Silver-Based Catalysts. *ACS Appl. Mater. Interfaces* **2020**, *12*, 54266–54284.

(24) Christopher, P.; Moskovits, M. Hot Charge Carrier Transmission from Plasmonic Nanostructures. *Annu. Rev. Phys. Chem.* **2017**, *68*, 379–398.

(25) Boerigter, C.; Aslam, U.; Linic, S. Mechanism of Charge Transfer from Plasmonic Nanostructures to Chemically Attached Materials. *ACS Nano* **2016**, *10*, 6108–6115.

(26) Boerigter, C.; Campana, R.; Morabito, M.; Linic, S. Evidence and Implications of Direct Charge Excitation as the Dominant Mechanism in Plasmon-Mediated Photocatalysis. *Nat. Commun.* **2016**, *7*, 10545.

(27) Ma, J.; Wang, Z.; Wang, L.-W. Interplay between Plasmon and Single-Particle Excitations in a Metal Nanocluster. *Nat. Commun.* **2015**, *6*, 1–11.

(28) Zhang, R.; Bursi, L.; Cox, J. D.; Cui, Y.; Krauter, C. M.; Alabastri, A.; Manjavacas, A.; Calzolari, A.; Corni, S.; Molinari, E.; et al. How To Identify Plasmons from the Optical Response of Nanostructures. *ACS Nano* **2017**, *11*, 7321–7335.

(29) Bernadotte, S.; Evers, F.; Jacob, C. R. Plasmons in Molecules. *J. Phys. Chem. C* **2013**, *117*, 1863–1878.

(30) Zohar, N.; Chuntonov, L.; Haran, G. The Simplest Plasmonic Molecules: Metal Nanoparticle Dimers and Trimers. *J. Photochem. Photobiol. C Photochem. Rev.* **2014**, *21*, 26–39.

(31) Guidez, E. B.; Aikens, C. M. Plasmon Resonance Analysis with Configuration Interaction. *Phys. Chem. Chem. Phys.* **2014**, *16*, 15501–15509.

(32) Guidez, E. B.; Aikens, C. M. Quantum Mechanical Origin of the Plasmon: From Molecular Systems to Nanoparticles. *Nanoscale* **2014**, *6*, 11512–11527.

(33) Wu, Q.; Zhou, L.; Schatz, G. C.; Zhang, Y.; Guo, H. Mechanistic Insights into Photocatalyzed H_2 Dissociation on Au Clusters. *J. Am. Chem. Soc.* **2020**, *142*, 13090–13101.

(34) Zhang, Y.; Nelson, T.; Tretiak, S.; Guo, H.; Schatz, G. C. Plasmonic Hot-Carrier-Mediated Tunable Photochemical Reactions. *ACS Nano* **2018**, *12*, 8415–8422.

(35) Hull, O. A.; Lingerfelt, D. B.; Li, X.; Aikens, C. M. Electronic Structure and Nonadiabatic Dynamics of Atomic Silver Nanowire–N_2 Systems. *J. Phys. Chem. C* **2020**, *124*, 20834–20845.

(36) Yan, L.; Ding, Z.; Song, P.; Wang, F.; Meng, S. Plasmon-Induced Dynamics of H_2 Splitting on a Silver Atomic Chain. *Appl. Phys. Lett.* **2015**, *107*, 083102.

(37) Zhang, Y.; Yan, L.; Guan, M.; Chen, D.; Xu, Z.; Guo, H.; Hu, S.; Zhang, S.; Liu, X.; Guo, Z.; et al. Indirect to Direct Charge Transfer Transition in Plasmon-Enabled CO_2 Photoreduction. *Adv. Sci.* **2022**, *9*, 2102978.

(38) Kumar, P. V.; Rossi, T. P.; Kuisma, M.; Erhart, P.; Norris, D. J. Direct Hot-Carrier Transfer in Plasmonic Catalysis. *Faraday Discuss.* **2019**, *214*, 189–197.

(39) Rossi, T. P.; Kuisma, M.; Puska, M. J.; Nieminen, R. M.; Erhart, P. Kohn–Sham Decomposition in Real-Time Time-Dependent Density-Functional Theory: An Efficient Tool for Analyzing Plasmonic Excitations. *J. Chem. Theory Comput.* **2017**, *13*, 4779–4790.

(40) Libisch, F.; Cheng, J.; Carter, E. A. Electron-Transfer-Induced Dissociation of H_2 on Gold Nanoparticles: Excited-State Potential Energy Surfaces via Embedded Correlated Wavefunction Theory. *Z. Für Phys. Chem.* **2013**, *227*, 1455–1466.

(41) Gieseking, R. L. M. Plasmons: Untangling the Classical, Experimental, and Quantum Mechanical Definitions. *Mater. Horiz.* **2022**, *9*, 25–42.

(42) Dillon, A. D.; Gieseking, R. L. M. Evolution of Plasmon-like Excited States in Silver Nanowires and Nanorods. *J. Chem. Phys.* **2022**, *156*, 074301.

(43) Rohrdanz, M. A.; Martins, K. M.; Herbert, J. M. A Long-Range-Corrected Density Functional That Performs Well for Both Ground-State Properties and Time-Dependent Density Functional Theory Excitation Energies, Including Charge-Transfer Excited States. *J. Chem. Phys.* **2009**, *130*, 054112.

(44) Hay, P. J.; Wadt, W. R. Ab Initio Effective Core Potentials for Molecular Calculations. Potentials for the Transition Metal Atoms Sc to Hg. *J. Chem. Phys.* **1985**, *82*, 270–283.

(45) Hay, P. J.; Wadt, W. R. Ab Initio Effective Core Potentials for Molecular Calculations. Potentials for K to Au Including the Outermost Core Orbitals. *J. Chem. Phys.* **1985**, *82*, 299–310.

(46) Wadt, W. R.; Hay, P. J. Ab Initio Effective Core Potentials for Molecular Calculations. Potentials for Main Group Elements Na to Bi. *J. Chem. Phys.* **1985**, *82*, 284–298.

(47) Rabilloud, F. Description of Plasmon-like Band in Silver Clusters: The Importance of the Long-Range Hartree-Fock Exchange in Time-Dependent Density-Functional Theory Simulations. *J. Chem. Phys.* **2014**, *141*, 144302.

(48) Rabilloud, F. Assessment of the Performance of Long-Range-Corrected Density Functionals for Calculating the Absorption Spectra of Silver Clusters. *J. Phys. Chem. A* **2013**, *117*, 4267–4278.

(49) Silverstein, D. W.; Jensen, L. Assessment of the Accuracy of Long-Range Corrected Functionals for Describing the Electronic and Optical Properties of Silver Clusters. *J. Chem. Phys.* **2010**, *132*, 194302.

(50) Moore, J. E.; Morton, S. M.; Jensen, L. Importance of Correctly Describing Charge-Transfer Excitations for Understanding the Chemical Effect in SERS. *J. Phys. Chem. Lett.* **2012**, *3*, 2470–2475.

(51) Frisch, M. J.; Trucks, G. W.; Schlegel, H. B.; Scuseria, G. E.; Robb, M. A.; Cheeseman, J. R.; Scalmani, G.; Barone, V.; Petersson, G. A.; Nakatsuji, H., et al. *Gaussian 16*, Revision C.01; Gaussian, Inc.: Wallingford, CT, 2016.

(52) Li, X.; Govind, N.; Isborn, C.; DePrince, A. E.; Lopata, K. Real-Time Time-Dependent Electronic Structure Theory. *Chem. Rev.* **2020**, *120*, 9951–9993.

(53) Li, X.; Tully, J. C.; Schlegel, H. B.; Frisch, M. J. Ab Initio Ehrenfest Dynamics. *J. Chem. Phys.* **2005**, *123*, 084106.

(54) Kar, T.; Sannigrahi, A. B. Effect of Basis Set on Mulliken and Löwdin Atomic Charges, Bond Orders and Valencies of Some Polar Molecules. *J. Mol. Struct. THEOCHEM* **1988**, *165*, 47–54.

(55) Habteyes, T. G. Anions as Intermediates in Plasmon Enhanced Photocatalytic Reactions. *J. Phys. Chem. C* **2020**, *124*, 26554–26564.

Chapter 5 - H_2 on Au(111)

5.1 Introduction

In plasmon-mediated photocatalysis, chemical interface damping (CID) refers to the phenomenon in which a nearby adsorbate modifies the behavior of the plasmon modes of a nanoparticle.[1–4] CID is thought to play an important role in plasmon-mediated photocatalysis, as it allows for direct excitation from the plasmon resonance to an adsorbed small molecule.[4] In addition to CID, an indirect mechanism in which the plasmon mode facilitates molecular activation by first decaying into hot electrons and hot holes, which then transfer to the molecule, also enables plasmon-mediated photocatalysis, and has received considerable attention.[5–12] The indirect mechanism is thought to be inefficient because the hot electrons relax quickly via electron-electron scattering, which prevents their transfer to the small molecule.[12,13] In 2015, Wu et. al demonstrated that plasmon excitation can lead to direct transfer of an electron to the empty orbitals of the adsorbate, a process that yielded a quantum efficiency of 24% in their study.[1] With this result came a resurgence of work investigating CID, which remains relatively poorly understood. Link and co-workers note in ref. [14] that CID is "often simply invoked when all other explanations fail."[14] Thus, more investigation is required.

In chapters 3 and 4, we investigate plasmon-mediated photocatalysis directly in the sense that we obtain real-time coupled nuclear-electron simulation data that demonstrates activation or dissociation of a small molecule upon excitation of the plasmon resonance mode of a nearby atomic Ag wire. In those works, we found that significant small molecule hybridization into the wire molecular orbitals that participate in the quantum plasmon excitations was likely not the primary driver of activation, since the systems in which large amounts of hybridization occurred were the systems that activated the least. Such a result does not imply that CID is not present or

important in those cases, or that the indirect mechanism is the definitive and sole cause of activation, only that more investigation is required. Thus, we seek to approach the problem of CID from a different direction.

We are interested in exploring how the presence of a small molecule chemically damps the plasmon modes of a metal. More specifically, we want to study how the presence of H_2 at the beginning and ending orientations in a dissociative adsorption process modifies the plasmon modes of the Au(111) surface that the H_2 sits atop. We can investigate such a system via computation of the RPA polarizability, from which we can obtain a simulated electron energy loss spectrum (EELS).[15] Depending on the system, the low-loss region of EELS contains excitations of the surface plasmon, the bulk plasmon, and interband transitions.[16] Thus, investigation of low-loss EELS of the H_2-Au(111) system informs us of many electronic features that may be relevant to plasmon-mediated photocatalysis. Traditionally, plasmons are well-described by electromagnetic theory that treats the surrounding chemical environment as an effective medium.[16–18] However, it is also known that the presence of adsorbates has a strong impact on the electron density-sensitive surface plasmon modes.[19]

We must be somewhat careful about language here, and what precisely we are, and are not, studying when we compute simulated EELS of these H_2-Au(111) systems. Conceptually, the excitation of the surface plasmon resonance of a nanoparticle causes a collective oscillation of the free surface electrons. The free surface electrons are collectively displaced from the particle, then experience a restoring force due to the coulombic attraction between the positive charges of the nanoparticle nuclei and the displaced electron density. This displacement and the subsequent restoring force give rise to the classic "sloshing" picture of the localized surface plasmon resonance of a nanoparticle (LSPR). In a nanoparticle, these localized surface plasmon

resonances are standing waves (i.e. non-propagating) that decay to zero away from the particle, and the frequencies of the standing waves are related to the morphology of the particle, somewhat analogous to the particle-in-a-box problem (e.g. the diameter of the particle directly influences the LSPR frequency). Clearly, we do not have such a confinement effect when modeling a surface with periodic boundary conditions. However, recent work has revealed that some nanoparticles can indeed host propagating plasmons, like surface plasmon polaritons, in addition to these standing-wave surface plasmon resonances, and additionally has shown that nanoparticles can host bulk plasmons along with surface plasmons.[20]

Bulk plasmons can be described with much the same qualitative picture as above, and are often discussed in terms of a plasma model. Plasma is a medium comprised of equal amounts of positive and negative charge, with at least one of the two free to move. Since a metal has a sea of free valence electrons interacting with fixed, positively charged nuclei, we can describe the collective behavior of metals in these terms. If we displace a small zone of electrons, we induce a uniform charge imbalance on account of this displaced electron density, and an excess positive charge density also appears as a result. This generates an electric field, which forces the electron cloud to move as a whole on account of the fact that the nuclei, being fixed in place, cannot move.[21] This electron density oscillation is called a plasma oscillation, and a quantum of this oscillation is called a plasmon. The difference between this picture of a plasmon in a bulk material and a nanoparticle is that, in the bulk material, the plasmon is a longitudinal wave, while the LSPR is a standing wave. Longitudinal waves cannot couple to transverse waves, like electromagnetic waves. Thus, unlike the LSPR of nanoparticles, bulk plasmons cannot be excited by light[21] but can be excited by a moving charged particle, e.g. what is done in experimental EELS.

The description above corresponds to the Drude model of plasmons. The Drude model has found success in describing simple metals, but breaks down for noble metals on account of their d-band structure.[22] In the Drude model, the bulk plasmon frequency is given by $\omega_p(\boldsymbol{q} = 0) = \sqrt{\frac{4\pi e^2 n}{m}}$, where *e* is the electron charge, *m* is the mass of the electron, and *n* is the electron density. The surface plasmon is given as $\omega_{sp} = \frac{\omega_p}{\sqrt{2}}$, and the dielectric function is given as $\varepsilon(\omega) = 1 - \frac{{\omega_p}^2}{\omega(\omega + i\gamma)}$, with γ the damping time.[23] One can combine this term with that of a bound Lorentz oscillator to develop a phenomenological model of how the plasmon mode shifts in relation to an optical absorption band, which we discuss in the context of d-bands in section 5.3.3.[22,24,25] While the Drude model is extremely useful for developing a conceptual understanding of plasmons, it fails for noble metals in practice.

EELS can measure both surface and bulk plasmons. Again, we must be careful with terminology and what exactly we measure with RPA EELS. The term "surface plasmon" is often used interchangeably with "surface plasmon polariton." A surface plasmon is, like a bulk plasmon, a charge density oscillation. A surface plasmon occurs at the surface of a material, and unlike bulk plasmons, surface plasmons can couple to photons, and hence can form surface plasmon polaritons, which is a quasiparticle arising from the coupling of light with the surface plasmon.[18,26,27] The theoretical study of surface plasmon polaritons is a different problem than the study only of the surface plasmons,[28] i.e. the collective charge density oscillations of the metal surface, though the two physical phenomena are closely related.

In experimental EELS of metals, we may find both the bulk and surface plasmon peaks, where the latter become prominent in thin samples or small particles, with the surface plasmon peak occurring at lower energy than the bulk.[29] Additionally, noble metal surfaces have been

found to support another type of surface plasmon, called an acoustic surface plasmon.[30,31] While conventional surface plasmons have a finite energy for all wave vectors, the energy of the acoustic surface plasmon energy approaches zero as the wave vector **q** approaches zero.[32] Finally, around the same energy regions as bulk and surface plasmon peaks appear, interband transitions appear. Interband transitions have many interesting effects on the plasmon modes of materials. Each of these types of peaks appear in the EELS "low loss region," which is defined to be the region of the spectrum from 0 eV to about 50 eV.[33] We discuss these peaks in more depth in section 5.3.2.

Theoretically, we can generate an EEL spectrum as -Im($\varepsilon_M^{-1}(\boldsymbol{q},\omega)$), the negative of the inverse of the macroscopic dielectric function. Within the random phase approximation, the macroscopic dielectric function is given by:[34]

$$\varepsilon_M = \frac{1}{\varepsilon_{00}^{-1}(\boldsymbol{q},\omega)} \qquad \text{(Eq. 5.1)}$$

i.e., we take only the **G** = 0**, G′** = 0 components of:

$$\varepsilon_{\boldsymbol{GG'}}^{-1}(\boldsymbol{q},\omega) = \delta_{\boldsymbol{GG'}} + \frac{4\pi}{|\boldsymbol{q}+\boldsymbol{G}|^2}\chi_{\boldsymbol{GG'}}(\boldsymbol{q},\omega) \qquad \text{(Eq. 5.2)}$$

Thus, once we obtain the inverse dielectric, we can directly generate an EEL spectrum. Additional theoretical details are discussed in other sections; please see Chapter 6.1 for more information on how this quantity is obtained in BerkeleyGW and Chapter 2.3.3 for a more general overview of RPA methods.

The wave-vector **q** is an important component of EELS. The limit **q** → 0 is called the long-wavelength limit, and this limit determines the optical properties in the regime accessible to optical and electronic probes.[35] For example, the absorption spectrum is given as Im($\varepsilon_M(\boldsymbol{q}\rightarrow 0,\omega)$.[36] We are interested in the long-wavelength limit; however, difficulties arise in attempting

to compute equation 5.2 directly for **q** = 0 because of the $\frac{1}{|q+G|^2}$ term, which diverges when **G** = **q** = 0, which is the situation we are after. There are a few ways to handle computation of the macroscopic dielectric function in the long-wavelength limit.[15,35,37] In BerkeleyGW, for metals, the code numerically approximates **q** → 0 with the smallest **q** = **k** – **k**′ possible given the choice of k-grid.[15]

We choose specifically to investigate H_2 on Au(111) for a few reasons. First is in the inspiration from the theory (and theoretical follow-up paper) found within the seminal work of Halas, Nordlander, Carter, and co-workers.[38] In this paper, Au nanoparticles of diameters ranging from 5.5 to 21 nm loaded onto a TiO_2 substrate were demonstrated to dissociate H_2 and D_2 to form HD upon excitation of the Au plasmon resonance. A subsequent theory paper was published that built upon the initial theory component of this work.[39] This paper used an embedded correlated wavefunction method to investigate dissociation of H_2 on an Au(111) surface. The authors treated the region of H_2 and nearby Au atoms under a correlated wavefunction scheme, then coupled this to the remainder of the system, which is treated with planewave DFT. Here, the authors mapped out the H_2 dissociation pathway and examined reaction barriers of the process, but did not directly model the interaction of the collective excitations of the surface with the H_2 molecule. In addition to H_2 splitting, Au nanoparticles have been shown to convert CO_2 into methane and ethane under benign conditions, among a number of other interesting catalytic phenomena.[40–42] Finally, the electronic structure of H_2 is the simplest possible electronic structure of a diatomic molecule, on account of H_2 having only two electrons. Thus, as our goal is to develop an understanding of the influence of a nearby adsorbate on the plasmon modes of the Au(111) surface, choosing a simple adsorbate helps to limit the possible scope of influences.

We seek to make use of our subspace summation method developed in Chapter 6. In subspace summation, we can selectively include or exclude which bands are considered in equation 5.2 by specifying which *n* and *n'* enter into the summation for each matrix element of $\chi^{KS}_{\boldsymbol{G},\boldsymbol{G}'}(\boldsymbol{q},\omega)$. Thus, when we obtain the RPA simulated EELS for a particular subspace summation calculation, we examine the EEL spectrum without the influence of the excluded bands, producing a spectrum that arises from interactions of the included bands. We can use this as a tool to systematically investigate the effects that certain types of bands have on certain peaks. Thus, if we can identify which bands contain the most H_2 hybridization, we can attempt to identify how, and to what degree, these particular hybridized peaks influence the EEL spectrum, providing insight into how H_2 hybridization alters the plasmon modes of Au(111).

5.2 Methods

We are interested in three structures: (a) a clean Au(111) surface, (b) Au(111) with H_2 in the bridge-site "starting position," and (c) H in the two top-site positions, the "ending" position (Figure 5.1.a, 5.1.b-c, 5.1.d-e, respectively) in the dissociative adsorption process. To obtain the standard EEL spectrum with all bands included, we first optimize the structure geometries and then obtain mean-field eigenenergies and wavefunctions using the JDFTx program.[43] Then, we feed these inputs into the BerkeleyGW epsilon executable to produce the macroscopic inverse dielectric (eq. 5.1).[15] We plot the results via matplotlib in python.

To obtain the subspace summation EEL spectra, we must first identify bands of interest. To do this, we project the mean-field wavefunctions onto the H and Au atomic orbitals. We visualize these bands with the help of band structure and density of states plots obtained in JDFTx. The high-symmetry k-point path was chosen based on the SeekPath tool.[44,45] Once bands

of interest are identified, we utilize the subspace summation method of Chapter 6.1 to either include or exclude these bands from a subsequent BerkeleyGW epsilon calculation, which allows us to obtain eq. 5.1 of only the specified band subspace.

In order to generate the requisite inputs to obtain the RPA EELS in the BerkeleyGW program, density functional theory calculations are carried out in JDFTx. To obtain the Au(111) surface, bulk Au is relaxed using a Monkhorst-Pack 20 x 20 x 20 k-point grid,[46] 30 Hartree planewave cutoff energy, and 0.1 eV MP-1 smearing,[47] with the PBE functional[48] and SG15 pseudopotential.[49] The relaxed lattice constant is found to be 4.16 Å, in reasonable agreement with experiment (4.07 Å).[50] The Au(111) surface is cut from relaxed bulk Au with the VESTA program.[51] We construct a supercell with three layers of Au, a z-directional vacuum of 13.8 Å and a 1 x 2 surface unit cell. We relax the top two layers of this surface with a 20 x 20 x 1 k-point grid, and otherwise keep the same calculation parameters as the bulk. Like many other theoretical works, we do not account for the herringbone rearrangement that occurs for the Au(111) surface that leads to a to a 22 x $\sqrt{3}$ unit cell.[52] Based on the results of others, we expect that this approximation is reasonable.[32]

Upon obtaining the relaxed Au(111) structure, we create two new structures: the "bridge site" structure by adding the H_2 molecule 4 Å above the central bridge position. Second, for the "top-site" system, we add two H atoms 2.86 Å above the Au(111) surface in the bridge-to-top dissociated positions (Figure 5.1.d-e). These particular structures are chosen based on the DFT potential energy surface-mapping work of H_2 on Au(111) by Wijzenbroek and coworkers.[53] For these two structures, we allow only the H atoms to relax, and otherwise follow the same calculation parameters as the Au(111) case. This allows us to attribute differences in the EELS to electronic effects on account of the presence of the hydrogen without the confounding influence

of geometric changes to the Au(111) surface. To generate the mean-field wavefunction and eigenenergy inputs to the BerkeleyGW program, we compute and converge the first 6100 bands in JDFTx (approx. 50x the number of occupied bands) with an 8 x 8 x 1 k-point grid for each of the three systems.

For the BerkeleyGW Epsilon calculation, we employ the real axis-formalism frequency-dependent method, computing up to 30 eV with a 0.1 eV frequency step and 12.5 Ha cut-off energy. We approximate q_0 as 0.16 1/Å. Using the partial occupation method developed in Chapter 6.2, we employ 0.1 eV smearing in the MP-1 scheme, consistent with the JDFTx DFT input calculations.

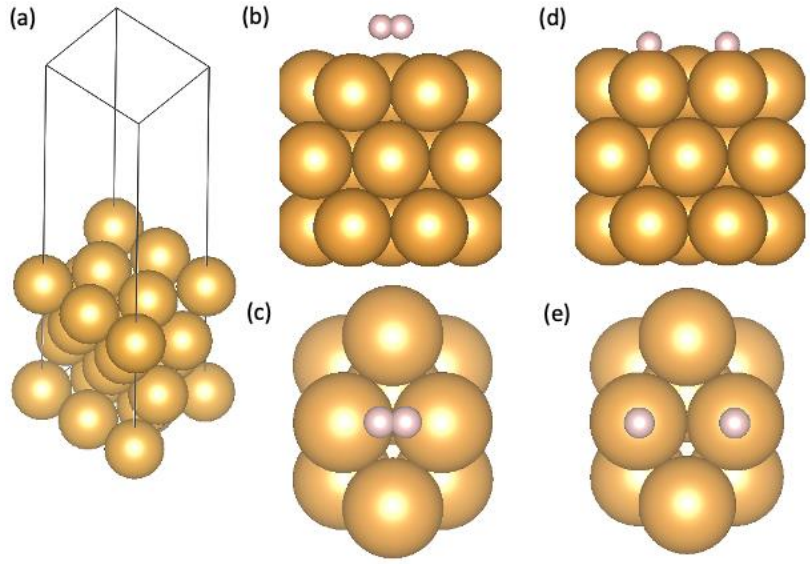

Figure 5.1 (a) View of the Au(111) 1x2 3-layer surface supercell. (b) Side-view of "bridge position" structure. (c) Cropped top-down view of "bridge position" structure. (d) Side view of "top-site position" structure. (e) Cropped top-down view of "top-site position structure".

5.3 Results and Discussion

5.3.1 Identification of Bands of Interest: Band Structure and Projected Density of States

To identify bands of interest, we first compute the band structure and projected density of states (pDOS) of each system. The band structure and pDOS of the clean Au(111) surface are shown in Figure 5.2. For the band structure of the two H_2-Au(111) systems (Figures 5.3 and 5.4), we construct a weighted plot, with each band color-mapped from gray to red depending on the value of the projection of the band onto the two H 1s orbitals (i.e., a bright red-colored band denotes a high amount of H 1s character, and a gray-colored band denotes no H 1s character). The bridge site system (Figure 5.3) has a distinct region of bands with a high amount of H 1s projection, which we will call "H-character." It is important to note that, unlike in atom-centered DFT where the basis set is a collection of atomic orbitals and so the degree of "H-character" can be directly identified by c-squared population analysis (e.g., for a real atom-centered basis set with a molecular orbital given by $\varphi_i = \sum_a^{Nbasis} c_{a,i}\phi_a$, the contribution of basis function ϕ_a into molecular orbital φ_i is given by $\frac{c_{a,i}^2}{\sum_b c_{b,i}^2}$), in planewave DFT, we project the planewave expansion onto a set of atomic orbitals, so the term "character" is not exactly analogous to how we often use it in atom-centered quantum chemistry calculations.

Since we are interested in determining how mixing of the H 1S into the Au(111) surface affects the EEL spectra, the high H 1s character region is a good target range with which to include or exclude bands from subsequent EEL calculations. Because our method does not allow for the exclusion of bands at particular k-points (if a band is excluded, it must be excluded at all k-points), we sum the projection of a given planewave-expanded wavefunction onto a given atomic orbital across k-points. Then, we can determine bands of interest based on the degree of

H-character relative to the band that contains the highest amount of projection onto the H atomic orbitals. In the bridge-site case, this cut-off corresponds to bands with approximately 15% the maximum projection, and the bands involved correspond to bands 50-53 and 55-63. These bands are found in a region around -6.7 to -5.0 eV (where 0.0 eV is the Fermi level), except the lowest index which sits at slightly lower energy (it is the second lowest-energy band at the Γ point). We select bands based on 15% of the maximum rather than, for example, percent of H 1s relative to percent Au s, p, or d in a given band, because the atomic orbitals do not exactly span the same space, so the sum of the squares of the atomic orbital projections for a given band at a given k-point are not guaranteed to sum to 1. For this reason, relative percentages of atom-angular momentum-types are less desirable for determining bands of interest.

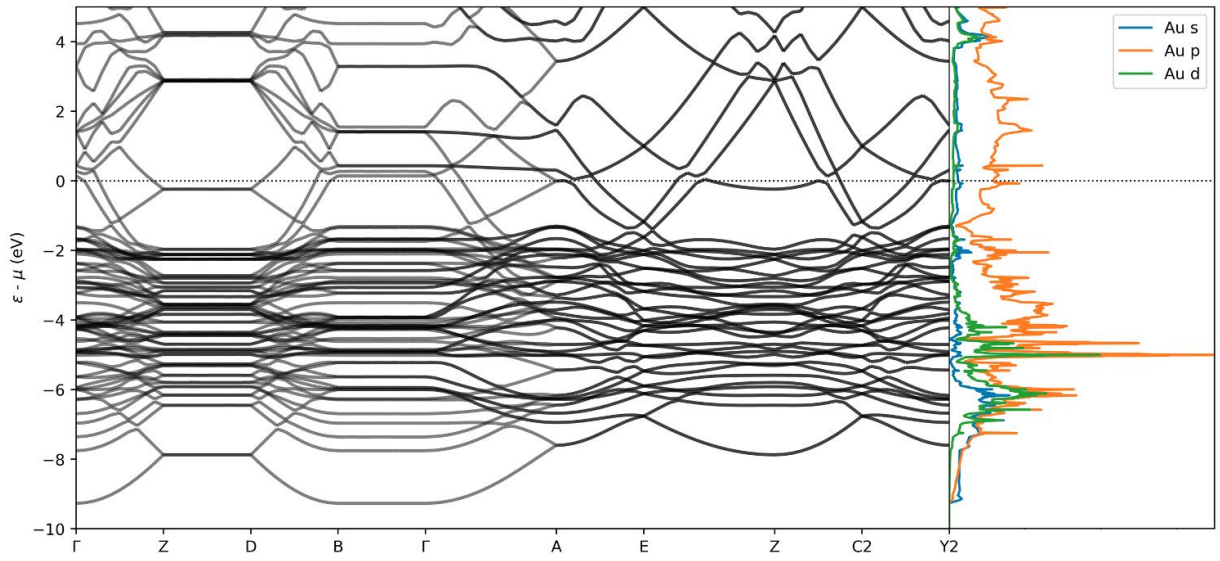

Figure 5.2 Band structure (left-hand side) and projected density of states (right-hand side) of the Au(111) surface.

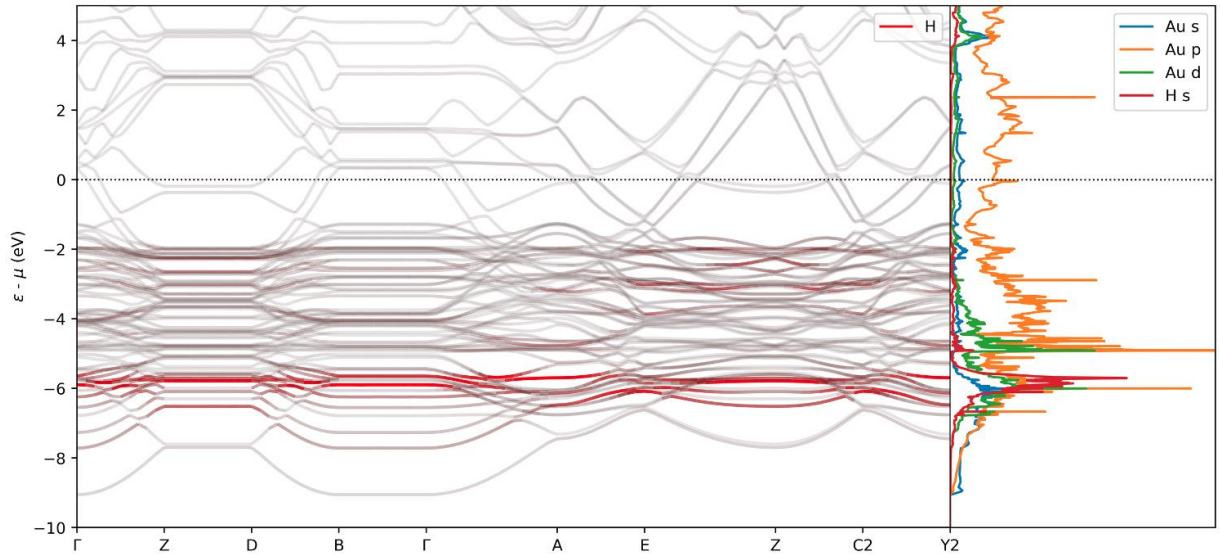

Figure 5.3 Band structure and projected density of states of the "starting position" bridge-site system. Bands are colored based on a grey-red color map of how much the H 1s orbitals are hybridized into the band.

We can conduct a similar analysis to determine the bands of interest in the top-site (ending position) system. The H-1s weighted band structure and pDOS are shown in Figure 5.4. In this system, the hybridized bands of interest are clustered predominantly around two energy regions, one between average energies of -7.6 and -6.6 eV corresponding to bands 50 – 55, and a higher energy region around the Fermi level, about -1.3 eV to 0.50 eV on average, corresponding to bands 113 – 117. There is one higher-energy band (band 120, $E_{min,120}$ = 0.75 eV, $E_{max,120}$ = 3.2 eV), and one lower-energy band (band 49, which is the lowest energy band shown on the band-structure, $E_{min,49}$ = -9.2 eV, $E_{max,49}$ = -7.2 eV). We note that the higher energy region achieves the 15%-of-maximum cut-off in the top-site structure but not in the bridge-site structure because there is a larger disparity in the amount of projection between the higher energy and lower energy region in the bridge-site structure.

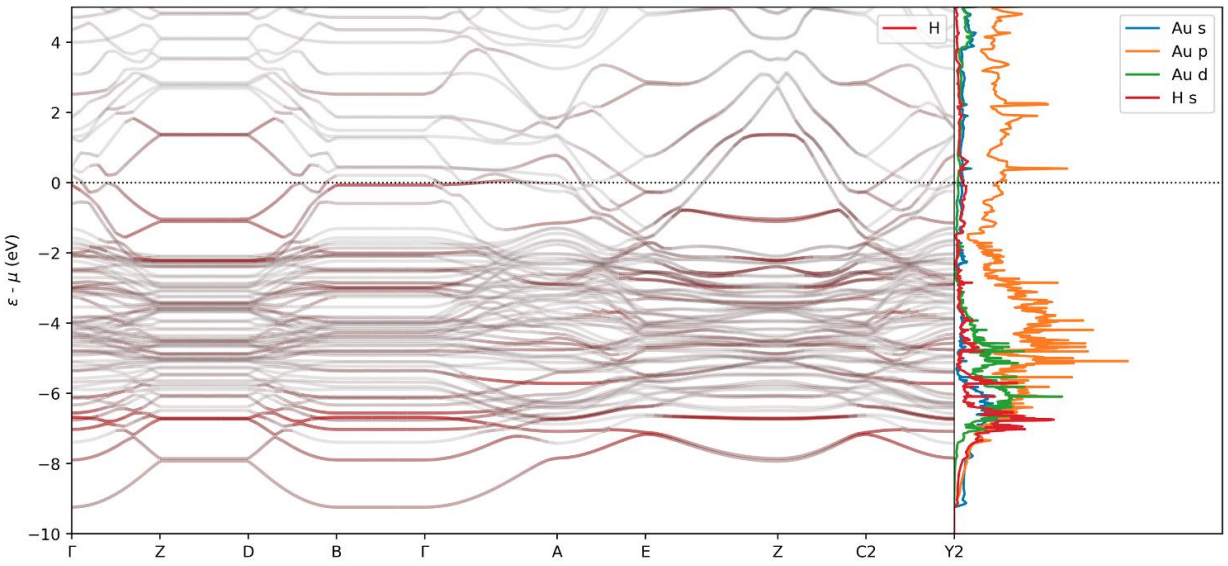

Figure 5.4 Band structure and projected density of states of the "ending position" top-site system. Bands are colored based on a grey-red color map of degree of projection of the band onto the H 1s atomic orbitals.

The electronic d-band plays an important role in the behavior of collective excitations, and a d-only pDOS for the three systems is shown in Figure 5.5. We discuss the role of the d-band in more depth in section 5.3.3. In our systems, the width and lineshape of the d-band remain largely unchanged between the three systems. The bridge site d-band pDOS is slightly upshifted from Au(111) (orange line vs. blue line), and in the energy region around 5.2 – 4.8 eV produces two lower intensity peaks for the top-site system on either side of the prominent peak at ~4.9 eV for Au(111). The d-band of Au(111) corresponds to bands 50 – 81, which will be a target of inclusion/exclusion in section 5.3.3.

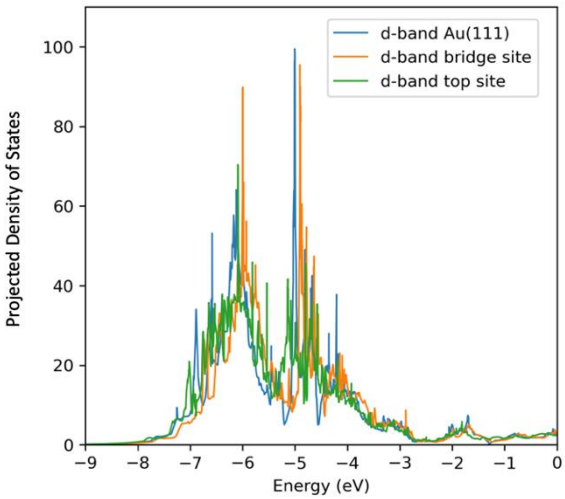

Figure 5.5 Projected density of states for Au 5d orbitals of the three systems: Au(111) (blue), bridge site H_2-Au(111) (orange), top site H_2-Au(111) (green).

5.3.2 Total Electron Energy Loss Spectra

The loss functions we obtain for Au(111) and the two H_2-Au(111) systems are shown in Figure 5.6, with (a) the full 30 eV spectrum, (b) the 0 – 10 eV range, and (c) the low energy features in the 0 – 4 eV range. We focus predominantly on the features from 0 – 10 eV. In this range, there are two areas of interest: the low energy peaks from around 0 – 4 eV, and the region around the sharp peak at 7.7 eV. On the top site structure, this peak is upshifted to 8.2 eV. The low energy range (Figure 5.6.c) produces four peaks for Au(111): prominent peaks at 1.0 eV and 1.6 eV, and smaller peaks at 2.8 eV and 3.7 eV. In the bridge site system, there are peaks at 0.7 and 1.6 eV. In the top site system, there are peaks at 0.7, 1.6, and 2.3 eV, though with minimal prominence, and significantly attenuated relative to Au(111).

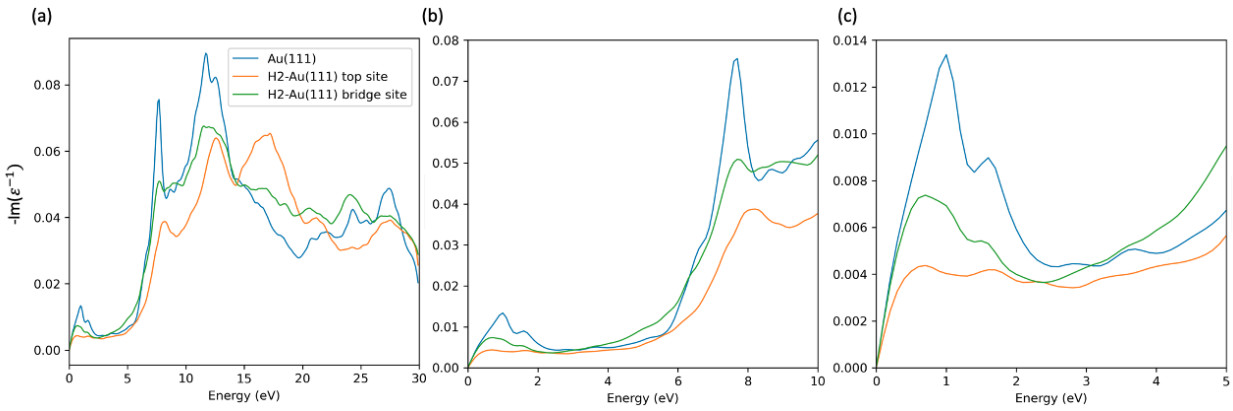

Figure 5.6 EEL spectrum of the three systems: Au(111) shown in blue, top site H_2-Au(111) in green, and bridge-site H_2-Au(111). (a) Full spectrum, 0 – 30 eV. (b) The spectrum "zoomed in" to the 0 – 10 eV region, and (c) The spectrum "zoomed in" further to the 0 – 5 eV region.

In the energy region of 0 – 4 eV in experimental and theoretical studies of Au(111), an acoustic surface plasmon (ASP), a conventional surface plasmon (CSP, ~2.6 eV), and interband transitions (onset ~2 eV) have all been reported.[54–57] Because the onset of interband (d to sp) transitions for Au films lies below the surface plasmon, the plasmon loss peak tends to become obscured. In addition to these peaks, broad distributions around 3.5 eV and 6.0 eV are expected to occur on account of additional interband transitions, though others have attributed a broad feature at 6.0 eV to a surface plasmonic excitation.[54,56] This same work notes that a dipolar single-particle transition occurs at 0.67 eV.[56] It has been suggested that the broad feature that arises from 9 – 12 eV can be assigned to electron-hole pair excitations, based on works on Cu(111).[55,58,59] A group notes that in studies of bulk Au, from 12 eV onward, the spectrum is dominated by interband transitions, while interband transitions < 12 eV mix with plasmon excitations.[60] Motornyi derived a surface loss function for Au(111) from this bulk result, noting that the result is much the same (interband transitions from 12 eV onward).[23]

The acoustic surface plasmon displays a linear dispersion, approaching 0 eV as $q \rightarrow 0$. One group reports that the acoustic plasmon survives up to 2.2 eV with increasing q.[61] At

comparable values of q to that used in our work, one experimental group finds a peak at 0.6 eV, assigned to the ASP, and another peak at ~1.4 eV, assigned to an interplay between the state involved in the ASP and interband transitions of the bulk states.[62] Another group reports an experimental ~1.0 eV ASP peak at similar q alongside a theoretically computed ~0.8 eV ASP peak, with a ~2.6-2.7 eV CSP.[32] Identification of the acoustic surface plasmon peak can be achieved by calculating EELS at various q, as it has a distinctly linear dispersion relation.[23,32]

It is important to note that attempting to make quantitative assignments to the above peaks with the model system we have employed is difficult because the thickness of our surface is sufficiently thinner than what is needed to observe converged surface behavior. The two sides of the surface can interact with each other, coupling together to form new modes. In theoretical TDDFT-based works, it has been reported that, in order to converge the acoustic surface plasmon, thick slabs (> ~5nm, or 24 layers) are required on account of the fact that both sides of the slab can form plasmons, and the acoustic surface plasmon originates from a surface band that extends fairly far into the bulk.[23,32] However, such a slab thickness is computationally intractable given our chosen system.

While direct comparison with results obtained with thick Au(111) surfaces may be difficult on account of the difference in surface thickness, comparison with other ultrathin film works, which investigate several mono-layer thick systems, can be made. When the surface is sufficiently thin, the conventional surface plasmon splits into two modes: a higher energy antisymmetric mode, and a lower energy symmetric mode.[19,63,64] Thus, one man's "unconverged plasmon" is another man's "quantum confinement effects." Each mode occurs on one side of the surface. In a Drude metal, as the thickness of the slab increases, the frequencies of these two peaks converge to the surface plasmon energy, $\omega_p/\sqrt{2}$, and the frequencies of the two peaks are

given by the relation $\omega = \frac{\omega_p}{\sqrt{2}}(1 \pm e^{-qa})^{1/2}$, where a is the thickness of the thin film and q is the regular q (wave vector).[27,65] Further, in very thin films, the acoustic plasmon may appear as multiple low-energy peaks, and the number of acoustic plasmon modes that appear is related to the number of bands that cross the Fermi level.[66] A number of other phenomena related to quantum confinement effects have been shown to arise in Na thin films.[67] There have been a several studies employing the jellium model to study metallic ultrathin films.[19,64,68,69] Jellium replaces the lattice of positive ionic charges with a uniform background charge, so it neglects interband transitions induced by the lattice potential, but is a computationally attractive alternative to full RPA.[70]

If we compute the predicted frequency of the antisymmetric Drude metal surface plasmon peak using the parameters of our system (with $\omega_p \approx 9.1$ eV for Au)[71] we find an energy of ω_{sp}^{+}= 7.8 eV, which is extremely close to the prominent peak at 7.7 eV. However, theoretical thin film studies on jellium models show that the antisymmetric peak tends to be broad, rather than sharp.[64,69] Additionally, if we compute ω_{sp}^{-}, we find a value of 4.7 eV. No obvious peak is visible in this region, though it could be hidden by interband transitions, as discussed above. Further, the Drude model works best for simple metals that do not have d-band structure, and is well-known for its failures in describing noble metals. For example, the Ag(111) plasmon peak is found experimentally to be 3.71 eV, while the Drude model predicts the peak to be 6.4 eV.[72,73] This failure occurs because the Ag d-bands screen the plasmon, causing significant downshifting. So, this agreement with ω_{sp}^{+} is likely coincidence.

Clearly, making definitive peak assignments in these systems is no simple task, and thus this chapter will not attempt to make exact assignments. Future calculations will include computing the EELS spectra at multiple q-vectors, which can provide us clues as to which type

of peak is which. Despite this, we can observe the qualitative differences in the spectra between our three systems and observe the changes that application of the subspace summation yields in these spectra. Having now identified the bands of interest and the regions of interest and discussed what these peaks may (or may not) be, we can apply the subspace summation method to these systems.

One final note before we dive into the subspace summation spectra: an issue arises when attempting to compare the magnitude of peaks when different numbers of bands have been excluded. For example, a subspace summation calculation whose only occupied states are d-bands would contain just a portion of the electrons involved in an "all bands" calculation. We expect the loss function to obey the *f*-sum rule, which states:[74,75]

$$\int_0^\infty d\omega' \omega' Im(\varepsilon^{-1}(\omega')) = -\frac{\pi}{2}\omega_p^2 \qquad \text{(Eq. 5.3)}$$

where $\omega_p^2 = \frac{4\pi N e^2}{m}$ and N is the electron density, $N = \frac{N_{elec}}{\Omega_{cell}}$. In other words, we can relate the loss function to the number of electrons, and equation 5.3 tells us something about the magnitude of the peaks in the loss function. However, we are not computing the loss function as $\omega \rightarrow \infty$, but only to 30 eV. At finite ω, a "partial sum rule" exists:[76]

$$n_{eff}(\omega) = -\frac{m}{2\pi^2 e^2}\int_0^\omega d\omega' \omega' Im(\varepsilon^{-1}(\omega')) \qquad \text{(Eq. 5.4)}$$

Thus, we expect some relation between the magnitude of our peaks within the subspace summation approximation and within the all-bands result. An approximation would be to assume $\frac{n_{eff,sub}}{n_{eff,full}} = \frac{N_{elec,sub}}{N_{elec,full}}$ up to the computed ω_{max}. We can compute the right-hand side for ω = 30 eV directly with the knowledge of how many electrons we have excluded in the subspace calculation, and we can compute the left-hand side via numerical integration once the loss

function has been found. To ensure equality, we can then find a factor with which to scale $n_{eff,sub}$. However, scaling all points on the calculated loss function by a fixed factor implies that the n_{eff} ratio is constant across all ω that we have computed, which is not necessarily true. We apply the above approximation to subspace summation loss functions with this in mind.

5.3.3 Subspace Summation EELS of Au(111)

In Figure 5.7, we partition the Au(111) bands into two sets of subspace summation calculations: (a) the non-intersecting set of "only frontier bands" and "no frontier bands," and (b) the non-intersecting set of "no d-bands" and "only d-bands." In both cases, these sets refer to sets of fully- and partially-occupied bands; all fully unoccupied bands are included in every calculation. The "only frontier bands" set corresponds to those bands that are partially occupied at at least one k-point. These bands are *sp* in nature, and we expect them to contribute strongly to the collective modes of the system. This follows from the fact that these are the most "free-electron"-like bands. The results of set (a) are shown in Figure 5.7.a, and the results of set (b) are shown in Figure 5.7.b.

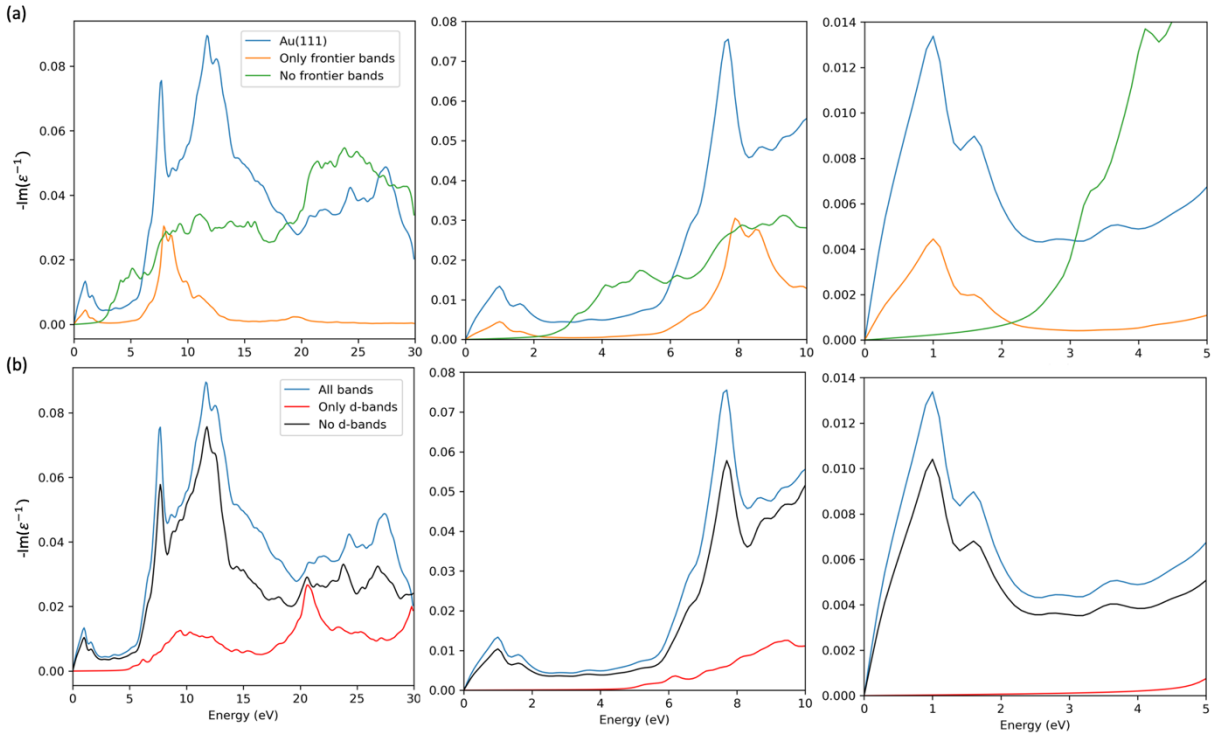

Figure 5.7 (a) Top row: shows the EELS of Au(111) partitioned into all bands (blue), only frontier bands (orange), and no frontier bands (green) (b) Bottom row: shows EELS of Au(111) partitioned into all bands (blue), only d-bands (red), and no d-bands (black).

In Figure 5.7.a., we see that, when we include only the frontier bands, we retain the two dominant peaks in the 0 – 5 eV range (1.0 and 1.6 eV), but the smaller peaks at 2.8 and 3.7 eV have vanished in the frontier-only calculation. The sharp feature at 7.7 eV persists, but has been attenuated relative to the small peak at ~8.7 eV and has shifted to 7.9 eV. When we exclude frontier bands, we are left with lower energy sp-bands (below -0.74 eV) and d-bands (along with lower energy bands from -56 to 105 eV, which we do not expect to contribute to the spectrum at all, given that the energy difference taken in the denominator in equation 2.46 will clearly drive the term to 0 for these states.) Excitations in this subset of bands start to occur around ~2 eV, with a shoulder around 3.2 eV and peaks at 4.1, 4.6, and 5.1 eV. The spectrum of no frontier bands continues to grow with increasing eV as a background of excitations.

In Figure 5.7.b, we examine how calculations of "only d-bands" versus "no d-bands" affect the spectrum. It is interesting to note, first, that in the "no d-bands" calculations (i.e. includes all of the sp-bands of the valence region), we see that the peak at 7.7 eV has regained its prominence relative to the shoulder peak at ~8.7 eV, as compared to the "frontier only" calculation of Figure 5.7.a. I attribute this to the fact that the prominence of the peak is restored on inclusion of *all* occupied sp-bands, rather than only the frontier bands.

If we examine the d-band only contributions (red line in Figure 5.7.b), we see that the onset of excitations occurs around ~5 eV, with a broad peak present between 5 and 15 eV, and a sharp feature occurring around 22.8 eV. In the 0 – 5 eV region, removal of the d-bands from Au(111) reproduces the two prominent peaks at 1.0 and 1.6 eV, consistent with the idea that these peaks originate from the valence sp-band. It is curious that the "no d-bands" subspace summation calculation reproduces the "all bands" calculation quite well up to about 14 eV, suggesting that the dominant peaks in this lower energy region are not strongly affected by inclusion or exclusion of the d-band from the computation of the polarizability. Because the input DFT wavefunctions and eigenenergies *do* include the effects of d-bands, it is possible that, for this system, these effects are already "baked in" to the system. In the simple bulk GaN example shown in Chapter 6.2.2, however, we do see clear changes to the spectrum on exclusion of only the d-bands.

It is important to note that the energy of the d-band relative to the free valence electrons is critical in determining the properties of plasmonic excitations.[25,77] Interband transitions arising from the d-band can damp and shift the energy of plasmonic excitations depending on the location and width of the d-band. It has been shown previously that LDA and GGA functionals are prone to underestimating the energetic position of the Au d-bands in both bulk Au and the

Au(111) surface in theoretical calculations.[32,78] This incorrect d-band position leads to over-screening of the plasmon excitations. In calculations of bulk and surface Au, Ag, and Cu, this shift causes the surface plasmon peak to become significantly damped, downshift, and in some cases disappear, depending on the width and location of the d-band.[25,32,60,77] This phenomenon can be explained in part by a simple model developed by Wilson of a frequency-dependent dielectric function involving Drude-type electrons with a plasma frequency ω_p alongside an optical absorption band, which predicts how ω_p shifts depending on its energetic location relative to the optical absorption band.[24]

Alkauskas and coworkers employ Wilson's model alongside theoretical results for response functions obtained with GGA band structures and (separately) with approximate GW corrections that help shift the d-band energy downward in GGA and LDA.[24,25,78] They find that GGA does not predict the formation of plasmons in the bulk Au loss function, and find that GW corrections downshift the d-bands so that a weak plasmon-like peak appears at 2.65 eV, and a broad peak in the 5.5 – 6.0 eV range forms. Using Wilson's model and treating the onset of d-state transitions as the optical absorption bands, Alkauskas et. al explain that when a model underestimates the d-band energy, it causes, for example, the Au surface plasmon to downshift and broaden.[25]

Similar results were found for the Au(111) surface in theoretical calculations by Thygesen and coworkers, who note that the LDA functional does not predict the Au(111) conventional surface plasmon on account of overestimation of the d-band position.[32] However, they find quantitatively correct band positions with the GLLBSC functional, which also yields quantitatively correct surface plasmon energies. In Thygesen and coworkers' surface calculations, they find a GLLBSC d-band range of -2 to -8 eV for a 24-layer Au(111) surface.[32]

The bulk of our d-band range is thus quite low energy, with over 90% of the occupied d-band contributions in Figure 5.5 occurring between 3 and 7 eV. It is possible that we do not see strong d-band effects in Figure 5.7.b on account of this. Thus, a future direction will be to compute the band structure with a higher level of theory and see if this significantly affects the onset energy of the d-band range.

5.3.4 Subspace Summation EELS of Bridge-site H_2-Au(111)

We have computed the subspace summation EELS for two different sets for the bridge-site H_2 system: the non-intersecting set of frontier bands vs. no frontier bands, and the non-interacting set of hybridized bands vs. no hybridized bands, shown in Figure 5.8. For the bridge-site system, the hybridized bands are predominantly found within the range of -6.7 eV to -5.0 eV (with one band sitting lower, see sec. 5.3.1). The results of the frontier partitions are qualitatively very similar to Au(111) (Figure 5.7.a): the frontier bands contribute to the low energy peaks < 2.0 eV, and the non-frontier bands do not. The frontier bands feature a prominent peak at 7.7 eV, while the non-frontier bands contribute a broad background signal starting around 2.0 eV. The primary difference between the "all bands" spectra between bridge-position H_2-Au(111) and the clean Au(111) surface in the 0-10 eV region is that the 7.7 eV peak is significantly attenuated. Given the high sensitivity of surface plasmons to nearby perturbations (e.g., with a molecule), especially in thin films, if this peak is indeed a surface plasmon peak (See section 5.3.2 for discussion) this signifies that the presence of the H_2 nearby the surface has affected this sensitive collective mode, but has minimally affected every other feature in the < 10 eV region. In such a case, it would be an interesting future investigation to place an additional H_2 symmetrically on

the other side of the surface, since the plasmon mode would be occurring at this energy on account of quantum confinement effects.

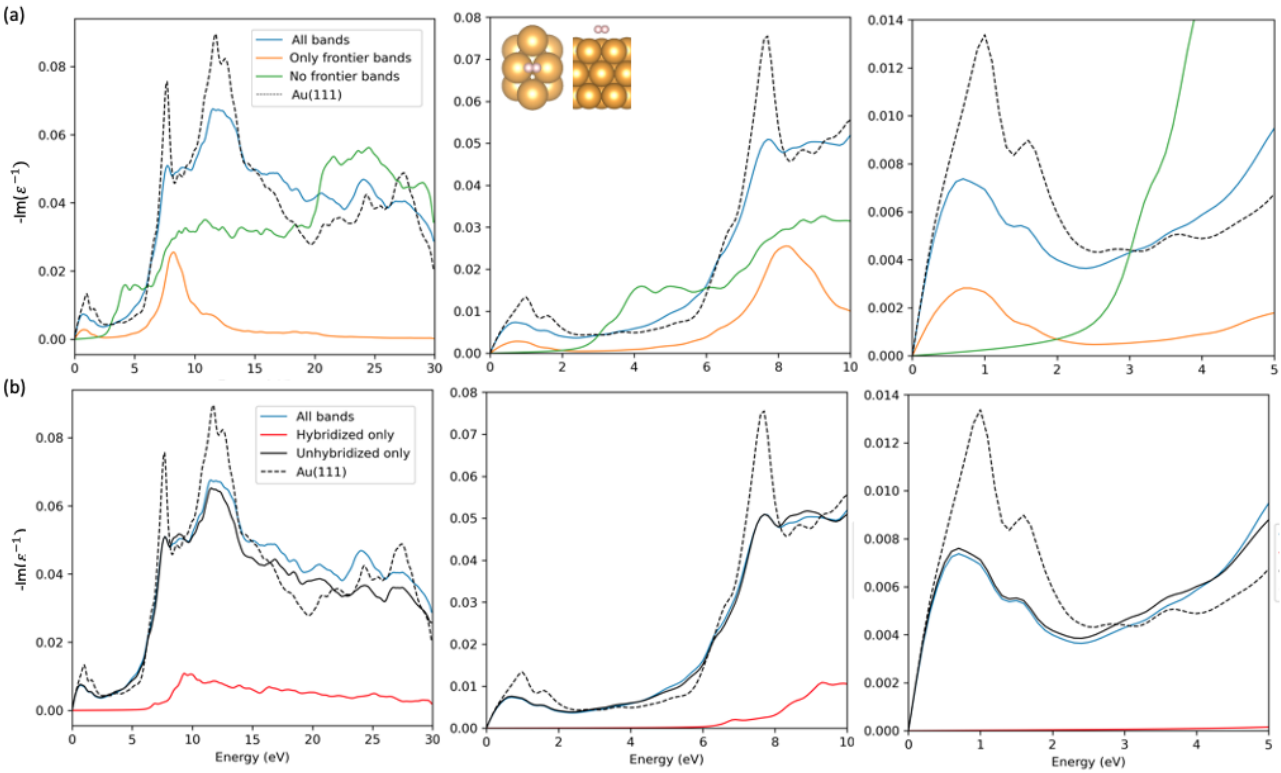

Figure 5.8 Subspace summation EELS for the bridge-site H_2 system. (a) Top row: "only frontier" bands vs. "no frontier bands" partition. (b) Bottom row: "hybridized only" vs. "unhybridized only" partitions. In each row, the black-dashed line shows the result for the Au(111) all bands calculation. Inset in the top-middle figure is the system geometry.

For the "hybridized vs. unhybridized" partition (Figure 5.8.b), we find that the unhybridized result matches well to the "all bands" spectrum at < 10 eV. The "hybridized only" bands contribute a background signal starting around ~6.5 eV, with a small peak at 9.3 eV. H_2 is 2.4 Å away from the surface in the bridge-site orientation, so it is logical that the bands it hybridizes into most strongly do not directly significantly alter the spectrum < 10 eV on their own.

5.3.5 Subspace Summation EELS of Top-site H_2-Au(111)

For the top-site H_2 system, we have obtained the subspace summation EELS partitions for the "hybridized" vs "unhybridized" set, shown in Figure 5.9. We have not yet obtained the H_2 top site "no frontier orbitals" EELS calculation, but have obtained the EELS of the frontier bands-only top-site H_2. We show this result alongside the frontier bands-only calculations for Au(111) and the bridge-site system, for comparison, in Figure 5.10 below.

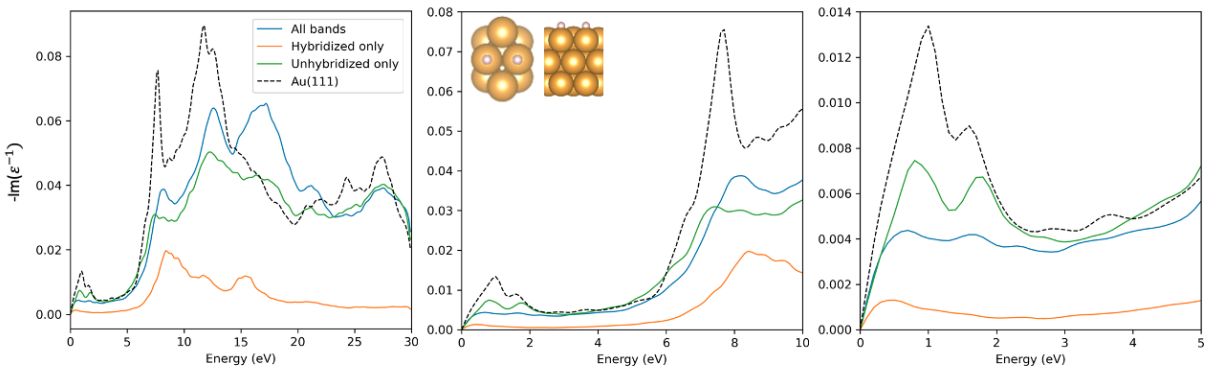

Figure 5.9 Subspace summation EELS for the top-site H_2 system partitioned into "only hybridized" bands (orange) vs. "no hybridized bands" (green). Blue line shows top-site with all bands included, and the black dashed line shows the all bands result for Au(111). Inset in the middle figure is the system geometry.

In the top-site system, bands that project strongly onto H_2 appear in two regions: close to the frontier region (between ~1.0 eV and ~0.50 eV), and in a lower energy region around ~7.6 eV to ~6.6 eV. Because the H_2-hybridized bands of the top-site system involve some, but not all, frontier bands, and some, but not all, bands overlapping with the d-band region, this plot is difficult to parse. Like the in bridge-site case, we see that the peak around 7.7 eV has been significantly attenuated. Unlike in the bridge-site case, the peak has also blueshifted to 8.2 eV.

Park and Palmer have experimentally investigated changes to the Au(111) surface plasmon (the converged peak at ~2.5 eV that occurs for non-ultrathin film surfaces) upon

chemisorption of alkane-thiol self-assembled monolayers (SAMs). They find at q = 0 that the bare surface plasmon peak blue-shifts on addition of the SAMs. They suggest that the origin of this effect is due to shifts in the Au 5d-bands to lower energy, and that if this shift is associated with increased localization of the Au d-bands, that this reduces interband screening of the 6s electron plasmon, causing a blueshift of the mode towards the free-electron result (i.e. the Drude model). Yan, Jacobsen, and Thygesen use a similar line of reasoning to explain a result of H bound on an Ag(111) surface. They find the surface plasmon of the H-Ag(111) system is slightly redshifted, and the dispersion relation is similar to that found by Park and Palmer. They attribute this result to the idea that the adsorbed H-atoms make the surface more free electron-like. In our case, because we have not definitively identified surface plasmon peaks, we cannot make similar arguments. Further, again supposing that the 7.7 eV peak is plasmonic, this peak blue-shifts, but not towards the free-electron result (~ 6.4 eV for the surface plasmon)

The low energy region between 0-4 eV reveals interesting behavior for the top-site system. The "all bands" top-site EELS shows that the two prominent low-energy peaks of Au(111) are suppressed. However, when we include only the unhybridized bands, these peaks are partially restored, suggesting that H-hybridization may attenuate these peaks.

In Figure 5.10, we show the results for the "frontier bands only" subspace summation calculations for each of the three systems. Au(111) and the bridge site system share similar qualitative features, except that the bridge site is missing the sharp feature at 8.5 eV. The primary feature in this region (7.9 eV for Au(111)) is blueshifted for the top-site system (8.5 eV), and this feature is significantly broadened for the top site, though not the bridge site. The feature in the 0-2 eV region is significantly attenuated relative to both the bridge site and the clean Au(111)

surface. Thus, contributions of the bands in the frontier region to the Au(111) EELS are significantly affected by the presence of H in the top sites.

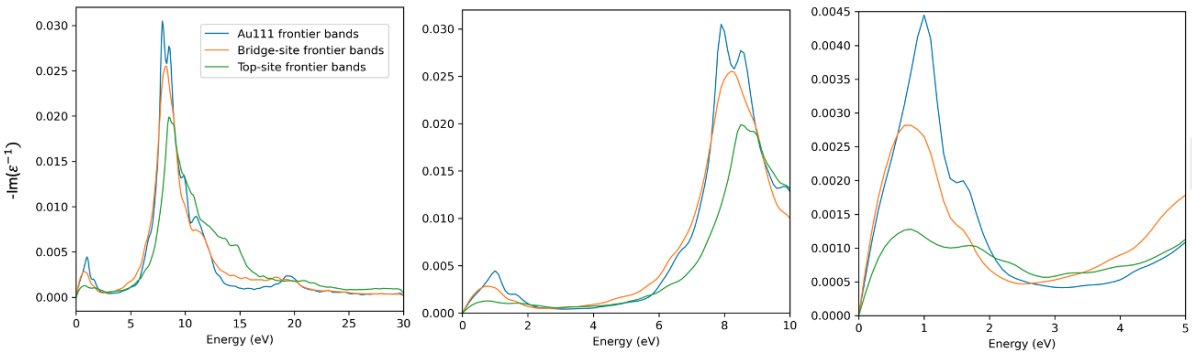

Figure 5.10 Subspace summation EELS for the frontier bands of the three systems: blue line corresponds to Au(111), orange line corresponds to bridge site frontier bands, and green line corresponds to top-site frontier bands.

5.4 Conclusion

We have investigated how the presence of hydrogen on the Au(111) surface influences features of the Au(111) EEL spectrum. We have applied the subspace summation method and partial occupation developments, detailed in sections 6.2 and 6.3 respectively, to obtain these results. The subspace summation method allows us to probe how the presence or absence of H_2 on the surface modifies the loss function with band-by-band granularity. However, these results demonstrate that establishing a clear picture of exactly how hydrogen modifies the modes of low-loss EELS is difficult, even with the granularity offered by the subspace summation method.

We find that H_2 in the bridge site acts perturbatively on the EEL spectra in the < 10 eV region, whose primary differences come in the form of attenuated peaks in the 0-2 eV region and ~ 8 eV region. Spectral features arising from the “hybridized bands only” subspace first appear around 6 eV. These bands form a background signal with no clear features. When there are two H-atoms on either top site, we see more significant changes to the spectrum relative to the clean

Au(111) surface. The peaks in the 0 – 2 eV region are flattened for an "all bands" top-site EELS calculation, but are revived when only unhybridized bands are included in the calculation. In a comparison of "frontier bands only" subspace summation calculations between the three systems, we see that the frontier bands of the top site system produce a blueshifted and broadened feature in the ~ 8 eV region, relative to the clean Au(111) and bridge site H_2 results, signifying that the presence of H in the top-sites influences how the frontier bands contribute to the spectrum.

There is a complex interplay between H_2 and the Au(111) surface, and this work only scratches the surface of these interactions. The most immediate next step for these calculations will be to perform them at various wave-vectors q, since how EELS features vary with q can be a signature of the kind of excitation they correspond to (e.g., acoustic plasmon, surface plasmon, etc.). Carrying out additional computations on thicker surfaces would also be enlightening, as quantum confinement effects that allow modes of one side of the surface to interact with the other side of the surface are likely playing a role in the spectra of our three-layer surface. An additional development to the subspace summation method would be to allow for band inclusion or exclusion at specified k-points, which would provide additional granularity for bands that are identified as important. Finally, we must more rigorously formalize a sum-rule for the subspace summation spectra, which will allow us to produce quantitative differential EELS spectra.

5.5 References

(1) Wu, K.; Chen, J.; McBride, J. R.; Lian, T. Efficient Hot-Electron Transfer by a Plasmon-Induced Interfacial Charge-Transfer Transition. *Science* **2015**, *349* (6248), 632–635. https://doi.org/10.1126/science.aac5443.

(2) Boerigter, C.; Campana, R.; Morabito, M.; Linic, S. Evidence and Implications of Direct Charge Excitation as the Dominant Mechanism in Plasmon-Mediated Photocatalysis. *Nat. Commun.* **2016**, *7* (1), 10545. https://doi.org/10.1038/ncomms10545.

(3) Boerigter, C.; Aslam, U.; Linic, S. Mechanism of Charge Transfer from Plasmonic Nanostructures to Chemically Attached Materials. *ACS Nano* **2016**, *10* (6), 6108–6115. https://doi.org/10.1021/acsnano.6b01846.

(4) Lee, S. Y.; Tsalu, P. V.; Kim, G. W.; Seo, M. J.; Hong, J. W.; Ha, J. W. Tuning Chemical Interface Damping: Interfacial Electronic Effects of Adsorbate Molecules and Sharp Tips of Single Gold Bipyramids. *Nano Lett.* **2019**, *19* (4), 2568–2574. https://doi.org/10.1021/acs.nanolett.9b00338.

(5) Brongersma, M. L.; Halas, N. J.; Nordlander, P. Plasmon-Induced Hot Carrier Science and Technology. *Nat. Nanotechnol.* **2015**, *10* (1), 25–34. https://doi.org/10.1038/nnano.2014.311.

(6) Shan, H.; Yu, Y.; Wang, X.; Luo, Y.; Zu, S.; Du, B.; Han, T.; Li, B.; Li, Y.; Wu, J.; Lin, F.; Shi, K.; Tay, B. K.; Liu, Z.; Zhu, X.; Fang, Z. Direct Observation of Ultrafast Plasmonic Hot Electron Transfer in the Strong Coupling Regime. *Light Sci. Appl.* **2019**, *8* (1), 9. https://doi.org/10.1038/s41377-019-0121-6.

(7) Christopher, P.; Moskovits, M. Hot Charge Carrier Transmission from Plasmonic Nanostructures. *Annu. Rev. Phys. Chem.* **2017**, *68* (1), 379–398. https://doi.org/10.1146/annurev-physchem-052516-044948.

(8) Jermyn, A. S.; Tagliabue, G.; Atwater, H. A.; Goddard, W. A.; Narang, P.; Sundararaman, R. Transport of Hot Carriers in Plasmonic Nanostructures. *Phys. Rev. Mater.* **2019**, *3* (7), 075201. https://doi.org/10.1103/PhysRevMaterials.3.075201.

(9) Tagliabue, G.; Jermyn, A. S.; Sundararaman, R.; Welch, A. J.; DuChene, J. S.; Pala, R.; Davoyan, A. R.; Narang, P.; Atwater, H. A. Quantifying the Role of Surface Plasmon Excitation and Hot Carrier Transport in Plasmonic Devices. *Nat. Commun.* **2018**, *9* (1), 3394. https://doi.org/10.1038/s41467-018-05968-x.

(10) Zhou, L.; Swearer, D. F.; Zhang, C.; Robatjazi, H.; Zhao, H.; Henderson, L.; Dong, L.; Christopher, P.; Carter, E. A.; Nordlander, P.; Halas, N. J. Quantifying Hot Carrier and Thermal Contributions in Plasmonic Photocatalysis. *Science* **2018**, *362* (6410), 69–72. https://doi.org/10.1126/science.aat6967.

(11) Clavero, C. Plasmon-Induced Hot-Electron Generation at Nanoparticle/Metal-Oxide Interfaces for Photovoltaic and Photocatalytic Devices. *Nat. Photonics* **2014**, *8* (2), 95–103. https://doi.org/10.1038/nphoton.2013.238.

(12) Liu, Y.; Chen, Q.; Cullen, D. A.; Xie, Z.; Lian, T. Efficient Hot Electron Transfer from Small Au Nanoparticles. *Nano Lett.* **2020**, *20* (6), 4322–4329. https://doi.org/10.1021/acs.nanolett.0c01050.

(13) Foerster, B.; Joplin, A.; Kaefer, K.; Celiksoy, S.; Link, S.; Sönnichsen, C. Chemical Interface Damping Depends on Electrons Reaching the Surface. *ACS Nano* **2017**, *11* (3), 2886–2893. https://doi.org/10.1021/acsnano.6b08010.

(14) Foerster, B.; Spata, V. A.; Carter, E. A.; Sönnichsen, C.; Link, S. Plasmon Damping Depends on the Chemical Nature of the Nanoparticle Interface. *Sci. Adv.* **2019**, *5* (3), eaav0704. https://doi.org/10.1126/sciadv.aav0704.

(15) Deslippe, J.; Samsonidze, G.; Strubbe, D. A.; Jain, M.; Cohen, M. L.; Louie, S. G. BerkeleyGW: A Massively Parallel Computer Package for the Calculation of the Quasiparticle and Optical Properties of Materials and Nanostructures. *Comput. Phys. Commun.* **2012**, *183* (6), 1269–1289. https://doi.org/10.1016/j.cpc.2011.12.006.

(16) Liebsch, A. Surface Plasmons. In *Electronic Excitations at Metal Surfaces*; Liebsch, A., Ed.; Physics of Solids and Liquids; Springer US: Boston, MA, 1997; pp 49–143. https://doi.org/10.1007/978-1-4757-5107-9_3.

(17) Egerton, R. F. *Electron Energy-Loss Spectroscopy in the Electron Microscope*; Springer US: Boston, MA, 2011. https://doi.org/10.1007/978-1-4419-9583-4.

(18) Grosso, G.; Parravicini, G. P. VII - Excitons, Plasmons and Dielectric Screening in Crystals. In *Solid State Physics*; Grosso, G., Parravicini, G. P., Eds.; Academic Press: London, 2000; pp 230–267. https://doi.org/10.1016/B978-012304460-0/50007-4.

(19) Yuan, Z.; Gao, S. Linear-Response Study of Plasmon Excitation in Metallic Thin Films: Layer-Dependent Hybridization and Dispersion. *Phys. Rev. B* **2006**, *73* (15), 155411. https://doi.org/10.1103/PhysRevB.73.155411.

(20) Tsoulos, T. V.; Batson, P. E.; Fabris, L. Multipolar and Bulk Modes: Fundamentals of Single-Particle Plasmonics through the Advances in Electron and Photon Techniques. *Nanophotonics* **2020**, *9* (15), 4433–4446. https://doi.org/10.1515/nanoph-2020-0326.

(21) Mattheakis, M.; Tsironis, G. P.; Kaxiras, E.; Mattheakis, M.; Tsironis, G. P.; Kaxiras, E. *Graphene and Active Metamaterials: Theoretical Methods and Physical Properties*; IntechOpen, 2017. https://doi.org/10.5772/67900.

(22) Raether, H. The Dielectric Function and the Loss Function of Bound Electrons. In *Excitation of Plasmons and Interband Transitions by Electrons*; Raether, H., Ed.; Springer Tracts in Modern Physics 88; Springer: Berlin, Heidelberg, 1980; pp 14–22. https://doi.org/10.1007/BFb0045954.

(23) Motornyi, O. Ab Initio Study of Electronic Surfaces States and Plasmons of Gold : Role of the Spin-Orbit Coupling and Surface Geometry. These de doctorat, Université Paris-Saclay (ComUE), 2018. https://www.theses.fr/2018SACLX116 (accessed 2023-01-03).

(24) Wilson, C. B. A Phenomenological Theory of the Characteristic Energy Losses of Fast Electrons in Metals. *Proc. Phys. Soc.* **1960**, *76* (4), 481–488. https://doi.org/10.1088/0370-1328/76/4/304.

(25) Alkauskas, A.; Schneider, S. D.; Hebert, C.; Sagmeister, S.; Draxl, C. Supplemental Material for “Dynamic Structure Factors of Cu, Ag, and Au: A Comparative Study from FIrst Principles.”

(26) Luo, X.; Qiu, T.; Lu, W.; Ni, Z. Plasmons in Graphene: Recent Progress and Applications. *Mater. Sci. Eng. R Rep.* **2013**, *74* (11), 351–376. https://doi.org/10.1016/j.mser.2013.09.001.

(27) Pitarke, J. M.; Silkin, V. M.; Chulkov, E. V.; Echenique, P. M. Theory of Surface Plasmons and Surface-Plasmon Polaritons. *Rep. Prog. Phys.* **2007**, *70* (1), 1–87. https://doi.org/10.1088/0034-4885/70/1/R01.

(28) Bernardi, M.; Mustafa, J.; Neaton, J. B.; Louie, S. G. Theory and Computation of Hot Carriers Generated by Surface Plasmon Polaritons in Noble Metals. *Nat. Commun.* **2015**, *6* (1), 7044. https://doi.org/10.1038/ncomms8044.

(29) Egerton, R. F. An Introduction to EELS. In *Electron Energy-Loss Spectroscopy in the Electron Microscope*; Egerton, R. F., Ed.; Springer US: Boston, MA, 2011; pp 1–28. https://doi.org/10.1007/978-1-4419-9583-4_1.

(30) Pitarke, J. M.; Nazarov, V. U.; Silkin, V. M.; Chulkov, E. V.; Zaremba, E.; Echenique, P. M. Theory of Acoustic Surface Plasmons. *Phys. Rev. B* **2004**, *70* (20), 205403. https://doi.org/10.1103/PhysRevB.70.205403.

(31) Silkin, V. M.; Pitarke, J. M.; Chulkov, E. V.; Echenique, P. M. Acoustic Surface Plasmons in the Noble Metals Cu, Ag, and Au. *Phys. Rev. B* **2005**, *72* (11), 115435. https://doi.org/10.1103/PhysRevB.72.115435.

(32) Yan, J.; Jacobsen, K. W.; Thygesen, K. S. Conventional and Acoustic Surface Plasmons on Noble Metal Surfaces: A Time-Dependent Density Functional Theory Study. *Phys. Rev. B* **2012**, *86* (24), 241404. https://doi.org/10.1103/PhysRevB.86.241404.

(33) Roest, L. I.; van Heijst, S. E.; Maduro, L.; Rojo, J.; Conesa-Boj, S. Charting the Low-Loss Region in Electron Energy Loss Spectroscopy with Machine Learning. *Ultramicroscopy* **2021**, *222*, 113202. https://doi.org/10.1016/j.ultramic.2021.113202.

(34) Valerio Olevano. TDDFT, Excitations and Spectroscopy. In *Structures on Different Time Scales: Volume 1*; De Gruyter, 2018; p 101. https://doi.org/10.1515/9783110433920.

(35) Gajdoš, M.; Hummer, K.; Kresse, G.; Furthmüller, J.; Bechstedt, F. Linear Optical Properties in the Projector-Augmented Wave Methodology. *Phys. Rev. B* **2006**, *73* (4), 045112. https://doi.org/10.1103/PhysRevB.73.045112.

(36) Sottile, F.; Bruneval, F.; Marinopoulos, A. G.; Dash, L. K.; Botti, S.; Olevano, V.; Vast, N.; Rubio, A.; Reining, L. TDDFT from Molecules to Solids: The Role of Long-Range Interactions. *Int. J. Quantum Chem.* **2005**, *102* (5), 684–701. https://doi.org/10.1002/qua.20486.

(37) Yan, J.; Mortensen, Jens. J.; Jacobsen, K. W.; Thygesen, K. S. Linear Density Response Function in the Projector Augmented Wave Method: Applications to Solids, Surfaces, and Interfaces. *Phys. Rev. B* **2011**, *83* (24), 245122. https://doi.org/10.1103/PhysRevB.83.245122.

(38) Mukherjee, S.; Libisch, F.; Large, N.; Neumann, O.; Brown, L. V.; Cheng, J.; Lassiter, J. B.; Carter, E. A.; Nordlander, P.; Halas, N. J. Hot Electrons Do the Impossible: Plasmon-Induced Dissociation of H2 on Au. *Nano Lett.* **2013**, *13* (1), 240–247. https://doi.org/10.1021/nl303940z.

(39) Libisch, F.; Cheng, J.; Carter, E. A. Electron-Transfer-Induced Dissociation of H2 on Gold Nanoparticles: Excited-State Potential Energy Surfaces via Embedded Correlated Wavefunction Theory. *Z. Für Phys. Chem.* **2013**, *227* (9–11), 1455–1466. https://doi.org/10.1524/zpch.2013.0406.

(40) Yu, S.; Wilson, A. J.; Heo, J.; Jain, P. K. Plasmonic Control of Multi-Electron Transfer and C–C Coupling in Visible-Light-Driven CO2 Reduction on Au Nanoparticles. *Nano Lett.* **2018**, *18* (4), 2189–2194. https://doi.org/10.1021/acs.nanolett.7b05410.

(41) Zhang, Y.; He, S.; Guo, W.; Hu, Y.; Huang, J.; Mulcahy, J. R.; Wei, W. D. Surface-Plasmon-Driven Hot Electron Photochemistry. *Chem. Rev.* **2018**, *118* (6), 2927–2954. https://doi.org/10.1021/acs.chemrev.7b00430.

(42) Li, H.; Li, Z.; Yu, Y.; Ma, Y.; Yang, W.; Wang, F.; Yin, X.; Wang, X. Surface-Plasmon-Resonance-Enhanced Photoelectrochemical Water Splitting from Au-Nanoparticle-Decorated 3D TiO $_2$ Nanorod Architectures. *J. Phys. Chem. C* **2017**, *121* (22), 12071–12079. https://doi.org/10.1021/acs.jpcc.7b03566.

(43) Sundararaman, R.; Letchworth-Weaver, K.; Schwarz, K. A.; Gunceler, D.; Ozhabes, Y.; Arias, T. A. JDFTx: Software for Joint Density-Functional Theory. *SoftwareX* **2017**, *6*, 278–284. https://doi.org/10.1016/j.softx.2017.10.006.

(44) Hinuma, Y.; Pizzi, G.; Kumagai, Y.; Oba, F.; Tanaka, I. Band Structure Diagram Paths Based on Crystallography. *Comput. Mater. Sci.* **2017**, *128*, 140–184. https://doi.org/10.1016/j.commatsci.2016.10.015.

(45) Togo, A.; Tanaka, I. $\texttt{Spglib}$: A Software Library for Crystal Symmetry Search. arXiv August 5, 2018. https://doi.org/10.48550/arXiv.1808.01590.

(46) Monkhorst, H. J.; Pack, J. D. Special Points for Brillouin-Zone Integrations. *Phys. Rev. B* **1976**, *13* (12), 5188–5192. https://doi.org/10.1103/PhysRevB.13.5188.

(47) Methfessel, M.; Paxton, A. T. High-Precision Sampling for Brillouin-Zone Integration in Metals. *Phys. Rev. B* **1989**, *40* (6), 3616–3621. https://doi.org/10.1103/PhysRevB.40.3616.

(48) Perdew, J. P.; Burke, K.; Ernzerhof, M. Generalized Gradient Approximation Made Simple. *Phys. Rev. Lett.* **1996**, *77* (18), 3865–3868. https://doi.org/10.1103/PhysRevLett.77.3865.

(49) Schlipf, M.; Gygi, F. Optimization Algorithm for the Generation of ONCV Pseudopotentials. *Comput. Phys. Commun.* **2015**, *196*, 36–44. https://doi.org/10.1016/j.cpc.2015.05.011.

(50) Spreadborough, J.; Christian, J. W. High-Temperature X-Ray Diffractometer. *J. Sci. Instrum.* **1959**, *36* (3), 116. https://doi.org/10.1088/0950-7671/36/3/302.

(51) Momma, K.; Izumi, F. VESTA 3 for Three-Dimensional Visualization of Crystal, Volumetric and Morphology Data. *J. Appl. Crystallogr.* **2011**, *44* (6), 1272–1276. https://doi.org/10.1107/S0021889811038970.

(52) Hanke, F.; Björk, J. Structure and Local Reactivity of the Au(111) Surface Reconstruction. *Phys. Rev. B* **2013**, *87* (23), 235422. https://doi.org/10.1103/PhysRevB.87.235422.

(53) Wijzenbroek, M.; Helstone, D.; Meyer, J.; Kroes, G.-J. Dynamics of H2 Dissociation on the Close-Packed (111) Surface of the Noblest Metal: H2 + Au(111). *J. Chem. Phys.* **2016**, *145* (14), 144701. https://doi.org/10.1063/1.4964486.

(54) Pulisciano, A.; Park, S. J.; Palmer, R. E. Surface Plasmon Excitation of Au and Ag in Scanning Probe Energy Loss Spectroscopy. *Appl. Phys. Lett.* **2008**, *93* (21), 213109. https://doi.org/10.1063/1.3006435.

(55) Politano, A.; Chiarello, G. The Influence of Electron Confinement, Quantum Size Effects, and Film Morphology on the Dispersion and the Damping of Plasmonic Modes in Ag and Au Thin Films. *Prog. Surf. Sci.* **2015**, *90* (2), 144–193. https://doi.org/10.1016/j.progsurf.2014.12.002.

(56) Politano, A.; Chiarello, G. Electronic Properties of Gold Thin Films Studied by Electron Energy Loss Spectroscopy. *Gold Bull.* **2009**, *42*, 195–200. https://doi.org/10.1007/BF03214934.

(57) Johnson, P. B.; Christy, R. W. Optical Constants of the Noble Metals. *Phys. Rev. B* **1972**, *6* (12), 4370–4379. https://doi.org/10.1103/PhysRevB.6.4370.

(58) Lazić, P.; Silkin, V. M.; Chulkov, E. V.; Echenique, P. M.; Gumhalter, B. Ultrafast Dynamics and Decoherence of Quasiparticles in Surface Bands: Preasymptotic Decay and Dephasing of Quasiparticle States. *Phys. Rev. B* **2007**, *76* (4), 045420. https://doi.org/10.1103/PhysRevB.76.045420.

(59) Lazić, P.; Silkin, V. M.; Chulkov, E. V.; Echenique, P. M.; Gumhalter, B. Extreme Ultrafast Dynamics of Quasiparticles Excited in Surface Electronic Bands. *Phys. Rev. Lett.* **2006**, *97* (8), 086801. https://doi.org/10.1103/PhysRevLett.97.086801.

(60) Motornyi, O.; Vast, N.; Timrov, I.; Baseggio, O.; Baroni, S.; Dal Corso, A. Electron Energy Loss Spectroscopy of Bulk Gold with Ultrasoft Pseudopotentials and the Liouville-Lanczos Method. *Phys. Rev. B* **2020**, *102* (3), 035156. https://doi.org/10.1103/PhysRevB.102.035156.

(61) Park, S. J.; Palmer, R. E. Acoustic Plasmon on the Au(111) Surface. *Phys. Rev. Lett.* **2010**, *105* (1), 016801. https://doi.org/10.1103/PhysRevLett.105.016801.

(62) Vattuone, L.; Smerieri, M.; Langer, T.; Tegenkamp, C.; Pfnuer, H.; Silkin, V. M.; Chulkov, E. V.; Echenique, P. M.; Rocca, M. Correlated Motion of Electrons on the Au(111) Surface: Anomalous Acoustic Surface-Plasmon Dispersion and Single-Particle Excitations. *Phys. Rev. Lett.* **2013**, *110* (12), 127405. https://doi.org/10.1103/PhysRevLett.110.127405.

(63) Qin, H.; Jiang, Y.; Zhang, G.; Wu, K. Interaction of Surface and Interface Plasmons in Extremely Thin Al Films on Si(111). *Appl. Phys. Lett.* **2013**, *102* (5), 051605. https://doi.org/10.1063/1.4790289.

(64) Marušić, L.; Despoja, V.; Šunjić, M. Surface Plasmon and Electron–Hole Structures in the Excitation Spectra of Thin Films. *J. Phys. Condens. Matter* **2006**, *18* (17), 4253. https://doi.org/10.1088/0953-8984/18/17/013.

(65) Politano, A.; Chiarello, G. Plasmonic Modes in Thin Films: Quo Vadis? *Front. Mater.* **2014**, *1*.

(66) Zubizarreta, X.; Chulkov, E. V.; Chernov, I. P.; Vasenko, A. S.; Aldazabal, I.; Silkin, V. M. Quantum-Size Effects in the Loss Function of Pb(111) Thin Films: An Ab Initio Study. *Phys. Rev. B* **2017**, *95* (23), 235405. https://doi.org/10.1103/PhysRevB.95.235405.

(67) Andersen, K.; Jacobsen, K. W.; Thygesen, K. S. Spatially Resolved Quantum Plasmon Modes in Metallic Nano-Films from First-Principles. *Phys. Rev. B* **2012**, *86* (24), 245129. https://doi.org/10.1103/PhysRevB.86.245129.

(68) Silkin, V. M.; Nagao, T.; Despoja, V.; Echeverry, J. P.; Eremeev, S. V.; Chulkov, E. V.; Echenique, P. M. Low-Energy Plasmons in Quantum-Well and Surface States of Metallic Thin Films. *Phys. Rev. B* **2011**, *84* (16), 165416. https://doi.org/10.1103/PhysRevB.84.165416.

(69) Yuan, Z.; Gao, S. Landau Damping and Lifetime Oscillation of Surface Plasmons in Metallic Thin Films Studied in a Jellium Slab Model. *Surf. Sci.* **2008**, *602* (2), 460–464. https://doi.org/10.1016/j.susc.2007.10.040.

(70) Liebsch, A. *Electronic Excitations at Metal Surfaces*; Springer US: Boston, MA, 1997. https://doi.org/10.1007/978-1-4757-5107-9.

(71) Le Ru, E. C.; Etchegoin, P. G. Chapter 3 - Introduction to Plasmons and Plasmonics. In *Principles of Surface-Enhanced Raman Spectroscopy*; Le Ru, E. C., Etchegoin, P. G.,

Eds.; Elsevier: Amsterdam, 2009; pp 121–183. https://doi.org/10.1016/B978-0-444-52779-0.00009-X.

(72) Moresco, F.; Rocca, M.; Zielasek, V.; Hildebrandt, T.; Henzler, M. ELS-LEED Study of the Surface Plasmon Dispersion on Ag Surfaces. *Surf. Sci.* **1997**, *388* (1), 1–4. https://doi.org/10.1016/S0039-6028(97)00426-3.

(73) Yan, J.; Jacobsen, K. W.; Thygesen, K. S. First-Principles Study of Surface Plasmons on Ag(111) and H/Ag(111). *Phys. Rev. B* **2011**, *84* (23), 235430. https://doi.org/10.1103/PhysRevB.84.235430.

(74) Hybertsen, M. S.; Louie, S. G. Electron Correlation in Semiconductors and Insulators: Band Gaps and Quasiparticle Energies. *Phys. Rev. B* **1986**, *34* (8), 5390–5413. https://doi.org/10.1103/PhysRevB.34.5390.

(75) Johnson, D. L. Local Field Effects and the Dielectric Response Matrix of Insulators: A Model. *Phys. Rev. B* **1974**, *9* (10), 4475–4484. https://doi.org/10.1103/PhysRevB.9.4475.

(76) Smith, D. Y.; Shiles, E. Finite-Energy f -Sum Rules for Valence Electrons. *Phys. Rev. B* **1978**, *17* (12), 4689–4694. https://doi.org/10.1103/PhysRevB.17.4689.

(77) Zhukov, V. P.; Aryasetiawan, F.; Chulkov, E. V.; Gurtubay, I. G. de; Echenique, P. M. Corrected Local-Density Approximation Band Structures, Linear-Response Dielectric Functions, and Quasiparticle Lifetimes in Noble Metals. *Phys. Rev. B* **2001**, *64* (19), 195122. https://doi.org/10.1103/PhysRevB.64.195122.

(78) Alkauskas, A.; Schneider, S. D.; Hébert, C.; Sagmeister, S.; Draxl, C. Dynamic Structure Factors of Cu, Ag, and Au: Comparative Study from First Principles. *Phys. Rev. B* **2013**, *88* (19), 195124. https://doi.org/10.1103/PhysRevB.88.195124.

Chapter 6 - Subspace Summation and Partial Occupations Method Developments

6.1 Introduction

Under the GW approximation, the self-energy of a system of electrons is approximated by expanding in terms of a single electron Green's function (G) and a screened coulomb interaction (W). The GW method has found success in computing quantities such as band gaps, plasmon energies, lifetimes, and many other electronic properties with quantitative accuracy.[1,2] The evaluation of quantities of interest within the GW approximation requires a double summation over occupied/virtual state pairs. Thus, information regarding which individual quantum states contribute to a specific quantity is encoded in the computation of the quantity.[3] An understanding of how a change in conditions (e.g. addition of a solvent, or a change to the electronic structure via addition of an adsorbate) affects the system as a whole can be developed by examining how the influence of the quantum states evolve under the change in condition for a given quantity.

The random phase approximation (RPA) polarizability matrix is at the core of the "W" in a GW calculation, and is the quantity of interest for the developments contained in this chapter. The evaluation of the RPA polarizability is one such quantity requiring a double summation over occupied/virtual state pairs.[4,5] Thus, information regarding which individual quantum states contribute to the polarizability is embedded in its computation. The relative importance of a particular state to the polarizability can be ascertained by examining how the presence or absence of the state affects the computed value of the polarizability. In other words, if we can choose which states to include in the computation, then we can evaluate which quantum states are polarized most strongly by an electric field. The development of a method that allows access to

such an evaluation is the purpose of this work, which we call the subspace summation method. The polarizability can be used to obtain spectroscopic quantities like an electron energy loss spectrum (EELS).[6,7] The low-loss region of EELS contains information on collective excitations like bulk and surface plasmons, among other electronic structure properties.[8–11] EELS is a powerful spectroscopic method that can be used to study the plasmon modes and other electronic structure features of nanoparticles.[12–16] Enabling a band-by-band understanding of the EELS of metallic systems is the motivation of this work.

This chapter addresses two separate developments, each necessary to develop this "band-by-band" approach for EELS of metals. First, we focus on the development of the subspace summation method. The second development involves incorporating partial occupations into the BerkeleyGW code. We note that the application work in Chapter 5 would be impossible without each.

6.2 Subspace Summation

The BerkeleyGW code is an implementation of the GW method whose massive parallelism has made GW calculations on systems of hundreds of atoms tractable. BerkeleyGW's parallelization scheme is intimately related to the sum-over-states computation, as it distributes occupied/virtual state pairs over MPI tasks.[2] In this work, we modify the BerkeleyGW parallelization scheme of the Epsilon executable so that any number of individual states can be excluded from the double summation involved in calculating a quantity of interest. A simplified version of this capability, which excludes valence bands starting from the lowest energy valence band, exists already and was used to understand how d-states in the valence band of GaN give rise to a significantly different EELS spectrum than for AlN.[3] However, this method is inflexible,

as it does not allow for singling out desired states of interest regardless of location in the energetic spectrum, as only the consecutive lowest energy bands can be excluded. Our work extends this feature by allowing any arbitrary state to be isolated in the summation. This extension will allow for the analyses carried out in Ref. [3] to be applied to systems whose states of interest are not necessarily the lowest energy valence states. Using the new method, we visit the computation of the simulated EEL spectrum of GaN, and this time we are able to consider 1) including all valence bands, 2) including only gallium d-bands, and 3) including no gallium d-bands in the calculation to study how the plasmon peak in the spectrum evolves under these changes, rather than excluding all states below a given threshold state. A more substantial application, in which we examine how the chemical interface damping of H_2 affects the Au(111) plasmon mode at the starting and ending points of an H_2 dissociative absorption pathway, is presented in Chapter 5.

The BerkeleyGW code is divided into several distinct executables, each performing a calculation step on the way to a full Bethe-Salpeter equation calculation, but also each useful as a standalone executable for other applications. In this work, we focus on the epsilon executable, whose primary output is the dielectric matrix ("epsilon") and its inverse. The dielectric matrix in BerkeleyGW is calculated within the random phase approximation (RPA). To quickly recapitulate the relevant portions of 2.2.1 and 2.2.2, in spectroscopy, the macroscopic dielectric function is a useful quantity, and is obtained from the RPA microscopic dielectric matrix as $\varepsilon_M = \frac{1}{\varepsilon_{00}^{-1}(\boldsymbol{q},\omega)}$. The macroscopic dielectric function provides us with the ability to compute an absorption spectrum as $\mathrm{Im}(\varepsilon_M(\boldsymbol{q} \to 0, \omega))$, or an electron energy loss spectrum as $-\mathrm{Im}(\varepsilon_M^{-1}(\boldsymbol{q}, \omega))$.[17] Thus, through RPA, we have access to important spectroscopic observables.

To detail the subspace summation method, we present here the static ($\omega = 0$) RPA polarizability. The method generalizes to the dynamic polarizability discussed in 2.2.2 without issue. BerkeleyGW computes the dielectric matrix as:

$$\varepsilon_{\boldsymbol{GG'}}(\boldsymbol{q};0) = \delta_{\boldsymbol{GG'}} - v(\boldsymbol{q}+\boldsymbol{G})\chi_{\boldsymbol{GG'}}(\boldsymbol{q};0) \qquad \text{(Eq. 6.1)}$$

with $v(\boldsymbol{q}+\boldsymbol{G})$ the bare Coulomb interaction, and χ given by:[1]

$$\chi_{\boldsymbol{GG'}}(\boldsymbol{q};0) = \sum_{n,n',\boldsymbol{k}} (f(\varepsilon_{n,\boldsymbol{k}+\boldsymbol{q}}) - f(\varepsilon_{n',\boldsymbol{k}})) \frac{\langle n',\boldsymbol{k}|e^{-i(\boldsymbol{q}+\boldsymbol{G})\cdot\mathbf{r}}|n,\boldsymbol{k}+\boldsymbol{q}\rangle\langle n,\boldsymbol{k}+\boldsymbol{q}|e^{i(\boldsymbol{q}+\boldsymbol{G'})\cdot\mathbf{r'}}|n',\boldsymbol{k}\rangle}{\varepsilon_{n,\boldsymbol{k}+\boldsymbol{q}} - \varepsilon_{n',\boldsymbol{k}}}$$

(Eq. 6.2)

In BerkeleyGW, the occupation factor f is given as 1 if the mean-field eigenenergy $\varepsilon < \varepsilon_{fermi}$, 0 if $\varepsilon > \varepsilon_{fermi}$, and 0.5 if $\varepsilon = \varepsilon_{fermi}$ (though we will implement alternate functions for f in section 6.3). For simplicity, we can write $M_{nn'}(\boldsymbol{k},\boldsymbol{q},\boldsymbol{G}) = \langle n,\boldsymbol{k}+\boldsymbol{q}|e^{i(\boldsymbol{q}+\boldsymbol{G'})\cdot\mathbf{r'}}|n',\boldsymbol{k}\rangle$. With these definitions of f and M, equation 6.2 simplifies to:

$$\chi_{\boldsymbol{GG'}}(\boldsymbol{q};0) = \sum_{n}^{occ}\sum_{n'}^{emp}\sum_{\boldsymbol{k}} M^{*}_{nn'}(\boldsymbol{k},\boldsymbol{q},\boldsymbol{G}) M_{nn'}(\boldsymbol{k},\boldsymbol{q},\boldsymbol{G}) \frac{1}{\varepsilon_{n,\boldsymbol{k}+\boldsymbol{q}} - \varepsilon_{n',\boldsymbol{k}}} \qquad \text{(Eq. 6.3)}$$

Thus, the polarizability is computed as a double summation over all possible pairs of occupied and virtual states, which we call "(valence, conduction) pairs" in the coming sections. If we obtain a low-loss EEL spectrum in which certain bands have been excluded from the calculation of equation 6.3, then we learn about how those bands affect the collective modes of the system, like plasmons. In this section, we focus on the implementation of this method. Additionally, while this method offers the means to understand a system's polarizability on a state-by-state basis, it also offers computational savings when particular types of bands that do not affect the property under study can be excluded, which can be the case for energetically lower-lying bands.

While the computational savings of band exclusion are not the primary motivator for this development, they are a useful bonus, and some benchmarks are discussed.

6.2.1 Implementation

The parallel MPI distribution scheme in BerkeleyGW is the linchpin of its success. To carry out this development, we must maintain the core parallelism, despite disrupting this parallelism with the removal of bands and thus possible (valence, conduction) band pairings. The native parallelism in the epsilon code distributes (valence, conduction) pairs across MPI tasks. The exclusion of arbitrary bands necessarily interferes with this scheme. The core of this project involves the identification and development of a scheme that is as compatible as possible with the native scheme.

To describe the native parallelism and our modification, we use an example system with 4 valence bands (n = 1-4), 8 conduction bands (n′ = 5-12), and 4 MPI tasks. In an unmodified calculation, we must compute:

$$\chi_{GG'} = \sum_{n=1}^{4} \sum_{n'=5}^{12} \sum_{\boldsymbol{k}} M^{*}_{nn'}(\boldsymbol{k},\boldsymbol{q},\boldsymbol{G}) M_{nn'}(\boldsymbol{k},\boldsymbol{q},\boldsymbol{G}) \frac{1}{\varepsilon_{n,\boldsymbol{k}+\boldsymbol{q}} - \varepsilon_{n',\boldsymbol{k}}} \qquad \text{(Eq. 6.4)}$$

We can visualize these bands as rows in a matrix, as shown in Figure 6.1.

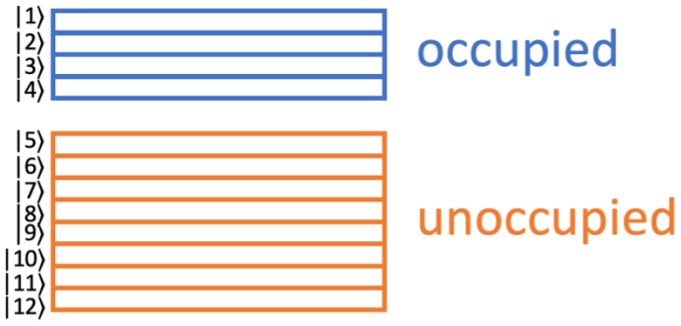

Figure 6.1 Bands visualized as rows. We consider four occupied bands and eight unoccupied bands.

With our method, we want to exclude any arbitrary band from the calculation. We choose to exclude bands 1, 2, 6, 9, and 10, so that we compute all valence, conduction pairs between valence bands 3 and 4 with conduction bands 5, 7, 8, 11, and 12. In other words, equation 6.4 becomes:

$$\chi_{GG'} = \sum_{n=3,4} \sum_{n'=5,7,8,11,12} \sum_{\boldsymbol{k}} M^{*}_{nn'}(\boldsymbol{k},\boldsymbol{q},\boldsymbol{G}) M_{nn'}(\boldsymbol{k},\boldsymbol{q},\boldsymbol{G}) \frac{1}{\varepsilon_{n,\boldsymbol{k}+\boldsymbol{q}} - \varepsilon_{n',\boldsymbol{k}}} \qquad \text{(Eq. 6.5)}$$

We can visualize this restricted set as Figure 6.2.

Figure 6.2 Visualization of the subset of bands to be included in the calculation.

In the unmodified calculation, the distribution of (valence, conduction) pairs is determined in such a way to minimize memory cost for each MPI task while balancing workload. The tasks are divided into pools, where each task in a pool is assigned the same set of valence (occupied) bands. The number of pools is found by testing the amount of memory required for a number of pools ranging from 1 to the number of valence bands. If there were to be no pools, then each MPI task would hold all valence bands, and some subset of conduction bands, which can result in large memory requirements for each task. Once the number of pools are determined, each task is assigned to a pool. Each pool is given a set of contiguous valence bands (and each task in the pool is given a copy of these bands), then all conduction bands are divided amongst the MPI tasks in the pool in contiguous blocks to each MPI task.

For our example, this parallelization scheme can be visualized as in Figure 6.3. Here, the MPI tasks are color-coded, as are the bands. If the color corresponding to a task is shown on a band, then that task owns a copy of the band. In our example, there is only one valence pool (i.e. one pool containing all four valence bands), so the valence bands are colored red, green, blue, and purple, to signify that task 1 (red), task 2 (green), task 3 (blue), and task 4 (purple) all own a copy of these bands. Then, conduction bands 4 and 5 are colored red only, because only MPI task 1 has a copy of these bands. Bands 7 and 8 are colored green and owned only by task 2, etc. An MPI task "owns" a band if it holds a copy of this band in memory.

Clearly, to maintain the most reasonable load balancing and per-task memory requirements, we must intervene in the distribution process before the point at which a given MPI task comes into possession of a given band. If we begin excluding bands after this point, then one of two issues arise. Either the load balancing becomes suboptimal (e.g. in Figure 6.3, we could set all elements in bands 1, 2, 6, 9 and 10 to zero and this would achieve our goal, but it would leave MPI task 3 with no work to do since it is responsible only for (valence, conduction) pairs with conduction bands 9 and 10), or additional MPI communication must be introduced to to re-distribute the bands in a more optimal way.

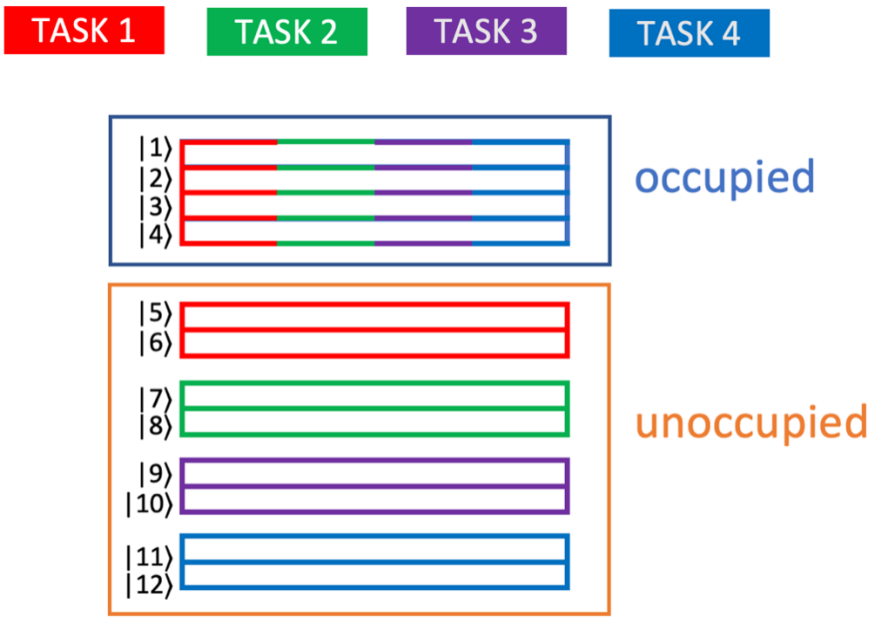

Figure 6.3 Visualization of the distribution of the unoccupied and occupied bands in the full calculation. Each task owns a copy of the valence bands, while the conduction bands are divided amongst the MPI tasks.

The native band distribution algorithm only requires as input the number of valence bands, the number of conduction bands, and the number of MPI tasks to distribute the bands under the scheme shown in Figure 6.3. Thus, we can apply this same distribution algorithm to our subset of bands to obtain the equivalent distribution. To do this, we must only know how many valence and conduction bands each that the user wants to exclude from the calculation. Continuing our example, passing to the distribution algorithm two valence bands and five conduction bands produces the distribution scheme shown in Figure 6.4. Ultimately, the band indexing is inconsequential to the distribution. That the two valence bands are, in the full wavefunction file, bands 3 and 4, rather than 1 and 2, does not affect the distribution scheme. Instead, it affects what we read in from the wavefunction file, and how we read it.

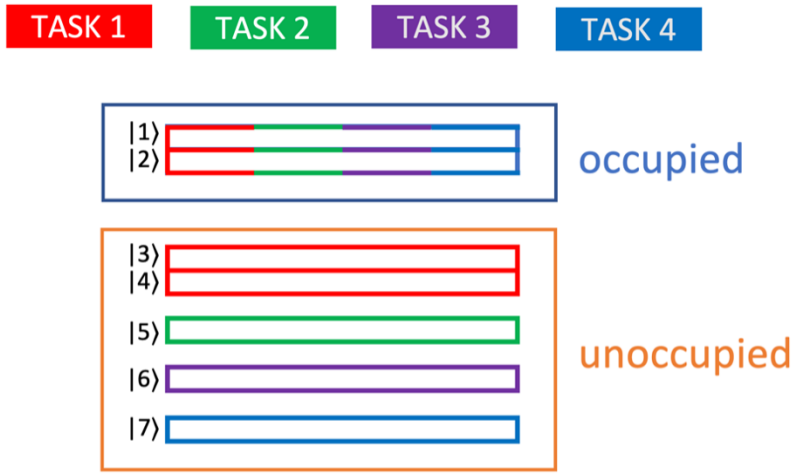

Figure 6.4 The optimal distribution of bands within the restricted calculation. Note that the indexing produced by the distribution algorithm does not align with the bands to be included in the calculation.

In the epsilon code, there are two separate methods of wavefunction read-in. The first involves reading the wavefunction data, stored as Fortran binary file, into the code band-by-band, then for each band, distributing it to the MPI tasks that require a copy. The second involves reading an HDF5 wavefunction file. HDF5 is a file format, and HDF5 files can be read using HDF5 library functions. HDF5 supports parallel file I/O and involves defining a region of the file to read in, which can be unique for each MPI task making the read. Since we specifically want each MPI task reading particular sets of bands, and the parallel HDF5 library functions are well-suited for reading arbitrary regions of a file, we develop this method to be compatible with the HDF5 wavefunction file only.[17,18]

In an HDF5 read, a “hyperslab” is a rectangular pattern of data. A hyperslab can be defined, then read into program. Unions of hyperslabs can also be created, and then read into the program. Thus, any arbitrary region of data can be read into the program using a single HDF5 read call. In the HDF5 read for the native wavefunction read-in routine, each MPI task can define

a hyperslab corresponding to its contiguous blocks of assigned valence and conduction bands. In our new method, since the bands that an MPI task must read may or may not be contiguous or be arranged in any regular pattern, we take unions of hyperslabs until all bands that an MPI task has been assigned are included in the hyperslabs.

Before creating these unions of hyperslabs, we must know which MPI task has been given which band. We have discussed that the distribution algorithm only needs to know the new number of (included) valence and conduction bands, and the number of available MPI tasks, to create the scheme shown in Figure 6.4. However, this distribution scheme is not aware that the indexing of bands in the file is not the same as the indexing of bands as assigned in the distribution routine. For example, in Figure 6.4, MPI task 1 would be assigned conduction bands 3 and 4 (the first two conduction bands), when in the file, it needs bands 5 and 6, the actual indexing of the first two conduction bands. It would also need valence bands 3 and 4 as indexed in the wavefunction file, which appear as valence bands 1 and 2 in the distribution scheme. Thus, we must devise a way for the MPI task to retain which bands, as properly indexed in the wavefunction file, it requires, and how these bands map to the band indices it has been assigned by the distribution algorithm.

The user must provide a list of bands to include in the calculation in the input file. Rather than list every band, since there can be thousands, we accept an array that details the band ranges of included bands. In our example, the input file keyword and data would appear as:

```
begin band ranges
3 5
7 8
11 12
end
```

This input section is then converted into a 2-d array inside the program, which we call the global inclusion array. The input states that the included band ranges are 3 – 5, 7 – 8, and 11 – 12 (i.e., bands 3, 4, 5, 7, 8, 11, and 12). Now, given the user-provided band ranges information, which tells us the "true" wavefunction band index for the included bands, and given that we have the distribution scheme information, which tells us how many valence and conduction bands each MPI task should have and indexes these in a "shifted" way (e.g. 3 → 1, 4 → 2, 5 → 3, 7 → 4, 8 → 5, 11 → 6, 12 → 7), we can write our own algorithm to figure out MPI task-specific inclusion arrays. To generate the task-specific inclusion arrays, we must know the global inclusion array, how many valence bands the MPI task has been assigned, how many conduction bands the task has been assigned, and the indexing of these valence and conduction bands in the native distribution scheme (i.e., the native distribution scheme tells us that MPI task 2 needs the "first two" valence bands and the "second two" conduction bands; see Figure 6.4). In our example, this becomes Figure 6.5.

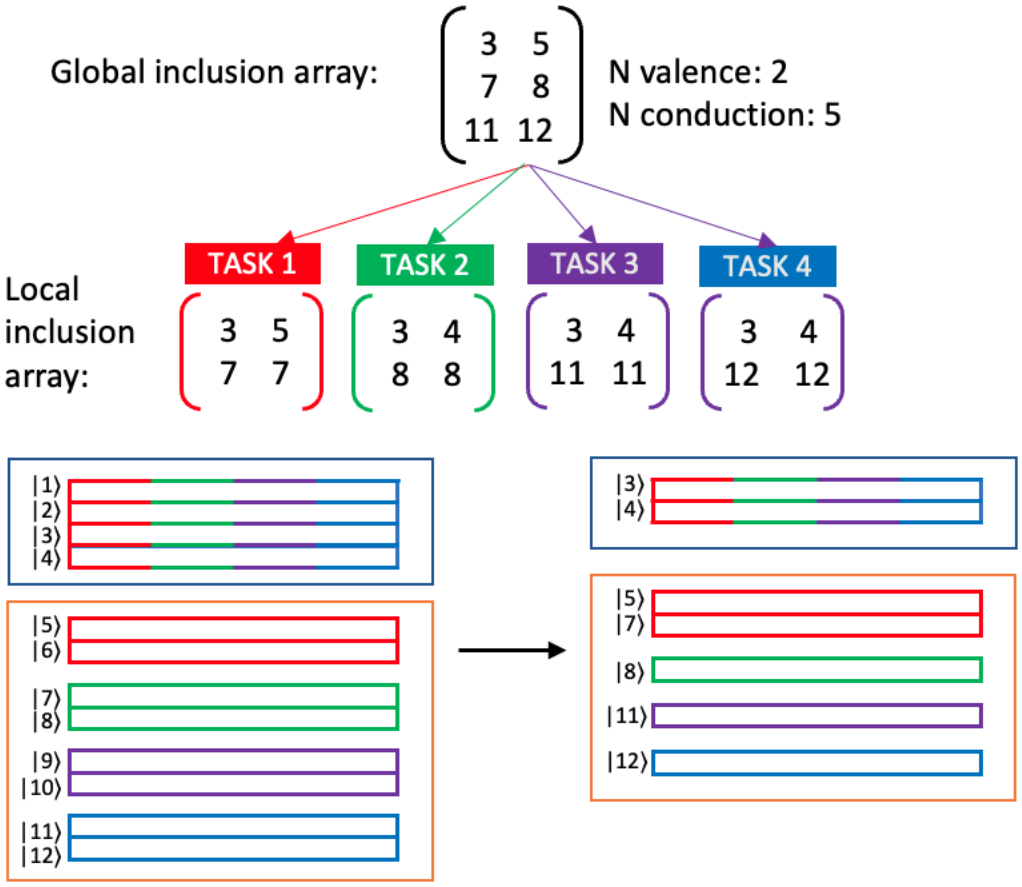

Figure 6.5 Schematic of the full subspace summation read-in algorithm. The new number of valence and conduction bands are computed from the global inclusion array, which allows us to produce the distribution shown in Figure 6.4. Given the number of valence and conduction bands and the global inclusion array, task-specific inclusion arrays are created, which dictate how to form the hyperslabs utilized in the HDF5 read-in. Finally, given the global inclusion array, we can properly index the bands in the subspace calculation.

Now that each task has its own inclusion array, we can begin building the HDF5 hyperslabs necessary to read in the band ranges that the task needs. By design, each row in the task-specific inclusion array represents one of the HDF5 hyperslabs that the task will take the union of. That is, the task loops over the number of rows in the task-specific inclusion array (i.e. the number of hyperslabs to union), creates a hyperslab for each row in the inclusion array based on its corresponding band range, and then union this hyperslab with previous hyperslabs in the

loop, in order to construct the complete hyperslab that will read in all of the bands that the MPI task needs from the HDF5 file simultaneously.

After this HDF5 read completes, each task has the band information that it requires. The rest of the code is unaware of the re-indexing that has taken place. Because the band energies are read into an array from the wavefunction file, we must re-index the band energies to match the included bands only. In our example, the eigenenergies array would look something like eigenenergy(k-point, band, spin) where "band" ranges from 1 to 12. We must re-index this array so that it ranges from 1 to 7 only, and these 7 energies correspond to the bands that were included (3 → 1, 4 → 2, 5 → 3, 7 → 4, 8 → 5, 11 → 6, 12 → 7). This can be done straightforwardly given the global inclusion array information. Once this re-indexing is complete, the code can proceed as normal, computing what appears to be equation 6.4 with n = 1, 2 and n' = 1, .., 5 but is, in actuality, equation 6.5 instead. We call this method subspace summation, as it sums over (valence, conduction) pairs in a subspace of only the included bands.

In order to verify the accuracy of the implementation, we can test in several ways. First, we can employ the previous method that can exclude the contiguous lowest energy bands, and compare the results of this calculation to a subspace summation calculation where the subspace corresponds to all bands except these lowest energy bands. There is also a BerkeleyGW keyword to "cap" the number of conduction bands (e.g., include only the first n conduction bands, when the wavefunction file may contain $m > n$ conduction bands total). We can again compare the results of this capped calculation to a subspace summation calculation whose range caps at this same value n. However, neither of these methods can test the accuracy of a subspace summation calculation in which non-contiguous blocks of bands are included. To do this, we can directly compare our read-in wavefunction array and corresponding eigenenergies to the "full"

wavefunction arrays and eigenenergies by printing out each of these quantities, to ensure that we have properly read-in and indexed the included bands and their energies. Now that we have a tested, working implementation of our subspace summation method, we can apply it to some problem of interest.

6.2.2 Example Computation

We choose to apply the new subspace summation method to GaN. In GaN, free valence electrons give rise to a collective (plasmon) mode. This mode appears in the low-loss region of EELS. It has been shown by Dhall, et al. that as the Ga content of epitaxial quantum wells of AlGaN is increased, the plasmon mode using experimental EELS develops two shoulder peaks.[3] That is, AlN demonstrates a single, uniform peak, while GaN contains two shoulders, and quantum wells of mixed content smoothly vary between the two (i.e. as Ga content is increased and Al content is decreased, EELS reveals the two shoulder peaks growing).

The computed band structure of GaN is shown in Figure 6.6. The lowest-lying states are nitrogen s-states. Next, there is an energy region containing Gallium d-states. Finally, the valence bonding states lie near the Fermi energy. AlN contains no d-band region. Since the Gallium d-states are nestled between states that we want to include in the calculation (the valence states and the nitrogen s states), this is an ideal system with which to apply our new subspace summation method.

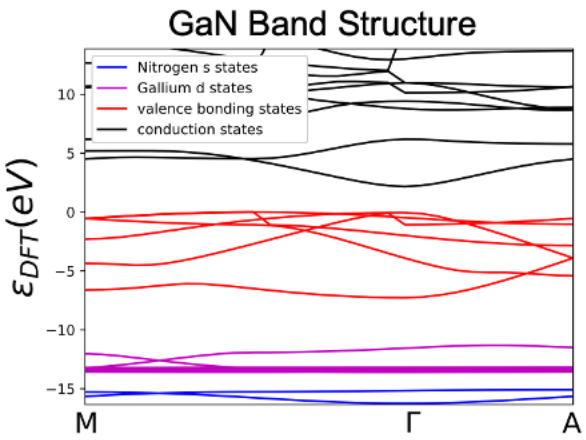

Figure 6.6 Band structure of GaN. Bands are colored by atomic orbital projections, and show clear energy gaps between the N s-states, the Ga d-states, the valence states, and the conduction states. Figure received in a private correspondence.[19]

We compute three separate EEL spectra: a full calculation including all occupied states, a subspace summation calculation that excludes the Gallium d-states, and a subspace summation calculation that includes only the Ga d-states (i.e., excludes the Nitrogen s-states and the valence bonding states). The results of these calculations are shown in Figure 6.7. These results reveal interference effects between the Ga d-states and valence electrons. The all-states peak downshifts relative to the d-state-excluded peak, which is consistent with the results found in [3]. In the subspace summation calculation of only Ga d-states, we see only a small and very broad signal, suggesting that it is particularly the interaction of the Ga d-states with the valence bonding states that give rise to the additional spectral features.

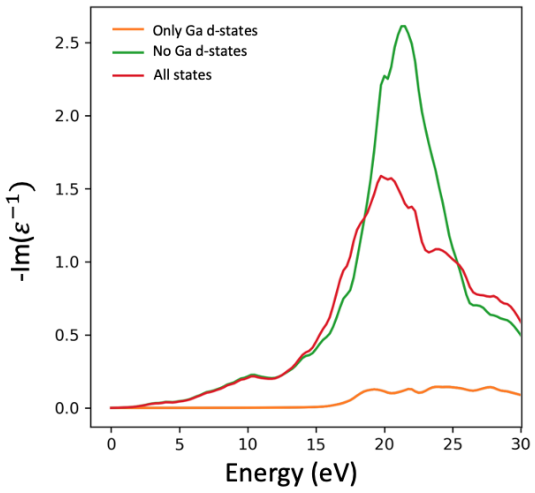

Figure 6.7 EELS of GaN for an all-bands calculation and two subspace summation calculations. Red line corresponds to all states. Green corresponds to a subspace summation calculation with the Ga d-states excluded, and orange corresponds to a subspace summation calculation with the valence states and N s-states excluded (i.e., only Ga d-states included as occupied states).

Finally, we can use this system as a test for the computational gains of the subspace summation method. These results are shown in Table 6.1. Since the polarizability is obtained in part by computing all of the (valence, conduction) pairs, and there are typically more conduction bands than valence bands, substantial savings can be obtained by excluding valence bands that do not strongly affect the polarizability (and therefore EEL spectrum, also). We note that the bands excluded in the timing table *do* affect the EEL spectrum, so treating the method like a restricted active space calculation is not appropriate in this case. Regardless, the timings reveal that when the eight gallium d-states are excluded, the run-time decreases by nearly half. When only the 10 valence non-Ga d-states are included, we see a similar decrease in run time.

Table 6.1 Run time in seconds of the three calculations shown in Figure 6.7.

	All states	No Ga d-states	Only Ga d-states
Time (s)	126.6	61.6	72.8
Total number of states	150	140	142

6.2.3 Conclusion

We have successfully implemented a subspace summation method for the computation of polarizability and dielectric in the BerkeleyGW code, which can be used to obtain EEL spectra. This method allows us to study specific band contributions to the polarizability. We apply this method to GaN (building on previous theoretical calculations of a collaborator, ref. [3]), which shows how interaction between Ga d-states and valence bonding states yield the shoulder peaks. We examine how the exclusion of states affects the timings of the calculations, finding that excluding states can result in significant savings, on account of the number of coupling elements in equation 6.3 that must be computed for a given valence band.

6.3 Partial Occupations

6.3.1 Introduction

We are interested in the plasmon properties of noble metal nanoparticles. The subspace summation method provides a tool to probe how bands originating from a part of the system (e.g., in the Ga d-states in GaN) can affect the plasmon mode of the system as a whole. Thus, we can apply this new development to chemical interface damping, analyzing how interacting adsorbate states influence the plasmon mode of a noble metal, as shown in Chapter 5 for H_2 on

Au(111). However, the subspace summation development alone is incomplete to study this problem.

Because we are interested in plasmon properties of metals specifically, we benefit from implementing partial occupations in the BerkeleyGW code. The BerkeleyGW code is massively parallel, and can scale across tens of thousands of CPUs. BerkeleyGW has, in one instance, achieved 100s of petaflops-level performance, scaling across over 27,000 GPUs.[20] BerkeleyGW achieves this massive scalability through its highly efficient parallelism (discussed more in Chapter 7). The numerous parallelism schemes employed in BerkeleyGW are tied closely to the physics of the code. In fact, exploiting this tie between the parallelism and the physics is how the first development discussed in this chapter, the subspace summation method, is implemented. However, BerkeleyGW was originally developed as a code for semiconductors.[1,2] Because semiconductors have clearly defined occupation factors (1 or 0), BerkeleyGW is able to make simplifications to the equations it implements, and is able to employ parallelism schemes based on these simplifications to obtain the coupling elements between occupied and unoccupied states (e.g., equation 6.3 compared to 6.2. In 6.2 n, n' run over occupied and empty bands respectively because of the definition of the occupation factor f used).

Metals have a complex electronic structure at the Fermi energy, and no well-defined band gap.[21] Quantities of interest in a periodic system represented in reciprocal space that are computed via a sum over all states (or all occupied states, like the electron density) requires an integration across the Brillouin zone.[22] Numerically, this integration is carried out on the k-point mesh.[23,24] When an occupied band crosses the Fermi energy, its occupation changes from 1 to 0. In other words, in systems with such crossings, we must integrate a discontinuous function. Thus, converging these calculations requires a very fine k-point mesh.[25] However, the steep

scaling of RPA with system size renders this type of convergence method computationally infeasible for many systems.

An alternative solution is to employ partial occupations, or "smearing," in the code. In this case, the occupation factor step function f_{ik} (where, with no smearing, $f_{ik} = 0$ if band i is unoccupied at k-point k, and 1 if band i is occupied at k-point k) is converted to a function that varies smoothly between 0 and 1 as it crosses the Fermi level, which removes the discontinuity in the occupation function, and therefore the discontinuities when integrating across the Brillouin zone. There are several schemes to define a continuous f_{ik}. We implement Gaussian smearing and Methfessel-Paxton smearing to the first order (MP1).[26,27] The principal challenge of the implementation is in determining a distribution scheme for these partially occupied states that both fully accounts for all of their interactions, or band pairings, and maintains the massive scalability of the code.

This development enables us to perform the subspace summation work in chapter 5, and facilitates the computation of metals within the BerkeleyGW codes. We stress that while some RPA packages with partial occupations already exist, in general, there is significant variation amongst RPA codes in terms of approach.[28] These differences range from formulation, basis set choices, parallelism, approximations used to achieve a particular target scaling, and a number of other algorithmic and numeric differences.[2,29–39] The lack of consensus in these areas gives rise to the diversity of implementations, applicable systems for a given implementation, and subsequent results. Our developments represent an independent algorithmic approach to partial occupations within the RPA.

6.3.2 Implementation

In BerkeleyGW, because the code was originally designed for semiconductors and thus without support for partial occupations, each band at each k-point and spin is assigned an occupation of either 0 or 1 (or 0.5 if exactly degenerate with the Fermi energy). Specifically, BerkeleyGW implements equation 6.3, which is a case of 6.2 where the occupation function *f* is given by: [2,4,5]

$$f(\epsilon) = \begin{cases} 1, & \epsilon < \mu \\ 0, & \epsilon > \mu \\ 0.5, & \epsilon = \mu \end{cases} \quad \text{(Eq. 6.6)}$$

with ϵ the energy and μ the Fermi energy. Now, we seek to implement a scheme where *f* is determined by Gaussian or MP1 smearing, with:[26]

$$f(\epsilon) = \frac{1}{2}\left(1 - \text{erf}\left(\frac{\epsilon - \mu}{\sigma}\right)\right) \quad \text{(Eq. 6.7)}$$

for Gaussian smearing and

$$f(\epsilon) = \frac{1}{2}\left(1 - \text{erf}\left(\frac{\epsilon - \mu}{\sigma}\right)\right) - \frac{1}{2\sqrt{\pi}} \frac{\epsilon - \mu}{\sigma} e^{-\left(\frac{\epsilon - \mu}{\sigma}\right)^2} \quad \text{(Eq. 6.8)}$$

for MP1 smearing, where $\sigma = k_B T$ is the broadening.[27]

We discuss in detail the parallelization scheme of the RPA polarizability matrix in the Section 6.2. To summarize, without partial occupations, the computation of the polarizability is performed by distributing (valence, conduction) state pairs across MPI tasks (see Figure 6.3). Thus, the crux of the problem is in determining how to distribute the partially occupied states, while ensuring that all (valence, conduction) pairings, which now include (valence, partial), (partial, partial), and (partial, conduction) are included in the computation of the polarizability.

As each MPI task has access to each mean-field band energy, regardless of whether the MPI task would own the corresponding band, each MPI task can create a global occupation array

that contains the occupation for each band at each k-point and each spin. It is necessary for each MPI task to compute all partial occupations, because the number of valence, conduction, and partially occupied bands determines the distribution of state pairs. The occupation is determined either through Gaussian smearing (equation 6.7), MP1 smearing (equation 6.8), or the native no-smearing scheme (equation 6.6).

Once the occupations have been determined, we must re-compute the number of valence bands (fully occupied), number of partially occupied bands, and number of conduction bands (fully unoccupied), as these values may shift after application of smearing. To classify a band as fully occupied, partially occupied, or fully unoccupied, we define an energy window about the Fermi energy. If $|\epsilon_{\text{band}} - \mu|$ falls within this energy window, then the band is classified as partially occupied. If $\epsilon_{\text{band}} < \mu - \epsilon_{\text{window}}$, then the band is classified as fully occupied. If $\epsilon_{\text{band}} > \mu + \epsilon_{\text{window}}$, then the band is classified as fully unoccupied. We visualize this in Figure 6.8. A natural way to determine the width of the energy window is as some factor of the user-provided smearing. The larger the smearing value, the wider the energy range for which bands become partially occupied. If the factor is constant regardless of the chosen smearing, this ensures that a particular occupation cut-off is applied. Specifically, we want to consider bands that have a partial occupation less than $1\text{x}10^{-6}$ to be fully unoccupied, and bands with a partial occupation greater than $1 - 1\text{x}10^{-6}$ to be fully occupied. The factor necessary to ensure this cut-off can be solved for using equations 6.7 and 6.8.

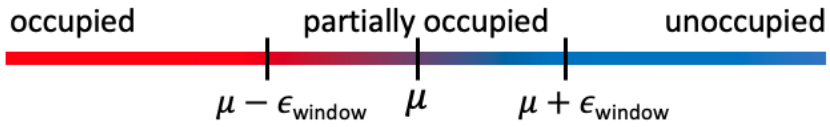

Figure 6.8 Schematic of f(ϵ) and visualization of the partially occupied window. Red color corresponds to fully occupied and blue corresponds to fully unoccupied. The gradient between red and blue represents the unoccupied states. The function used to determine this smooth transition between occupied and unoccupied can be chosen as equation 6.7 or 6.8 inside the code.

Now, with the cut-off value in hand, we can determine whether a band at a given k-point and spin is classified as fully occupied, partially occupied, or fully unoccupied by testing where its energy falls relative to the partial occupation energy window around the Fermi energy. If a band is fully occupied at some k-points but partially occupied at others, it is counted as partially occupied, and similarly, if a band is fully unoccupied at some k-points but partially occupied at others, it is counted as partially occupied. Identifying the occupation types in this way ensures that the difference in occupation factors taken in equation 6.2 will appropriately "zero out" the valence → partial pairings for the k-points at which the partially occupied band is fully occupied, and "zero out" the partial → conduction pairings for the k-points at which the partially occupied band is fully unoccupied.

Once the new number of valence, conduction, and partially occupied bands has been determined, we must distribute these bands to the MPI tasks in order to begin computation. BerkeleyGW implements equation 6.3, which is what equation 6.2 reduces to when *f* is defined as equation 6.6. To reconcile equation 6.3 with equation 6.2, in which the partially occupied states are explicitly considered, we retain the (valence, conduction) pairings for the fully occupied and fully unoccupied states. For the partially occupied states, we require four types of pairings: (valence, partial), (partial, conduction), (partial_i, partial_j), and (partial_j, partial_i) pairs,

with *i, j* denoting that both $i < j$ and $j < i$ pairing between partial bands are considered. This requirement initially appears to disrupt the distribution scheme quite significantly, since we no longer distribute over simple (valence, conduction) pairs, but instead must contend with three additional types of pairings. However, considering Figure 6.3, it suffices to count the partially occupied bands as both occupied *and* unoccupied to ensure that all four pairing types are accounted for. In the BerkeleyGW code, these pairings are computed in a nested loop. The outer-most loop runs over the number of q-vectors for which the polarizability and dielectric are computed. The next loop runs over the number of k-points, then the occupied states owned by the MPI task, then spin. Inside the spin loop, a subroutine is called that calculates the matrix elements. In this subroutine, a loop is run over the unoccupied states that the task owns. Thus, for a given occupied state owned by the task (at a particular k-point, for a particular q-point), for a particular spin, the pairing of that occupied state with each unoccupied state owned by the task is found. If a partially occupied state *i* is counted as an occupied state in this loop and partially occupied state *j* is counted as unoccupied, then all pairings (partial_i, conduction), (valence, partial_j), and (partial_i, partial_j) are computed. Now, if we count *i* and *j* both as occupied and unoccupied, then we additionally find the pairings (partial_j, conduction), (valence, partial_i), and (partial_j, partial_i). In other words, we exhaust the pairings that we need, and we reduce a distribution problem that is complicated on the face to including partial bands in the loops over occupied and unoccupied states (i.e. consider the partial bands to be both simultaneously).

In the computation of the matrix elements, care must be taken in the computation of the energy denominator both to avoid division by zero, and to not erroneously exclude particular (partial, partial) pairings. In the code, there is a check to ensure that the energy denominator

between valence band with energy ϵ_v and conduction band with energy ϵ_c is not computed for degenerate states and to explicitly avoid forbidden pairs:

if($\epsilon_v - \epsilon_c$ < Degeneracy tolerance and $occ_v - occ_c$ > zero) then
  energy denominator = ($\epsilon_v - \epsilon_c$)
else
  energy denominator = 0
endif

On the face, this check should apply also to cases where partially-occupied bands are involved. However, if both valence and conduction are partially occupied, then ($\epsilon_v - \epsilon_c <$ Degeneracy tolerance) evaluates to false for any ($partial_i$, $partial_j$) pairings such that $\epsilon_i > \epsilon_j$. To overcome this issue, we replace the above pseudocode with the following:

if($\epsilon_v - \epsilon_c$ < 2*Energy Window and $|\epsilon_v - \epsilon_c|$ > degeneracy tolerance) then
  energy denominator = ($\epsilon_v - \epsilon_c$)
else
  energy denominator = 0
endif

We can see that all possible (valence, conduction) pairings are now accounted for, as shown in Table 6.2.

Table 6.2 Logic table. Each cell contains logic justifying why the given pairing evaluates to true.

	Conduction		
Valence		fully unoccupied	partially occupied
	fully occupied	$\epsilon_v < \epsilon_c$	$\epsilon_v < \epsilon_c$ ($\epsilon_v < \epsilon_{partial}$)
	partially occupied	$\epsilon_v < \epsilon_c$ ($\epsilon_{partial} < \epsilon_c$)	$\epsilon_v < \epsilon_c + 2\epsilon_{window}$

The (fully occupied, fully unoccupied) pairing always evaluates $\epsilon_v - \epsilon_c < 2\epsilon_{window}$ to true because $\epsilon_v < \epsilon_c$ by definition. The (fully occupied, partially occupied) case also evaluates to true by definition, because $\epsilon_v < \epsilon_{partial}$, as does the (partially occupied, fully unoccupied) case, since $\epsilon_{partial} < \epsilon_c$. Finally, the (partially occupied, partially occupied) case is covered because $\epsilon_{partial,i} < \epsilon_{partial,j} + 2\epsilon_{window}$ for any partially occupied bands *i* and *j*, because $2\epsilon_{window}$ is the energy range that defines a band as partially occupied. We no longer use this check to explicitly ensure that forbidden pairs are excluded. Instead, we guarantee this in the new occupation-based counting routine to determine the number of valence, conduction, and partially occupied bands after smearing is applied.

Now that we have all possible required pairings accounted for, all that remains is to include the occupation factor in the full computation of a given term in the sum in equation 6.2, which is straightforward, since all MPI tasks create the global array detailing the band occupations. To test the accuracy of the method, we compare the RPA energies and inverse dielectric matrix elements obtained on a 1-atom Pt system with and without smearing applied, where the smearing applied is vanishingly small. With a small enough smearing, these quantities will match to the precision for which the value is computed. For larger smearing values, we can compute by hand what the value of the partial occupations should be, then count by hand the new number of valence, partially occupied, and conduction bands, then ensure that these states are indeed distributed properly.

Lastly, we must reconcile the partial occupations work with the subspace summation work from section 6.2, since each changes the number of valence and conduction bands in the calculation. To handle cases in which partial occupations are required for a subspace summation calculation, we apply smearing and re-count the number of valence, conduction, and partially

occupied bands first. Then, we determine the new number of valence, conduction, and partially occupied bands based on the user-provided inclusion array. Like the band energies matrix discussed in the subspace summation section (6.2.1), we re-index the partial occupation array so that only the included bands are present in the array (whose indices have been shifted by the subspace summation recounting routine). Then, we re-count the number of bands again, now with the shifted occupation array and the corresponding energies of the included bands. We distribute the bands based on this updated count, then proceed with the rest of the subspace summation procedure: make the global and task-specific inclusion arrays, read-in the bands dictated by these arrays, and proceed with the rest of the calculation.

6.4 Conclusion

We have developed two methods in the BerkeleyGW code. First, we develop a method that enables the arbitrary inclusion or exclusion of bands from the calculation of the polarizability, dielectric, and inverse dielectric matrices. Such development enables us to study how individual bands or groups of bands affect these quantities and related quantities like simulated EELs. We demonstrate this method on a GaN system, in which we show how the EEL spectrum changes as we include or exclude the Ga d-states. We implement partial occupations into the RPA portion of the BerkeleyGW program while maintaining the massive scalability of the code, which enables us to study metals using modest amounts of k-points. Together, these developments enable us to study the coupling of an adsorbate to a metal, among other systems. We apply these methods in chapter 5, demonstrating both the utility of the combined partial occupations/subspace summation method and the critical importance of maintaining the scalability of the code.

6.5 References

(1) Hybertsen, M. S.; Louie, S. G. Electron Correlation in Semiconductors and Insulators: Band Gaps and Quasiparticle Energies. *Phys. Rev. B* **1986**, *34* (8), 5390–5413. https://doi.org/10.1103/PhysRevB.34.5390.

(2) Deslippe, J.; Samsonidze, G.; Strubbe, D. A.; Jain, M.; Cohen, M. L.; Louie, S. G. BerkeleyGW: A Massively Parallel Computer Package for the Calculation of the Quasiparticle and Optical Properties of Materials and Nanostructures. *Comput. Phys. Commun.* **2012**, *183* (6), 1269–1289. https://doi.org/10.1016/j.cpc.2011.12.006.

(3) Dhall, R.; Vigil-Fowler, D.; Houston Dycus, J.; Kirste, R.; Mita, S.; Sitar, Z.; Collazo, R.; LeBeau, J. M. Probing Collective Oscillation of D-Orbital Electrons at the Nanoscale. *Appl. Phys. Lett.* **2018**, *112* (6), 061102. https://doi.org/10.1063/1.5012742.

(4) Adler, S. L. Quantum Theory of the Dielectric Constant in Real Solids. *Phys. Rev.* **1962**, *126* (2), 413–420. https://doi.org/10.1103/PhysRev.126.413.

(5) Wiser, N. Dielectric Constant with Local Field Effects Included. *Phys. Rev.* **1963**, *129* (1), 62–69. https://doi.org/10.1103/PhysRev.129.62.

(6) Egerton, R. F. *Electron Energy-Loss Spectroscopy in the Electron Microscope*; Springer US: Boston, MA, 2011. https://doi.org/10.1007/978-1-4419-9583-4.

(7) Nicholls, R. J. Advances in Modelling Electron Energy Loss Spectra from First Principles. *J. Phys. Mater.* **2021**, *4* (2), 024008. https://doi.org/10.1088/2515-7639/abebd2.

(8) Hofer, F.; Schmidt, F. P.; Grogger, W.; Kothleitner, G. Fundamentals of Electron Energy-Loss Spectroscopy. *IOP Conf. Ser. Mater. Sci. Eng.* **2016**, *109*, 012007. https://doi.org/10.1088/1757-899X/109/1/012007.

(9) Mkhoyan, K. A.; Babinec, T.; Maccagnano, S. E.; Kirkland, E. J.; Silcox, J. Separation of Bulk and Surface-Losses in Low-Loss EELS Measurements in STEM. *Ultramicroscopy* **2007**, *107* (4), 345–355. https://doi.org/10.1016/j.ultramic.2006.09.003.

(10) Shu, G.-J.; Liou, S.-C.; Chun-Hsin Kuo, W.; Wu, C.-T.; Wu, P.-C.; Klingshirn, C. J.; Kwo, J.; Hong, M. Unraveling the Electronic Structures in Different Phases of Gadolinium Sesquioxides Performed by Electron Energy Loss Spectroscopy. *AIP Adv.* **2020**, *10* (10), 105022. https://doi.org/10.1063/5.0025978.

(11) Kapetanakis, M. D.; Zhou, W.; Oxley, M. P.; Lee, J.; Prange, M. P.; Pennycook, S. J.; Idrobo, J. C.; Pantelides, S. T. Low-Loss Electron Energy Loss Spectroscopy: An Atomic-Resolution Complement to Optical Spectroscopies and Application to Graphene. *Phys. Rev. B* **2015**, *92* (12), 125147. https://doi.org/10.1103/PhysRevB.92.125147.

(12) Wu, Y.; Li, G.; Camden, J. P. Probing Nanoparticle Plasmons with Electron Energy Loss Spectroscopy. *Chem. Rev.* **2018**, *118* (6), 2994–3031. https://doi.org/10.1021/acs.chemrev.7b00354.

(13) Nelayah, J.; Kociak, M.; Stéphan, O.; García de Abajo, F. J.; Tencé, M.; Henrard, L.; Taverna, D.; Pastoriza-Santos, I.; Liz-Marzán, L. M.; Colliex, C. Mapping Surface Plasmons on a Single Metallic Nanoparticle. *Nat. Phys.* **2007**, *3* (5), 348–353. https://doi.org/10.1038/nphys575.

(14) Olafsson, A.; Khorasani, S.; Busche, J. A.; Araujo, J. J.; Idrobo, J. C.; Gamelin, D. R.; Masiello, D. J.; Camden, J. P. Imaging Infrared Plasmon Hybridization in Doped Semiconductor Nanocrystal Dimers. *J. Phys. Chem. Lett.* **2021**, *12* (42), 10270–10276. https://doi.org/10.1021/acs.jpclett.1c02741.

(15) Olafsson, A.; Busche, J. A.; Araujo, J. J.; Maiti, A.; Idrobo, J. C.; Gamelin, D. R.; Masiello, D. J.; Camden, J. P. Electron Beam Infrared Nano-Ellipsometry of Individual Indium Tin Oxide Nanocrystals. *Nano Lett.* **2020**, *20* (11), 7987–7994. https://doi.org/10.1021/acs.nanolett.0c02772.

(16) Cherqui, C.; Thakkar, N.; Li, G.; Camden, J. P.; Masiello, D. J. Characterizing Localized Surface Plasmons Using Electron Energy-Loss Spectroscopy. *Annu. Rev. Phys. Chem.* **2016**, *67* (1), 331–357. https://doi.org/10.1146/annurev-physchem-040214-121612.

(17) The HDF Group. Hierarchical Data Format, Version 5, 1997. https://www.hdfgroup.org/HDF5/.

(18) Byna, S.; Breitenfeld, S.; Dong, B.; Koziol, Q.; Pourmal, E.; Robinson, D.; Soumagne, J.; Tang, H.; Vishwanath, V.; Warren, R. ExaHDF5: Delivering Efficient Parallel I/O on Exascale Computing Systems. *J. Comput. Sci. Technol.* **2020**, *35* (1), 145–160. https://doi.org/10.1007/s11390-020-9822-9.

(19) Derek Vigil-Fowler. GaN bandstructure. (private correspondence) 2019.

(20) Ben, M. D.; Yang, C.; Li, Z.; Jornada, F. H. da; Louie, S. G.; Deslippe, J. Accelerating Large-Scale Excited-State GW Calculations on Leadership HPC Systems; IEEE Computer Society, 2020; pp 1–11. https://doi.org/10.1109/SC41405.2020.00008.

(21) *Introduction to Solid State Physics, 8th Edition | Wiley*. Wiley.com. https://www.wiley.com/en-us/Introduction+to+Solid+State+Physics%2C+8th+Edition-p-9780471415268 (accessed 2022-11-30).

(22) Blöchl, P. E.; Jepsen, O.; Andersen, O. K. Improved Tetrahedron Method for Brillouin-Zone Integrations. *Phys. Rev. B* **1994**, *49* (23), 16223–16233. https://doi.org/10.1103/PhysRevB.49.16223.

(23) Monkhorst, H. J.; Pack, J. D. Special Points for Brillouin-Zone Integrations. *Phys. Rev. B* **1976**, *13* (12), 5188–5192. https://doi.org/10.1103/PhysRevB.13.5188.

(24) Evarestov, R. A.; Smirnov, V. P. Modification of the Monkhorst-Pack Special Points Meshes in the Brillouin Zone for Density Functional Theory and Hartree-Fock Calculations. *Phys. Rev. B* **2004**, *70* (23), 233101. https://doi.org/10.1103/PhysRevB.70.233101.

(25) Choudhary, K.; Tavazza, F. Convergence and Machine Learning Predictions of Monkhorst-Pack k-Points and Plane-Wave Cut-off in High-Throughput DFT Calculations. *Comput. Mater. Sci.* **2019**, *161*, 10.1016/j.commatsci.2019.02.006. https://doi.org/10.1016/j.commatsci.2019.02.006.

(26) Fu, C.-L.; Ho, K.-M. First-Principles Calculation of the Equilibrium Ground-State Properties of Transition Metals: Applications to Nb and Mo. *Phys. Rev. B* **1983**, *28* (10), 5480–5486. https://doi.org/10.1103/PhysRevB.28.5480.

(27) Methfessel, M.; Paxton, A. T. High-Precision Sampling for Brillouin-Zone Integration in Metals. *Phys. Rev. B* **1989**, *40* (6), 3616–3621. https://doi.org/10.1103/PhysRevB.40.3616.

(28) Barker, B. A.; Deslippe, J.; Lischner, J.; Jain, M.; Yazyev, O. V.; Strubbe, D. A.; Louie, S. G. Spinor GW/Bethe-Salpeter Calculations in BerkeleyGW: Implementation, Symmetries, Benchmarking, and Performance. *Phys. Rev. B* **2022**, *106* (11), 115127. https://doi.org/10.1103/PhysRevB.106.115127.

(29) Harl, J.; Kresse, G. Cohesive Energy Curves for Noble Gas Solids Calculated by Adiabatic Connection Fluctuation-Dissipation Theory. *Phys. Rev. B* **2008**, *77* (4), 045136. https://doi.org/10.1103/PhysRevB.77.045136.

(30) Schurkus, H. F.; Ochsenfeld, C. Communication: An Effective Linear-Scaling Atomic-Orbital Reformulation of the Random-Phase Approximation Using a Contracted Double-Laplace Transformation. *J. Chem. Phys.* **2016**, *144* (3), 031101. https://doi.org/10.1063/1.4939841.

(31) Furche, F. Developing the Random Phase Approximation into a Practical Post-Kohn–Sham Correlation Model. *J. Chem. Phys.* **2008**, *129* (11), 114105. https://doi.org/10.1063/1.2977789.

(32) Nguyen, H.-V.; de Gironcoli, S. Efficient Calculation of Exact Exchange and RPA Correlation Energies in the Adiabatic-Connection Fluctuation-Dissipation Theory. *Phys. Rev. B* **2009**, *79* (20), 205114. https://doi.org/10.1103/PhysRevB.79.205114.

(33) Del Ben, M.; Hutter, J.; VandeVondele, J. Electron Correlation in the Condensed Phase from a Resolution of Identity Approach Based on the Gaussian and Plane Waves Scheme. *J. Chem. Theory Comput.* **2013**, *9* (6), 2654–2671. https://doi.org/10.1021/ct4002202.

(34) Hehn, A.-S.; Tew, D. P.; Klopper, W. Explicitly Correlated Ring-Coupled-Cluster-Doubles Theory. *J. Chem. Phys.* **2015**, *142* (19), 194106. https://doi.org/10.1063/1.4921256.

(35) Eshuis, H.; Yarkony, J.; Furche, F. Fast Computation of Molecular Random Phase Approximation Correlation Energies Using Resolution of the Identity and Imaginary Frequency Integration. *J. Chem. Phys.* **2010**, *132* (23), 234114. https://doi.org/10.1063/1.3442749.

(36) Yan, J.; Li, L.; O'Grady, C. Graphics Processing Unit Acceleration of the Random Phase Approximation in the Projector Augmented Wave Method. *Comput. Phys. Commun.* **2013**, *184* (12), 2728–2733. https://doi.org/10.1016/j.cpc.2013.07.014.

(37) Kaoui, F.; Rocca, D. Random Phase Approximation Correlation Energy Using a Compact Representation for Linear Response Functions: Application to Solids. *J. Phys. Condens. Matter* **2016**, *28* (3), 035201. https://doi.org/10.1088/0953-8984/28/3/035201.

(38) Ren, X.; Rinke, P.; Blum, V.; Wieferink, J.; Tkatchenko, A.; Sanfilippo, A.; Reuter, K.; Scheffler, M. Resolution-of-Identity Approach to Hartree–Fock, Hybrid Density Functionals, RPA, MP2 and GW with Numeric Atom-Centered Orbital Basis Functions. *New J. Phys.* **2012**, *14* (5), 053020. https://doi.org/10.1088/1367-2630/14/5/053020.

(39) Scuseria, G. E.; Henderson, T. M.; Sorensen, D. C. The Ground State Correlation Energy of the Random Phase Approximation from a Ring Coupled Cluster Doubles Approach. *J. Chem. Phys.* **2008**, *129* (23), 231101. https://doi.org/10.1063/1.3043729.

Chapter 7 - Parallel I/O High Performance Computing Developments

7.1 Introduction

BerkeleyGW is a highly accurate, massively parallel *ab initio* quantum mechanics-based physics code used to understand the electronic structure and optical properties of molecules, solids, and surfaces, with a focus on structures that contain translational symmetry.[1–3] The code is a solid-state physics-based implementation of the GW method, which can be thought of as a systematic improvement to quantum mechanical mean-field theories like density functional theory.[4] The GW method enables quantitative calculation of quantities like band gaps, carrier lifetimes, plasmon energies, and more.[5,6] BerkeleyGW was originally developed to run optimally on massively parallel machines, and today scales favorably to hundreds of thousands of cores, enabling GW calculations on systems of thousands of atoms.[7-9] However, the parts of the code employ a wavefunction parallel file I/O algorithm that creates a bottleneck with large wavefunction files. BerkeleyGW must read in the necessary mean-field quantities as a starting point for the calculation, and this read-in process can consume an outsized portion of wall time. For example, in a private communication sent to me, a collaborator noted that on a BerkeleyGW calculation of 78 atoms across 14,400 CPU cores, 80% of the 1-hour wall run time was spent reading in the mean-field wavefunction.[8] In this work, we alleviate this severe file I/O bottleneck by developing an HDF5-enabled read-in method for the mean-field wavefunction in two portions of the BerkeleyGW code, replacing the present method of reading in a Fortran binary file. This work enhances the efficiency of the BerkeleyGW code, enabling calculations on larger structures by conserving compute hours for systems that may require thousands of CPUs.

The pre-existing wavefunction read-in method involves reading and broadcasting the mean-field wavefunction bands one at a time from a Fortran binary file. The method reads the mean-field wavefunction over two large loops: over the k-point dimension and over the band dimension of the wavefunction file. For each band, for each k-point, the master MPI task reads a band from the binary file, then broadcasts the data to all worker MPI tasks. If a given MPI task requires the broadcasted band, then it stores and sorts the band into an MPI task-specific wavefunction array. If an MPI task does not need the band, it discards it and waits for the master task to send the next band. This is visualized in the flowchart in Figure 7.1.

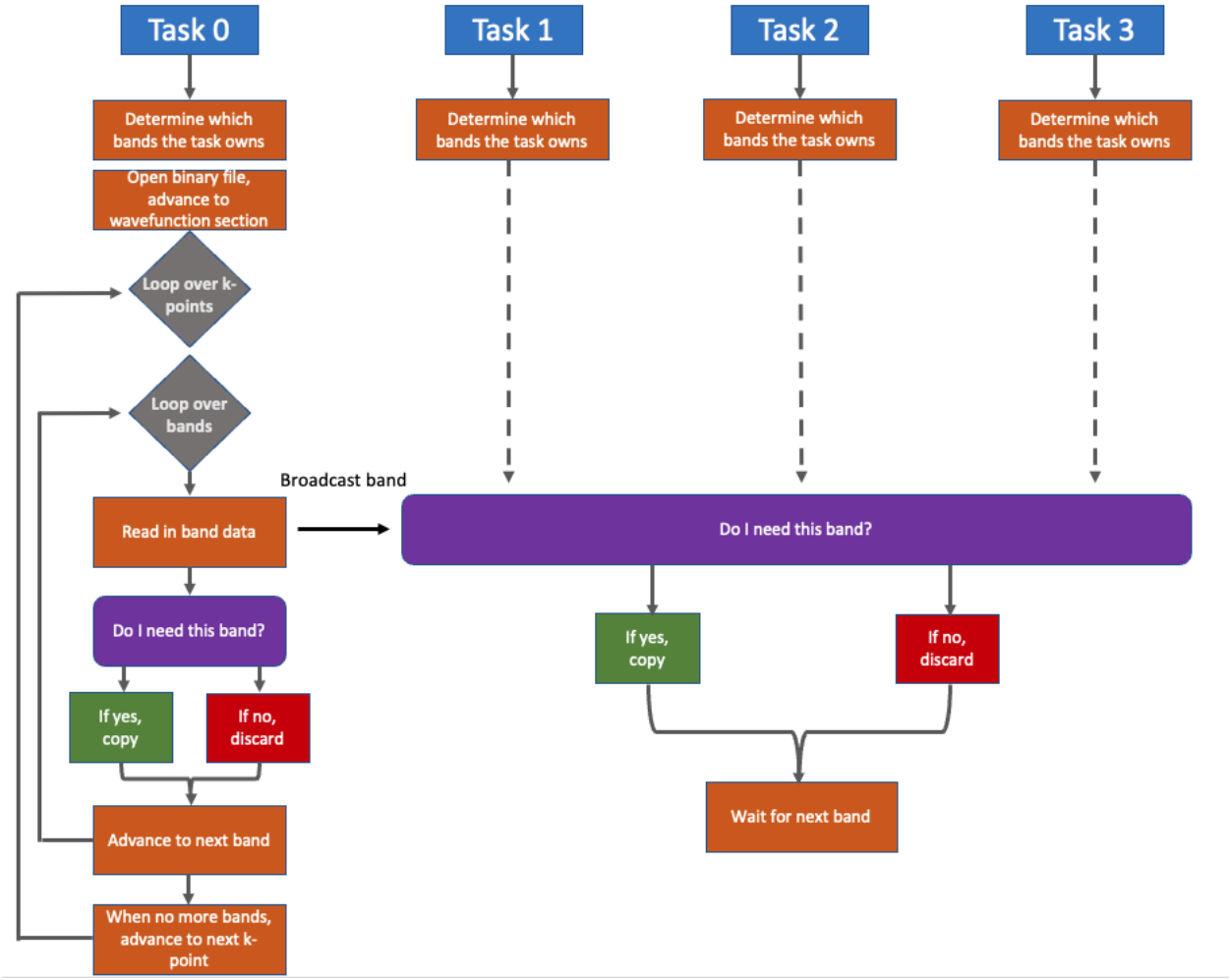

Figure 7.1 Flowchart of Sigma code read-in and distribution of binary wavefunction file.

This design works well for modestly sized systems that, in my benchmarking, utilize fewer than 100 MPI tasks and are less than 1 GB in size. The I/O performance becomes increasingly sluggish as the size of the system grows. The number of k-points and bands, and the g-vectors that constitute the size of the bands, grow with the system size, which increases the amount of data that must be sent, either through the number of broadcast calls required, or the amount of data being sent per call. Further, as the calculation size grows, the user must request more computational resources for the calculation to complete within a reasonable time frame and

avoid running out of memory, which means that during the broadcasting process, more MPI tasks must receive the data, accumulating additional communication overhead, depending on the available hardware and broadcast algorithm used.[9,10] Thus, as state-of-the-art high performance computing evolves to ever-more compute nodes, the read-in method places increasing stress on the HPC, despite the near-perfect scaling of the core of the code.[7]

Implementing an HDF5 version of the wavefunction read-in process serves as an appealing solution to this problem. HDF5 stands for "hierarchical data format," and is a data format that can efficiently write, read, and store large quantities of information and associated metadata.[11] With the HDF5 data format comes a set of flexible and performant MPI-I/O based file I/O calls that can be invoked inside of a program.[12] These calls allow for parallel access to HDF5-formatted files, and data can be read into a program in arbitrary sized and shaped "chunks" called hyperslabs.[11] While other parallel file I/O libraries exist, like Parallel netCDF[13] and ADIOS,[14] HDF5 is popular for scientific applications, and can achieve performance that approaches the maximum practical performance of the distributed filesystem it sits atop.[15,16] Further, there is pre-existing HDF5 functionality in the epsilon executable of the BerkeleyGW code. Thus, precedence, performance, and ease-of-use encourage the use of HDF5 over other parallel I/O middleware.

The HDF5 library acts as an intermediate layer between the developer and MPI-IO routines. Thus, an alternative option would be to work directly with MPI-IO. However, the Fortran binary files that MPI-IO reads can suffer portability issues, while HDF5 files are highly portable across operating systems. HDF5 bindings exist for a number of languages, like Fortran, C, and python. Further, HDF5 is relatively user-friendly compared to MPI-IO, and can see similar performance.[16] Thus, there is no clear advantage to working directly with MPI-IO.

Similar to MPI-IO, HDF5's parallel library makes use of MPI communicators to allow all processes to communicate. Once a file is opened, processes can access any part of the file or any object in the file. HDF5 manages the minutia of MPI-IO for the developer.

In this work, we develop a method of reading a highly multi-dimensional wavefunction quantity from an HDF5 file to a wavefunction structure in the BerkeleyGW code. This structure depends on the reciprocal-space basis vectors $\{\boldsymbol{G}\}$ along with the band number *n*, the k-point **k**, and the spin. Each of these quantities contributes to the dimensionality of the wavefunction. The BerkeleyGW code is divided into several main executables: the epsilon executable, which computes the random phase approximation polarizability and inverse dielectric matrix, the sigma executable, which computes the GW quasiparticle energies, the kernel executable, which computes electron-hole interactions, and the absorption executable, which computes excitation energies and excitons via the Bethe-Salpeter equations. In this work, we focus on the sigma and absorption parts of the code. First, we discuss the sigma code, our new approach, and benchmarks on the new approach.

7.2 Sigma Code

7.2.1 Overview

The sigma code computes the quasiparticle energies, E^{qp}, from the following equation:[1]

$$\langle n\boldsymbol{k}|\sum\quad|n\boldsymbol{k}\rangle = -\sum_{\boldsymbol{q},\boldsymbol{G},\boldsymbol{G}'}\sum_{\boldsymbol{n}''}\langle n\boldsymbol{k}|e^{-i(\boldsymbol{q}+\boldsymbol{G})\cdot\mathbf{r}}|n''\boldsymbol{k}-\boldsymbol{q}\rangle\langle n''\boldsymbol{k}-\boldsymbol{q}|e^{i(\boldsymbol{q}+\boldsymbol{G})\cdot\mathbf{r}}|n\boldsymbol{k}\rangle F(\boldsymbol{q},\boldsymbol{G},\boldsymbol{G}')$$

(eq. 7.1)

The quantities $|n\boldsymbol{k}\rangle$ represent a given *n* band at k-point **k**. *M* is the coupling matrix element, the same as in equation 6.3. *F* is a term collecting the details of different implementations of eq. 7.1

that are not relevant to our developments (see section 4.3 of ref [1]). $\boldsymbol{G}, \boldsymbol{G}'$ are the basis vectors. The "outer" wavefunction refers to the set of bands for which the quasiparticle energy corrections (eq. 7.1) are to be calculated, and are called "outer" because they appear in the bra and ket of $\langle n\boldsymbol{k}|\sum|n\boldsymbol{k}\rangle$. The "inner" wavefunctions refers to the bands that appear as $|n''\mathbf{k}\text{-}\mathbf{q}\rangle\langle n''\mathbf{k}\text{-}\mathbf{q}|$ on the *inside* of the equation. Note that **q**, the transition vector, is defined as $\mathbf{q} = \mathbf{k} - \mathbf{k}'$, so that $\mathbf{k} - \mathbf{q} = \mathbf{k}'$, another k-point. The sum over the finite, truncated set of inner wavefunctions is an approximation to the resolution of identity, with $\hat{1} = \sum_{n''}^{\infty}|n''\boldsymbol{k} - \boldsymbol{q}\rangle\langle n''\boldsymbol{k} - \boldsymbol{q}|$. Thus, the number of requested inner bands is directly related to the convergence of the calculation, and it is almost always the case that many more inner bands must be read in relative to the number of outer bands. One outer band may need 100s or 1000s of inner bands to achieve reasonable convergence. Further, the inner and outer bands do not necessarily have to originate from the same mean-field calculation, which allows the user to construct the sigma operator in one basis (inner), but evaluate in another (outer),[1] though such a choice is less common. Thus, the code may read in one or two mean-field wavefunction files.

Whether the code requires one or two mean-field wavefunction files, the approach is the same. The crux of the problem is to ensure that each MPI task receives the set of bands, k-points, g-vectors, and spins describing the wavefunction that the MPI task needs to compute its assigned sigma quantities, and that this process is completed as quickly as possible. For a given outer band, the code must compute every possible pairing between that outer band and all inner bands. The sigma code employs a two-fold parallelization scheme. First, MPI tasks are divided into "pools," where each MPI task in a pool is assigned the same outer bands, and these outer bands are divided round-robin amongst the pools. In other words, each pool is responsible for a subset of the quasiparticle energies to be computed. Then, each task in the pool is assigned a separate

set of contiguous inner bands, and this task is responsible for computing each of the "pairings" of eq. 7.1 between the outer bands assigned to its pool, and the inner bands assigned only to the MPI task. Such as a scheme can be visualized in Figure 7.2 for a calculation with four MPI tasks, four outer bands, and 8 inner bands. The number of pools is determined in a pre-existing algorithm in BerkeleyGW that minimizes the memory requirements across MPI tasks.

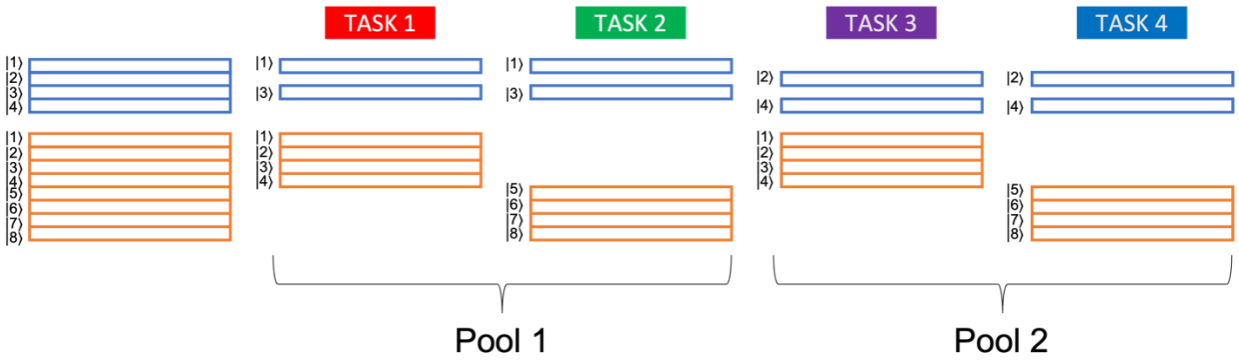

Figure 7.2 Distribution scheme of Sigma code for an example with four MPI tasks, four outer bands, and eight inner bands. MPI tasks in a given pool share the same outer bands.

7.2.2 Implementation

The sigma code works as follows: the main executable calls the input module almost immediately. Here, we read the sigma input file that specifies the number of inner and outer bands requested, among other user-specified calculation parameters. Then, we determine the distribution scheme, which sets the number of pools and assigns each MPI task its set of inner and outer bands. Next, we proceed to the actual wavefunction read-in. This is the pre-existing binary read-in routine that executes an MPI broadcast call for each band, for each k-point. Upon completion, this routine populates the wavefunction arrays (inner and outer). Once setup is complete, we return to the main executable, which uses these wavefunction quantities to compute eq. 7.1.

For this work, we create a new subroutine that will be called in place of the standard read-in routine when HDF5 functionality is requested by the user. Inside the new routine, four tasks must be completed. First, we must read the inner wavefunction into the code and store its quantities in memory such that, in the end of the routine, each MPI task is given the data corresponding to its assigned set of (bands, k-points, spin). Then, we must sort the inner wavefunction data so that its organization matches the internal wavefunction structure, since the wavefunction as stored in the HDF5 file is not stored with the same layout. Third, we must read in the outer wavefunction, which may or may not be the same as the inner wavefunction. Finally, we sort the outer wavefunction. We note that sorting the subset of the wavefunction belonging to each MPI task, in both the inner and outer case, represents a trivial amount of time relative to the wavefunction reading. We do not benchmark these steps, and focus only on the time it takes to read the wavefunction file.

The inner wavefunctions are distributed in contiguous blocks (see Figure 7.2). We can match this distribution pattern in the HDF5 read-in routine with the HDF5 construct "hyperslabs," which are specified slices of data within an HDF5 array object to be manipulated. To create a hyperslab, special HDF5 variables must be set that specify the "count," or the number of quantities in a given dimension of the array, and the "offset", or where the data starts in a given dimension, for each MPI task (see section 2.3.3). In the HDF5 wavefunction file, the k-points are implicit by stacking g-vectors. The g-vector dimension count is set as the total number of inner wavefunction g-vectors, since we want all g-vectors for all k-points. The count in the spin dimension is the total number of spin dimensions (spin*spinor). The count in the band dimension is the number of inner bands that the MPI task has been assigned. If the number of MPI tasks is not evenly divisible into the number of inner bands, then the count will vary by MPI

task. The offset in the band dimension is the first band that the specific MPI task is responsible for, which we determine from the input distribution scheme, which assigns inner bands to MPI tasks. Luckily, in the case of the Sigma code, the data as-arranged in the HDF5 file is written such that for each band, the g-vectors (stacked, for all k-points) and spin are stored contiguously, so that for a given set of adjacent bands, all associated data is also memory-contiguous. We will find that in the case of the absorption code, such fortune escapes us.

Once the inner wavefunction data has been read, it must be sorted to match the expected wavefunction structure required by the rest of the program. This sorting is simplified relative to the binary routine, because in the HDF5 routine, the MPI task already owns a wavefunction subset containing only the inner bands it needs. It only needs to re-index these quantities to reflect how the wavefunction needs to be organized so that other parts of the program can use it. Once this is complete, the inner wavefunction is ready to be used.

The outer wavefunction read-in is more complicated than the inner wavefunction read-in because the outer bands that a given MPI task owns are not contiguous with each other whenever there is more than one distribution pool, since outer bands are distributed to pools round-robin. If there is only one pool, then the method described for the inner wavefunction directly applies to the outer wavefunction, as the outer bands are guaranteed to be contiguous in memory. Otherwise, we must take a different approach.

We use different HDF5 features to overcome this limitation: striding and blocks. We keep this new method inside the same read routine for the sake of consistency and clarity, since it accomplishes the same task as the rest of the routine, albeit in a different way. If a stride in a given array dimension is set to integer n, then HDF5 will read in every n^{th} entry of that dimension. The pools are organized so that, if there are m pools, then each pool gets every m^{th}

outer band, where the first pool starts at the first band, and the m^{th} pool starts at the m^{th} band. Thus, we can set the stride in the band dimension to be the number of pools, and the offset to be the rank of the pool (e.g., pool 1, pool 2, etc.). HDF5 blocks give the size of the data in each stride. Since we are only taking one band per stride, the block size in the band dimension is 1. The count in the band dimension is the number of outer bands that the MPI task has been assigned, and the g-vector count is the sum of the g-vector coefficients associated with the outer bands. The spin count, as well as all other offsets, remain the same as the inner case.

Once the read is complete, the outer wavefunction is sorted, then the routine exits back to input, and the program moves on. Since the HDF5 routine returns the exact same quantities as the original binary routine (though with drastically different inner workings), no further changes need to be made to the code, and the rest of the calculation proceeds as normal. Ensuring the accuracy of the new read-in method is straightforward. Since both read routines output the exact same wavefunction quantities, we can modify the code to read in the wavefunction with both methods into separate wavefunction arrays, then check equality between these two arrays.

7.2.3 Benchmarking

We test and benchmark the new implementation on two different systems, the K-State HPC cluster, Beocat, and the National Renewable Energy Lab HPC, Eagle. Beocat is a system in which heterogenous hardware communicates through heterogenous interconnects, and Eagle is a system in which all hardware and interconnects are completely homogenous (i.e., all compute nodes are the exact same). Since we seek to improve the amount of real-time it takes for wavefunction read-in to occur, we measure wall time rather than node-hours.

We report performance for three different systems. Key parameters of these systems are summarized in Table 7.1:

Table 7.1 Summary of benchmark systems.

	inner bands	outer bands	k-points	g-vectors	spin	HDF5 file size
Small system	18	10	1	2897	1	184 Kb
Medium system	50	12	31	55967	1	203 Mb
Large system	4000	40	4	910383	1	123 Gb

We benchmark the small and medium system on Beocat, restricting to nodes with 2x 8-core Xeon E5-2690 processors, 64 GB ram, and 10 Gb/sec quad data-rate (QDR) infiniband. Three runs were performed for each system. We benchmark the medium and large system on NREL's supercomputer Eagle, with 2x Xeon Gold Skylake 6154 18-core processors, 96 GB ram, and 100 Gb/sec enhanced data-rate (EDR) infiniband. Since the NREL system charges by core hour, we ran each Eagle benchmark only once. Note that in the results tables below, the HDF5 version reports a timing for both the inner and outer wavefunction read-in, while the binary method has only one timing. This is because the binary method performs both simultaneously. On Eagle, we use OpenMPI 3.6.1 and HDF5 1.10.6. On Beocat, we use OpenMPI 3.1.3 and HDF5 1.10.5. We employ only the default OpenMPI MPI communication algorithms in all benchmarks. We implement a simple benchmarking procedure, collecting the time immediately before and after the operation under question has been executed on the master task. While this procedure ignores some of the nuance of MPI-based parallel performance benchmarking, it reasonably highlights the timing differences between the two read methods.

7.2.4 Results and Discussion

7.2.4.1 Small System

Table 7.2 Small system timings on Beocat in seconds.

	HDF5			
MPI Tasks	Inner	Outer	Total	Binary
1	0.032	0.00	0.032	0.00
2	0.038	0.00	0.038	0.00
4	0.065	0.00	0.065	0.00
8	0.046	0.00	0.046	0.001
16	1.30	0.001	1.30	0.35
32	2.65	6.98	9.63	0.49

For the small system, we observe that the HDF5 version performs worse than the binary version, shown in Table 7.2. This is a sensible result, since the bottlenecks from the binary MPI broadcast call do not occur when only a handful of small broadcasts are being made. There is overhead associated with using HDF5 that is absent for the binary file read-in, which is due to the coordinating of the simultaneous reads of multiple MPI tasks. Since only a few bands are read in, the binary method overhead is minute, while the HDF5 overhead is relatively large. We note that the 32-task outer wavefunction read-in timing is significantly higher than all other trials. This is due to the fact that many MPI tasks are trying to access the same small file at once. In fact, more MPI tasks are trying to read the file than there are bands in the file, resulting in a drastic slow-down.

7.2.4.2 Medium System

Table 7.3 Medium system timings on Beocat in seconds

	HDF5			
MPI Tasks	Inner	Outer	Total	Binary
1	0.62	0.08	0.70	0.43
2	0.48	0.07	0.55	0.51
4	0.22	0.06	0.28	0.83
8	1.05	0.07	1.12	1.00
16	2.57	2.97	5.54	1.95
32	3.68	6.84	10.52	1.19
60	4.62	19.37	23.99	1.52
80	4.88	27.03	31.92	4.48

Table 7.4 Medium system timings on Eagle

	HDF5			
MPI Tasks	Inner	Outer	Total	Binary
1	0.32	0.06	0.38	0.45
2	0.19	0.08	0.27	0.55
4	0.14	0.09	0.23	0.55
8	0.11	0.12	0.23	0.62
16	0.26	0.11	0.37	0.60
32	0.32	0.14	0.47	1.41
64	0.37	0.27	0.65	1.40
80	0.37	0.31	0.68	0.67

For the medium system on Beocat (Table 7.3), we again see that the binary method outperforms the HDF5 method. The inner timings are comparable to the binary timings. The outer timings show poor scaling with MPI task size and consume a disproportionate amount of time per band. We discuss the outer wavefunction performance in more depth in section 7.2.4.3. In the small and medium cases, we expect the binary routine to perform well. For the medium system on Eagle (Table 7.4), we see timings that are competitive with the binary routine. This is a reflection of the larger cache sizes and high-speed interconnects between nodes on Eagle relative to Beocat.

7.2.4.3 Large System

Table 7.5 Timings for large system on Eagle in seconds.

	HDF5			
MPI Tasks	Inner	Outer	Total	Binary
72	20.9	12.7	33.6	752.1
144	36.0	4.5	40.5	741.6
288	18.4	4.8	23.2	709.9
576	21.7	5.0	26.7	736.6
1296	61.7	9.6	71.3	721.0

Table 7.6 Per-band timings for large system on Eagle, s/band

	HDF5			
MPI Tasks	Inner	Outer	Total	Binary
72	0.00523	0.317	0.00832	0.186
144	0.0103	0.0424	0.0527	0.0150
288	0.0211	0.0694	0.0905	0.0289
576	0.0446	0.0920	0.137	0.0282
1296	0.108	0.0641	0.172	0.0277

For the large system on Eagle, we see favorable results, with the total wavefunction read-in time with HDF5 outperforming the binary read-in method by an order of magnitude (Table 7.5). The HDF5 method takes, at worst, 71 seconds to read in the wavefunction data, while the

binary method for the same number of MPI tasks (144) takes 742 seconds. Our method scales favorably with number of MPI tasks. Table 7.6 shows these same timings on a per-band basis (Total time/number of bands). The number of inner, outer, and total bands is 4000, 40, and 4040, respectively. We see that on a per-band basis, the inner read is significantly faster than the binary, and the outer read timings are competitive with the binary. Note that nodes on Eagle contain 36 CPU cores, so these jobs are for 16, 8, 4, and 2 nodes. For 1 node/36 cores, the wavefunction required too much memory per MPI task to be read in. We did not attempt to run this calculation on Beocat, since 72 MPI tasks was the minimum task-count that Eagle could handle for both the binary and HDF5 methods, and internode communication on Beocat is significantly slower than intranode communication.

The new HDF5 read-in method contains a check for if the number of pools is greater than 1. If so, it uses the striding-based HDF5 subroutine for the outer wavefunction read. In the small system, there is only 1 pool up until the 32-MPI task case. In the medium system, there is 1 pool until the 16-MPI task case. The significant increase in outer wavefunction read-in time at these MPI task counts reflects the use of the striding routine. The large system uses two pools for all MPI task configurations. The improved performance on Eagle over Beocat for the 16-MPI task case on the medium system is a reflection of the upgraded cache configuration and size, and data transfer speeds.

While these results establish that the HDF5 method is far superior for large-sized wavefunction files, these results are obtained using a wavefunction stored on only a single object storage target (OST). In high performance computing, typically parallel filesystems are deployed, and both Beocat and Eagle use a particular parallel filesystem implementation called Lustre. In Lustre, a file may be stored on several nodes (OSTs), split up into “chunks.” The size

of the chunks is called the stripe size, and the number of OSTs is called the stripe count. When a parallel program must read or write a large file, it benefits from the file being "striped." That is, storing parts of the file on multiple OSTs allows the MPI tasks to read the data that it needs while unimpeded by other MPI tasks trying to access the data, since file locking is managed by each OST separately. Finally, MPI-I/O provides two modes of data reading and writing, "collective" and "independent." Since HDF5 works as an intermediate layer between the developer and MPI-I/O, the MPI-I/O collective and independent modes can be set through HDF5. The MPI-I/O independent mode allows each MPI task to act completely separately from all others. The collective mode performs some "under the hood" optimizations of the read-in. For example, it may condense requested reads from multiple MPI tasks down to one MPI task, which then distributes the data to the others.[18] Thus, we next test the large wavefunction read-in performance for independent and collective MPI-I/O modes, along with the default striping (1 OST, 1 mb stripe sizes) and a stripe count of 60. These results are summarized in Table 7.7.

Table 7.7 Timings for stripe counts of one and 60, with independent and collective MPI-I/O modes for large system on Eagle with 1296 MPI tasks.

		Inner	Outer	Total
Stripe count = 60	Independent	8.19	0.883	9.07
	Collective	9.27	10.1	19.4
	Binary	-	-	721
Stripe count = 1	Independent	70.0	0.492	71.2
	Collective	62.0	9.58	71.6
	Binary	-	-	721

We find that the inner wavefunction read benefits massively from an increased stripe count, with a stripe count of 60 completing 8.5x faster for the independent case, and 6.7x faster for the collective case. We find that independent vs. collective MPI-IO modes make little difference for the inner wavefunction. Conversely, the outer wavefunction sees little performance change between 1 OST and 60 OSTs, but benefits massively from MPI-IO independent mode over collective mode. The inner wavefunction result can be explained from the fact that it allows each MPI task this "unimpeded access" to its required data, which are large, contiguous blocks of data. On the other hand, the outer wavefunction data is sufficiently small such that the striping makes little difference. However, the overhead associated with constructing an MPI-IO collective call, on account of the optimizations that MPI-IO makes, significantly impacts the read-in time of the outer wavefunction. It may not impact the inner read as the optimization overhead for the collective call may balance out with the improved speed, resulting in little performance difference between the two modes for the inner wavefunction.

7.2.5 Conclusion

We see significant performance increase on the large wavefunction read-in between the binary method and the new HDF5 method, and we tune this improvement by identifying that the wavefunction benefits from increased Lustre striping. For the large wavefunction case, we ultimately obtain a wavefunction read-in time of 9.1 seconds using 1296 MPI tasks, in contrast to the binary method, which achieves its fastest time of 710 seconds with 288 MPI tasks. Thus, we achieve a 78x speed-up in the best-case scenarios.

Additional improvements may be made to the HDF5 read-in process by altering the outer wavefunction scheme, which, in our developments, performs similarly to the binary method on a

per-band basis. We developed this read-in scheme for the general case that the outer wavefunction may not be read from the same wavefunction file as the inner wavefunction, unaware at the time of implementation that HDF5 striding would incur a large performance penalty. Because the case that the inner and outer wavefunctions come from the same wavefunction file is more common, we can develop a method that reads only the inner wavefunction file according to the inner wavefunction distribution, then further distribute the inner bands that are also required as part of the outer bands. This approach requires only a single file read and avoids the costly striding of the outer wavefunction read routine. Such a change would further accelerate the HDF5 method for its most common use-case.

7.3 Absorption Code

7.3.1 Overview

Based on the HDF5 results of the last chapter for sigma and the known performance for epsilon, alongside HDF5's general advantages over the use of Fortran binary files, we want to convert the read-in process for the remaining portions of the code to HDF5. We focus on the absorption executable, which is used to obtain optical properties via the Bethe-Salpeter equations. The absorption code is parallel over the k-point dimension of the wavefunction, whereas the sigma code discussed above, and the epsilon code discussed in Chapter 6, are both parallel over the band dimension. That is, in the absorption code, each MPI task has some k-point information for all bands, while in the sigma and epsilon codes, each MPI task has all k-point information for some bands. Thus, there is a severe mismatch in the data layout of the HDF5 wavefunction file and the parallelism of the absorption code, since the data is band-contiguous in the HDF5 file. This is a more difficult scenario than in the Sigma case. If the

wavefunction data is read-in in data-local "chunks," resulting in favorable read-in times, i.e., by reading in multiple bands at once for all k-points and for all spins, then the data must be re-distributed in a complicated way, resulting in poor MPI communication times. If the data is read-in the way that it must be distributed, by making use of HDF5 blocks and striding, then the result is poor read-in times due to the non-locality of the data in file, as was seen to a lesser degree in the read-in of the round-robin distributed outer bands in Sigma in the section 7.2. This data layout mismatch is visualized in Figure 7.3.

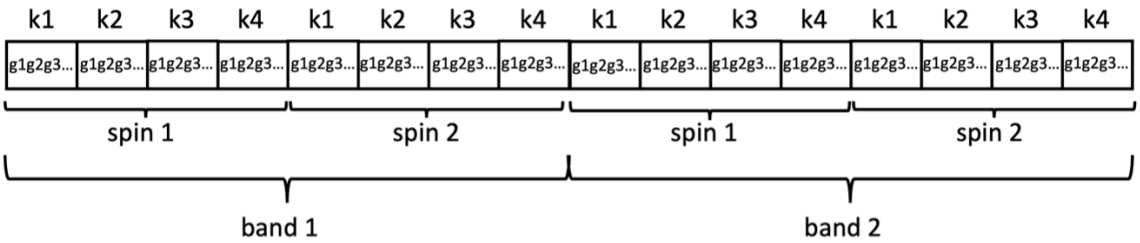

Figure 7.3 Layout in memory for two bands in a wavefunction with four k-points. g-vector coefficients for a given k-point are contiguous, then k-points for a given spin, then k-points for a given band. The data that a given MPI task needs for a given k-point is spaced (*n* k-points)*(*m* g-vectors) entries apart from each other.

The Absorption code implements three different parallelization schemes depending on thresholds between the number of k-points, number of bands, and number of MPI tasks. In each of the three cases, the code distributes k-points round-robin amongst the MPI tasks. On account of the data layout/parallelization scheme mismatch, there is no obviously best HDF5 read-in pattern to implement. Before we discuss possible HDF5 implementations, we first outline the pre-existing Fortran binary file method. In this case, the code loops over irreducible k-points and determines which MPI tasks need the wavefunction data associated with the current k-points. Note that the wavefunction file contains the irreducible set of k-points, while the code itself

distributes k-points based on the non-reduced k-grid, such that some of these k-points may reduce to the same irreducible k-point, resulting in multiple MPI tasks needing to receive the wavefunction data associated with the same irreducible k-point, despite the full grid k-points being round-robin distributed. Then, the code loops over each band, the master task reads in the current band for the current k-point, and sends this band information to all MPI tasks that need it (i.e. the MPI tasks who have been assigned the current k-point).

Since the Fortran binary method makes MPI send/receive calls for each band, for each k-point (sending the band to the MPI tasks who need the band data for the k-points they have been assigned), the result is a relatively large MPI communication overhead. In some ways, a large communication overhead is unavoidable on account of the memory layout/distribution scheme mismatch. The code cannot efficiently read a Fortran binary file "out of order" (i.e. it must read the data one band at a time). On the other hand, an HDF5 file *can* be read out of order using HDF5 strides, offsets, and blocks, but we find this results in poor performance in the sigma code. Thus, our HDF5 method will rely on a large number of MPI communications.

7.3.2 Implementations

There are many ways to approach this problem, and no obvious answer for what sort of read-in method will result in the highest performance. In the simplest case, we could implement the exact same scheme as the current binary method, except make an HDF5 read call to the HDF5 wavefunction for each band, rather than a binary read call to the binary wavefunction. This will almost certainly net no notable performance gain, but would accomplish the task of making an HDF5-compatible version of the code, and would be minimally invasive to the current scheme. Alternatively, we can make use of hybrid HDF5 read-in/MPI distribution

routines to either reduce the number of MPI calls, or make more efficient MPI calls. We explore two such options. The first step of both methods is the same: divide the number of bands into even blocks, and assign an MPI task to read that block, similar to the Sigma wavefunction inner read routine. Once each task has its assigned set of contiguous bands, the methods diverge.

The first method we call the "broadcast and sort" approach, which relies on broadcasting band data for several bands and for all k-points simultaneously, rather than making the appropriate send/receive calls for each band, for each k-point, as is done in the current binary method. In this method, we loop over MPI tasks, and broadcast the bands belonging to the current MPI task. Then, each MPI task determines whether it needs the broadcasted bands. Over a large number of bands and k-points, such a method may see significant performance improvements over the binary method because it reduces the number of MPI calls from (*n* k-points)*(*m* bands) to the number of MPI tasks. This method requires broadcasting excess data, and requires more sorting for each task, since for a given broadcast call, most tasks will not need to store most of the data. Despite that the duration of a broadcast call increases as the size of data being broadcasted increases, this method is advantageous in terms of reducing the number of MPI calls.[9,10] This chunked-broadcast method works similarly to the binary method, except instead of reading one band at a time for each k-point, it loops over MPI tasks and broadcasts the data of the current MPI task to all other tasks, then performs the exact same (k-point, band) double loop as the binary method. Except, instead of looping over all bands, it loops only over the bands that belong to the current MPI task. In this way, the broadcast method is conceptually similar to the binary method, and integrates readily into the existing routine.

The second method we call the "sort and reduce" approach. Once each MPI task has read its set of assigned contiguous bands, we loop over k-points and tasks, rather than k-points and

bands. For each k-point, every task stages the k-point data that it owns (i.e. the band data it owns for the current k-point). Then, the code loops over MPI tasks, checking if the MPI task needs the current k-point data. If so, we perform a MPI reduce call so that each task sends this staged data to the current task being looped over. This essentially involves (number of reducible k-points) MPI calls to communicate the data. However, it only sends the data that the current task needs, resulting in a smaller, but potentially more frequent, MPI communication calls. The shared set-up of the two approaches can be visualized in Figure 7.4 for two MPI tasks, with Figure 7.5a visualizing the sort-and-reduce method, and Figure 7.5b visualizing the broadcast-and-sort method.

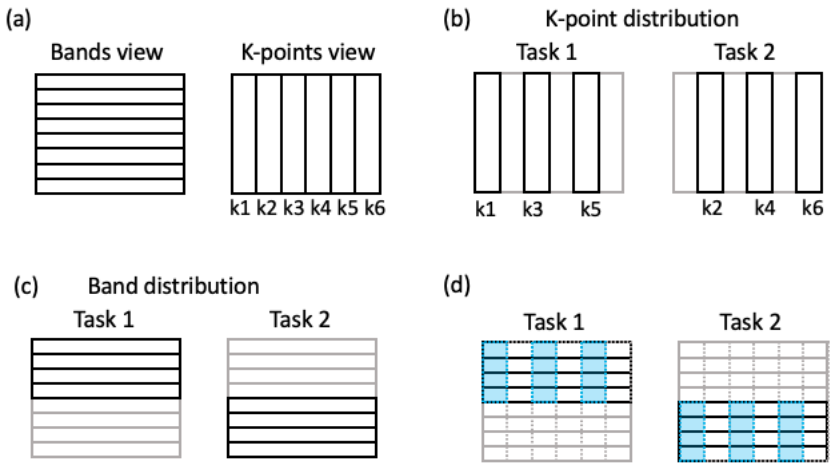

Figure 7.4 Visualization of bands as rows and k-points as columns. We note that we visualize bands as rows for consistency throughout the document; however, because Fortran is a column-major language, the view is swapped in memory (see Figure 7.3) (b) k-points are distributed round-robin. A black outline denotes which k-points have been assigned to which task. (c) The first step in both HDF5-based methods is to read-in contiguous blocks of bands. We divide these blocks evenly amongst tasks. In the case of two tasks, task 1 reads in the first half of bands, and task 2 reads in the second half of bands. (d) The blue stripes denote the data that task 1 must acquire to proceed with the calculation. The two HDF5 methods diverge in how they deliver this data.

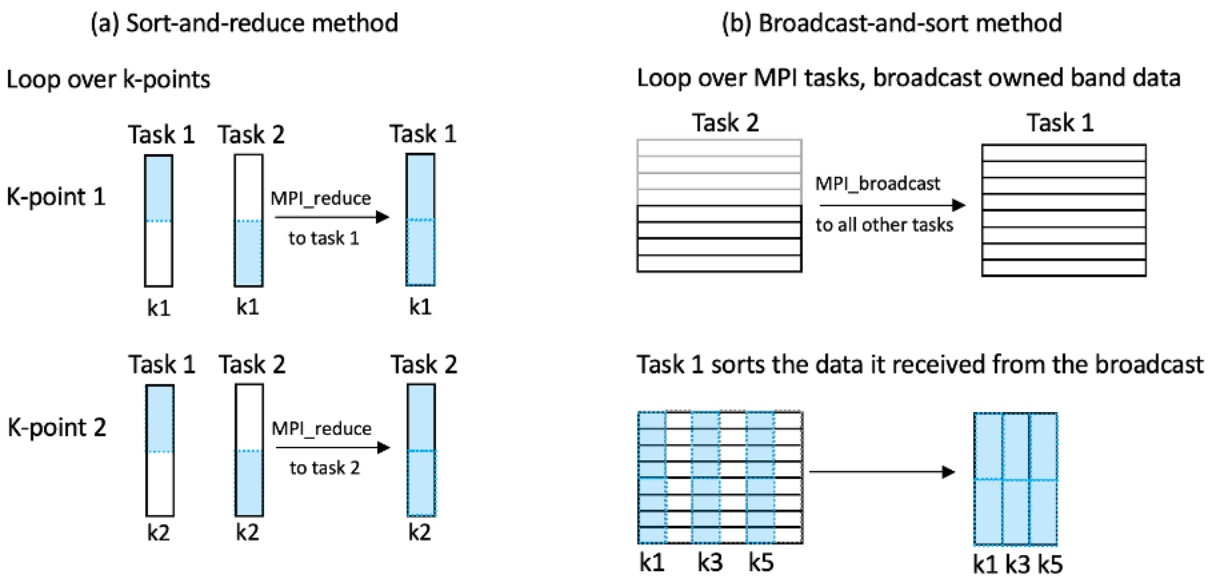

Figure 7.5 (a) Sort-and-reduce method. For k-point 1, task 1 already has the first half of the data it needs. Task 2 owns the second half. Each task creates an array, populates all entries of the array with 0, fills the appropriate region of the array with its k-point 1 data, then performs a sum reduction to task 1. Because each task's array contains a non-zero region that does not overlap with any other task's non-zero region, this is an effective way to send the data to task 1 without performing individual send/receive calls. For k-point 2, the procedure is identical, except the data is sum-reduced to task 2 instead of task 1. We iterate through all k-points, reducing to the tasks that own the k-point. (b) Broadcast-and-sort method. Figure depicts the task 2 broadcast step. In this case, task 1 receives a broadcast of all of task 2's band data. Task 1 sorts the band data and stores only the data corresponding to the k-points it has been assigned. In a general case with *m* MPI tasks, after one broadcast call, Task 1 will have 2/*m* the total data it needs. In this case, because there are only two tasks, Task 1 has all required data after just the task 2 broadcast.

7.3.3 Results

Benchmarking MPI-based parallel performance is a nuanced topic, and it is difficult to predict a priori which of the two methods will perform better, given the vast array of factors that influence the performance of MPI collective calls.[18–22] Because it is unclear which method may ultimately out-perform the other, we concurrently implement the sort-and-reduce method and the broadcast-and-sort method, where a coworker implemented the broadcast method, and the author developed the reduce method.[23] A comparison of benchmark timings for the chunked-broadcast

method, the reduce method, and the binary method is shown in Table 7.8 for a 6.7 GB wavefunction file with 50 bands and 976 k-points.

Table 7.8 Benchmarks for sort-and-reduce, broadcast-and-sort, and binary read-in methods.

	HDF5		
MPI tasks	Sort-Reduce	Broadcast-Sort	Binary
4	21	2	57
36	8	3	67
144	8	4	67
288	8	6	59
576	8	2	61
1296	18	2	59

The broadcast-and-sort method outperforms both the binary and the reduce method. The fact that the reduce method sends less data per MPI task ultimately does not offset the fewer overall MPI calls of the broadcast-and-reduce method. Given this, the broadcast-and-reduce method is likely to be superior for any case where a large number of k-points are involved, as its number of MPI calls are k-point-independent. The reduce method may prove superior in cases of "few k-points, many bands"-type systems, as it avoids broadcasting a large amount of unnecessary data in these scenarios. However, while the sigma and epsilon codes are often run as "few k-points, many bands," the most common use-case for the absorption code is "many k-points, few bands." Thus, the broadcast-and-sort method is the superior general-use algorithm, and its lack of k-point dependence in number of MPI calls is likely the cause of its stability in read-time across 4 to 1296 MPI tasks.

A logical next step in development would be to re-work the reduce method so that the reduce call is extracted from the k-point loop. That is, make the reduction once per MPI task, such that all staging and reducing is performed for all k-points assigned to an MPI task simultaneously. This requires a more compute-intensive staging step, but makes MPI calls for the exact amount of data required, and does it only once for each MPI task, combining the best features of the two methods. An additional future step would be to probe the underlying MPI implementations, and run additional tests on other implementations beyond OpenMPI.

7.4 Conclusion

We have introduced HDF5 wavefunction read-in capability to two parts of the BerkeleyGW code: the sigma and absorption executables. In sigma, we see major improvement in read time for the wavefunction, and have successfully alleviated a severe bottleneck in the code. In the absorption code, we implement two read-in algorithms, finding that the "broadcast-and-sort" method outperforms the "sort-and-reduce" method. The new HDF5 method in absorption outperforms the previous Fortran binary method by an order of magnitude. The HDF5 method in sigma outperforms its previous Fortran binary method by two orders of magnitude. This difference in degree of improvement is on account of the fact that the sigma code parallelization scheme is compatible with the manner in which the wavefunction is stored in the HDF5 file, while the absorption parallelization scheme is at odds with the file layout. These developments enable compute-efficient access to GW calculations on larger systems than previously possible.

7.5 References

1) Deslippe, J.; Samsonidze, G.; Strubbe, D. A.; Jain, M.; Cohen, M. L.; Louie, S. G. BerkeleyGW: A Massively Parallel Computer Package for the Calculation of the Quasiparticle and Optical Properties of Materials and Nanostructures. *Comput. Phys. Commun.* **2012**, *183* (6), 1269–1289. https://doi.org/10.1016/j.cpc.2011.12.006.

(2) Rohlfing, M.; Louie, S. G. Electron-Hole Excitations and Optical Spectra from First Principles. *Phys. Rev. B* **2000**, *62* (8), 4927–4944. https://doi.org/10.1103/PhysRevB.62.4927.

(3) Hybertsen, M. S.; Louie, S. G. Electron Correlation in Semiconductors and Insulators: Band Gaps and Quasiparticle Energies. *Phys. Rev. B* **1986**, *34* (8), 5390–5413. https://doi.org/10.1103/PhysRevB.34.5390.

(4) van Setten, M. J.; Weigend, F.; Evers, F. The GW-Method for Quantum Chemistry Applications: Theory and Implementation. *J. Chem. Theory Comput.* **2013**, *9* (1), 232–246. https://doi.org/10.1021/ct300648t.

(5) Golze, D.; Dvorak, M.; Rinke, P. The GW Compendium: A Practical Guide to Theoretical Photoemission Spectroscopy. *Front. Chem.* **2019**, *7*.

(6) Reining, L. The GW Approximation: Content, Successes and Limitations. *WIREs Comput. Mol. Sci.* **2018**, *8* (3), e1344. https://doi.org/10.1002/wcms.1344.

(7) Del Ben, M.; da Jornada, F. H.; Canning, A.; Wichmann, N.; Raman, K.; Sasanka, R.; Yang, C.; Louie, S. G.; Deslippe, J. Large-Scale GW Calculations on Pre-Exascale HPC Systems. *Comput. Phys. Commun.* **2019**, *235*, 187–195. https://doi.org/10.1016/j.cpc.2018.09.003.

(8) Derek Vigil-Fowler. Some Interesting Eagle Timings (private correspondence), 2019.

(9) de Supinski, B. R.; Karonis, N. T. Accurately Measuring MPI Broadcasts in a Computational Grid. In *Proceedings. The Eighth International Symposium on High Performance Distributed Computing (Cat. No.99TH8469)*; IEEE Comput. Soc: Redondo Beach, CA, USA, 1999; pp 29–37. https://doi.org/10.1109/HPDC.1999.805279.

(10) Hoefler, T.; Siebert, C.; Rehm, W. A Practically Constant-Time MPI Broadcast Algorithm for Large-Scale InfiniBand Clusters with Multicast. In *2007 IEEE International Parallel and Distributed Processing Symposium*; IEEE: Long Beach, CA, USA, 2007; pp 1–8. https://doi.org/10.1109/IPDPS.2007.370475.

(11) Folk, M.; Heber, G.; Koziol, Q.; Pourmal, E.; Robinson, D. An Overview of the HDF5 Technology Suite and Its Applications. In *Proceedings of the EDBT/ICDT 2011 Workshop on Array Databases*; AD '11; Association for Computing Machinery: New York, NY, USA, 2011; pp 36–47. https://doi.org/10.1145/1966895.1966900.

(12) Byna, S.; Chou, J.; Rubel, O.; Prabhat; Karimabadi, H.; Daughter, W. S.; Roytershteyn, V.; Bethel, E. W.; Howison, M.; Hsu, K.-J.; Lin, K.-W.; Shoshani, A.; Uselton, A.; Wu, K. Parallel I/O, Analysis, and Visualization of a Trillion Particle Simulation. In *2012 International Conference for High Performance Computing, Networking, Storage and Analysis*; IEEE: Salt Lake City, UT, 2012; pp 1–12. https://doi.org/10.1109/SC.2012.92.

(13) Li, J.; Liao, W.; Choudhary, A.; Ross, R.; Thakur, R.; Gropp, W.; Latham, R.; Siegel, A.; Gallagher, B.; Zingale, M. Parallel NetCDF: A High-Performance Scientific I/O Interface. In *SC '03: Proceedings of the 2003 ACM/IEEE Conference on Supercomputing*; 2003; pp 39–39. https://doi.org/10.1109/SC.2003.10053.

(14) Lofstead, J.; Zheng, F.; Klasky, S.; Schwan, K. Adaptable, Metadata Rich IO Methods for Portable High Performance IO. In *2009 IEEE International Symposium on Parallel & Distributed Processing*; 2009; pp 1–10. https://doi.org/10.1109/IPDPS.2009.5161052.

(15) Byna, S.; Breitenfeld, S.; Dong, B.; Koziol, Q.; Pourmal, E.; Robinson, D.; Soumagne, J.; Tang, H.; Vishwanath, V.; Warren, R. ExaHDF5: Delivering Efficient Parallel I/O on Exascale Computing Systems. *J. Comput. Sci. Technol.* **2020**, *35* (1), 145–160. https://doi.org/10.1007/s11390-020-9822-9.

(16) Howison, M.; Koziol, Q.; Knaak, D.; Mainzer, J.; Shalf, J. *Tuning HDF5 for Lustre File Systems*; LBNL-4803E; Lawrence Berkeley National Lab. (LBNL), Berkeley, CA (United States), 2010. https://www.osti.gov/biblio/1050648 (accessed 2022-11-22).

(17) Devendran, D.; Byna, S.; Dong, B.; Straalen, B. V.; Johansen, H.; Keen, N.; Samatova, N. F. Collective I/O Optimizations for Adaptive Mesh Refinement Data Writes on Lustre File System. 7.

(18) Hoefler, T.; Schneider, T.; Lumsdaine, A. Accurately Measuring Collective Operations at Massive Scale. In *2008 IEEE International Symposium on Parallel and Distributed Processing*; IEEE: Miami, FL, USA, 2008; pp 1–8. https://doi.org/10.1109/IPDPS.2008.4536494.

(19) Hoefler, T.; Lumsdaine, A.; Rehm, W. Implementation and Performance Analysis of Non-Blocking Collective Operations for MPI. In *Proceedings of the 2007 ACM/IEEE conference on Supercomputing - SC '07*; ACM Press: Reno, Nevada, 2007; p 1. https://doi.org/10.1145/1362622.1362692.

(20) Pjeˇsivac, J.; Angskun, T.; Bosilca, G.; Fagg, G. E. Performance Analysis of MPI Collective Operations. 18.

(21) Hunold, S.; Carpen-Amarie, A. MPI Benchmarking Revisited: Experimental Design and Reproducibility. 38.

(22) Worsch, T.; Reussner, R.; Augustin, W. On Benchmarking Collective MPI Operations. In *Recent Advances in Parallel Virtual Machine and Message Passing Interface*; Kranzlmüller, D., Volkert, J., Kacsuk, P., Dongarra, J., Eds.; Goos, G., Hartmanis, J., van Leeuwen, J., Series Eds.; Lecture Notes in Computer Science; Springer Berlin

Heidelberg: Berlin, Heidelberg, 2002; Vol. 2474, pp 271–279. https://doi.org/10.1007/3-540-45825-5_43.

(23) Mauro del Ben. Unpublished Results (private correspondence), 2021.

Chapter 8 - Conclusion

Our efforts in modeling the noble metal-adsorbate systems contained herein have allowed us some insight into the interactions between the two. In Chapters 3 and 4, we probe the interactions of the N_2 and H_2 adsorbates with silver atomic wires. Chapter 3 sets the stage for Chapter 4, performing benchmarking on DFT functionals for key parameters in the Ag_xN_2 (x = 4, 6, 8) systems, like binding energy and dipole moment, by comparing against higher level wavefunction-based methods like coupled cluster singles and doubles (CCSD). Additionally, we conduct a series of comparisons between the GGA functional BP86 and the long-range corrected functional LC-ωPBE. Here, we find that the GGA functional predicts a different ground-state geometry than LC-ωPBE. In absorption spectra computed with the same geometry, we find that BP86 gives rise to a number of spurious low-oscillator strength transitions and breaks the x- y- symmetry of the transverse plasmon excitation. Thus, we conclude that treatment of these systems with a long-range corrected DFT functional is important.

Based on orbital analysis on the hybridization of N_2 with the wires alongside analysis of the linear combinations of single-particle transitions that give rise to the peaks in the LR-TDDFT absorption spectrum, we identify transitions of interest at which to excite the wire: the longitudinal plasmon peak, the transverse plasmon peak, and a charge transfer peak whose energy in the LR-TDDFT absorption spectrum lay between the two. Through RT-TDDFT/ED calculations exciting at these energies, we find that excitation at high field strength into the charge transfer peak and the transverse plasmon mode lead to similar degrees of modest activation, while excitation into the longitudinal plasmon peak results in dissociation of the N_2. These results provided a starting point for the work carried out in Chapter 4.

In Chapter 4, we expand our initial RT-TDDFT/ED results on the activation and dissociation of N_2 by including a new orientation of the N_2 on the wire, by additionally probing the activation and dissociation of H_2 on the same wires, and by expanding the quantities of interest that we extract from our RT-TDDFT/ED calculations. In particular, we make heavy use of charge analysis to explore how charge is exchanged between the wire and adsorbate subsystems. We find that formation of a transient negative ion occurs in the systems that dissociate or strongly activate. N_2 demonstrates a clear trend in the degree of charge transfer with increasing electric field, whereas in H_2 this trend is less clear. In general, H_2 activates more readily than N_2 for the same electric field strength, adsorbate orientation, and excitation energy. We find that the activation of both H_2 and N_2 is dependent on the field strength and geometry, and that the longitudinal plasmon mode results in significantly more adsorbate activation than the transverse plasmon mode.

In Chapter 5, we take a drastically different approach to the investigation of the interaction of a small molecule with a noble metal system in order to investigate the interaction of the plasmon modes with the adsorbate. We apply the subspace summation method (Chapter 6) to probe how the presence or absence of the H_2 on the surface modifies the loss function (or simulated electron energy loss (EEL) spectrum). We learn that this interaction is quite complicated, and parsing out the various contributions to these interactions proved difficult. Despite this, we were able to observe qualitative changes to the EEL spectra between a clean Au(111) surface, an Au(111) surface with an H_2 molecule above the bridge site, and two H atoms adsorbed onto the top sites. We find that H_2 on the bridge site primarily mixes into an energy region that overlaps with the Au(111) d-band, though these bands project predominantly onto the H 1s. It is surprising that a relatively perturbative interaction between the H_2 and the

surface produces clear changes to the EEL spectrum. Two H atoms on the top sites hybridize significantly more into the "frontier region" of the surface, the bands around the Fermi level, and we observe large deviations of this EEL spectrum from the clean Au(111) surface.

This project was an exciting foray into application work utilizing approaches that have traditionally been in the domain of solid-state physics and materials science. The solid-state physics picture of plasmons and collective excitations is quite different than the quantum chemistry view. In the latter, we often think of plasmons as a type of linear combination of single-particle excitations, and systems large enough that the plasmon can be fully characterized with classical means to simply be one end of the limiting cases. This "quantum plasmon" view is central to our silver atomic wire work, and affords us a molecular orbital framework with which to relate our results. On the other hand, the solid-state physics picture often frames plasmons in the context of a free electron gas, relating quantum mechanical results like those obtained within the RPA back to the (familiar in their own domain) classical Drude model. I am still unsure quite how to conceptually merge these two pictures together in the context of plasmon-adsorbate interactions in (very) thin films, but my hope is that this work serves as a stepping-stone in this direction.

The works in Chapters 6 and 7 are computational development works at their core, performed in collaboration with Derek Vigil-Fowler (Chapters 6 and 7) and Mauro del Ben (Chapter 7). Chapter 5 is a particular application of the two computational developments in Chapter 6. The first development, the "subspace summation method," enables the exclusion or inclusion of arbitrary bands in the RPA polarizability of a material. The second development involves implementation of partial occupations to the BerkeleyGW code, which allows us to model metals in a computationally efficient way. Chapter 7 turns towards more "pure" high

performance computing work. That is, while the works of Chapter 6 require careful consideration of, and interfacing with, the underlying parallelism of the code, the works in Chapter 7 involve implementing changes to the parallel I/O of the code for the sole purpose of improving its performance on high performance computing machines. In doing so, we alleviated file I/O bottlenecks that surface when running large-scale calculations. I am grateful to have been afforded the opportunity to work on these sorts of projects, despite them being a bit outside the tradition view of physical chemistry research.

Overall, our investigations into plasmon-adsorbate interactions, ranging from the linear response and real-time electron-nuclear dynamics of atomic nanowires with H_2 and N_2, to the RPA EELS of H_2 on an Au(111) surface, provide us insight into the nature of these interactions. Our works in method developments and high performance computing developments facilitate the study of these interactions.

Appendix A - Supplemental Information for Chapter 4

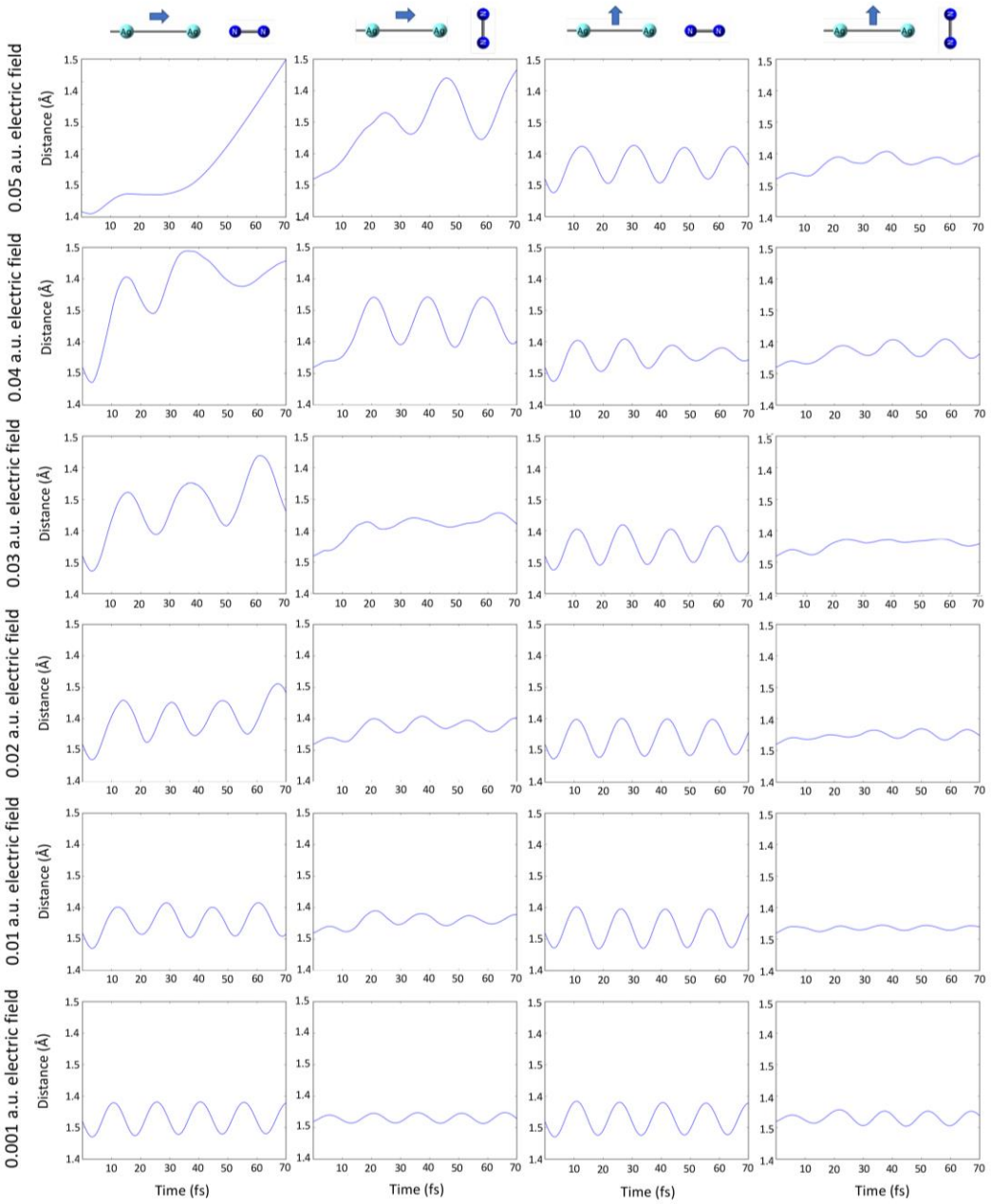

Figure A.1 RT-TDDFT/ED N-N bond lengths over 70 fs for each electric field polarization, electric field strength, and adsorbate orientation of Ag_8N_2.

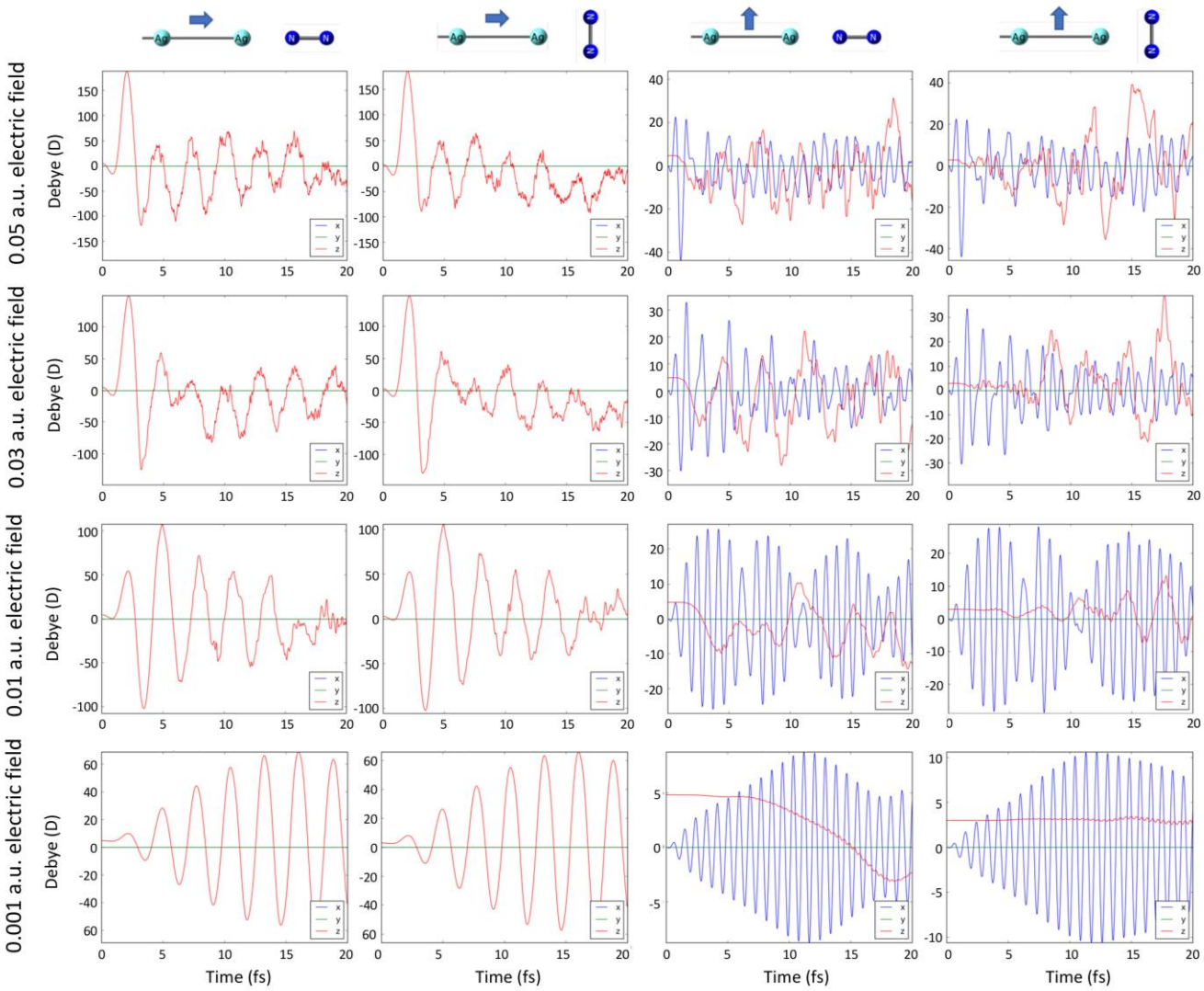

Figure A.2 Electron-only RT-TDDFT dipole moments over first 20 fs of simulation for each electric field polarization, electric field strength, and adsorbate orientation of Ag_8N_2. Note the y-axis scale varies by figure.

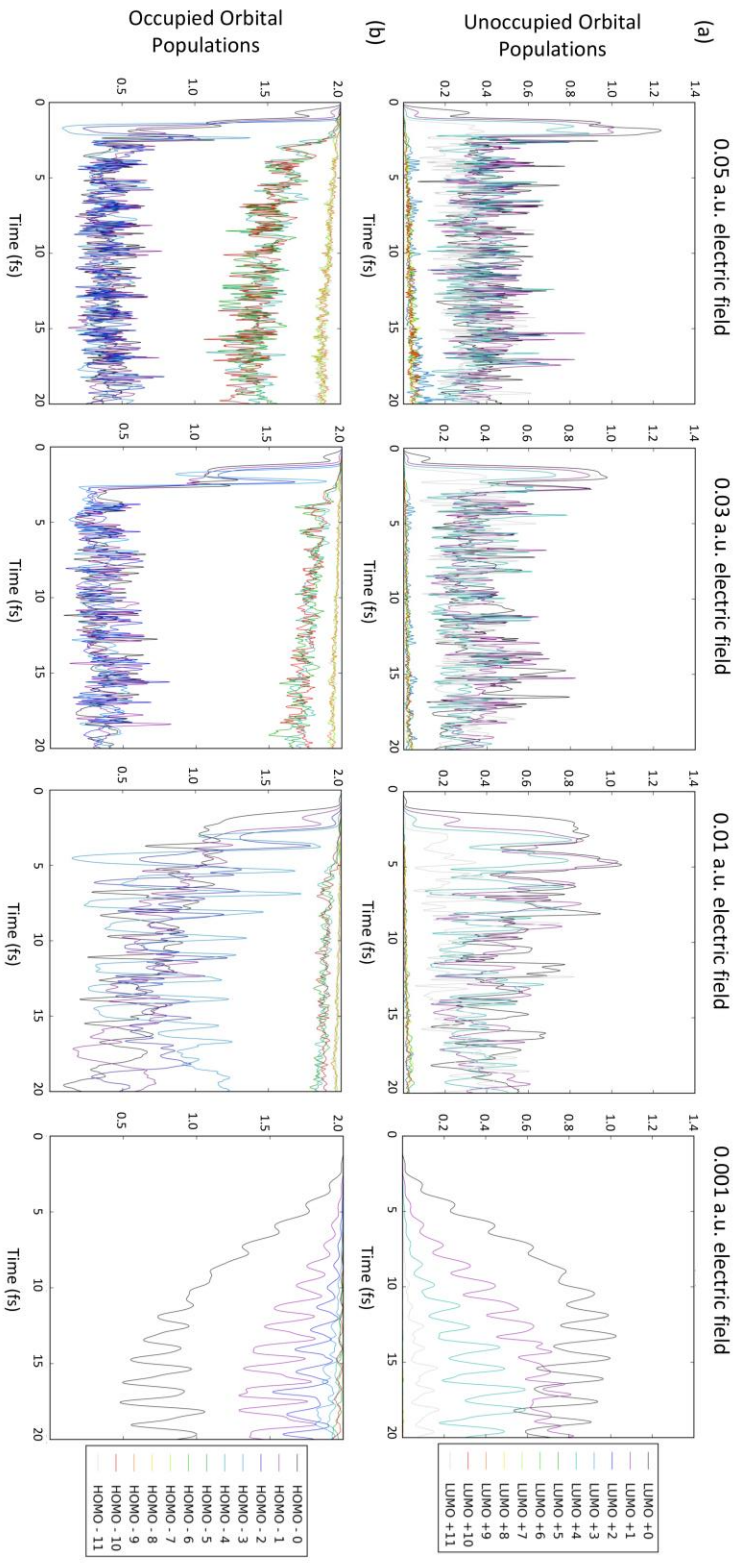

Figure A.3 Ag_8N_2 frontier orbital populations during first 20 fs of electron-only RT- TDDFT simulations for 0.05, 0.03, 0.01, and 0.001 a.u. electric field strengths of the longitudinal plasmon excitation and parallel-oriented N_2, (a) unoccupied orbitals, (b) occupied orbitals.

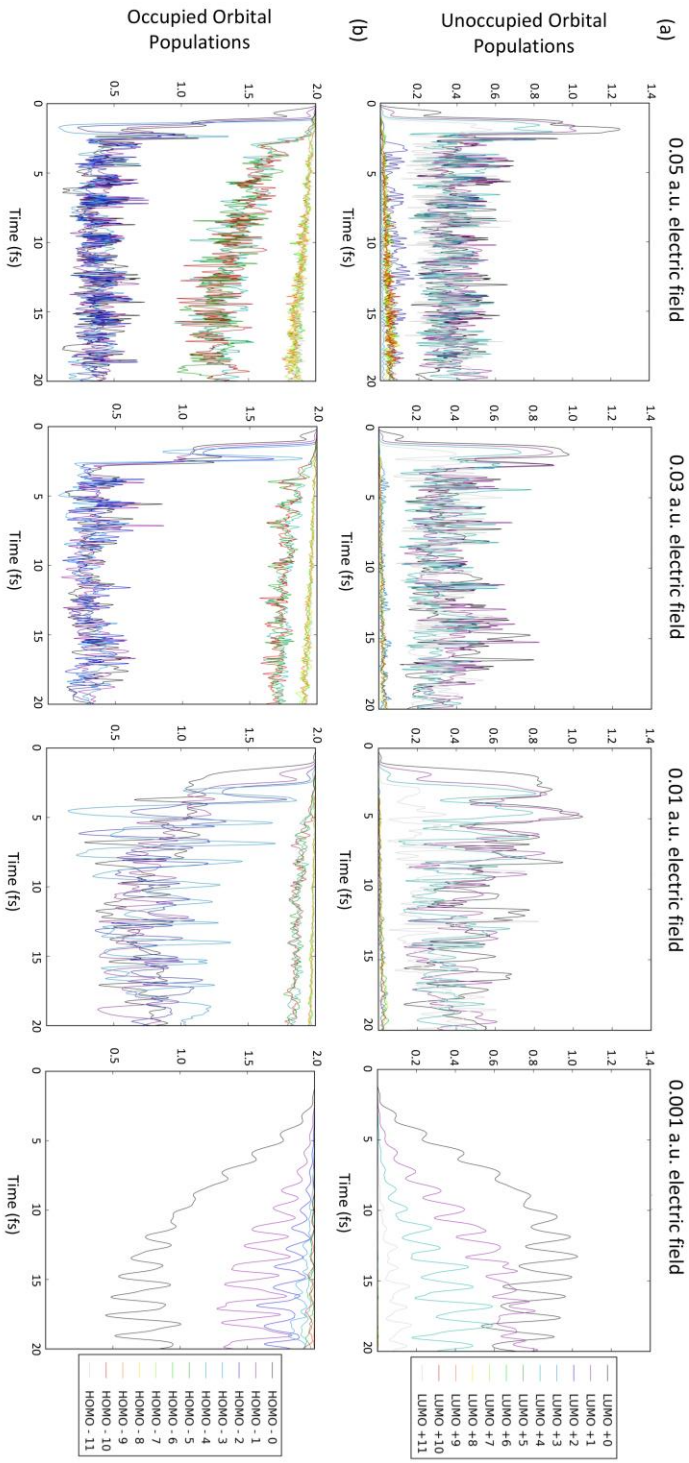

Figure A.4 Ag_8N_2 frontier orbital populations during first 20 fs of electron-only RT- TDDFT simulations for 0.05, 0.03, 0.01, and 0.001 a.u. electric field strengths of the longitudinal plasmon excitation and perpendicular-oriented N_2, (a) unoccupied orbitals, (b) occupied orbitals.

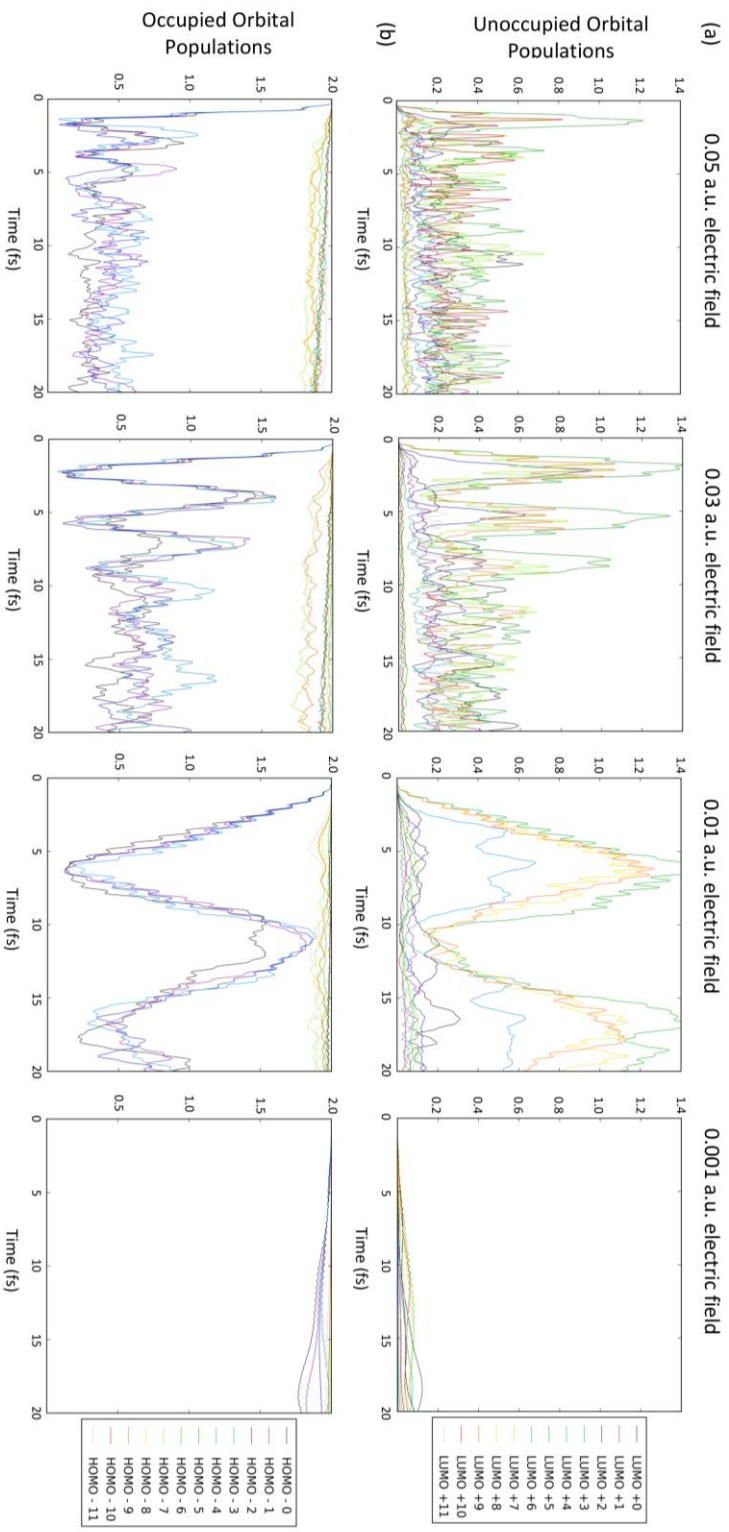

Figure A.5 Ag_8N_2 frontier orbital populations during first 20 fs of electron-only RT- TDDFT simulations for 0.05, 0.03, 0.01, and 0.001 a.u. electric field strengths of the transverse plasmon excitation and parallel-oriented N_2, (a) unoccupied orbitals, (b) occupied orbitals.

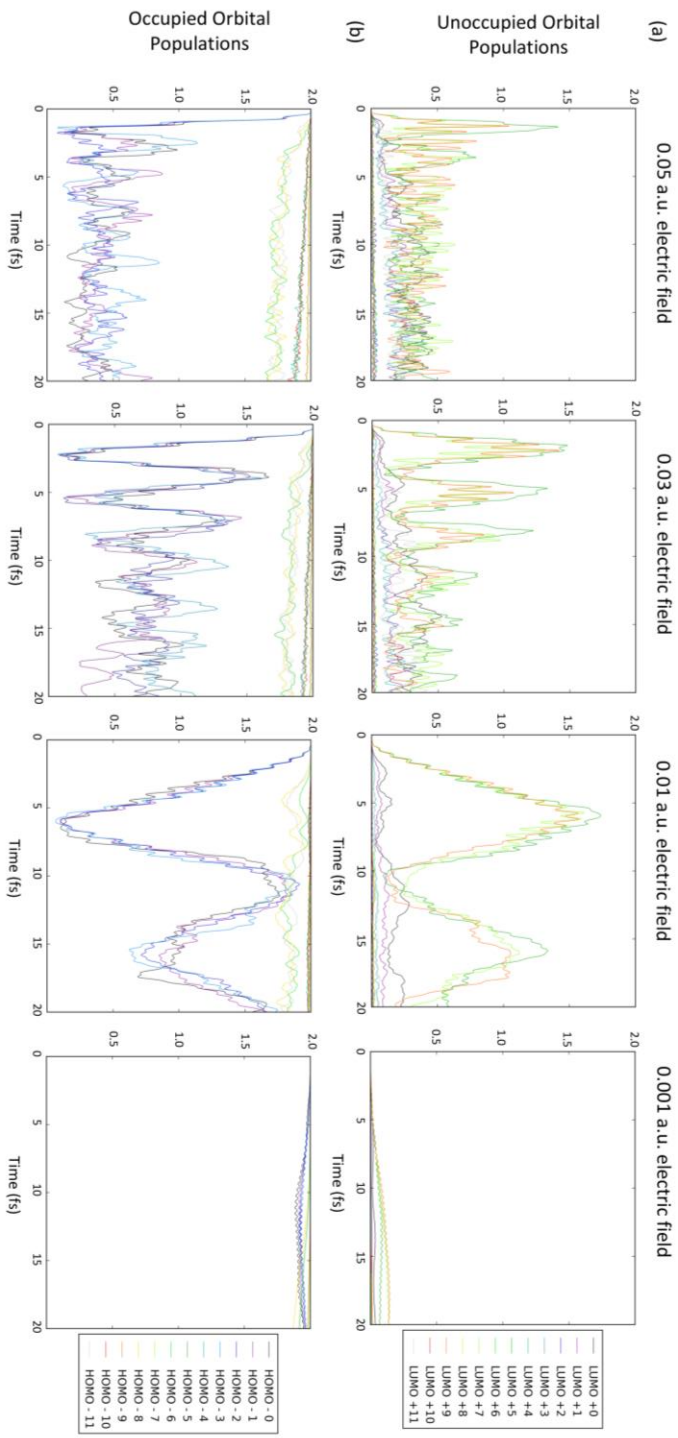

Figure A.6 Ag_8N_2 frontier orbital populations during first 20 fs of electron-only RT- TDDFT simulations for 0.05, 0.03, 0.01, and 0.001 a.u. electric field strengths of the transverse plasmon excitation and perpendicular-oriented N_2, (a) unoccupied orbitals, (b) occupied orbitals.

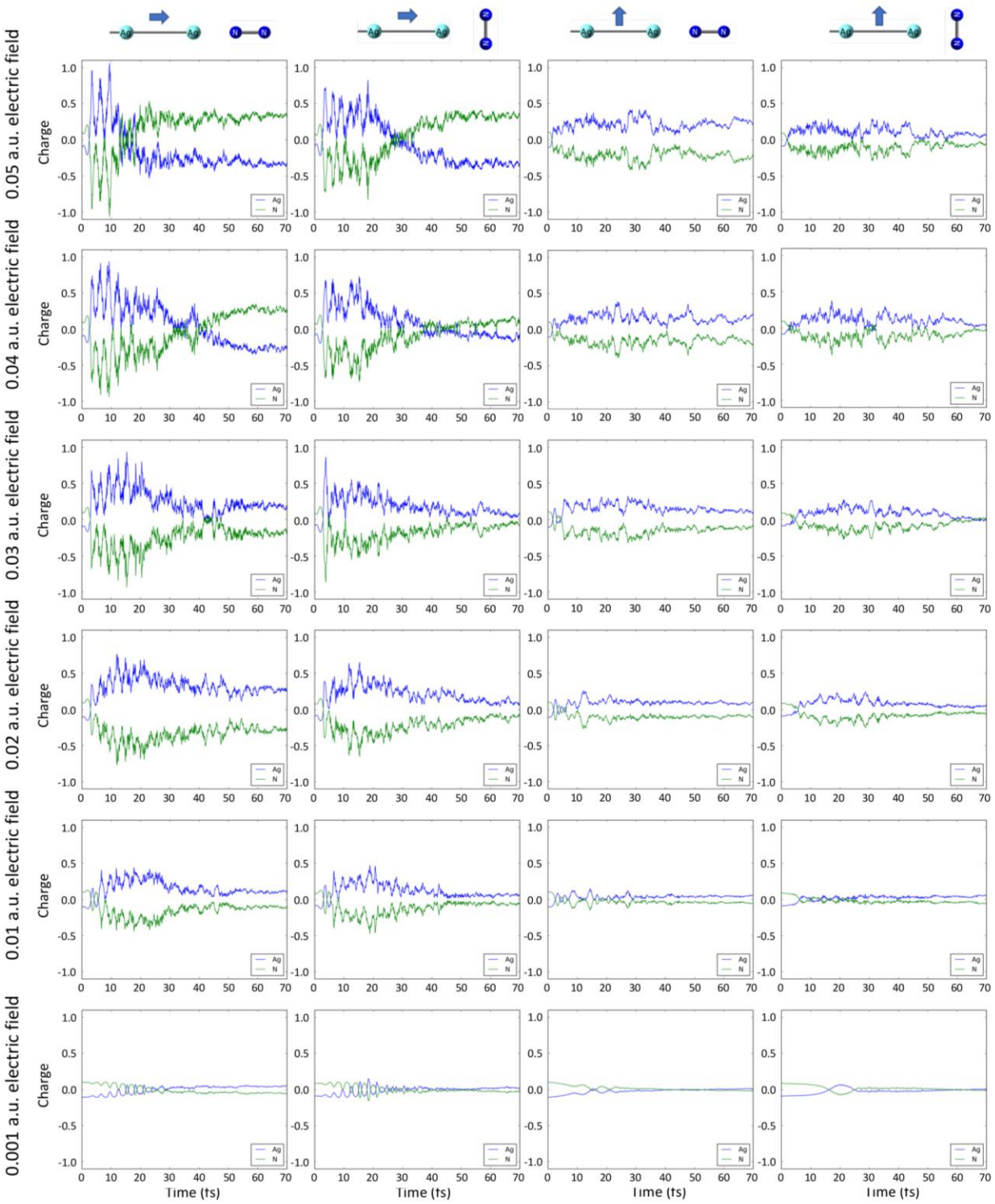

Figure A.7 Ag_8N_2 Hirshfeld charges over 70 fs of RT-TDDFT/ED simulation for each electric field polarization, electric field strength, and adsorbate orientation of Ag_8N_2, partitioned into Ag-charge and N-charge.

Table A.1 Time (fs) at which maximum Hirshfeld charge is obtained on N-subsystem ($|q_{N1} + q_{N2}|$) for each electric field polarization, electric field strength, and adsorbate orientation of Ag_8N_2.

	Field strength (a.u.)	0.05	0.04	0.03	0.02	0.01	0.001
Adsorbate orientation and electric field polarization	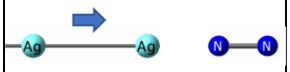	9.4	9.3	15.3	11.9	17.7	23.4
	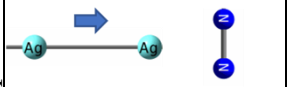	18.2	15.2	3.8	15.3	18.8	24.8
	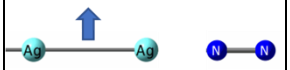	27.9	23.8	27.3	12.0	23.4	29.4
	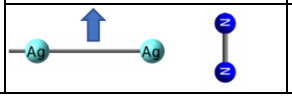	31.0	17.2	21.2	28.8	36.1	37.6

Table A.2 Time (fs) at which maximum Hirshfeld charge difference between N1 and N2 is obtained for each electric field polarization, electric field strength, and adsorbate orientation of Ag_8N_2.

	Field strength (a.u.)	0.05	0.04	0.03	0.02	0.01	0.001
Adsorbate orientation and electric field polarization	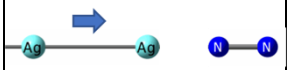	9.0	17.7	11.7	17.9	61.3	25.5
	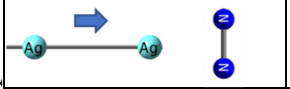	23.9	45.3	16.3	20.5	32.3	66.5
	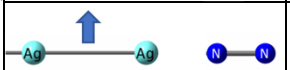	20.0	46.4	43.8	42.2	58.0	25.3
	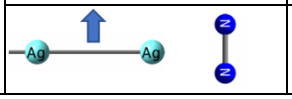	39.7	36.0	41.4	66.0	50.8	39.5

For high field strengths and longitudinal excitation, which are the more favorable conditions towards activation and dissociation, the time at which the maximum charge is obtained (Table A.1) and the time at which the maximum charge difference is obtained (Table A.2) is similar, except for the 0.04 a.u. field, longitudinal excitation, perpendicular case. For low activation cases, the trend is less clear.

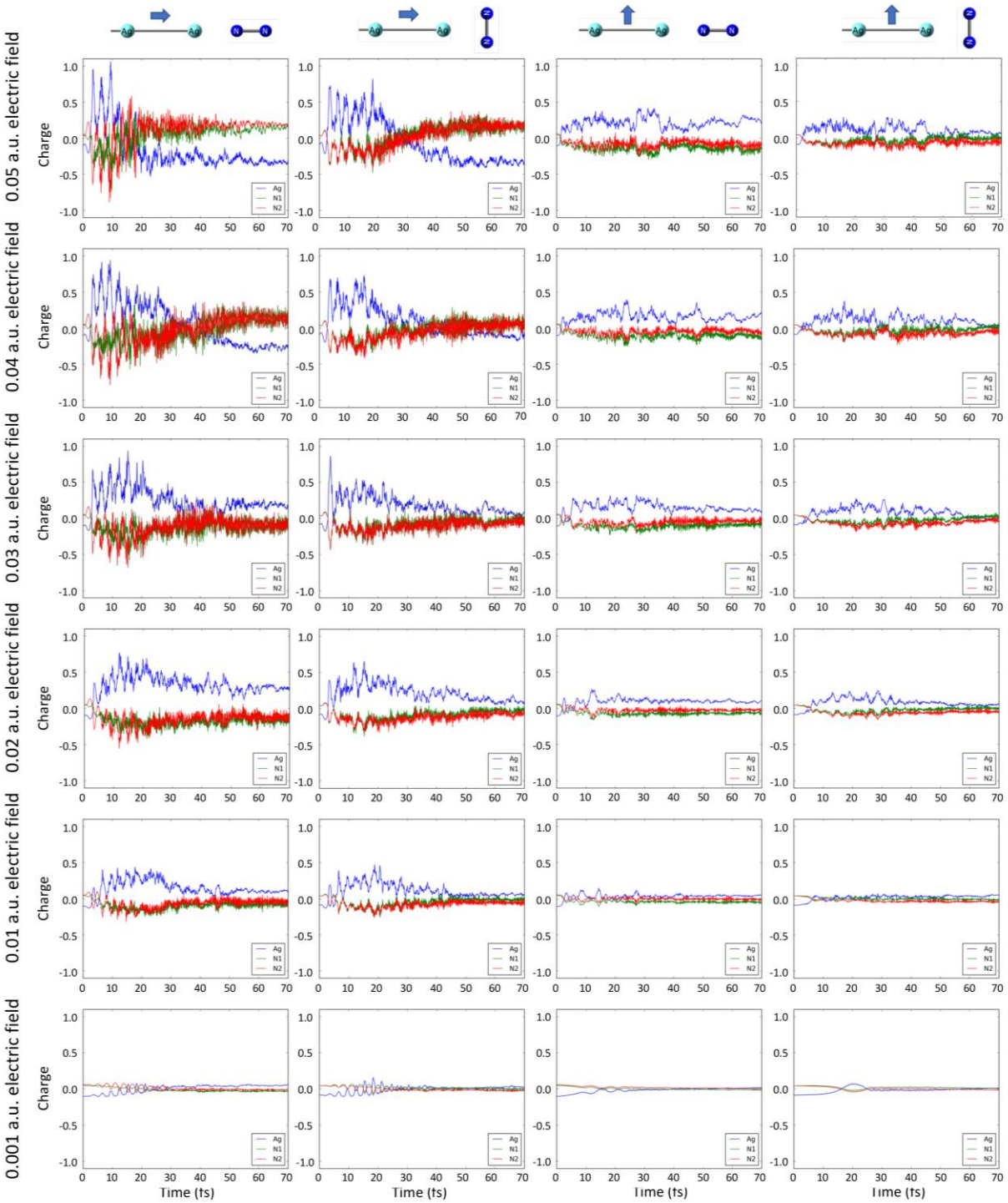

Figure A.8 Ag_8N_2 Hirshfeld charges over 70 fs of RT-TDDFT/ED simulation for each electric field polarization, electric field strength, and adsorbate orientation of Ag_8N_2, partitioned into Ag-charge, N1-charge, and N2-charge.

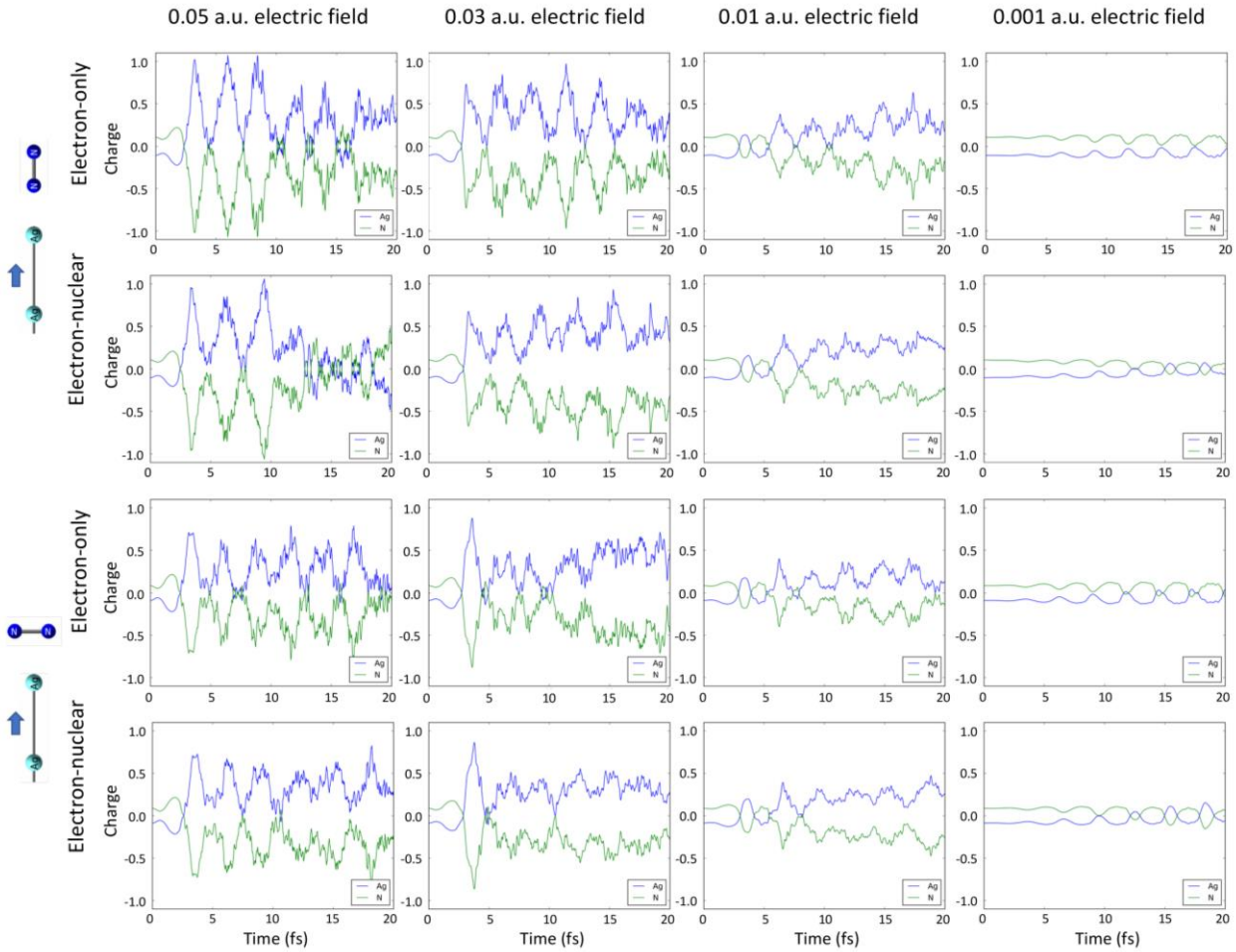

Figure A.9 Ag_8N_2 Hirshfeld charges over 70 fs of RT-TDDFT/ED simulation for each electric field polarization, electric field strength, and adsorbate orientation of Ag_8N_2, partitioned into Ag-charge, N1-charge, and N2-charge.

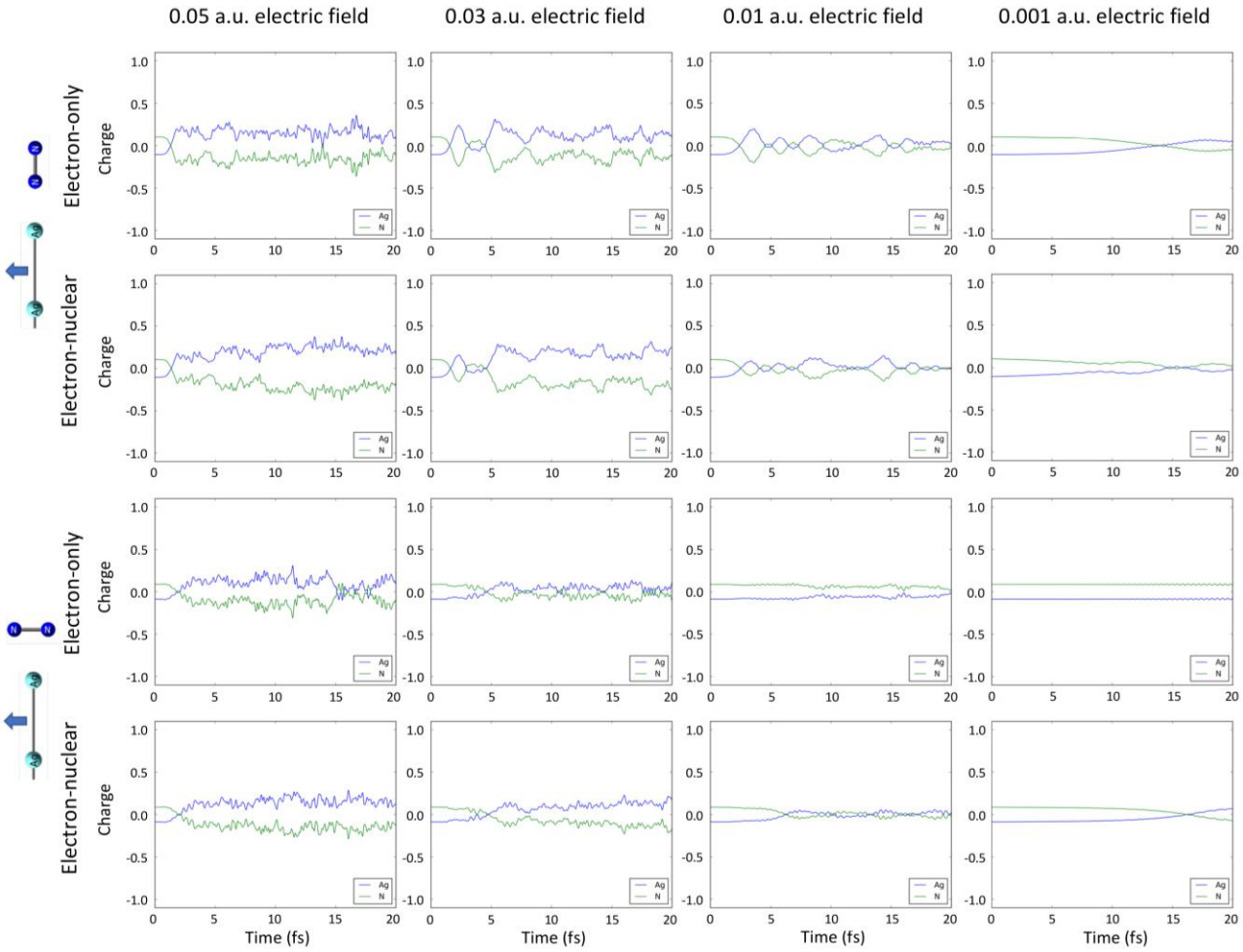

Figure A.10 Ag_8N_2 Hirshfeld charges over 20 fs of electron-only RT-TDDFT and 20 fs of RT-TDDFT/ED for the 0.05, 0.03, 0.01, and 0.001 a.u. field strengths of transverse plasmon excitation and parallel-oriented N_2 (top two rows) and perpendicular-oriented N_2 (bottom two rows).

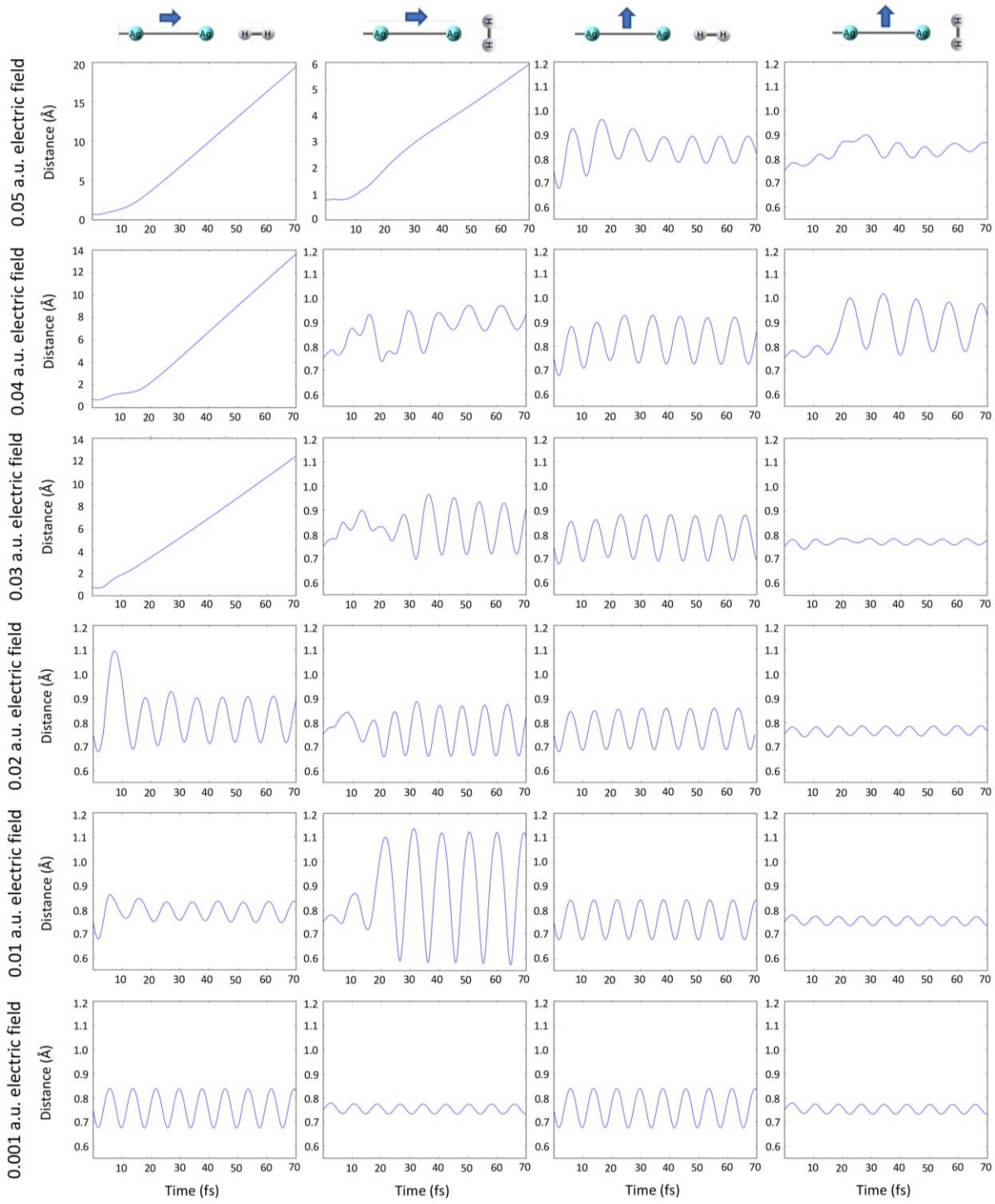

Figure A.11 RT-TDDFT/ED H-H bond lengths over 70 fs for each electric field polarization, electric field strength, and adsorbate orientation of Ag_8H_2.

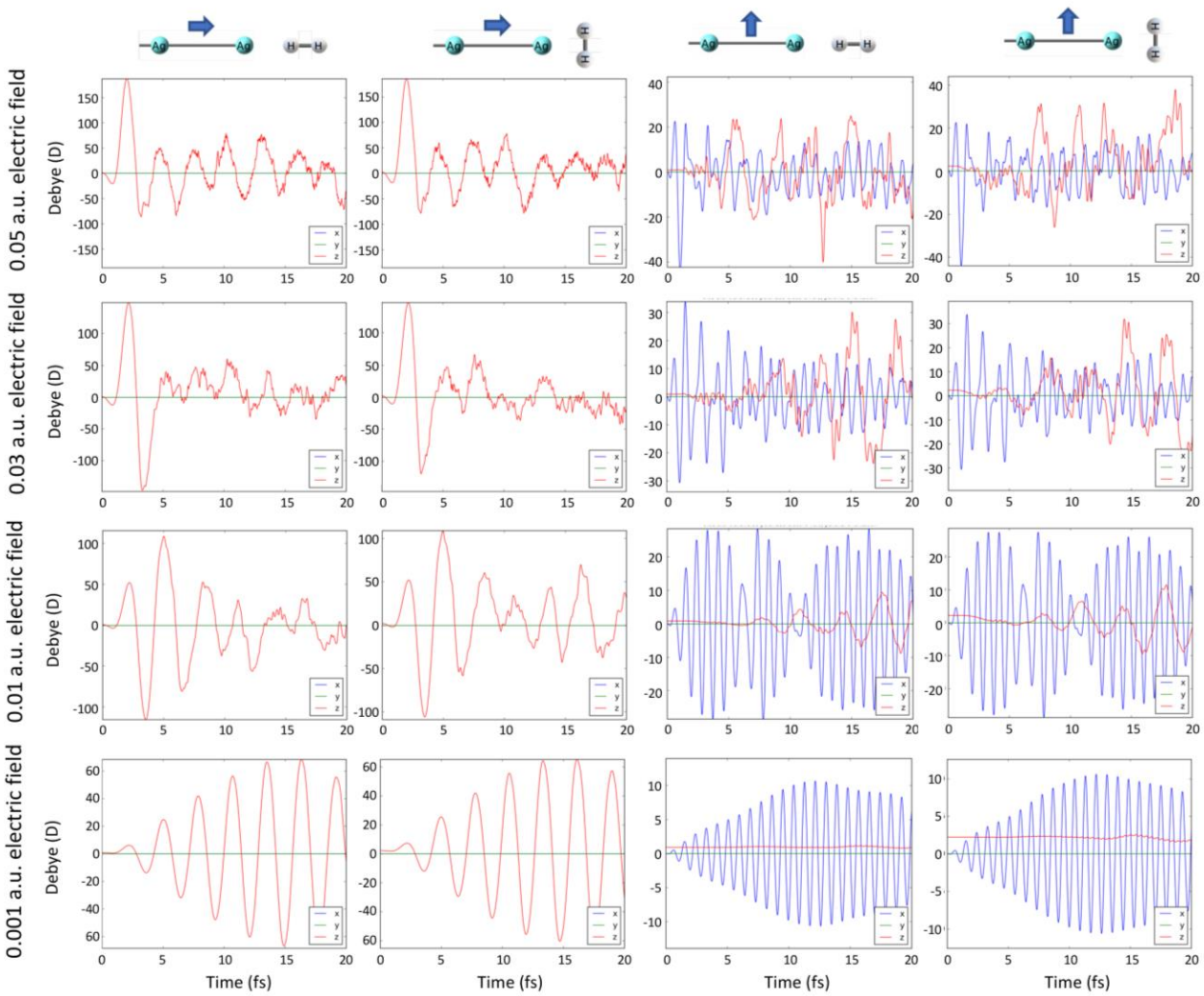

Figure A.12 Electron-only RT-TDDFT dipole moments over first 20 fs of simulation for each electric field polarization, electric field strength, and adsorbate orientation of Ag_8H_2. Note the y-axis scale varies by figure.

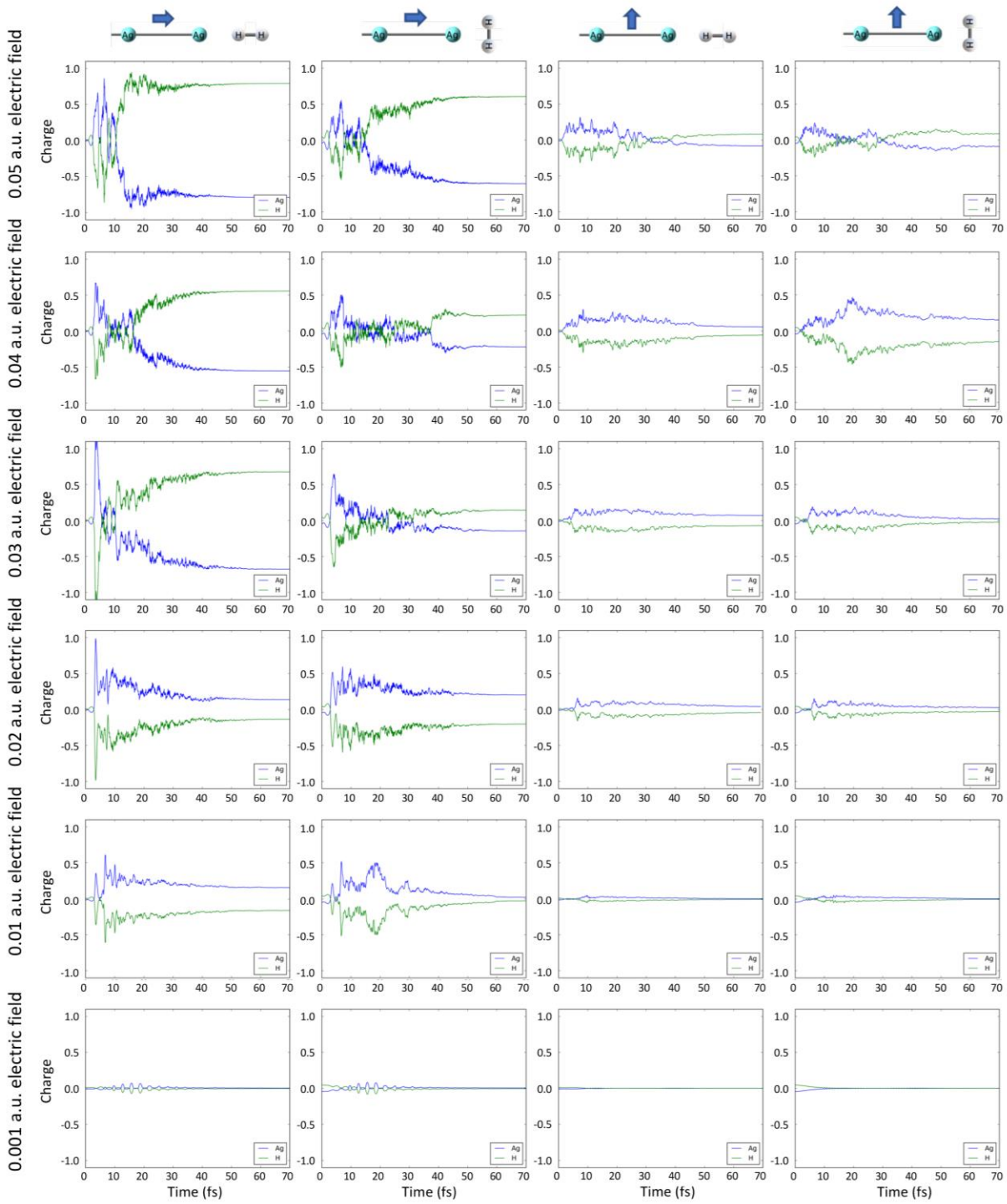

Figure A.13 Ag_8H_2 Hirshfeld charges over 70 fs of RT-TDDFT/ED simulation for each electric field polarization, electric field strength, and adsorbate orientation of Ag_8H_2, partitioned into Ag-charge and H-charge.

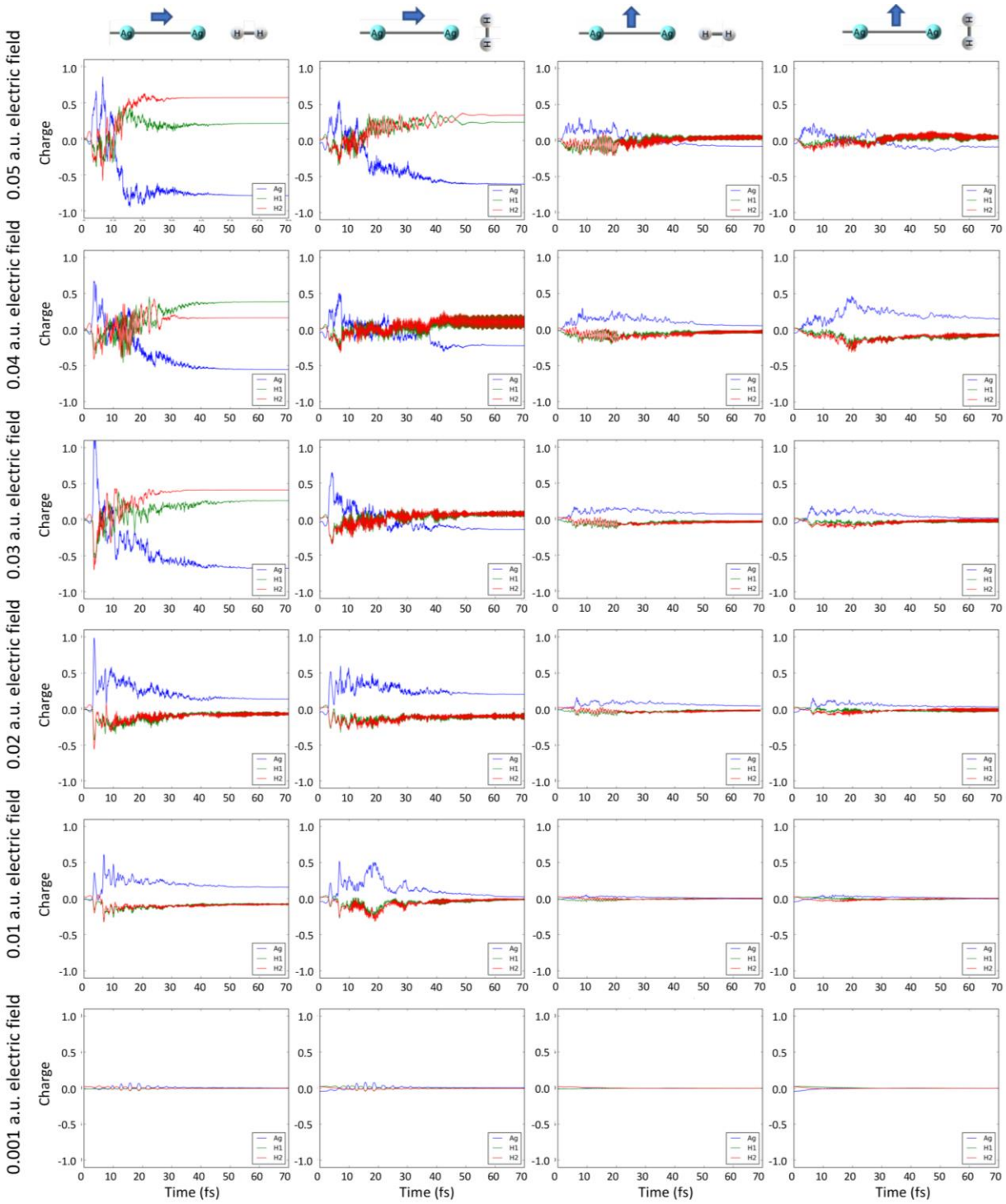

Figure A.14 Ag_8H_2 Hirshfeld charges over 70 fs of RT-TDDFT/ED simulation for each electric field polarization, electric field strength, and adsorbate orientation of Ag_8H_2, partitioned into Ag-charge, H1-charge, and H2-charge.

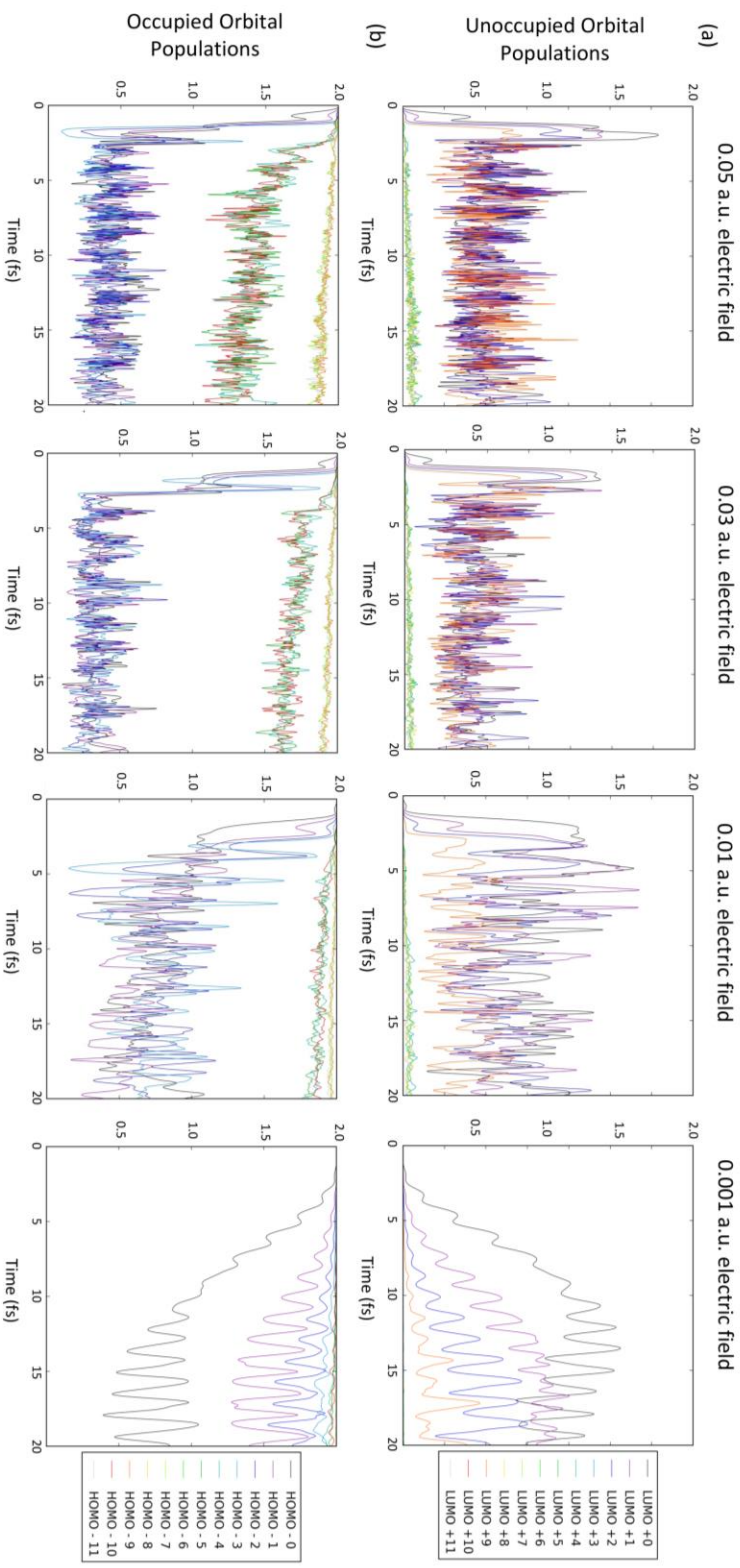

Figure A.15 Ag_8H_2 frontier orbital populations during first 20 fs of electron-only RT- TDDFT simulations for 0.05, 0.03, 0.01, and 0.001 a.u. electric field strengths of the longitudinal plasmon excitation and parallel-oriented H_2, (a) unoccupied orbitals, (b) occupied orbitals.

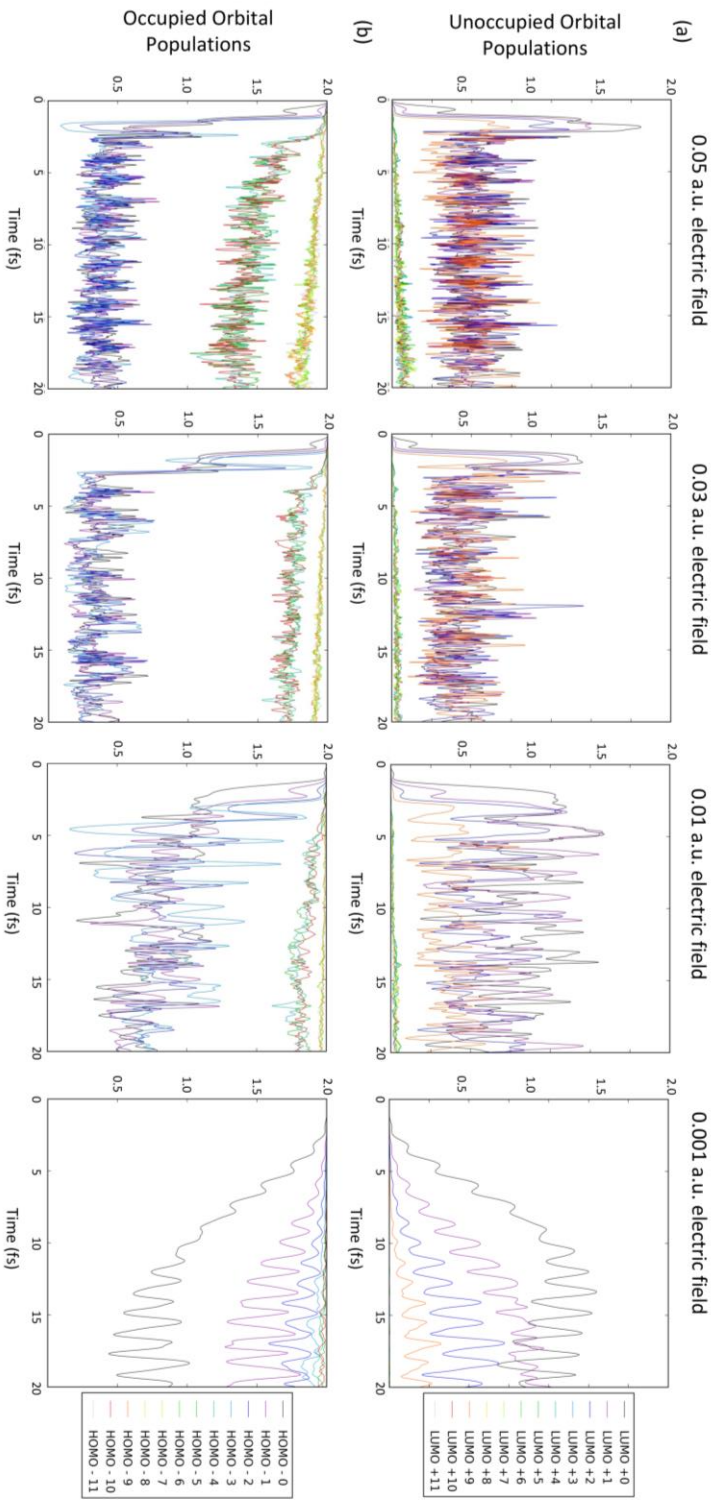

Figure A.16 Ag_8H_2 frontier orbital populations during first 20 fs of electron-only RT- TDDFT simulations for 0.05, 0.03, 0.01, and 0.001 a.u. electric field strengths of the longitudinal plasmon excitation and perpendicular-oriented H_2, (a) unoccupied orbitals, (b) occupied orbitals.

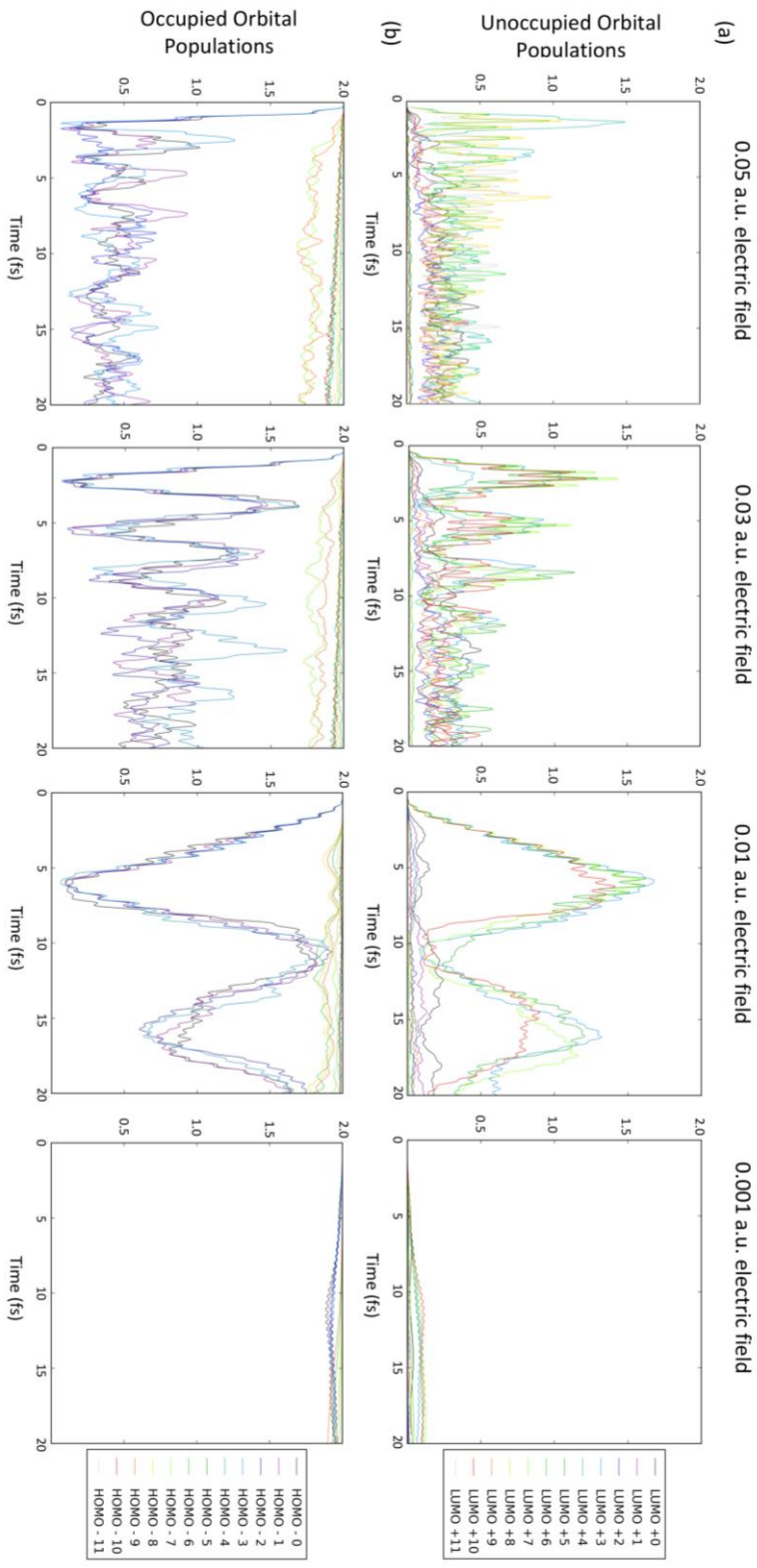

Figure A.17 Ag_8H_2 frontier orbital populations during first 20 fs of electron-only RT- TDDFT simulations for 0.05, 0.03, 0.01, and 0.001 a.u. electric field strengths of the transverse plasmon excitation and parallel-oriented H_2, (a) unoccupied orbitals, (b) occupied orbitals.

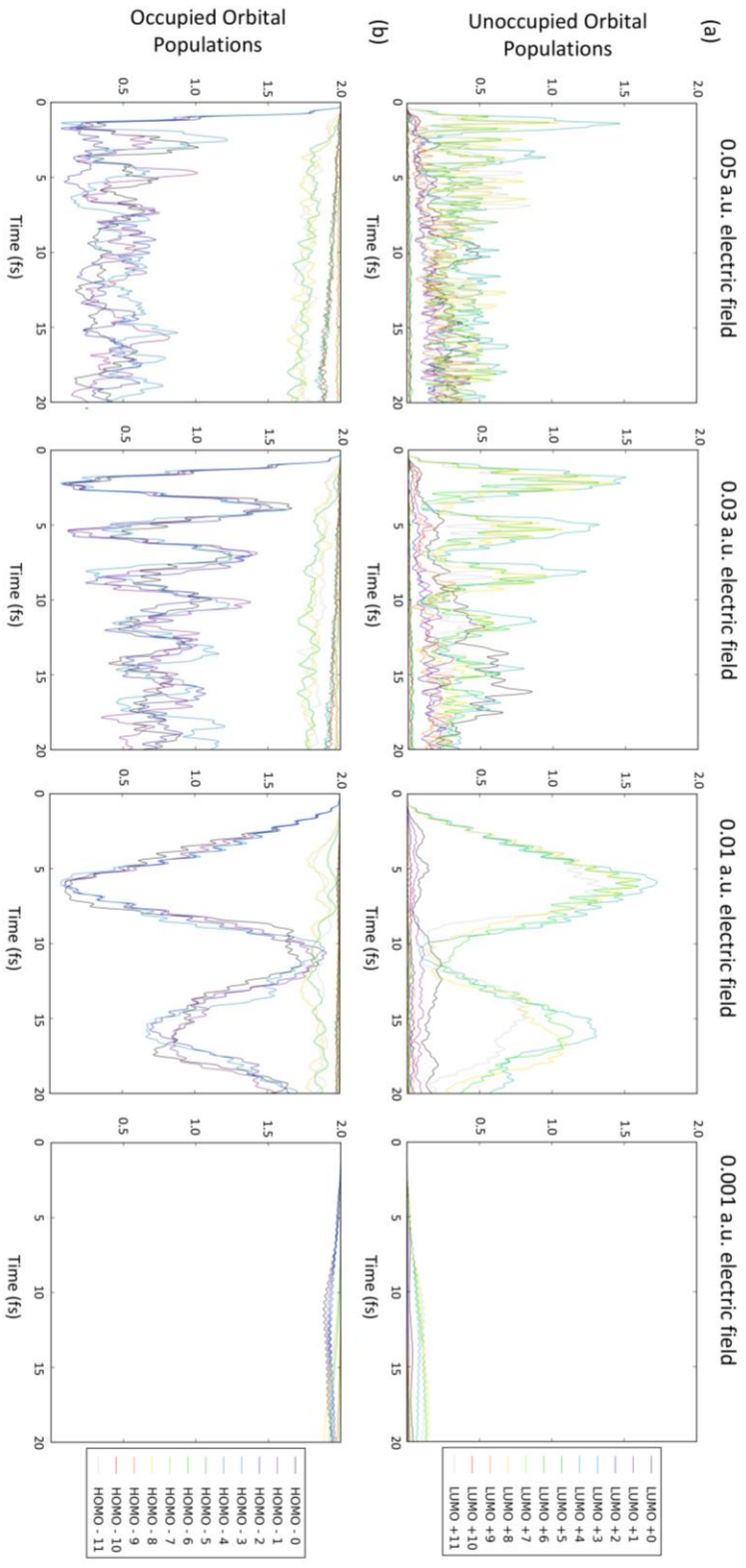

Figure A.18 Ag_8H_2 frontier orbital populations during first 20 fs of electron-only RT- TDDFT simulations for 0.05, 0.03, 0.01, and 0.001 a.u. electric field strengths of the transverse plasmon excitation and perpendicular-oriented H_2, (a) unoccupied orbitals, (b) occupied orbitals.

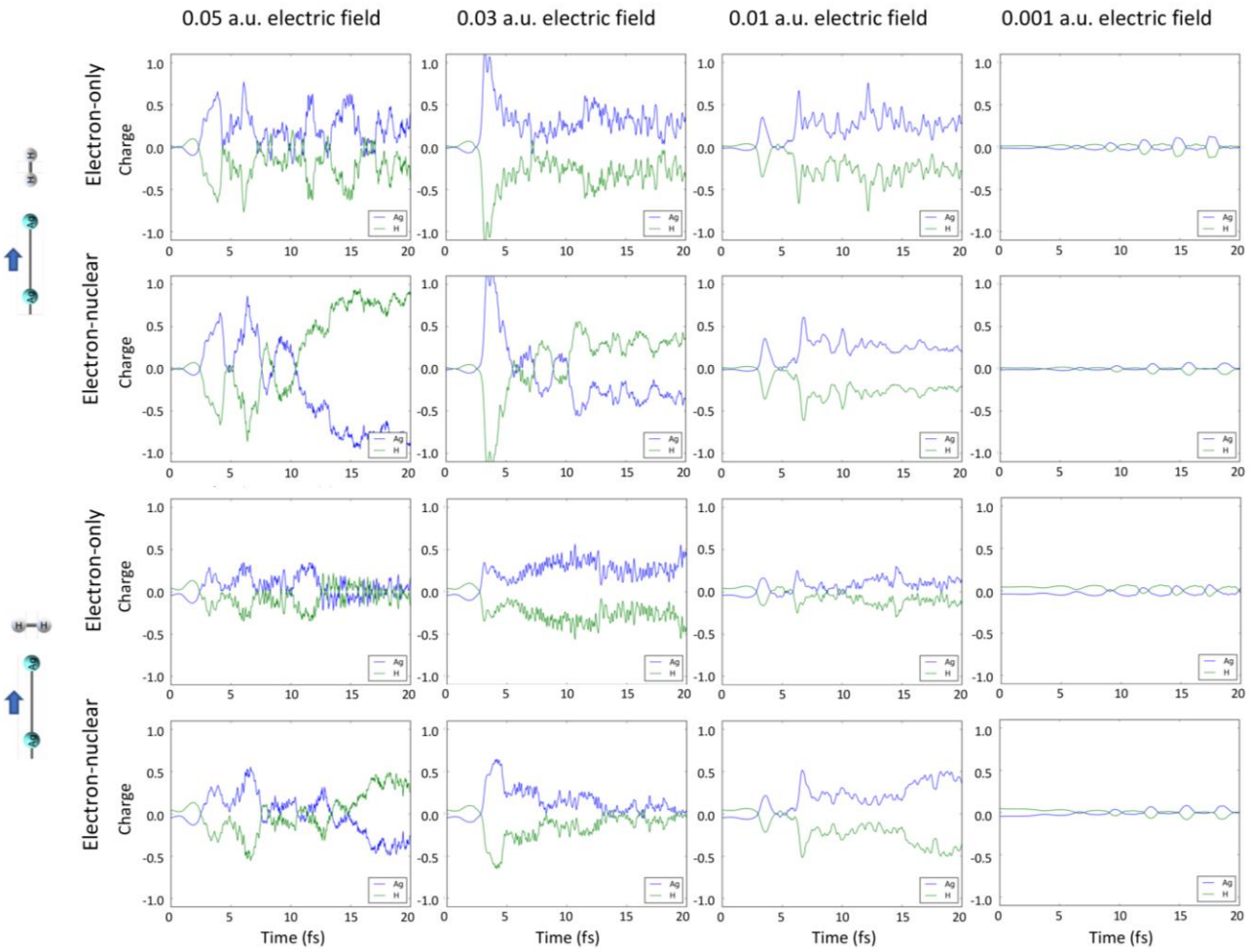

Figure A.19 Ag_8H_2 Hirshfeld charges over 20 fs of electron-only RT-TDDFT and 20 fs of RT-TDDFT/ED for the 0.05, 0.03, 0.01, and 0.001 a.u. field strengths of the longitudinal plasmon excitation and parallel-oriented H_2 (top two rows) and perpendicular-oriented H_2 (bottom two rows).

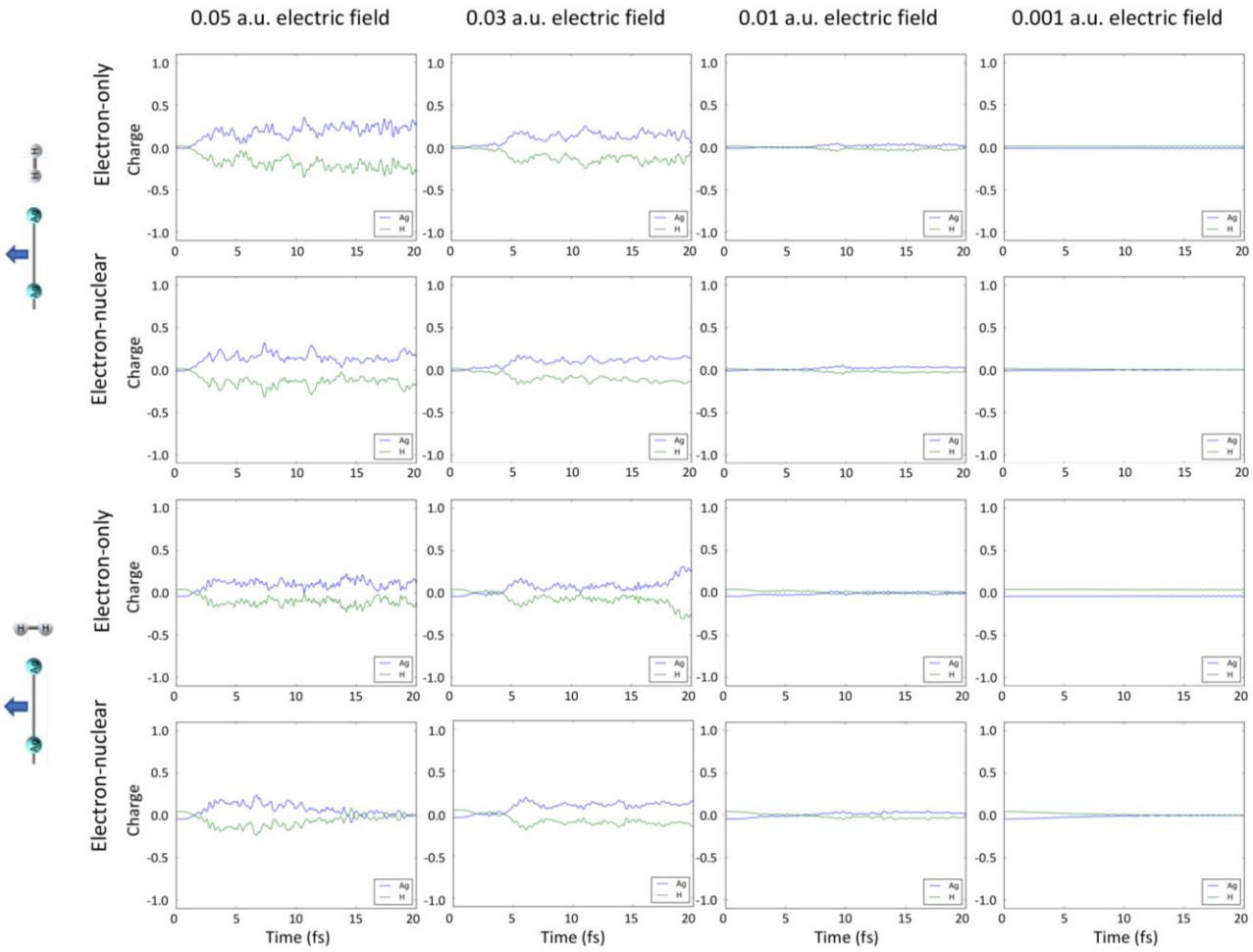

Figure A.20 Ag_8H_2 Hirshfeld charges over 20 fs of electron-only RT-TDDFT and 20 fs of RT-TDDFT/ED for the 0.05, 0.03, 0.01, and 0.001 a.u. field strengths of the transverse plasmon excitation and parallel-oriented H_2 (top two rows) and perpendicular-oriented H_2 (bottom two rows).

Table A.3 Time (fs) at which maximum Hirshfeld charge is obtained on H-subsystem ($|q_{H1} + q_{H2}|$) for each electric field polarization, electric field strength, and adsorbate orientation of Ag_8H_2.

Adsorbate orientation and electric field polarization	Field strength (a.u.)	0.05	0.04	0.03	0.02	0.01	0.001
	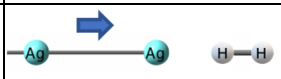	6.4	3.4	3.4	3.5	6.8	15.8
	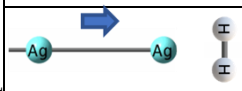	6.7	6.5	4.2	7.1	6.7	15.6
	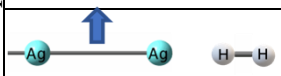	7.4	8.4	5.6	6.5	9.7	-
	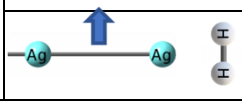	6.7	18.2	6.0	6.5	16.8	-

Table A.4 Time (fs) at which maximum Hirshfeld charge difference between H1 and H2 is obtained for each electric field polarization, electric field strength, and adsorbate orientation of Ag_8H_2.

Adsorbate orientation and electric field polarization	Field strength (a.u.)	0.05	0.04	0.03	0.02	0.01	0.001
	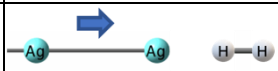	10.3	13.4	10.5	10.8	4.9	5.2
	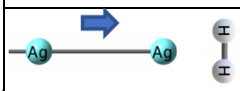	11.6	13.1	10.9	16.2	11.3	11.1
	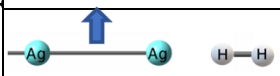	15.4	18.3	14.5	13.4	13.5	-
	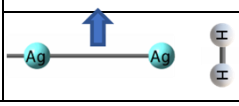	16.9	20.5	16.0	17.6	18.3	-

Compared to Ag_8N_2, both the maximum charge and maximum charge difference are obtained early in the simulation for the analogous Ag_8H_2 calculation, with a less clear correlation between degree of activation and the times that the maximum charge and charge differences are obtained.

Table A.5 Percent of N_2 atomic orbitals hybridized into the Ag_8N_2 molecular orbitals involved in longitudinal and transverse plasmon excitation.

Orbital		% N_2
L + 11		0.46
L + 9, 10	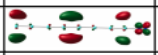	10.16
L + 7,8		18.97
L + 5,6	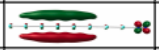	13.63
L + 4	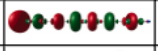	2.25
L + 2,3		82.36
L + 1	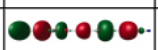	2.74
LUMO		1.17
HOMO		0.47
H - 1	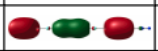	0.59
H - 2	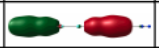	0.37
H - 3	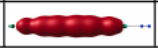	0.12

Table A.6 Percent of H_2 atomic orbitals hybridized into the Ag_8H_2 molecular orbitals involved in longitudinal and transverse plasmon excitation.

Orbital		% H_2
L + 10,11	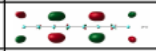	0.00
L + 9		0.32
L + 7,8	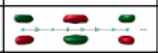	0.00
L + 5,6	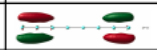	0.00
L + 3,4		0.00
L + 2	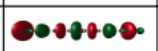	1.87
L + 1	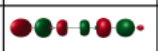	1.71
LUMO		0.60
HOMO		0.17
H - 1	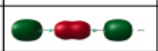	0.20
H - 2	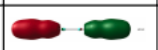	0.12
H - 3	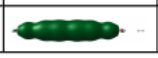	0.037

Appendix B - Permissions

Permission letter for Chapter 3:

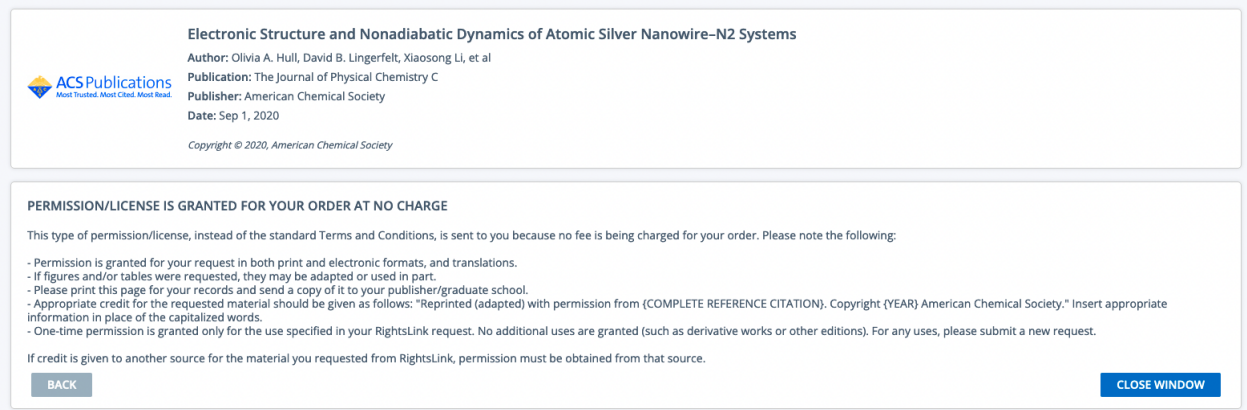

ACS Publications
Most Trusted. Most Cited. Most Read.

Electronic Structure and Nonadiabatic Dynamics of Atomic Silver Nanowire–N2 Systems

Author: Olivia A. Hull, David B. Lingerfelt, Xiaosong Li, et al
Publication: The Journal of Physical Chemistry C
Publisher: American Chemical Society
Date: Sep 1, 2020

Copyright © 2020, American Chemical Society

PERMISSION/LICENSE IS GRANTED FOR YOUR ORDER AT NO CHARGE

This type of permission/license, instead of the standard Terms and Conditions, is sent to you because no fee is being charged for your order. Please note the following:

- Permission is granted for your request in both print and electronic formats, and translations.
- If figures and/or tables were requested, they may be adapted or used in part.
- Please print this page for your records and send a copy of it to your publisher/graduate school.
- Appropriate credit for the requested material should be given as follows: "Reprinted (adapted) with permission from {COMPLETE REFERENCE CITATION}. Copyright {YEAR} American Chemical Society." Insert appropriate information in place of the capitalized words.
- One-time permission is granted only for the use specified in your RightsLink request. No additional uses are granted (such as derivative works or other editions). For any uses, please submit a new request.

If credit is given to another source for the material you requested from RightsLink, permission must be obtained from that source.

BACK CLOSE WINDOW

Permission letter for Figure 6.6:

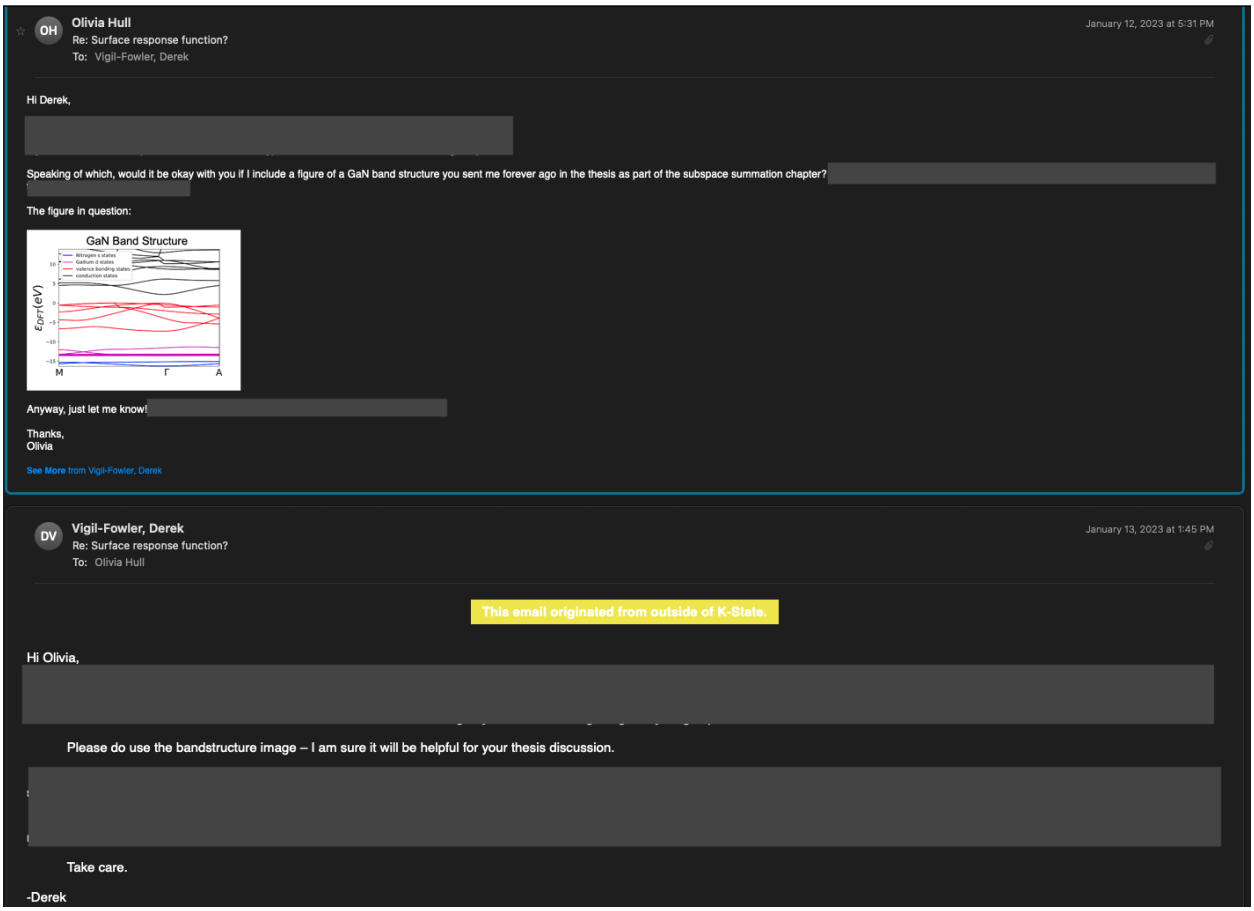

Olivia Hull January 12, 2023 at 5:31 PM
Re: Surface response function?
To: Vigil-Fowler, Derek

Hi Derek,

[redacted]

Speaking of which, would it be okay with you if I include a figure of a GaN band structure you sent me forever ago in the thesis as part of the subspace summation chapter? [redacted]

The figure in question:

Anyway, just let me know! [redacted]

Thanks,
Olivia

See More from Vigil-Fowler, Derek

Vigil-Fowler, Derek January 13, 2023 at 1:45 PM
Re: Surface response function?
To: Olivia Hull

This email originated from outside of K-State.

Hi Olivia,

[redacted]

Please do use the bandstructure image – I am sure it will be helpful for your thesis discussion.

[redacted]

Take care.

-Derek